Braunschweig Series on Mechanics No. 58-2005

Braunschweiger Schriften zur Mechanik

Dobromil Pryl

Influences of Poroelasticity on Wave Propagation: A Time Stepping Boundary Element Formulation

Mechanik-Zentrum

Technische Universität Braunschweig

Braunschweiger Schriften zur Mechanik Nr. 58-2005

Influences of Poroelasticity on Wave Propagation: A Time Stepping Boundary Element Formulation

von

Dobromil Pryl

aus Prag

Institut für Angewandte Mechanik

Technische Universität Braunschweig

Herausgegeben vom Mechanik-Zentrum der
Technischen Universität Braunschweig

Schriftleiter: Prof. Dr. rer. nat. H. Antes

Institut für Angewandte Mechanik
Postfach 3329
38023 Braunschweig

Tel.: 0531 / 391-7102
Fax: 0531 / 391-5843

Vom Fachbereich Bauingenieurwesen der Technischen Universität
Carolo-Wilhelmina zu Braunschweig zur Erlangung des Grades
eines Doktor-Ingenieurs (Dr.-Ing.) genehmigte Dissertation

Eingereicht am 21. Dezember 2004
Mündliche Prüfung am 21. Juni 2005

Berichterstatter
Univ.-Prof. Dr.-Ing. M. Schanz
Univ.-Prof. Dr.-Ing. W. Ehlers

BSM 58-2005
ISBN 3-920395-57-3

Dobromil Pryl

Kurzfassung

Zur Simulation von Wellenausbreitungsvorgängen in poroelastischen Kontinua wird in dieser Arbeit die Randelementmethode (BEM) benutzt. Mit den von Lubich entwickelten Faltungsquadraturverfahren kann ein Zeitschrittalgorithmus aufbauend auf den laplacetransformierten Fundamentallösungen formuliert werden. Die bestehende drei-dimensionale Formulierung wurde auf zwei-dimensionale Problemstellungen erweitert und eine Formulierung für inkompressible Konstituierende entwickelt. Weiterhin wurden gemischte Elemente implementiert und getestet.
Zweiphasenmaterialien weisen neben der Kompressibilität der Konstituierenden noch eine Strukturkompressibilität auf. Ist die Kompressibilität einer Komponente vernachlässigbar klein im Vergleich zur Strukturkompressibilität, kann die Komponente inkompressibel modelliert werden. Für den Fall, dass sowohl das Fluid als auch das Festkörpermaterial inkompressibel modelliert werden kann, wurden zwei- und drei-dimensionale Fundamentallösungen mit der Methode von Hörmander hergeleitet und implementiert. Die numerischen Ergebnisse bestätigen, dass bei manchen Materialien (z.B. Boden) die inkompressible Modellierung zulässig ist, und dazu noch eine Ersparnis an Rechenzeit (um 20%) bringen kann.
In den bisher publizierten poroelastischen BEM Formulierungen werden die gleichen Ansatzfunktionen für alle Unbekannte verwendet. In der FEM hingegen wird die Ansatzfunktion für den Porendruck um einen Grad niedriger als die der Verschiebung gewählt. Dies hat die Implementierung gemischter Elemente in die BEM motiviert. Die anschließend durchgeführte Studie zeigt jedoch, dass diese Elemente bei der BEM nur in Spezialfällen empfohlen werden können.
Die Validierung des entwickelten Programms wurde mit einer analytischen ein-dimensionalen Lösung durchgeführt. Nachfolgend wurden mit Blick auf Oberflächenwellen Wellenausbreitungsprobleme im poroelastischen Halbraum modelliert und diskutiert.

Abstract

Wave propagation phenomena in poroelastic continua are modeled with a Boundary Element (BE) formulation based on Biot's theory. The Convolution Quadrature Method (CQM) makes it possible to use the available Laplace domain fundamental solutions in a time domain BE formulation. Support for 2-d problems has been added to the existing 3-d implementation. Further, a formulation for incompressible constituents and mixed elements have been implemented and tested.
In a two-phase material not only each constituent, the solid and the fluid, may be compressible on the microscopic level but also the skeleton itself possesses a structural compressibility. If the compression modulus of a constituent is much larger than the compression modulus of the bulk material, this constituent is assumed to be materially incompressible. The fundamental solutions for incompressible poroelasticity in both 2-d and 3-d are derived using the method of Hörmander. Numerical experiments show that there are no noticeable differences for some materials (e.g., soil), and then the incompressible model can be recommended to obtain a speedup of about 20 percent.
In the conventional BEM implementation, the same shape functions are applied to all state variables. Motivated by the improvements due to mixed elements in FEM, i.e. the shape function for the pressure is chosen one degree lower than for the displacement, such elements have been added to the BEM implementation. A study about the influence of the mixed shape functions to the quality of numerical results and the stability of the time-stepping scheme shows that the mixed elements can only be recommended in special cases in BEM.
The proposed formulation is validated by comparison to a 1-d analytical solution. A poroelastic halfspace is modeled in both 2-d and 3-d numerical experiments to study wave propagation with emphasis on surface waves. The influence of material incompressibility on various wave types is also examined.

Contents

Introduction

Wave propagation is an important topic in engineering sciences. A description of wave propagation phenomena is given by Graff [56]: *The effect of a sharply applied, localized disturbance in a medium soon transmits or "spreads" to other parts of the medium*. These effects are familiar to everyone in various forms, e.g., as transmission of sound through the air, spreading of ripples on a water surface, or transmission of light or radio waves. From all wave types in nature, here, attention is focused solely on mechanical waves in solids, i.e., no electro-magnetic effects are considered.

In solids, there are two basic types of waves – compressional waves similar to the pressure waves in fluids and, additionally, shear waves. Due to continual reflections at boundaries and propagation of waves, a steady state is reached after some time in bounded solids. However, if the time interval of interest is comparable to the time needed to reach this steady state or shorter or if the load changes non-periodically (e.g., is applied only over a short time or increases rapidly from zero to a constant value in a short interval), wave propagation phenomena have to be considered.

On surfaces or interfaces, resulting from reflections and mode conversions, surface waves may travel long distances without being noticeably attenuated. That is especially important in large solids, as for example the earth mantle and crust, where waves induced by earthquakes can travel far and cause severe damage not only in the nearest vicinity of the fault. Knowledge about how waves propagate in the ground is therefore necessary to be able to prevent destruction of buildings, dams, or pipelines. Additionally, seismic waves are also used to study the interior composition of the earth.

Other applications of mechanical wave phenomena can be found in nearly every field of engineering. In non-destructive testing, disturbances of traveling waves are measured to identify cracks or inclusions in the material. In the field of mining, blasting induces intense stress waves to burst rocks or parts of it. Besides that, it is of interest to know how far and strong an impulse travels induced by a machine to protect persons in the surrounding of such an excitation from the vibrations.

This short and certainly incomplete listing demonstrates the importance of wave propagation problems in engineering mechanics. Modeling such problems correctly will lead to improvements in construction, reducing risks and increasing comfort. For a small number of special problems, an analytical solution is available, see, e.g., the books of Graff [56] and Achenbach [1]. But most cases, especially for two-dimensional (2-d) or three-dimensional (3-d) problems, involve numerical solutions of the governing equations like the Finite Element Method, e.g., [73] or raytracing, e.g., [23].

In many cases, an elastic model of the solid medium is sufficient, but for a wide range of fluid infiltrated materials, such as water saturated soils, oil impregnated rocks, air filled foams, or biological tissues, the elastic as well as a viscoelastic description of the material behavior is a crude approximation for the investigation of wave propagation in such media. Due to their porosity and due to the interaction of the skeleton and the pore content, a different theoretical approach, i.e., a poroelastic theory, is necessary to describe the observed effects like the second compressional wave.

Biot's Poroelasticity

A historical review on the subject of multiphase continuum mechanics identifies two poroelastic theories which have been developed and are used nowadays, namely Biot's theory and the Theory of Porous Media. For more details, the reader is directed to the work of de Boer and Ehlers [34, 35] or to the recently published monograph [32]. The early works on porous media are attributed to Fillunger in 1913 [52]. In this paper and in subsequent ones, Fillunger was concerned with the question of buoyancy of barrages. At the same time, a more intuitive theory has been developed by von Terzaghi [96]. These two works form the basis for the two different theories used up to day.

Based on the work of von Terzaghi, a theoretical description of porous materials saturated by a fluid was presented by Biot [9]. This was the starting point of the Biot's theory of poroelasticity. In the following years, Biot extended his theory to anisotropic cases [10] and also to poroviscoelasticity [11]. The dynamic extension of Biot's theory was published in 1956 in two papers, one covering the low frequency range [12] and the other one covering the high frequency range [13]. One of the significant findings in these papers was the identification of three different wave types for a 3-d continuum, namely two compressional waves and one shear wave. The additional compressional wave is also known as the slow wave and has been experimentally confirmed by Plona [77]. In Biot's original approach a fully saturated material was assumed. The extension to a nearly saturated (partially saturated) poroelastic solid was presented by Vardoulakis and Beskos [95].

Based on the work of Fillunger, a different approach, namely the Theory of Porous Media, has been developed. This theory is based on the axioms of continuum theories of mixtures [94, 17] extended by the concept of volume fractions by Bowen [18, 19] and the research group of Ehlers [33, 45, 47, 46, 40]. Thus the TPM proceeds from the assumption of immiscible and superimposed continua with internal interactions.

Remarks on the equivalence of both theories are found in the work of Bowen [19], Ehlers and Kubik [49], and Schanz and Diebels [87]. In all these publications, linear versions of both theories are compared and, finally, the equivalence can only be shown if Biot's apparent mass density is set to zero. More importantly, in [87] it is shown that the differential operators for both theories are equivalent. Therefore it is sufficient to discuss the fundamental solutions only for one of both theories. The result is simply transformed to the other theory by changing some material constants. As the Biot's theory is more common, this theory is used here.

In the following, a two-phase material consisting of an elastic solid skeleton and an interstitial fluid is assumed. Furthermore, the assumption of full saturation is made, e.g., the whole pore space is filled with the fluid. The balance laws and the constitutive equations contain the variables solid and fluid displacements and pore pressure. In most cases these variables are modified, introducing the seepage velocity, describing the fluid movement relative to the solid frame, instead of the absolute fluid displacements. The governing equations are then usually formulated using one of two different sets of unknowns: either the pore pressure is eliminated and the solid displacements and seepage velocity remain, which is denoted as u_i^s-u_i^f-formulation in the following, or the seepage velocity is eliminated, and the solid displacements and pore pressure are selected as unknowns. Bonnet [14] has shown that the latter choice is sufficient to describe a poroelastic continuum. This reduction of unknowns, denoted as u_i^s-p-formulation, is only possible in a transformed domain, e.g., in the Laplace domain. Zienkiewicz [99] introduced a simplified poroelastic model to make a u_i^s-p-formulation in time domain possible.

The main focus of this work is on wave propagation problems. Therefore, a linear description of the

geometry in terms of small displacements and small deformation gradients is assumed. Furthermore, linear constitutive equations are considered. The combination of both assumptions leads to a set of linear differential equations.

Incompressibility In a two-phase material, not only each constituent, the solid and the fluid, may be compressible on the microscopic level but also the skeleton itself possesses a structural compressibility. If the compression modulus of one constituent on the microscopic level is much larger than the compression modulus of the bulk material, it is sufficient to approximate this constituent as materially incompressible. A common example for a materially incompressible solid constituent is soil. In this case, the individual grains are much stiffer than the skeleton itself. If both the fluid and the solid constituents are modeled as incompressible, only the structural compressibility remains and the propagation speed of the fast compressional wave becomes infinite. In the following references, the governing equations are given for materially compressible and incompressible constituents [18, 19, 47, 46, 40].

If only one of the constituents is assumed incompressible, e.g., a compressible fluid and an incompressible solid or an incompressible fluid and a compressible solid, it only corresponds to a change of the material parameters in the compressible model, the governing equations remain the same as with both constituents modeled compressible. When both constituents are assumed incompressible, the differential operator is different than in the compressible case. This, of course, also results in changes later in the numerical solution procedure. For the Boundary Element Method used here, the most important difference is in the fundamental solutions.

Fundamental Solutions

A mandatory requirement for every boundary element formulation is the knowledge of fundamental solutions. These solutions solve the underlying differential equation with the inhomogeneity of a Dirac distribution. Physically spoken, the response of a system due to a unit impulse is looked for. These solutions exist for many linear problems [74].

As mentioned earlier, a poroelastic continuum is described by a set of coupled differential equations where two possible choices of unknowns are used. Either, in the u_i^s-u_i^f-formulation, the solid displacements and fluid displacements are chosen or, in the u_i^s-p-formulation, the solid displacements and the pore pressure are chosen. As in any time dependent problem, the governing equations may be formulated in frequency or Laplace domain or directly in time domain. The latter is the more complicated case because then a hyperbolic system has to be solved contrary to the elliptic system in the transformed domain.

In case of consolidation processes, a quasi-static theory is sufficient. For this special case, a survey of fundamental solutions is given in [29]. But, for treating wave propagation problems, a full dynamic model is required. In this case, the first approach to develop fundamental solutions was made by Burridge and Vargas [24] for the u_i^s-u_i^f-formulation. As inhomogeneity only a point force in the solid was chosen which is not sufficient for the usage of such a fundamental solution in a BE formulation. Later, Norris [71] derived the time harmonic fundamental solutions for the same formulation using a point force in the solid as well as a point force in the fluid as load. He also obtained explicit asymptotic approximations for far-field displacements, as well as those for low and high frequency responses. For the same set of unknowns but in Laplace domain Manolis and Beskos [65] published fundamental solutions (see also the correc-

tions in [66]). Additionally to the derivation of these solutions, they pointed out the analogy between poroelasticity and thermoelasticity. However, this analogy is only possible for the u_i^s-p-formulation. This was also shown by Bonnet [14] when he presented the fundamental solution for the u_i^s-p-formulation in frequency domain. Additionally to the three-dimensional (3-d) solutions which he converted from the thermoelastic solutions published by Kupradze [61], he has given the two-dimensional (2-d) solutions. Further, he has concluded that the u_i^s-p-formulation is sufficient and the u_i^s-u_i^f-formulation is overdetermined. In the following, this statement is confirmed. It should be mentioned, however, that in Bonnet's paper [14] there is some confusing regarding the sign of the time variation assumed for the harmonic variables which in the poroelastic equations is different to that of the thermoelastic ones. This has been corrected by Domínguez [42, 43]. Boutin et al. [16] published fundamental solutions for Biot's theory but they neglect the inertia terms of the fluid. The respective governing equations are motivated by a homogenization process [4].

With one exception, in all the above cited papers fundamental solutions are given in transformed domains. A time domain fundamental solution was presented by Norris [71] and Wiebe and Antes [97] for the u_i^s-u_i^f-formulation. However, in these solutions the viscous coupling of the solid and fluid is neglected. Without this restriction, Chen presented in two papers, for a 2-d continuum [25] and a 3-d continuum [26], fundamental solutions for the u_i^s-p-formulation. These solutions are obtained from the corrected Laplace domain solutions of [14] by inverse transformation resulting partly in an integral which must be solved numerically.

The above cited fundamental solutions are mainly derived by two methods. First, there is the possibility to split the operator by introducing three potentials or, second, to reduce the highly complicated differential operator matrix to a simple scalar operator by the use of Hörmander's method [58]. The latter is also used here to derive the fundamental solutions for both the u_i^s-u_i^f-and the u_i^s-p-formulations.

Numerical Models for Poroelastic Materials

The Finite Element Method, probably the most common numerical approach in engineering, has also been applied to model the behavior of poroelastic materials. Lewis and Schrefler [62], who mainly concentrated on consolidation problems, have presented several formulations based on the solid displacement and the pore pressure and on the solid displacement and the seepage velocity. Both consolidation and wave propagation for incompressible TPM in a 2-d domain have been studied by Breuer [22], choosing the solid displacements, the seepage velocity, and the pore pressure as the degrees of freedom. A nonlinear 2-d FEM formulation for incompressible TPM with the solid displacement, the seepage velocity, and the pore pressure as unknowns has been published by Diebels and Ehlers [41]. Embankment problems for unsaturated soils, i.e., triphasic materials composed of an incompressible elasto-plastic or elasto-viscoplastic solid frame, an incompressible pore liquid, and a compressible pore gas have been studied by Ehlers et al. [48]. A time domain FEM has been developed by Zienkiewicz [100], based on a simplified poroelastic model neglecting the inertia effects of the fluid but not those of the solid skeleton, which makes the model applicable for low frequency wave propagation.

Nevertheless, the Finite Element Method has a significant disadvantage in the case of semi-infinite domains. Reflections on artificial boundaries, i.e., where the discretization ends, make it hard to fulfill the Sommerfeld radiation condition [90]. Therefore, the finite element mesh usually has to cover a large region of the unbounded domain, or special tricks, e.g., so-called infinite elements [3], need to be used to reasonably approximate the behavior in infinity.

Boundary Element Method

The efficiency of the Boundary Element Method (BEM) in dealing with semi-infinite domain problems, e.g., soil-structure interaction, has long been recognized by researchers and engineers. One reason is that unlike with finite elements, the Sommerfeld radiation condition in infinity is implicitly fulfilled. Another principal advantage is the dimension reduction of the mesh, as only the boundary has to be discretized. This is especially interesting for problems like crack propagation, e.g., [50], where remeshing contributes substantially to the computational costs.

Based on previous developments in integral equations, e.g., by Fredholm [53] or Kupradze [61], the term BEM first appeared in 1977 in the works of Banerjee and Butterfield [5] and Brebbia and Domínguez [20]. A historical overview of boundary integral methods can be found in [7], an introduction to BEM is given, e.g., in Brebbia et al. [21]. The first boundary integral formulation for elastodynamics has been published by Cruse and Rizzo [31, 30] in Laplace domain, with an inverse transform to time domain. Mansur [68, 67] has developed a direct time stepping BEM. An overview of BEM in elastodynamics may be found in [6, 8].

To correctly model wave propagation in fluid saturated materials problems, a poroelastic constitutive model should be used in connection with a time-dependent BE formulation. Dynamic poroelastic BE formulations are published in frequency domain, e.g., Cheng et al. [28], in Laplace domain, e.g., Chen [27] or Manolis and Beskos [65], and in time domain, e.g., Wiebe and Antes [97], Chen and Dargush [27], and Schanz [83].

In all of these formulations, Biot's theory is used assuming compressible constituents. As stated before, the model with both constituents incompressible leads to another differential operator than the compressible case. Consequently, different fundamental solutions are required for a BEM formulation, but since the unknowns remain the same, the procedure of computing the fundamental solutions and establishing a boundary element formulation is not essentially different from the compressible case.

Concentrating on wave propagation problems, the time-dependent BE formulation based on the Convolution Quadrature Method as proposed by Schanz [84] is used here. The BEM formulation employs the fundamental solutions with solid displacements and pore pressure as independent variables.

Element types As in all other poroelastic BE formulations, only isoparametric elements are used in [83, 84], i.e., identical shape functions for all variables and the geometry. Here, so-called mixed elements, i.e., different shape functions for displacements and tractions than for pore pressure and flux, have been implemented besides isoparametric ones. This approach is common in finite elements and advantageous over isoparametric elements for many problems. In some cases, e.g., incompressible elasticity or when the undrained material properties play a significant role in poroelasticity, mixed elements are needed to fulfill the Babuška-Brezzi stability condition [62]. Contrary to FEM, for boundary elements, only one publication regarding mixed elements is known to the author [92]. For a different problem, i.e., not poroelasticity, it gives theoretical results on convergence verified on a numerical example with the Laplace operator.

Scope of this Work

The goals of this work are to add 2-d to the existing 3-d time dependent BEM implementation, develop the fundamental solutions for incompressible poroelasticity in both 2-d and 3-d, and implement this model. Further, to add mixed elements combining linear and constant shape functions and compare their numerical behavior to isoparametric elements. Finally, the numerical model should be used to study wave propagation in poroelastic materials, especially the influence of incompressible modeling on various wave types in semi-infinite domains.

In chapter 1, the Biot's constitutive equations are recalled and the assumptions for incompressibility are given. The incompressibility conditions in the governing equations are discussed for the Biot model using two different sets of unknowns, the solid displacements and fluid pressure and the solid and fluid displacements. The novel fundamental solutions for the incompressible case are derived using Hörmander's method. Also the fundamental solutions for the compressible case are recalled, not only for completeness, but also to show how the physical approximation of incompressibility is represented in the mathematics of the formulas. As the fundamental solutions are the basis of BE formulations also their singular behavior is discussed. Finally, a visualization of the fundamental solutions is presented.

In chapter 2, a boundary element formulation for poroelasticity is presented. The time stepping procedure is explained. The implemented boundary element types, i.e., isoparametric and mixed, are described. Some numerical aspects are discussed.

To validate the BEM program, test problems for two different materials are solved in chapter 3. For this purpose, the examples are selected such that both the 2-d and 3-d BEM results can be compared to a 1-d analytical solution for a poroelastic column. More numerical examples comparing the isoparametric and mixed elements can be found in chapter 4.

In chapter 4, an overview of waves propagating in elastic and poroelastic materials is given, and related to the numerical results. To demonstrate the limits of the incompressible approximation for a poroelastic medium, two different cases of materials, a rock and a soil, are used. The results of the incompressible modeling are compared with the compressible modeling at the example of a half space.

Throughout this work, the Einstein summation convention is applied over repeated indices in a monomial. Latin indices receive the values 1,2 in two-dimensions (2-d), respectively 1,2,3 in three-dimensions (3-d). A list of used symbols can be found on page 108.

1 Biot's Theory of Poroelasticity

Following Biot's approach to model the behavior of porous media, an elastic skeleton with a statistical distribution of interconnected pores is considered [10]. This porosity is denoted by

$$\phi = \frac{V^f}{V} \,, \tag{1.1}$$

where V^f is the volume of the interconnected pores contained in a sample of bulk volume V. Contrary to these pores the sealed pores will be considered as part of the solid. Full saturation is assumed leading to $V = V^f + V^s$ with V^s the volume of the solid, i.e., a two-phase material is given.

1.1 Constitutive Assumptions

If the constitutive equations are formulated for the elastic solid and the interstitial fluid, a partial stress formulation is obtained [10]

$$\sigma^s_{ij} = 2G\varepsilon^s_{ij} + \left(K - \frac{2}{3}G + \frac{Q^2}{R}\right)\varepsilon^s_{kk}\delta_{ij} + Q\varepsilon^f_{kk}\delta_{ij} \tag{1.2a}$$

$$\sigma^f = -\phi p = Q\varepsilon^s_{kk} + R\varepsilon^f_{kk} \,, \tag{1.2b}$$

with $()^s$ and $()^f$ indicating either solid or fluid, respectively. The respective stress tensor is denoted by σ^s_{ij} and σ^f and the corresponding strain tensor by ε^s_{ij} and ε^f_{kk}. The elastic skeleton is assumed to be isotropic and homogeneous where the two elastic material constants compression modulus K and shear modulus G refer to the bulk material. The coupling between the solid and the fluid is characterized by the two parameters Q and R. In the above, the sign conventions for stress and strain follow that of elasticity, namely, tensile stress and strain is denoted positive. Therefore, in equation (1.2b) the pore pressure p is the negative hydrostatic stress in the fluid σ^f.

An alternative representation of the constitutive equation (1.2) is used in Biot's earlier work [9]. There, the total stress $\sigma_{ij} = \sigma^s_{ij} + \sigma^f\delta_{ij}$ is introduced and with Biot's effective stress coefficient $\alpha = \phi\,(1 + Q/R)$ the constitutive equation with the solid strain ε^s_{ij} and the pore pressure p

$$\sigma_{ij} = 2G\varepsilon^s_{ij} + \left(K - \frac{2}{3}G\right)\varepsilon^s_{kk}\delta_{ij} - \alpha\delta_{ij}p \tag{1.3a}$$

is obtained. Additionally to the total stress σ_{ij}, as a second constitutive equation, the variation of fluid volume per unit reference volume ζ is introduced

$$\zeta = \alpha\varepsilon^s_{kk} + \frac{\phi^2}{R}p \,. \tag{1.3b}$$

This variation of fluid ζ is defined by the mass balance over a reference volume, i.e., by the continuity equation

$$\dot{\zeta} + q_{i,i} = a \tag{1.4}$$

with the specific flux $q_i = \phi\left(\dot{u}_i^f - \dot{u}_i^s\right)$ and a source term $a(t)$. Equation (1.4) identifies ζ as a kind of strain describing the motion of the fluid relative to the solid which takes a source in the fluid into account. This source term is not motivated by any physical reason[1] but it is later needed for the derivation of the fundamental solutions.

In a two-phase material not only each constituent, the solid and the fluid, may be compressible on a microscopic level but also the skeleton itself possesses a structural compressibility. If the compression modulus of one constituent is much larger on the microscale than the compression modulus of the bulk material, this constituent is assumed to be materially incompressible. A common example for a materially incompressible solid constituent is soil. In this case, the individual grains are much stiffer than the skeleton itself. The respective conditions for such incompressibilities are [39]

$$\frac{K}{K^s} \ll 1 \quad \text{incompressible solid,} \qquad \frac{K}{K^f} \ll 1 \quad \text{incompressible fluid}\,, \tag{1.5}$$

where K^s denotes the compression modulus of the solid grains and K^f the compression modulus of the fluid. With these conditions it is obvious that there are three possible cases: i) only the solid is incompressible, ii) only the fluid is incompressible, or iii) the combination of both.

To find the respective constitutive equations for each of these cases, the material parameters α, R, and Q have to be rewritten in a different way. Considerations of constitutive relations at the micro mechanical level as given in [39] lead to a more rational model for this purpose

$$\alpha = 1 - \frac{K}{K^s} \tag{1.6a}$$

$$R = \frac{\phi^2 K^f K^{s2}}{K^f\left(K^s - K\right) + \phi K^s\left(K^s - K^f\right)} \tag{1.6b}$$

$$Q = \frac{\phi\left(\alpha - \phi\right) K^f K^{s2}}{K^f\left(K^s - K\right) + \phi K^s\left(K^s - K^f\right)}\,. \tag{1.6c}$$

Inserting the conditions of incompressibility (1.5) into equations (1.6), the three different cases are found:

- Incompressible solid $K/K^s \ll 1$

  $$\alpha \approx 1 \qquad R \approx K^f \phi \qquad Q \approx K^f\left(1 - \phi\right) \tag{1.7}$$

  These limiting values can be inserted into the constitutive assumptions (1.2) or (1.3), respectively.

- Incompressible fluid $K/K^f \ll 1$

  $$\alpha \text{ unchanged} \qquad R \approx \frac{\phi^2 K^s}{1 - \phi - \dfrac{K}{K^s}} \qquad Q \approx \frac{\phi\left(\alpha - \phi\right) K^s}{1 - \phi - \dfrac{K}{K^s}} \tag{1.8}$$

  Also in this case, these limiting values can be inserted into the constitutive assumptions (1.2) or (1.3), respectively.

[1] e.g., a chemical reaction

- Both constituents are assumed to be incompressible $K/K^s \ll 1$ and $K/K^f \ll 1$

$$\alpha \approx 1 \qquad R \to \infty \qquad Q \to \infty \qquad \text{but} \qquad \frac{Q}{R} = \frac{1-\phi}{\phi} \tag{1.9}$$

The relation $R, Q \to \infty$ expresses that the values of R, Q become large, however, due to physical reasons they are in any case limited. But, the condition that R becomes large is used to neglect the influence of the pore pressure in (1.3b). This condition and $\alpha = 1$ results in the incompressible constitutive assumptions

$$\sigma_{ij} = 2G\varepsilon^s_{ij} + \left(K - \frac{2}{3}G\right)\varepsilon^s_{kk}\delta_{ij} - \delta_{ij}p \tag{1.10a}$$

$$\zeta = \varepsilon^s_{kk} \tag{1.10b}$$

for the total stress formulation. From (1.10), it is obvious that this special modeling of a porous continuum relates the variation of fluid volume directly to the volumetric solid strain and the pore pressure is added to the solid stress linearly without the weighting factor α.

For the partial stress formulation (1.2), a different point of view must be considered because inserting the infinite values of Q and R into the constitutive law (1.2) results in an infinite stress. Biot [10] has given as condition for incompressible constituents

$$(1-\phi)\,\varepsilon^s_{kk} + \phi\varepsilon^f_{kk} = 0\,, \tag{1.11}$$

i.e., it is assumed that the dilatation of the bulk material vanishes. Realizing the relation

$$\frac{Q}{R} = \frac{1-\phi}{\phi} \quad \Rightarrow \qquad \frac{Q}{R}\varepsilon^s_{kk} + \varepsilon^f_{kk} = 0 \tag{1.12}$$

also in the partial stress formulation the case of incompressible constituents can be included resulting in the constitutive assumptions

$$\sigma^s_{ij} = 2G\varepsilon^s_{ij} + \left(K - \frac{2}{3}G\right)\varepsilon^s_{kk}\delta_{ij} \tag{1.13a}$$

$$\sigma^f = -\phi p = R\left(\frac{Q}{R}\varepsilon^s_{kk} + \varepsilon^f_{kk}\right) \stackrel{!}{=} 0\,. \tag{1.13b}$$

To achieve the zero value in equation (1.13b), the condition that the value R becomes large but is limited must be used.

Contrary to the incompressible model formulated for the total stress formulation (1.10), in the partial stress formulation the assumption of incompressibility (1.11) results in an uncoupling of the solid and the fluid in the constitutive assumptions. Therefore, the two incompressible models (1.10) and (1.13) are different whereas the underlying compressible models (1.3) and (1.2), respectively, are identical. This is not really a contradiction. Keeping in mind that an incompressible model is always an approximation for the more realistic compressible case, it is clear that different approximations can exist. However, the question which approximation is better can only be answered by the respective application.

As shown earlier, if only one of the constituents is assumed incompressible, e.g., compressible fluid and incompressible solid or incompressible fluid and compressible solid, the governing equations remain the same as with both constituents modeled compressible. In these cases, just the material parameters α, R, and Q in the compressible model have to be changed according to (1.7) in the case of incompressible solid, respectively (1.8) in the case of incompressible fluid. Therefore, in the following, only the model with both constituents incompressible has to be handled separately.

To complete the set of equations, the relation between strains and displacements has to be specified. Aiming at the equations of motion to model wave propagation phenomena, it is sufficient to formulate a linear kinematic equation. Hence, in the following, the relation of the solid/fluid strain to the solid/fluid displacement is chosen linear, respectively

$$\varepsilon^s_{ij} = \frac{1}{2}\left(u^s_{i,j} + u^s_{j,i}\right) \qquad \varepsilon^f_{kk} = u^f_{k,k} \tag{1.14}$$

assuming small deformation gradients.

1.2 Governing Equations

In the preceding section, the constitutive equations and the kinematic relations have been given. The next step is to state the balances of momentum. In any two-phase material there are three possibilities to formulate the balances of momentum: First, the balance of momentum in the solid, second the balance of momentum in the fluid and, third, the balance of momentum for the bulk material. But, it is sufficient to choose two of them. First, the balances for the compressible case are presented and the governing equations established for two different sets of unknowns. Afterwards, the changes implied by the incompressibility conditions are introduced and the resulting incompressible equations are discussed.

1.2.1 Compressible Model

The first two balances are used by Biot in [12] using the solid displacement and the fluid displacement as unknowns

$$\sigma^s_{ij,j} + (1-\phi)\, f^s_i = (1-\phi)\,\rho_s \ddot{u}^s_i + \rho_a\left(\ddot{u}^s_i - \ddot{u}^f_i\right) + \frac{\phi^2}{\kappa}\left(\dot{u}^s_i - \dot{u}^f_i\right) \tag{1.15a}$$

$$\sigma^f_{,j} + \phi f^f_i = \qquad \phi\rho_f \ddot{u}^f_i - \rho_a\left(\ddot{u}^s_i - \ddot{u}^f_i\right) - \frac{\phi^2}{\kappa}\left(\dot{u}^s_i - \dot{u}^f_i\right)\,. \tag{1.15b}$$

The first balance equation (1.15a) is that for the solid skeleton and the second (1.15b) is that for the interstitial fluid. In equation (1.15), the body forces in the solid skeleton f^s_i and in the fluid f^f_i are introduced. Further, the respective densities are denoted by ρ_s and ρ_f. To describe the dynamic interaction between fluid and skeleton an additional density the apparent mass density ρ_a has been introduced by Biot [12]. It can be written as $\rho_a = C\phi\rho_f$ where C is a factor depending on the geometry of the pores and the frequency of excitation. At the low frequency range, Bonnet and Auriault [15] measured $C = 0.66$ for a sphere assembly of glass beads. In higher frequency ranges, a certain functional dependence of C on frequency has been proposed based on conceptual porosity structures, e.g., in [13] and [15]. The factor ϕ^2/κ in front of the damping term is usually denoted by b. Here, the simplification of a frequency independent, respectively time independent, value is taken which is only valid in the low frequency range.

Further, the above chosen factor ϕ^2/κ is given only in the case of circular pores when κ denotes the permeability. However, in the following, any other also frequency dependent factor b could easily be implemented.

The third above mentioned balance of momentum for the mixture is formulated in Biot's earlier work [9] for quasi-statics and in [12] for dynamics. This dynamic equilibrium is given by

$$\sigma_{ij,j} + F_i = \rho_s (1-\phi)\, \ddot{u}_i^s + \phi \rho_f \ddot{u}_i^f \,, \tag{1.16}$$

with the bulk body force per unit volume $F_i = (1-\phi)\, f_i^s + \phi f_i^f$. It is obvious that adding the two partial balances (1.15a) and (1.15b) results in the balance of the mixture (1.16).

In most papers using the total stress formulation, now, the constitutive assumption for the fluid transport in the interstitial space is given by Darcy's law. Here, it is also used, however, with the balance of momentum in the fluid (1.15b) Darcy's law is already given. Rearranging (1.15b) and taking the definition of the flux $q_i = \phi \left(\dot{u}_i^f - \dot{u}_i^s \right)$ as well as $\sigma^f = -\phi p$ into account the dynamic version of Darcy's law

$$q_i = -\kappa \left(p_{,i} + \frac{\rho_a}{\phi} \left(\ddot{u}_i^f - \ddot{u}_i^s \right) + \rho_f \ddot{u}_i^f - f_i^f \right) \tag{1.17}$$

is achieved.

Aiming at the equation of motion, the constitutive equations have to be combined with the corresponding balances of momentum and the kinematic conditions. To do this, first, the degrees of freedom must be determined. There are several possibilities: i) to use the solid displacement u_i^s and the fluid displacement u_i^f (2 vectors, i.e., six unknowns in 3-d) or ii) a combination of the solid displacement u_i^s and the pore pressure p (1 vector and 1 scalar, i.e., four unknowns in 3-d). As shown in [14], it is sufficient to use the latter choice. Here, for completeness, both choices will be presented where the first will be referred to as u_i^s-u_i^f-formulation and the latter as u_i^s-p-formulation.

First, the equations of motion for a poroelastic body are presented for the unknowns solid displacement u_i^s and fluid displacement u_i^f. Inserting the constitutive equations (1.2) written for the partial stress tensors and the linear strain displacement relations (1.14) into (1.15) yields a set of equations of motion in time domain

$$\begin{aligned} G u_{i,jj}^s + \left(K + \frac{1}{3} G \right) u_{j,ij}^s + Q \left(\frac{Q}{R} u_{j,ji}^s + u_{j,ji}^f \right) + (1-\phi)\, f_i^s & \\ = (1-\phi)\, \rho_s \ddot{u}_i^s + \rho_a \left(\ddot{u}_i^s - \ddot{u}_i^f \right) + \frac{\phi^2}{\kappa} \left(\dot{u}_i^s - \dot{u}_i^f \right) & \qquad (1.18a) \\ R \left(\frac{Q}{R} u_{j,ji}^s + u_{j,ji}^f \right) + \phi f_i^f = \phi \rho_f \ddot{u}_i^f - \rho_a \left(\ddot{u}_i^s - \ddot{u}_i^f \right) - \frac{\phi^2}{\kappa} \left(\dot{u}_i^s - \dot{u}_i^f \right) . & \qquad (1.18b) \end{aligned}$$

Second, the respective equations of motion are presented for the pore pressure p and the solid displacement u_i^s as unknowns. To achieve this formulation the fluid displacement u_i^f has to be eliminated from equations (1.16), (1.17), (1.3), and (1.4). In order to do this, Darcy's law (1.17) is rearranged to obtain $u_i^f - u_i^s$. Since this relative displacement is given as second order time derivative in (1.17) and the flux is related to its first oder time derivative by $q_i = \phi \left(\dot{u}_i^f - \dot{u}_i^s \right)$, this is only possible in a transformed domain. After transformation to Laplace domain, the relative fluid to solid displacement is

$$\hat{u}_i^f - \hat{u}_i^s = - \underbrace{\frac{\kappa \rho_f \phi^2 s^2}{\phi^2 s + s^2 \kappa (\rho_a + \phi \rho_f)}}_{\beta} \frac{1}{s^2 \phi \rho_f} \left(\hat{p}_{,i} + s^2 \rho_f \hat{u}_i^s - \hat{f}_i^f \right) . \tag{1.19}$$

In equation (1.19), the abbreviation β is defined for further usage and $\mathscr{L}\{f(t)\} = \hat{f}(s)$ denotes the Laplace transform, with the complex variable s. Moreover, vanishing initial conditions for u_i^s and u_i^f are assumed here and in the following. Now, the final set of differential equations for the displacement $\hat{u}_i^s$ and the pore pressure $\hat{p}$ is obtained by inserting the constitutive equations (1.3) into the Laplace transformed dynamic equilibrium (1.16) and continuity equation (1.4) with $\hat{u}_i^f - \hat{u}_i^s$ from equation (1.19). This leads to the final set of differential equations for the displacement $\hat{u}_i^s$ and the pore pressure $\hat{p}$

$$G\hat{u}^s_{i,jj} + \left(K + \frac{1}{3}G\right)\hat{u}^s_{j,ij} - (\alpha - \beta)\,\hat{p}_{,i} - s^2(\rho - \beta\rho_f)\,\hat{u}^s_i = \beta\hat{f}^f_i - \hat{F}_i \tag{1.20a}$$

$$\frac{\beta}{s\rho_f}\hat{p}_{,ii} - \frac{\phi^2 s}{R}\hat{p} - (\alpha - \beta)\,s\hat{u}^s_{i,i} = -\hat{a} + \frac{\beta}{s\rho_f}\hat{f}^f_{i,i}\,. \tag{1.20b}$$

In the above equation (1.20), the bulk density $\rho = \rho_s(1-\phi) + \phi\rho_f$ is used. This set of equations describes the behavior of a poroelastic continuum completely as well as the u_i^s-u_i^f-formulation (1.18). Contrary to the formulation using the solid and fluid displacement (1.18) an analytical representation in time domain is only possible for $\kappa \to \infty$. This case would represent a negligible friction between solid and interstitial fluid.

1.2.2 Incompressible Model

As mentioned above, often the approximation of incompressible constituents can be used. Regarding the assumption of only one incompressible constituent (1.7) and (1.8) no special governing equations must be given because only the material data are changed and not the structure of the constitutive law. So, in the following, the expression 'incompressible' will denote the case when both constituents are modeled incompressible.

In this case of modeling both constituents as incompressible, a different set of governing equations is obtained. Inserting the incompressibility condition (1.12) into (1.18), the governing equations are given by

$$Gu^s_{i,jj} + \left(K + \frac{1}{3}G\right)u^s_{j,ij} + (1-\phi)\,f^s_i = (1-\phi)\,\rho_s\ddot{u}^s_i + \rho_a\left(\ddot{u}^s_i - \ddot{u}^f_i\right) + \frac{\phi^2}{\kappa}\left(\dot{u}^s_i - \dot{u}^f_i\right) \tag{1.21a}$$

$$\phi f^f_i = \quad \phi\rho_f\ddot{u}^f_i - \rho_a\left(\ddot{u}^s_i - \ddot{u}^f_i\right) - \frac{\phi^2}{\kappa}\left(\dot{u}^s_i - \dot{u}^f_i\right) \tag{1.21b}$$

using the solid displacement and fluid displacement as unknowns. In this incompressible version of the equations of motion, the uncoupling of the fluid and solid in the constitutive assumptions is clearly observed as commented in the last section. So, only the coupling by the acceleration and damping terms remains in equations (1.21). Further, the second equation (1.21b) is no longer independent. It can not be used to eliminate the fluid displacement u_i^f in (1.21a). As an additional equation the incompressibility condition (1.11) has to be used.

On the contrary, if the solid displacement and the pore pressure are used as unknowns a sufficient set of differential equations is obtained. Simply inserting the conditions (1.9) into (1.20), i.e., setting $\alpha = 1$ and taking the limit $R \to \infty$, the equations of motion under the assumption of incompressible constituents are

achieved resulting in

$$G\hat{u}^s_{i,jj} + \left(K + \frac{1}{3}G\right)\hat{u}^s_{j,ij} - (1-\beta)\,\hat{p}_{,i} - s^2\,(\rho - \beta\rho_f)\,\hat{u}^s_i = \beta\,\hat{f}^f_i - \hat{F}_i \tag{1.22a}$$

$$\frac{\beta}{s\rho_f}\hat{p}_{,ii} - (1-\beta)\,s\hat{u}^s_{i,i} = -\hat{a} + \frac{\beta}{s\rho_f}\,\hat{f}^f_{i,i}\,. \tag{1.22b}$$

The equation for the pore pressure (1.22b) shows that this variable is no longer a degree of freedom. Integrating of (1.22b) would yield the gradient of the pore pressure which could then be eliminated in (1.22a). Physically interpreted the pore pressure is in this case only determined by the deformation of the solid skeleton and no longer by any deformation of the fluid.

1.3 Fundamental Solutions

Fundamental solutions for the above given systems of differential equations are known in closed form only in Fourier domain or Laplace domain. The fundamental solutions for the system (1.20) are given in [26, 25] and for the Laplace transformed system of (1.18) in [65]. The fundamental solutions for the incompressible case have first been published in [88].

Here, the procedure of deriving them is presented step by step. Also the fundamental solutions for the compressible case are recalled to show how the physical approximation of incompressibility is represented in the mathematical formulas. In order to deduce these solutions, an operator notation is useful. For the u^s_i-p-formulation the governing equations of the compressible case (1.20) as well as for the incompressible case (1.22) are reformulated as

$$\mathbf{B4}\begin{bmatrix}\hat{u}^s_i\\ \hat{p}\end{bmatrix} + \begin{bmatrix}\hat{F}_i\\ \hat{a}\end{bmatrix} = \mathbf{0} \tag{1.23}$$

with the differential operators

$$\mathbf{B4}^{comp} = \begin{bmatrix}\left(G\nabla^2 - s^2\,(\rho - \beta\rho_f)\right)\delta_{ij} + \left(K + \frac{1}{3}G\right)\partial_i\partial_j & -(\alpha-\beta)\,\partial_i\\ -s\,(\alpha-\beta)\,\partial_j & \dfrac{\beta}{s\rho_f}\nabla^2 - \dfrac{\phi^2 s}{R}\end{bmatrix} \tag{1.24a}$$

$$\mathbf{B4}^{incomp} = \begin{bmatrix}\left(G\nabla^2 - s^2\,(\rho - \beta\rho_f)\right)\delta_{ij} + \left(K + \frac{1}{3}G\right)\partial_i\partial_j & -(1-\beta)\,\partial_i\\ -s\,(1-\beta)\,\partial_j & \dfrac{\beta}{s\rho_f}\nabla^2\end{bmatrix}\,. \tag{1.24b}$$

In equations (1.23) and (1.24), the operator is denoted by **B4** regardless if it is in 2-d ($i,j = 1,2$, i.e., 3 unknowns) or 3-d ($i,j = 1,2,3$, i.e., 4 unknowns). The corresponding representation of a poroelastic continuum using the u^s_i-u^f_i-formulation is

$$\mathbf{B6}\begin{bmatrix}\hat{u}^s_i\\ \hat{u}^f_i\end{bmatrix} + \begin{bmatrix}(1-\phi)\,\hat{f}^s_i\\ \phi\,\hat{f}^f_i\end{bmatrix} = \mathbf{0} \tag{1.25}$$

with the differential operators

$$\mathbf{B6}^{comp} = \begin{bmatrix} B_{ij}^{comp} & Q\partial_i\partial_j + \left(s^2\rho_a + s\frac{\phi^2}{\kappa}\right)\delta_{ij} \\ Q\partial_i\partial_j + \left(s^2\rho_a + s\frac{\phi^2}{\kappa}\right)\delta_{ij} & R\partial_i\partial_j - \left(s^2(\phi\rho_f + \rho_a) - s\frac{\phi^2}{\kappa}\right)\delta_{ij} \end{bmatrix} \tag{1.26a}$$

$$\text{with} \quad B_{ij}^{comp} = \left(G\nabla^2 - s^2((1-\phi)\rho_s + \rho_a) - s\frac{\phi^2}{\kappa}\right)\delta_{ij} + \left(K + \frac{1}{3}G + \frac{Q^2}{R}\right)\partial_i\partial_j$$

$$\mathbf{B6}^{incomp} = \begin{bmatrix} B_{ij}^{incomp} & \left(s^2\rho_a + s\frac{\phi^2}{\kappa}\right)\delta_{ij} \\ \left(s^2\rho_a + s\frac{\phi^2}{\kappa}\right)\delta_{ij} & \left(-s^2(\phi\rho_f + \rho_a) - s\frac{\phi^2}{\kappa}\right)\delta_{ij} \end{bmatrix} \tag{1.26b}$$

$$\text{with} \quad B_{ij}^{incomp} = \left(G\nabla^2 - s^2((1-\phi)\rho_s + \rho_a) - s\frac{\phi^2}{\kappa}\right)\delta_{ij} + \left(K + \frac{1}{3}G\right)\partial_i\partial_j \,.$$

As before in (1.24), the operator name **B6** is the same whether it is in 2-d (4 unknowns) or 3-d (6 unknowns). In the following, the same material parameters in both representations (1.26) and (1.24) will be used, so Q is replaced by $Q = R(\alpha/\phi - 1)$ to have comparable representations.

In equations (1.24) and (1.26), the partial derivative $()_{,i}$ is denoted by ∂_i and $\nabla^2 = \partial_{ii}$ is the Laplacian operator. Note that all the operators (1.24) and (1.26) are elliptic but only the operators **B6** in (1.26) are self adjoint whereas the operators **B4** in (1.24) are not self adjoint. Therefore, in the latter case for the deduction of fundamental solutions the adjoint operator to **B4** has to be used

$$\mathbf{B4}^* = \begin{bmatrix} A\delta_{ij} + B\partial_{ij} & sC\partial_i \\ C\partial_j & D \end{bmatrix} \qquad \begin{aligned} A &= G\nabla^2 - s^2(\rho - \beta\rho_f) \\ B &= K + \tfrac{1}{3}G \\ C &= \alpha - \beta \\ D &= \frac{\beta}{s\rho_f}\nabla^2 - \frac{\phi^2 s}{R} \end{aligned} \tag{1.27}$$

$$\mathbf{B6}^* = \mathbf{B6} \,. \tag{1.28}$$

A fundamental solution is mathematically spoken a solution of the equation

$$\mathbf{B}^*\mathbf{G} + \mathbf{I}\delta(\mathbf{x} - \mathbf{y}) = \mathbf{0} \,, \tag{1.29}$$

where the matrix of fundamental solutions is denoted by **G**, the identity matrix by **I**, and the Dirac distribution by $\delta(\mathbf{x} - \mathbf{y})$. Physically interpreted the solution at point **x** due to a single point force at point **y** is looked for. Concerning the interpretation of the 'single point force' the difference in the fundamental solutions for both representations of poroelastic governing equations (1.23) and (1.25) becomes obvious. In the system (1.25), the right hand side consists of forces acting in the solid part $(1-\phi)\,\hat{f}_i^s$ and in the fluid part $\phi\,\hat{f}_i^f$ of the porous media, respectively. On the other hand, in the system (1.23), the right hand side consists of a bulk body force $\hat{F}_i = (1-\phi)\,\hat{f}_i^s$ and a source term $\hat{a}$, i.e., no forces in the fluid $\hat{f}_i^f$ are present. Due to this, it can not be expected that the fundamental solutions of both systems coincide. Only the displacement solution due to a single force in the solid will be the same.

To find these solutions, the same method can be chosen for both representations. In all cases, for compressible as well as incompressible constituents and for both representations, respectively, Hörmander's

method [58] is used. The idea of this method is to reduce the highly complicated operators (1.24) and (1.26) to simple well known operators. For this purpose the definition of the inverse matrix operator

$$\mathbf{B}^{*\,-1} = \frac{\mathbf{B}^{*\,co}}{\det\left(\mathbf{B}^{*}\right)} \tag{1.30}$$

based on the matrix of cofactors $\mathbf{B}^{*\,co}$ is recalled (see appendix B.1). The ansatz

$$\mathbf{G} = \mathbf{B}^{*\,co}\varphi \tag{1.31}$$

for the matrix of fundamental solutions with an unknown scalar function φ inserted into the operator equation (1.29) yields a more convenient representation of equations (1.23) and (1.25)

$$\begin{aligned}\mathbf{B}^{*}\mathbf{B}^{*\,co}\varphi + \mathbf{I}\delta\left(\mathbf{x}-\mathbf{y}\right) = \det\left(\mathbf{B}^{*}\right)\mathbf{I}\varphi + \mathbf{I}\delta\left(\mathbf{x}-\mathbf{y}\right) = \mathbf{0}\\ \rightsquigarrow\quad \det\left(\mathbf{B}^{*}\right)\varphi + \delta\left(\mathbf{x}-\mathbf{y}\right) = 0\,.\end{aligned} \tag{1.32}$$

With this reformulation, the search for a fundamental solution is reduced to solve the simpler scalar equation (1.32). An overview of this method is found in the original work [58] and more exemplary in [84, 79].

Compressible model First, this method is applied to the compressible operators in (1.24). Following Hörmander's idea, first, the determinants of the operators $\mathbf{B4}^{*\,comp}$ and $\mathbf{B6}^{comp}$ are calculated, preferably, with the aid of computer algebra. This yields the results

2-d:

$$\det\left(\mathbf{B4}^{*\,comp}\right) = \frac{G\beta}{s\rho_f}\left(K+\frac{4}{3}G\right)\left(\nabla^2 - s^2\lambda_3^2\right)\left(\nabla^2 - s^2\lambda_1^2\right)\left(\nabla^2 - s^2\lambda_2^2\right) \tag{1.33}$$

$$\det\left(\mathbf{B6}^{comp}\right) = \frac{-s^2G\phi^2\rho_f}{\beta}\left(K+\frac{4}{3}G\right)R\left(\nabla^2 - s^2\lambda_3^2\right)\left(\nabla^2 - s^2\lambda_1^2\right)\left(\nabla^2 - s^2\lambda_2^2\right) \tag{1.34}$$

3-d:

$$\det\left(\mathbf{B4}^{*\,comp}\right) = \frac{G^2\beta}{s\rho_f}\left(K+\frac{4}{3}G\right)\left(\nabla^2 - s^2\lambda_3^2\right)^2\left(\nabla^2 - s^2\lambda_1^2\right)\left(\nabla^2 - s^2\lambda_2^2\right) \tag{1.35}$$

$$\det\left(\mathbf{B6}^{comp}\right) = \left(\frac{s^2G\phi^2\rho_f}{\beta}\right)^2\left(K+\frac{4}{3}G\right)R\left(\nabla^2 - s^2\lambda_3^2\right)^2\left(\nabla^2 - s^2\lambda_1^2\right)\left(\nabla^2 - s^2\lambda_2^2\right) \tag{1.36}$$

with the roots $\lambda_i,\ i = 1,2,3$

$$\begin{aligned}\lambda_{1,2}^2 = &\frac{1}{2}\left[\frac{\phi^2\rho_f}{\beta R} + \frac{\rho-\beta\rho_f}{K+\frac{4}{3}G} + \frac{\rho_f\left(\alpha-\beta\right)^2}{\beta\left(K+\frac{4}{3}G\right)}\right.\\ &\left.\pm\sqrt{\left(\frac{\phi^2\rho_f}{\beta R} + \frac{\rho-\beta\rho_f}{K+\frac{4}{3}G} + \frac{\rho_f\left(\alpha-\beta\right)^2}{\beta\left(K+\frac{4}{3}G\right)}\right)^2 - 4\frac{\phi^2\rho_f\left(\rho-\beta\rho_f\right)}{\beta R\left(K+\frac{4}{3}G\right)}}\right]\end{aligned} \tag{1.37a}$$

$$\lambda_3^2 = \frac{\rho-\beta\rho_f}{G}\,. \tag{1.37b}$$

Expressing the determinant using these roots the scalar equation corresponding to (1.32) is given by

$$\left(\nabla^2 - s^2\lambda_3^2\right)\left(\nabla^2 - s^2\lambda_1^2\right)\left(\nabla^2 - s^2\lambda_2^2\right)\psi + \delta(\mathbf{x}-\mathbf{y}) = 0 \tag{1.38}$$

using an appropriate abbreviation ψ for every operator, i.e.,

$$\begin{aligned}
\text{2-d:}\quad & \mathbf{B4}^{*comp}: \ \psi = G\frac{\beta}{s\rho_f}\left(K+\frac{4}{3}G\right)\varphi \\
& \mathbf{B6}^{comp}: \ \psi = -G\frac{s^2\phi^2\rho_f}{\beta}\left(K+\frac{4}{3}G\right)R\varphi \\
\text{3-d:}\quad & \mathbf{B4}^{*comp}: \ \psi = G^2\frac{\beta}{s\rho_f}\left(K+\frac{4}{3}G\right)\left(\nabla^2 - s^2\lambda_3^2\right)\varphi \\
& \mathbf{B6}^{comp}: \ \psi = G^2\left(\frac{s^2\phi^2\rho_f}{\beta}\right)^2\left(K+\frac{4}{3}G\right)R\left(\nabla^2 - s^2\lambda_3^2\right)\varphi\,.
\end{aligned} \tag{1.39}$$

The solution of the modified higher order Helmholtz equation (1.38) is

2-d:

$$\psi = \frac{1}{2\pi s^4}\left[\frac{K_0(\lambda_1 sr)}{(\lambda_1^2-\lambda_2^2)(\lambda_1^2-\lambda_3^2)} + \frac{K_0(\lambda_2 sr)}{(\lambda_2^2-\lambda_3^2)(\lambda_2^2-\lambda_1^2)} + \frac{K_0(\lambda_3 sr)}{(\lambda_3^2-\lambda_1^2)(\lambda_3^2-\lambda_2^2)}\right] \tag{1.40}$$

3-d:

$$\psi = \frac{1}{4\pi r s^4}\left[\frac{e^{-\lambda_1 sr}}{\left(\lambda_1^2-\lambda_2^2\right)\left(\lambda_1^2-\lambda_3^2\right)} + \frac{e^{-\lambda_2 sr}}{\left(\lambda_2^2-\lambda_1^2\right)\left(\lambda_2^2-\lambda_3^2\right)} + \frac{e^{-\lambda_3 sr}}{\left(\lambda_3^2-\lambda_2^2\right)\left(\lambda_3^2-\lambda_1^2\right)}\right] \tag{1.41}$$

with the zero order modified Bessel function of second kind $K_0(z)$. Further, the distance between the two points $\mathbf{x}$ and $\mathbf{y}$ is denoted by $r = |\mathbf{x}-\mathbf{y}|$.

Having in mind that the Laplace transformation of the function describing a traveling wave front with constant speed c is $e^{-rs/c} = \mathscr{L}\{H(t-r/c)\}$ (in 3-d), it is obvious that the above solution (1.41) represents three waves. However, as the roots λ_i are functions of s, here, the wave speeds are time dependent representing the dispersion[2] in a poroelastic continuum. This is in accordance with the well known three wave types of a poroelastic continuum [12]. The roots λ_1, λ_2, and λ_3 correspond to the wave speeds of the slow and fast compressional wave and to the shear wave, respectively. The same is true in 2-d where the dispersive wave fronts are represented in Laplace domain by the modified Bessel functions $K_0(z)$. It should be remarked that the root λ_3 representing the shear wave is a double root in 3-d whereas it is only a single root in 2-d, which, as in elasticity, corresponds to the number of polarization planes [81].

From a pure mathematical point of view, the determinant of the operator $\mathbf{B6}^{comp}$ can have four roots in 2-d and six roots in 3-d. However, in (1.34) or (1.36) only three or four roots are found, respectively. As above discussed, each root represents a different wave type whereas the shear wave corresponds to a double root in 3-d. Therefore, from a physical point of view $\mathbf{B6}^{comp}$ can be expected to have the same roots as $\mathbf{B4}^{*comp}$, despite the larger matrix dimension. This is confirmed in (1.34) and (1.36).

[2]The terms *dispersion*, *attenuation*, and *damping* are not always used for the same meanings. In this work, *dispersion* refers to the effects resulting from or related to the dependence of wave speeds on frequency, *attenuation* describes any decrease (e.g., of the amplitude of a wave), regardless of the reasons (e.g., geometrical attenuation, viscous damping, ...), and *damping* stands for a decrease related to loss of energy (e.g., resulting from friction).

As a consequence, it can be concluded that the representation of a poroelastic continuum with solid displacement and fluid displacement is overdetermined, i.e., the representation with pore pressure and solid displacement is sufficient. This confirms the considerations of [14].

The next steps are to insert the solution ψ back into the definition $\mathbf{G} = \mathbf{B}^{*co}\varphi$ taking into account the proper relation (1.39) between φ and ψ. After calculating the respective matrix of cofactors $\mathbf{B}^{*co}$, the fundamental solutions are found for the u_i^s-p–formulation

$$\begin{aligned}\mathbf{G4}^{comp} &= \begin{bmatrix} \hat{U}_{ij}^s & \hat{U}_i^f \\ \hat{P}_j^s & \hat{P}^f \end{bmatrix} \\ &= \frac{s\rho_f}{G\beta\left(K+\frac{4}{3}G\right)} \begin{bmatrix} \left(F\nabla^2 + AD\right)\delta_{ij} - F\partial_{ij} & -A\left(\alpha-\beta\right)s\partial_i \\ -A\left(\alpha-\beta\right)\partial_i & A\left(\left(K+\frac{1}{3}G\right)\nabla^2 + A\right) \end{bmatrix}\psi \end{aligned} \tag{1.42}$$

with the abbreviations $A = G\nabla^2 - s^2\left(\rho - \beta\rho_f\right)$, $D = \beta/\left(s\rho_f\right)\nabla^2 - \phi^2 s/R$, $F = \left(K + 1/3\,G\right)D - \left(\alpha-\beta\right)^2 s$, and for the u_i^s-u_i^f–formulation

$$\begin{aligned}\mathbf{G6}^{comp} &= \begin{bmatrix} \hat{U}_{ij}^{ss} & \hat{U}_{ij}^{sf} \\ \hat{U}_{ij}^{fs} & \hat{U}_{ij}^{ff} \end{bmatrix} \\ &= \frac{-\beta}{Gs^2\phi^2\rho_f\left(K+\frac{4}{3}G\right)} \begin{bmatrix} M_3\partial_{ij} + \left(M_5 - M_3\nabla^2\right)\delta_{ij} & M_1\partial_{ij} + \left(M_4 - M_1\nabla^2\right)\delta_{ij} \\ M_1\partial_{ij} + \left(M_4 - M_1\nabla^2\right)\delta_{ij} & M_2\partial_{ij} + \left(M_6 - M_2\nabla^2\right)\delta_{ij} \end{bmatrix}\psi \end{aligned} \tag{1.43}$$

with the abbreviations

$$\begin{aligned} M_1 &= CE\left[\frac{K+\frac{1}{3}G}{R} + \left(\frac{\alpha}{\phi}-1\right)^2\right] - C^2\left(\frac{\alpha}{\phi}-1\right) + C\nabla^2\left(K+\frac{1}{3}G\right) \\ &\quad + B\left[C - E\left(\frac{\alpha}{\phi}-1\right)\right] \\ M_2 &= 2BC\left(\frac{\alpha}{\phi}-1\right) - B^2 - B\nabla^2\left(K+\frac{1}{3}G\right) - C^2\left[\frac{K+\frac{1}{3}G}{R} + \left(\frac{\alpha}{\phi}-1\right)^2\right] \\ M_3 &= -E\nabla^2\left(K+\frac{1}{3}G\right) + 2EC\left(\frac{\alpha}{\phi}-1\right) - C^2 - E^2\left[\frac{K+\frac{1}{3}G}{R} + \left(\frac{\alpha}{\phi}-1\right)^2\right] \\ M_4 &= \frac{s^2\rho_f\phi^2 G}{\beta}\left(\nabla^2 - s^2\lambda_3^2\right)\left[\nabla^2\left(\frac{\alpha}{\phi}-1\right) + \frac{C}{R}\right] \\ M_5 &= \frac{s^2\rho_f\phi^2 G}{\beta}\left(s^2\lambda_3^2 - \nabla^2\right)\left[\nabla^2 + \frac{E}{R}\right] \\ M_6 &= \frac{s^2\rho_f\phi^2 G}{\beta}\left(s^2\lambda_3^2 - \nabla^2\right)\left[\nabla^2\left(\frac{K+\frac{1}{3}G}{R} + \left(\frac{\alpha}{\phi}-1\right)^2\right) + \frac{B}{R}\right] \\ B &= G\nabla^2 - s^2\left(1-\phi\right)\rho_s - C \qquad C = s\frac{\phi^2}{\kappa} + s^2\rho_a \qquad E = -s^2\phi\rho_f - C\,. \end{aligned}$$

The difference of the 2-d solution and the 3-d solution lies only in the different functions ψ from (1.40) or (1.41), respectively. The explicit expressions of all the above given fundamental solutions can be found in appendix A. Comparing the explicit expressions for $\hat{U}_{ij}^s$ and $\hat{U}_{ij}^{ss}$ in appendix A, it is obvious that both

fundamental solutions are identical. The other fundamental solutions have to differ simply because they correspond to a different physical problem: $\hat{U}_i^f$ and $\hat{P}^f$ are the response to a different load in the fluid than $\hat{U}_{ij}^{sf}$ and $\hat{U}_{ij}^{ff}$, namely the former to a source and the latter to a force, and $\hat{P}_j^s$ captures the effect of a force in the solid on a different quantity than $\hat{U}_{ij}^{sf}$, namely on the pore pressure versus the relative solid-fluid displacement.

Incompressible model In section 1.2, the governing equations for the u_i^s-p–formulation were obtained by taking a limit of $R \to \infty$ and setting $\alpha = 1$. Unfortunately, this limiting process can only be applied to the fundamental solutions of the compressible case in 3-d. In 2-d, this limit is not finite. These solutions must be calculated independently using the same procedure as before. First, the determinants with their respective roots are calculated. However, here, the u_i^s-p-and the u_i^s-u_i^f-formulations have different roots indicating that two different incompressible models are considered as discussed in section 1.2.

First, the u_i^s-p-formulation is discussed. In this representation, the determinants are

$$\text{2-d:} \quad \det\left(\mathbf{B4}^{*\,incomp}\right) = \frac{G\beta}{s\rho_f}\left(K+\frac{4}{3}G\right)\left(\nabla^2 - s^2\lambda_3^2\right)\left(\nabla^2 - s^2\lambda_1^2\right)\nabla^2 \tag{1.44}$$

$$\text{3-d:} \quad \det\left(\mathbf{B4}^{*\,incomp}\right) = \frac{G^2\beta}{s\rho_f}\left(K+\frac{4}{3}G\right)\left(\nabla^2 - s^2\lambda_3^2\right)^2\left(\nabla^2 - s^2\lambda_1^2\right)\nabla^2 \tag{1.45}$$

with the roots

$$\lambda_1^2 = \frac{\rho + \rho_f\left(\frac{1}{\beta} - 2\right)}{K + \frac{4}{3}G} \qquad \lambda_3^2 = \frac{\rho - \beta\rho_f}{G}\,. \tag{1.46}$$

This yields an operator equation similar to (1.38)

$$\left(\nabla^2 - s^2\lambda_3^2\right)\left(\nabla^2 - s^2\lambda_1^2\right)\nabla^2\psi + \delta(\mathbf{x}-\mathbf{y}) = 0 \tag{1.47}$$

using the appropriate abbreviation for ψ corresponding to (1.39). Due to the Laplacian operator in (1.47) this is no longer an iterated modified Helmholtz equation but can be solved in a similar way by splitting the operator in Helmholtz and Laplace equations. The solution is

$$\text{2-d:} \quad \psi = \frac{1}{2\pi s^4}\left[\frac{K_0(\lambda_1 sr)}{\left(\lambda_1^2 - \lambda_3^2\right)\lambda_1^2} - \frac{\ln r}{\lambda_1^2\lambda_3^2} + \frac{K_0(\lambda_3 sr)}{\left(\lambda_3^2 - \lambda_1^2\right)\lambda_3^2}\right] \tag{1.48}$$

$$\text{3-d:} \quad \psi = \frac{1}{4\pi r s^4}\left[\frac{e^{-\lambda_1 sr}}{\left(\lambda_1^2 - \lambda_3^2\right)\lambda_1^2} + \frac{1}{\lambda_1^2\lambda_3^2} + \frac{e^{-\lambda_3 sr}}{\left(\lambda_3^2 - \lambda_1^2\right)\lambda_3^2}\right]. \tag{1.49}$$

As remarked at the beginning of this subsection, in 3-d, the incompressible solutions (1.49) are the limit values of the compressible results (1.41) for $\lambda_2 \to 0$. Contrary to that, in 2-d, the compressible solutions (1.40) tend to infinity for $\lambda_2 \to 0$, i.e., to calculate the solution (1.48), the equation (1.47) has to be solved.

For the u_i^s-u_i^f–formulation the determinants are found to be

$$\text{2-d:} \quad \det\left(\mathbf{B6}^{incomp}\right) = \frac{s^4 G\phi^4\rho_f^2}{\beta^2}\left(K+\frac{4}{3}G\right)\left(\nabla^2 - s^2\lambda_3^2\right)\left(\nabla^2 - s^2\lambda_1^2\right) \tag{1.50}$$

$$\text{3-d:} \quad \det\left(\mathbf{B6}^{incomp}\right) = \frac{-s^6 G^2\phi^6\rho_f^3}{\beta^3}\left(K+\frac{4}{3}G\right)\left(\nabla^2 - s^2\lambda_3^2\right)^2\left(\nabla^2 - s^2\lambda_1^2\right) \tag{1.51}$$

with the roots

$$\lambda_1^2 = \frac{\rho - \beta\rho_f}{K + \frac{4}{3}G} \qquad \lambda_3^2 = \frac{\rho - \beta\rho_f}{G} \,. \tag{1.52}$$

Note that λ_1 differs from that in (1.46) and only λ_3 is identical to that of the $\mathbf{B4}^{incomp}$ operator. These determinants yield a modified iterated Helmholtz operator similar to (1.38)

$$\left(\nabla^2 - s^2\lambda_3^2\right)\left(\nabla^2 - s^2\lambda_1^2\right)\psi + \delta(\mathbf{x}-\mathbf{y}) = 0 \tag{1.53}$$

using the proper abbreviation

$$\begin{aligned} &\text{2-d:} \quad \mathbf{B6}^{incomp}: \;\; \psi = G\frac{s^4\phi^4\rho_f^2}{\beta^2}\left(K + \frac{4}{3}G\right)\varphi \\ &\text{3-d:} \quad \mathbf{B6}^{incomp}: \;\; \psi = -G^2\frac{s^6\phi^6\rho_f^3}{\beta^3}\left(K + \frac{4}{3}G\right)\left(\nabla^2 - s^2\lambda_3^2\right)\varphi \,. \end{aligned} \tag{1.54}$$

The solution of the modified Helmholtz equation (1.53) is

$$\text{2-d:} \quad \psi = \frac{1}{2\pi s^2}\frac{1}{\lambda_3^2 - \lambda_1^2}\left[K_0(\lambda_3 sr) - K_0(\lambda_1 sr)\right] \tag{1.55}$$

$$\text{3-d:} \quad \psi = \frac{1}{4\pi r s^2}\frac{1}{\lambda_3^2 - \lambda_1^2}\left[e^{-\lambda_3 sr} - e^{-\lambda_1 sr}\right] \,. \tag{1.56}$$

These solutions essentially differ from the corresponding ones in the u_i^s-p–formulation (1.48) and (1.49). The terms $\ln(r)/\left(\lambda_1^2\lambda_3^2\right)$ or $1/\left(\lambda_1^2\lambda_3^2\right)$ produced by the limit $\lambda_2 \to 0$ in (1.48) and (1.49) are no longer present. So, obviously, this simplified incompressible model will produce different results compared to the incompressible u_i^s-p-formulation.

Concerning the waves represented in both models the following observations are made. In both formulations, the third root λ_3 corresponding to the shear wave speed is not changed because incompressibility can only affect volumetric changes. On the other hand, the compressional waves have to change as observed by the vanishing root λ_2 and the different root λ_1. Here, also the difference between both formulations is obvious. In the u_i^s-p–formulation the smaller value λ_2, corresponding to the faster compression wave, goes to zero. The larger value λ_1, corresponding to the slower compressional wave, survives. Reflecting the physics behind these two compressional waves this behavior is explainable. In case of the fast compressional wave, the solid and the fluid move in phase. If the material is assumed to be incompressible it has no longer any volumetric deformation and, subsequently, the wave speed tends to infinity respective the corresponding λ_2 to zero. In case of the slow compressional wave, the solid and fluid move in opposite phase. This relative movement is still possible if both the material constituents are incompressible.

These physical considerations are well represented in the u_i^s-p-formulation. In the u_i^s-u_i^f-formulation, no root λ_2 exists at all, i.e., the determinants (1.50) or (1.51) are only of second or third order in ∇^2 in 2-d or 3-d, respectively. This reflects the fact that this incompressible model is not achieved by a limit as in the u_i^s-p-formulation. Only from physics it can be concluded that the fast compressional wave vanishes, however, the surviving wave has a different wave speed compared to the other formulation.

Finally, the incompressible fundamental solutions are found for the u_i^s-p-formulation

$$\mathbf{G4}^{incomp} = \frac{s\rho_f}{G\beta\left(K + \frac{4}{3}G\right)}\begin{bmatrix} \left(F^*\nabla^2 + AD^*\right)\delta_{ij} - F^*\partial_{ij} & -A(1-\beta)s\partial_i \\ -A(1-\beta)\partial_i & A\left(\left(K + \frac{1}{3}G\right)\nabla^2 + A\right) \end{bmatrix}\psi \tag{1.57}$$

with the function ψ taken from (1.48) in the 2-d case or from (1.49) in the 3-d case. Differently than in the compressible case, here, the constants are $D^* = \beta/(s\rho_f)\nabla^2$ and $F^* = (K+1/3G)D^* - (1-\beta)^2 s$. For the u_i^s-u_i^f-formulation the matrix of fundamental solutions is

$$\begin{aligned}\mathbf{G6}^{incomp} &= \begin{bmatrix} \hat{U}_{ij}^{ss} & \hat{U}_{ij}^{sf} \\ \hat{U}_{ij}^{fs} & \hat{U}_{ij}^{ff} \end{bmatrix} \\ &= \frac{\beta^2\left(K+\frac{1}{3}G\right)}{Gs^4\phi^4\rho_f^2\left(K+\frac{4}{3}G\right)} \begin{bmatrix} (M_0E+E^2\nabla^2)\delta_{ij} - E^2\partial_{ij} & -C(M_0+E\nabla^2)\delta_{ij} + CE\partial_{ij} \\ -C(M_0+E\nabla^2)\delta_{ij} + CE\partial_{ij} & B(M_0+\nabla^2E)\delta_{ij} - C^2\partial_{ij} \end{bmatrix} \psi \end{aligned} \tag{1.58}$$

with the abbreviations B,C and E from the compressible case and

$$M_0 = \frac{s^2\rho_f\phi^2 G}{\beta\left(K+\frac{1}{3}G\right)}\left(s^2\lambda_3^2 - \nabla^2\right) .$$

In equation (1.58), the function ψ has to be taken from (1.55) in the 2-d case or from (1.56) in the 3-d case. The final result can be summarized in the following form

$$\mathbf{G6}^{incomp} = \begin{bmatrix} 1 & \frac{\phi-\beta}{\phi} \\ \frac{\phi-\beta}{\phi} & \frac{(\phi-\beta)^2}{\phi^2} \end{bmatrix} \hat{U}_{ij}^{ss} . \tag{1.59}$$

The explicit expression of $\hat{U}_{ij}^{ss}$ is given in the appendix A. The solution (1.59) makes it obvious that the underlying model for incompressibility is not sufficient because this result can be interpreted as totally dominant solid displacements, i.e., the fluid influences only the material data of the bulk material but not the behavior. This seems to be a very crude approximation of the realistic behavior, especially under the aspect of wave propagation.

In general, all the above derived incompressible solutions show that the assumption of incompressible constituents yields an infinite wave speed of the fast compressional wave. Contrary to that, if only one constituent is assumed to be incompressible all wave types still have finite wave speeds. It was also shown that in the incompressible model of the u_i^s-u_i^f–formulation one compressional wave disappears. This makes no sense in author's opinion. However, the other model for incompressibility used in the u_i^s-p–formulation, i.e., $R \to \infty$ and $\alpha = 1$, which can not be introduced to the constitutive equations of the partial stress formulation, as discussed in section 1.2, can be inserted into the final fundamental solutions (A.17) and (A.18) of the compressible u_i^s-u_i^f–formulation. Due to the different model assumptions such incompressible fundamental solutions for the u_i^s-u_i^f–formulation are different from (1.59).

1.3.1 Singular Behavior

The singular behavior of the above given fundamental solutions can be found by a series expansion with respect to the variable r. This variable is found in these solutions either in the exponential function in the 3-d solutions or in the Bessel functions in case of 2-d. Else, only powers of r appear. So, it is sufficient to insert the following series expansions

$$e^{-\lambda_k sr} = \sum_{\ell=0}^{\infty} \frac{(-\lambda_k sr)^\ell}{\ell!} = 1 - \lambda_k sr + \lambda_k^2 s^2 r^2 + \mathscr{O}\left(r^3\right) \tag{1.60}$$

for the exponential function into the 3-d fundamental solutions (A.1), (A.8), (A.17), (A.19), and

$$K_0(\lambda_k sr) = -(\ln(\lambda_k sr) - \ln 2 + \gamma) + \mathscr{O}(r^2) \tag{1.61a}$$

$$K_1(\lambda_k sr) = \frac{1}{\lambda_k sr} + \frac{\lambda_k sr}{2}\left(\ln(\lambda_k sr) - \ln 2 + \gamma - \frac{1}{2}\right) + \mathscr{O}(r^3) \tag{1.61b}$$

$$\gamma = \lim_{n\to\infty}\left(\sum_{\nu=1}^{n}\frac{1}{\nu} - \ln n\right) \approx 0.577216 \text{ (Euler constant)}$$

for the Bessel functions into the 2-d fundamental solutions (A.6), (A.13), (A.18), and (A.20). Inserting these series into the fundamental solutions and a subsequent ordering with respect to the power of r yields the singular behavior.

u_i^s-p-formulation For the u_i^s-p-formulation the compressible as well as the incompressible solution behaves equal. In 3-d, it is found

$$\hat{P}_i^s,\ \hat{U}_i^f = \mathscr{O}(r^0) \tag{1.62a}$$

$$\hat{U}_{ij}^s = \underbrace{\frac{1}{16\pi G(1-\nu)}\left\{r_{,i}r_{,j} + (3-4\nu)\delta_{ij}\right\}\frac{1}{r}}_{\text{elastostatic fundamental solution}} + \mathscr{O}(r^0) \tag{1.62b}$$

$$\hat{P}^f = \frac{\rho_f s}{4\pi\beta}\frac{1}{r} + \mathscr{O}(r^0)\ , \tag{1.62c}$$

and in 2-d a similar result is achieved

$$\hat{P}_i^s,\ \hat{U}_i^f = \mathscr{O}(r^0) \tag{1.63a}$$

$$\hat{U}_{ij}^s = \underbrace{\frac{1}{8\pi G(1-\nu)}\left\{r_{,i}r_{,j} - (3-4\nu)\delta_{ij}\ln r\right\}}_{\text{elastostatic fundamental solution}} + \mathscr{O}(r^0) \tag{1.63b}$$

$$\hat{P}^f = \frac{-\rho_f s}{2\pi\beta}\ln r + \mathscr{O}(r^0)\ . \tag{1.63c}$$

So, the singular behavior is the same as in elastostatics or acoustics, i.e., the poroelastic fundamental solutions are only weakly singular or even regular. Again, note that there is no different behavior between the compressible or incompressible model. The singularities of the adjoint tractions and fluxes can be found in Appendix A.1.3.

u_i^s-u_i^f-formulation For the u_i^s-u_i^f-formulation, the singular behavior is different from the above discussed formulation. This is not surprising because looking at the differential operator **B6** (1.26) it is observed that this operator has in the lower part of the main diagonal no Laplacian operator contrary to the operator **B4** (1.24). This is also represented in the fact that the three members $\hat{U}_{ij}^{fs}$, $\hat{U}_{ij}^{sf}$, and $\hat{U}_{ij}^{ff}$ of **G6** are composed by the fundamental solution $\hat{U}_{ij}^{ss}$ and some additional term. In detail, the following

singularities are found for the 3-d case

$$\hat{U}_{ij}^{ss} = \underbrace{\frac{1}{16\pi G(1-\nu)}\left\{r_{,i}r_{,j} + (3-4\nu)\,\delta_{ij}\right\}\frac{1}{r}}_{\text{elastostatic fundamental solution}} + \mathscr{O}\left(r^0\right) \tag{1.64a}$$

$$\hat{U}_{ij}^{sf} = \hat{U}_{ij}^{fs} = \frac{1}{16\pi G(1-\nu)}\Big\{\frac{\phi-\beta}{\phi}\left(r_{,i}r_{,j} + (3-4\nu)\,\delta_{ij}\right) + \frac{\alpha-\beta}{\phi}\left(r_{,i}r_{,j} - \delta_{ij}\right)(1-2\nu)\Big\}\frac{1}{r} + \mathscr{O}\left(r^0\right) \tag{1.64b}$$

$$\hat{U}_{ij}^{ff} = \frac{\beta}{4\pi\phi^2 s^2 \rho_f}\left\{3r_{,i}r_{,j} - \delta_{ij}\right\}\frac{1}{r^3} + \mathscr{O}\left(r^{-1}\right) \tag{1.64c}$$

and for the 2-d case

$$\hat{U}_{ij}^{ss} = \underbrace{\frac{1}{8\pi G(1-\nu)}\left\{r_{,i}r_{,j} - (3-4\nu)\,\delta_{ij}\ln r\right\}}_{\text{elastostatic fundamental solution}} + \mathscr{O}\left(r^0\right) \tag{1.65a}$$

$$\hat{U}_{ij}^{sf} = \hat{U}_{ij}^{fs} = \frac{1}{8\pi G(1-\nu)}\Big\{\frac{\phi-\beta}{\phi}\left(r_{,i}r_{,j} - (3-4\nu)\,\delta_{ij}\ln r\right) + \frac{\alpha-\beta}{\phi}\left(r_{,i}r_{,j} + \delta_{ij}\ln r\right)(1-2\nu)\Big\} + \mathscr{O}\left(r^0\right) \tag{1.65b}$$

$$\hat{U}_{ij}^{ff} = \frac{\beta}{2\pi\phi^2 s^2 \rho_f}\left\{2r_{,i}r_{,j} - \delta_{ij}\right\}\frac{1}{r^2} + \mathscr{O}\left(\ln r\right)\ . \tag{1.65c}$$

In equations (1.64c) and (1.65c), it becomes obvious that these solutions are hyper-singular, whereas all other solutions are weakly singular. Also, in (1.64b) and (1.65b) the elastostatic singularity of (1.64a) and (1.65a), respectively, is identified with some additional poroelastic terms.

In case of the incompressible model, clearly, due to the connected form of (1.59) all four fundamental solutions have the same order of singularity namely that of $\hat{U}_{ij}^{ss}$. The limit of this solution (A.19) or (A.20) yields as in the compressible case the elastostatic fundamental solution. However, no hyper-singular behavior exists for the incompressible solutions.

1.3.2 Visualization of some Fundamental Solutions

Finally, some exemplary fundamental solutions are calculated to visualize the principal behavior and the difference between the compressible and incompressible model. Despite the differences in both incompressible models, i.e., in the u_i^s-p-formulation and in the u_i^s-u_i^f-formulation, the principal effects which can be visualized are similar. Therefore, next, only the visualization for the u_i^s-p-formulation and for this formulation only the displacement due to a point force $\hat{U}_{ij}^s$ and the pressure due to a source $\hat{P}^f$ in 3-d are presented.

Exemplary for a material which can be modeled incompressible as well as compressible a soil is chosen. The material data (see Tab. 3.1) are taken from literature [60]. The incompressibility condition (1.5) yields for this material

$$\frac{K}{K^s} = 0.019 \qquad \frac{K}{K^f} = 0.0636\ . \tag{1.66}$$

So, it can be expected that the fundamental solutions of the compressible and incompressible model show a similar behavior.

First, in figure 1.1, the displacement fundamental solution abs $\left(\hat{U}^s_{11}\right)$ is depicted versus the distance r and the frequency ω. To introduce in the fundamental solutions from appendix A the frequency instead of the

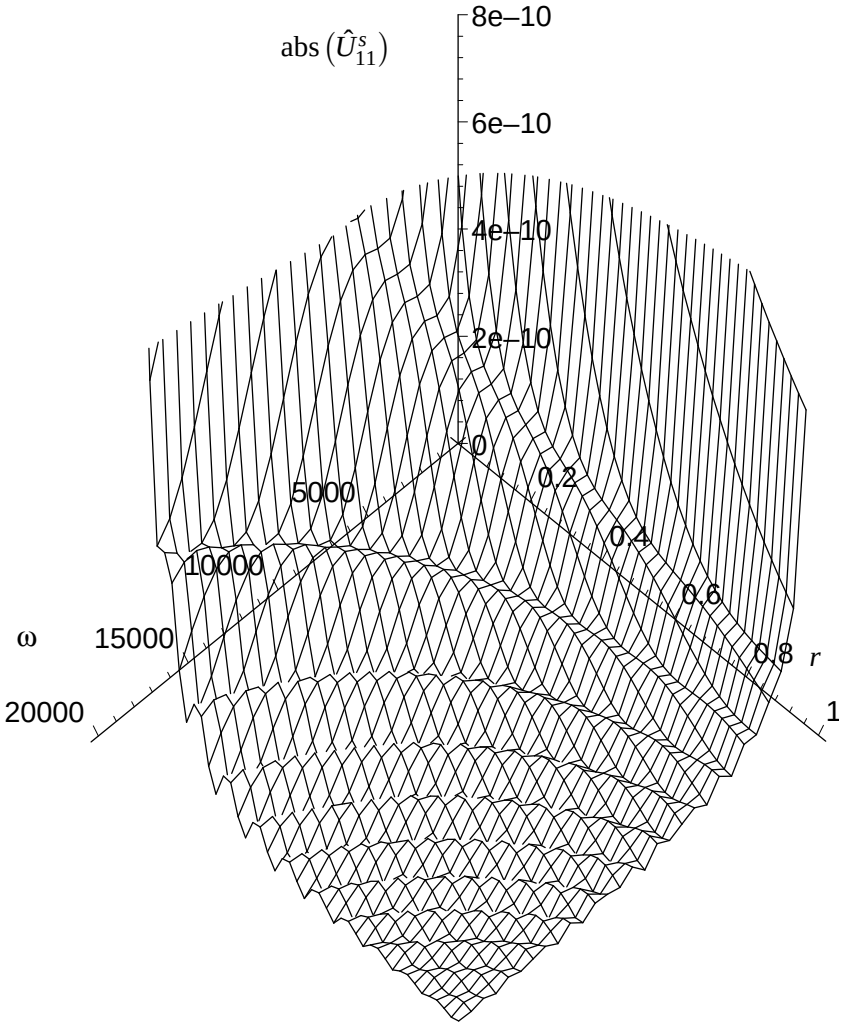

Figure 1.1: Displacement fundamental solution abs $\left(\hat{U}^s_{11}\right)$ versus frequency ω and distance r

complex Laplace variable s, simply the real part of s is set to zero, i.e., $s = \mathrm{i}\omega$. Further, the absolute value of the complex valued displacement solution, i.e., the amplitude, is given in figure 1.1 and the range of values is restricted at the singularity. The singular behavior for small values of r is nearly independent of the frequency. Away from the origin the solution shows a wave like form with smaller amplitudes for higher frequencies.

In the following, to have a better insight into the behavior of the fundamental solutions, the distance r is kept constant and the frequency ω is varied. Further, all results, i.e., the displacement and pressure results are normalized to their singular behavior (1.62b) and (1.62c), respectively. Additionally to the frequency results also the time-dependent fundamental solutions are calculated by an inverse Laplace transform. However, not the impulse response functions are presented but the response due to a Heaviside (unit step

function) time history of the load. This is achieved by the convolution between the fundamental solution and the Heaviside function. Both operations, the inverse transform and the convolution, are performed within one calculation using the Convolution Quadrature Method proposed by Lubich [63, 64].

In figure 1.2, the normalized displacement fundamental solution abs $\left(\hat{U}^s_{11}\right)$ is plotted versus frequency for the compressible and the incompressible model. This study is given for two points at $r = 0.1\,\mathrm{m}$ and at $r = 0.5\,\mathrm{m}$ distance from the origin. For moderate frequencies and small r both solutions, compressible and incompressible, are very similar whereas for higher frequencies differences are observed. This is in accordance with the model. The fast compressional wave which speed tends to infinity influences only the short time behavior, i.e., the higher frequencies. Hence, if this wave vanishes only the high frequency range of the solution is affected. The singular behavior, i.e., the limit $\omega \to 0$, is identical for the compressible and incompressible solution. However, for small but nonzero frequencies the solutions differ for the two models, which is well visible for $r = 0.1\,\mathrm{m}$. This difference may be explained with the change in the speed of the slow compressional wave.

Except for the last effect all these differences of the compressible and the incompressible model are also visible in time domain. Therefore, in figure 1.3 the time dependent displacement response due to a Heaviside load in time is depicted versus time at the distance $r = 0.5\,\mathrm{m}$. There are, as expected, not too much differences visible in the long time behavior. The two jumps in the graph at $t = 0.0004\,\mathrm{s}$ and at $t = 0.0031\,\mathrm{s}$ correspond to the fast compressional wave and to the shear wave, respectively. In the zoom, it becomes visible that in the incompressible model (dashed line) the compressional wave speed tends to infinity, i.e., the arrival time tends to zero. Else, this time dependent plot of the fundamental solution shows that for this material the incompressible model can be chosen if not the early time response is under consideration. However, it must be remarked that for other material data, especially if they violate the incompressibility condition (1.5), both models show large differences over the complete observation period.

Next, in figure 1.4, the normalized pressure due to a source in the fluid is considered. For this solution the largest differences are expected because the pore pressure is no longer a free variable in the incompressible model. Further, in an incompressible fluid a change in pressure is immediate at every point r, hence the pressure can not show a strong time, respectively frequency, dependence. These effects are observed in figure 1.4 where both results differ by several decades in the absolute values. The compressible pressure is much smaller than the solution in the incompressible model and shows a more pronounced frequency dependence. However, for very small frequency, i.e., for the long time behavior, both solutions tend to the same value. It should be remarked that in figure 1.4 a logarithmic scale for the pressure is used which on the one hand enables this representation at all but on the other hand distorts the frequency dependence.

In the time domain these considerations are confirmed. In figure 1.5, the pressure due to a Heaviside time history of the load is depicted versus time at the distance $r = 0.5\,\mathrm{m}$. Note, in figure 1.5 a different time scale compared to figure 1.3 is used. The pressure is mostly zero with the exception of the arrival time of the compressional wave at $t = 0.0004\,\mathrm{s}$. There, in the compressible solution an impulse is visible. The same impulse is also visible in the incompressible solution, however, at $t = 0\,\mathrm{s}$. Further, the characteristics of this shock wave is different for both models. In the more stiff incompressible model a more pronounced and larger impulse has been calculated compared to the compressible model. Naturally, the amplitude and sharpness of such a shock wave is dependent on the time discretization used and other parameters of the inverse transformation. However, in the comparison above for both the same parameters have been applied, so the results are comparable.

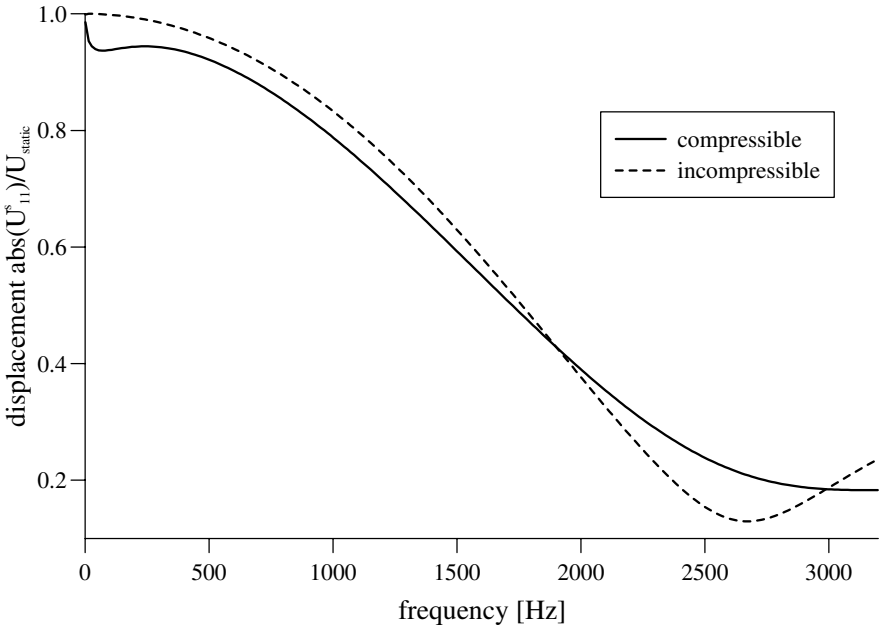

(a) $r = 0.1\,\mathrm{m}$

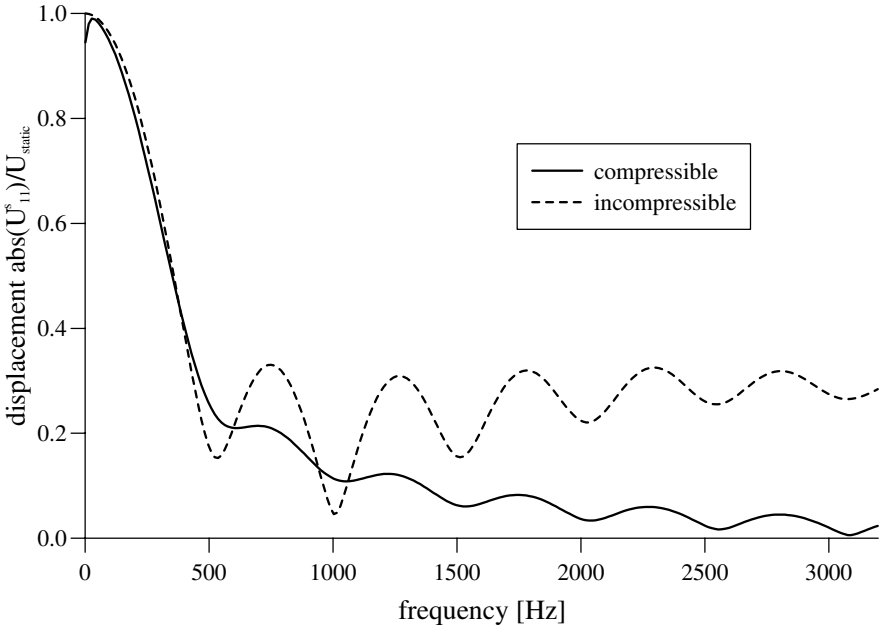

(b) $r = 0.5\,\mathrm{m}$

Figure 1.2: Displacement fundamental solution abs $\left(\hat{U}^s_{11}\right)$ normalized with U_{static} (1.62b) versus frequency ω: Comparison compressible and incompressible model at different distances r

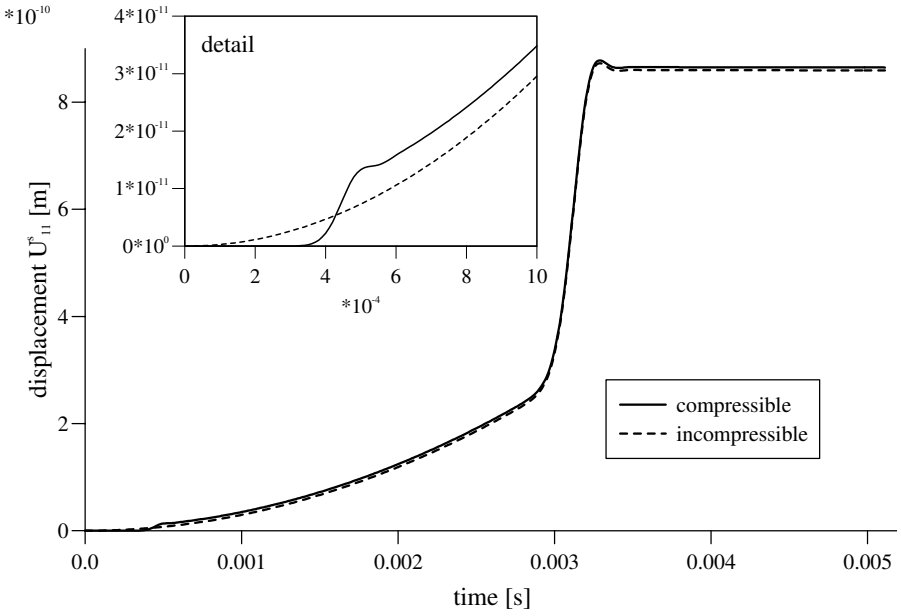

Figure 1.3: Displacement unit step response function U_{11}^s versus time t: Comparison compressible and incompressible model at the distance $r = 0.5\,\mathrm{m}$

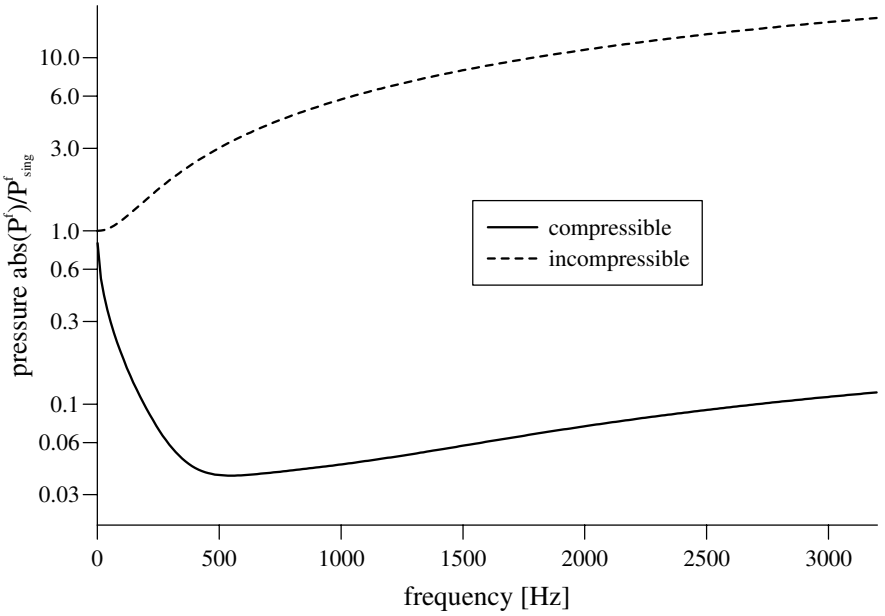

(a) $r = 0.1\,\mathrm{m}$

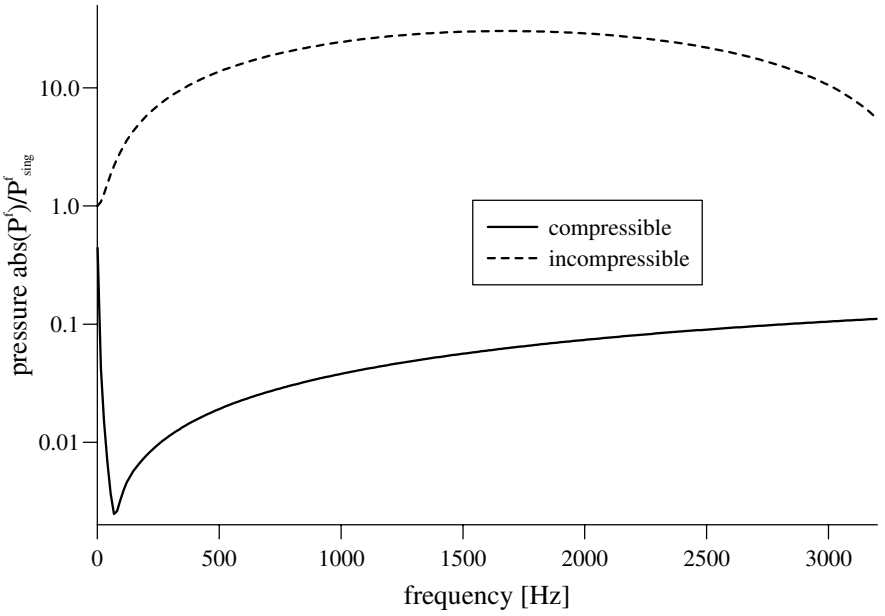

(b) $r = 0.5\,\mathrm{m}$

Figure 1.4: Pressure fundamental solution abs $\left(\hat{P}^f\right)$ normalized with $\hat{P}^f_{sing}$ (1.62c) versus frequency ω: Comparison compressible and incompressible model at different distances r

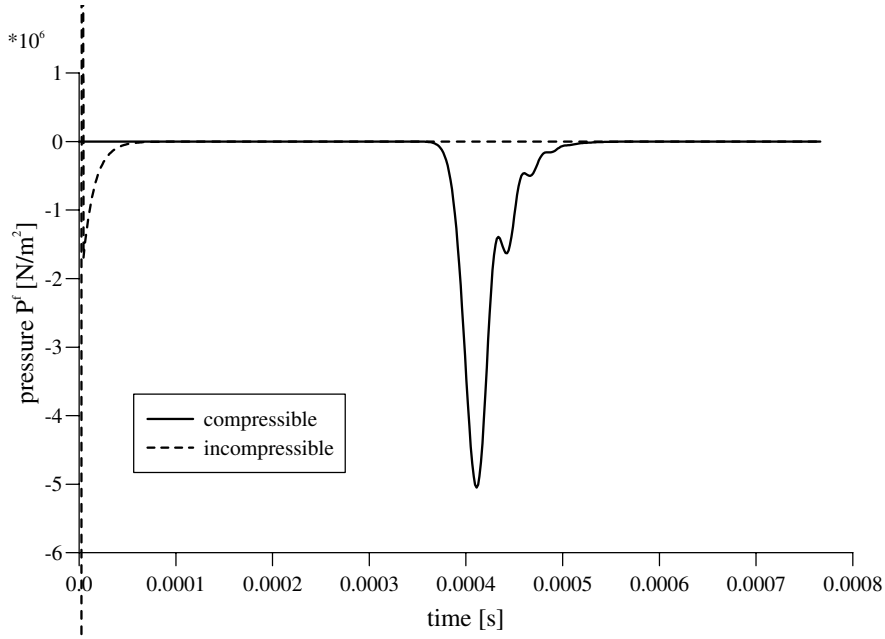

Figure 1.5: Pressure unit step response function P^f versus time t: Comparison compressible and incompressible model at the distance $r = 0.5\,\mathrm{m}$

2 Numerical Modeling of Poroelasticity

Numerical methods are needed to model the behavior of poroelastic materials in most cases, because analytical solutions are only available for a small number of special problems. As already mentioned, the Finite Element Method, probably the most common numerical approach in engineering, has also been applied to model the behavior of poroelastic materials. Nevertheless, this method has a significant disadvantage in the case of semi-infinite domains. Reflections on artificial boundaries, i.e., where the discretization ends, make it hard to fulfill the Sommerfeld radiation condition [90]. Therefore, the finite element mesh usually has to cover a large region of the unbounded domain, or special tricks, e.g., so-called infinite elements [3], need to be used to reasonably approximate the behavior in infinity.

The efficiency of the Boundary Element Method (BEM) in dealing with semi-infinite domain problems, e.g., soil-structure interaction, has long been recognized by researchers and engineers. One reason is that unlike with finite elements, the Sommerfeld radiation condition in infinity is implicitly fulfilled. Another principal advantage is the dimension reduction of the mesh, as only the boundary has to be discretized.

2.1 Boundary Element Formulation for Poroelasticity

The boundary integral equation for dynamic poroelasticity in Laplace domain can be obtained using either the corresponding reciprocal work theorem [28] or the weighted residuals formulation [43]. Here, the approach with weighted residuals will be presented. Bonnet [14] has shown that the solid displacements and the pore pressure are sufficient to describe a poroelastic continuum and the u_i^s-u_i^f-formulation is overdetermined. The previous chapter confirms both these facts. Therefore, the solid displacements u_i^s and the pore pressure p, i.e., one vector and one scalar, are used for the set of independent variables.

The poroelastodynamic integral equation can be derived directly by equating the inner product of (1.20) or (1.22), written in matrix form with operator matrix **B4** defined in (1.24), and the matrix of the fundamental solutions **G4** to a null vector, i.e.,

$$\int_\Omega \mathbf{G4}^T \mathbf{B4} \begin{bmatrix} \hat{u}_i^s(\mathbf{x},s) \\ \hat{p}(\mathbf{x},s) \end{bmatrix} \mathrm{d}\Omega = \mathbf{0} \qquad \text{where} \qquad \mathbf{G4} = \begin{bmatrix} \hat{U}_{ij}^s(\mathbf{x},\mathbf{y},s) & \hat{U}_i^f(\mathbf{x},\mathbf{y},s) \\ \hat{P}_j^s(\mathbf{x},\mathbf{y},s) & \hat{P}^f(\mathbf{x},\mathbf{y},s) \end{bmatrix}, \tag{2.1}$$

where the integration is performed over a domain Ω with boundary Γ and vanishing body forces F_i and sources a are assumed. By this inner product, essentially, the error in satisfying the governing differential equations (1.20) or (1.22) is forced to be orthogonal to **G4**. As only the u_i^s-p-formulation is used in the following, there is no danger of confusion with the u_i^s-u_i^f-formulation, and the 4 will be omitted from both **B** and **G**. Also the arguments $\mathbf{x}, \mathbf{y}$, and s will be left out as long as they remain unchanged.

According to the theory of Green's formula and using partial integration the operator **B** is transformed from acting on the vector of unknowns $[\hat{u}_i^s \ \hat{p}]^T$ to the matrix of fundamental solutions **G**.

These steps are easier understood looking at equation (2.1) written in index notation. This results in three (two) integral equations for the solid ($j = 1,2,3$ in 3-d and $j = 1,2$ in 2-d)

$$\begin{aligned}\int_\Omega \Bigg[& G\hat{u}^s_{i,kk}\hat{U}^s_{ij} + \left(K + \frac{1}{3}G\right)\hat{u}^s_{k,ik}\hat{U}^s_{ij} - (\alpha-\beta)\,\hat{p}_{,i}\hat{U}^s_{ij} - s^2(\rho - \beta\rho_f)\,\hat{u}^s_i\hat{U}^s_{ij} \\ & + \frac{\beta}{s\rho_f}\hat{p}_{,kk}\hat{P}^s_j - \frac{\phi^2 s}{R}\hat{p}\hat{P}^s_j - (\alpha-\beta)\,s\hat{u}^s_{k,k}\hat{P}^s_j \Bigg]\,\mathrm{d}\Omega = 0\end{aligned} \tag{2.2}$$

and one integral equation for the fluid

$$\begin{aligned}\int_\Omega \Bigg[& G\hat{u}^s_{i,kk}\hat{U}^f_i + \left(K + \frac{1}{3}G\right)\hat{u}^s_{k,ik}\hat{U}^f_i - (\alpha-\beta)\,\hat{p}_{,i}\hat{U}^f_i - s^2(\rho - \beta\rho_f)\,\hat{u}^s_i\hat{U}^f_i \\ & + \frac{\beta}{s\rho_f}\hat{p}_{,kk}\hat{P}^f - \frac{\phi^2 s}{R}\hat{p}\hat{P}^f - (\alpha-\beta)\,s\hat{u}^s_{k,k}\hat{P}^f \Bigg]\,\mathrm{d}\Omega = 0\,.\end{aligned} \tag{2.3}$$

In the above integral equations, either one or two differentiations have to be transformed by either one or two partial integrations. Two exemplary parts of integral equations (2.2) and (2.3) for the compressible case are presented in detail to show the principal procedure. All other partial integrations for the other parts in integral equations (2.2) and (2.3), and also for the incompressible case, can be performed analogously.

First, an integral with one differentiation in the kernel leads to (n_k is the outward normal vector)

$$\int_\Omega (\alpha-\beta)\,s\hat{u}^s_{k,k}\hat{P}^f\,\mathrm{d}\Omega = \int_\Gamma (\alpha-\beta)\,s\hat{u}^s_k n_k\hat{P}^f\,\mathrm{d}\Gamma - \int_\Omega (\alpha-\beta)\,s\hat{u}^s_k\hat{P}^f_{,k}\,\mathrm{d}\Omega \tag{2.4}$$

while an integral with two differentiation is transformed to

$$\begin{aligned}\int_\Omega G\hat{u}^s_{i,kk}\hat{U}^s_{ij}\,\mathrm{d}\Omega &= \int_\Gamma G\hat{u}^s_{i,k}n_k\hat{U}^s_{ij}\,\mathrm{d}\Gamma - \int_\Omega G\hat{u}^s_{i,k}\hat{U}^s_{ij,k}\,\mathrm{d}\Omega \\ &= \int_\Gamma G\hat{u}^s_{i,k}n_k\hat{U}^s_{ij}\,\mathrm{d}\Gamma - \int_\Gamma G\hat{u}^s_i\hat{U}^s_{ij,k}n_k\,\mathrm{d}\Gamma + \int_\Omega G\hat{u}^s_i\hat{U}^s_{ij,kk}\,\mathrm{d}\Omega\,.\end{aligned} \tag{2.5}$$

In both integrations by parts the divergence theorem is used. Obviously, one integration by parts changes the sign of the resulting domain integral while it remains unchanged in the case of two integration by parts, i.e., the operator **B** is transformed into its adjoint operator $\mathbf{B}^*$. This yields the following system of integral equations given in matrix notation as

$$\int_\Gamma \begin{bmatrix}\hat{U}^s_{ij} & -\hat{P}^s_j \\ \hat{U}^f_i & -\hat{P}^f\end{bmatrix}\begin{bmatrix}\hat{t}^s_i \\ \hat{q}\end{bmatrix}\mathrm{d}\Gamma - \int_\Gamma \begin{bmatrix}\hat{T}^s_{ij} & \hat{Q}^s_j \\ \hat{T}^f_i & \hat{Q}^f\end{bmatrix}\begin{bmatrix}\hat{u}^s_i \\ \hat{p}\end{bmatrix}\mathrm{d}\Gamma = -\int_\Omega (\mathbf{B}^*\mathbf{G})^T\begin{bmatrix}\hat{u}^s_i \\ \hat{p}\end{bmatrix}\mathrm{d}\Omega = \begin{bmatrix}\hat{u}^s_j \\ \hat{p}\end{bmatrix}\,. \tag{2.6}$$

To solve the domain integral in equation (2.6) for $\mathbf{y} \in \Omega$, the definition of fundamental solutions (1.29)

and the filter property of the Dirac distribution (B.9) is used. Additionally, the traction vector $\hat{t}_i^s = \hat{\sigma}_{ij} n_j$ and the flux $\hat{q} = -\beta/(s\rho_f)\left(\hat{p}_{,i} + \rho_f s^2 \hat{u}_i^s\right) n_i$ are introduced, and the abbreviations

$$\hat{T}_{ij}^s = \left(\left(K - \frac{2}{3}G\right) \hat{U}_{kj,k}^s + \alpha s \hat{P}_j \right) n_i + G\left(\hat{U}_{ij,l}^s + \hat{U}_{lj,i}^s\right) n_l \tag{2.7a}$$

$$\hat{Q}_j^s = \frac{\beta}{s\rho_f}\left(\hat{P}_{j,i}^s - s\rho_f \hat{U}_{ji}^s\right) n_i \tag{2.7b}$$

$$\hat{T}_i^f = \left((K - \frac{2}{3}G)\hat{U}_{k,k}^f + \alpha s \hat{P}^f \right) n_i + G\left(\hat{U}_{i,l}^f + \hat{U}_{l,i}^f\right) n_l \tag{2.7c}$$

$$\hat{Q}^f = \frac{\beta}{s\rho_f}\left(\hat{P}_{,j}^f - s\rho_f \hat{U}_j^f\right) n_j \tag{2.7d}$$

are used, where (2.7a) and (2.7b) can be interpreted as being the adjoint term to the traction vector $\hat{t}_i^s$ and the flux $\hat{q}$, respectively. With the fundamental solutions calculated in section 1.3 or the explicit form given in appendix A, the integral representation deduced starting from the weighted residuals is completely given.

Following the usual procedure as described, e.g., in [83], the load point $\mathbf{y}$ is shifted to the boundary Γ and the singular behavior of the fundamental solutions is taken into account. This results in the boundary integral equation

$$\int_\Gamma \begin{bmatrix} \hat{U}_{ij}^s & -\hat{P}_j^s \\ \hat{U}_i^f & -\hat{P}^f \end{bmatrix} \begin{bmatrix} \hat{t}_i^s \\ \hat{q} \end{bmatrix} \mathrm{d}\Gamma = \cancel{\int_\Gamma} \begin{bmatrix} \hat{T}_{ij}^s & \hat{Q}_j^s \\ \hat{T}_i^f & \hat{Q}^f \end{bmatrix} \begin{bmatrix} \hat{u}_i^s \\ \hat{p} \end{bmatrix} \mathrm{d}\Gamma + \begin{bmatrix} c_{ij} & 0 \\ 0 & c \end{bmatrix} \begin{bmatrix} \hat{u}_i^s \\ \hat{p} \end{bmatrix} \tag{2.8}$$

where c_{ij} and c are the integral free terms known from elastostatics and acoustics, respectively, and $\cancel{\int}$ denotes a Cauchy principal value integral. A transformation to time domain gives, finally, the time dependent integral equation for poroelasticity

$$\begin{aligned} &\int_0^t \int_\Gamma \begin{bmatrix} U_{ij}^s(t-\tau,\mathbf{y},\mathbf{x}) & -P_j^s(t-\tau,\mathbf{y},\mathbf{x}) \\ U_i^f(t-\tau,\mathbf{y},\mathbf{x}) & -P^f(t-\tau,\mathbf{y},\mathbf{x}) \end{bmatrix} \begin{bmatrix} t_i^s(\tau,\mathbf{x}) \\ q(\tau,\mathbf{x}) \end{bmatrix} \mathrm{d}\Gamma\,\mathrm{d}\tau = \\ &\quad \int_0^t \cancel{\int_\Gamma} \begin{bmatrix} T_{ij}^s(t-\tau,\mathbf{y},\mathbf{x}) & Q_j^s(t-\tau,\mathbf{y},\mathbf{x}) \\ T_i^f(t-\tau,\mathbf{y},\mathbf{x}) & Q^f(t-\tau,\mathbf{y},\mathbf{x}) \end{bmatrix} \begin{bmatrix} u_i^s(\tau,\mathbf{x}) \\ p(\tau,\mathbf{x}) \end{bmatrix} \mathrm{d}\Gamma\,\mathrm{d}\tau + \begin{bmatrix} c_{ij}(\mathbf{y}) & 0 \\ 0 & c(\mathbf{y}) \end{bmatrix} \begin{bmatrix} u_i^s(t,\mathbf{y}) \\ p(t,\mathbf{y}) \end{bmatrix} . \end{aligned} \tag{2.9}$$

A boundary element formulation is achieved following the usual procedure. First, the boundary surface Γ is discretized by E elements Γ_e where F polynomial shape functions $N_e^f(\mathbf{x})$ are defined. The boundary quantities are then approximated with the shape functions and the time dependent nodal values $u_i^{ef}(t)$, $t_i^{ef}(t)$, $p^{ef}(t)$, and $q^{ef}(t)$

$$\begin{aligned} u_i^s(\mathbf{x},t) &= \sum_{e=1}^{E} \sum_{f=1}^{{}^uF} {}^uN_e^f(\mathbf{x})\, u_i^{ef}(t) \quad & t_i^s(\mathbf{x},t) &= \sum_{e=1}^{E} \sum_{f=1}^{{}^tF} {}^tN_e^f(\mathbf{x})\, t_i^{ef}(t) \\ p(\mathbf{x},t) &= \sum_{e=1}^{E} \sum_{f=1}^{{}^pF} {}^pN_e^f(\mathbf{x})\, p^{ef}(t) \quad & q(\mathbf{x},t) &= \sum_{e=1}^{E} \sum_{f=1}^{{}^qF} {}^qN_e^f(\mathbf{x})\, q^{ef}(t) \ . \end{aligned} \tag{2.10}$$

In equations (2.10), four possibly different shape functions ${}^uN_e^f$, ${}^tN_e^f$, ${}^pN_e^f$, and ${}^qN_e^f$ are used. The most common choice are isoparametric elements with the same approximation level of all variables, i.e., a

single shape function ${}^{u}N_e^f = {}^{t}N_e^f = {}^{p}N_e^f = {}^{q}N_e^f = N_e^f$. Besides that, non-isoparametric elements employing different shape functions for displacements and pressure, as common in finite elements [62], are implemented. In that case, there are two different sets of shape functions, e.g., ${}^{u}N_e^f = {}^{t}N_e^f$ linear and ${}^{p}N_e^f = {}^{q}N_e^f$ constant. Only the notation corresponding to isoparametric elements is used in the rest of this section, more details related to mixed elements are presented in the next section. Inserting these shape functions (2.10) in the time dependent integral equation (2.9) yields

$$\begin{bmatrix} c_{ij}(\mathbf{y}) & 0 \\ 0 & c(\mathbf{y}) \end{bmatrix} \begin{bmatrix} u_i^s(\mathbf{y},t) \\ p(\mathbf{y},t) \end{bmatrix} = \sum_{e=1}^{E} \sum_{f=1}^{F} \left\{ \int_0^t \int_\Gamma \begin{bmatrix} U_{ij}^s(t-\tau,\mathbf{y},\mathbf{x}) & -P_j^s(t-\tau,\mathbf{y},\mathbf{x}) \\ U_i^f(t-\tau,\mathbf{y},\mathbf{x}) & -P^f(t-\tau,\mathbf{y},\mathbf{x}) \end{bmatrix} N_e^f(\mathbf{x}) \begin{bmatrix} t_i^{ef}(\tau) \\ q^{ef}(\tau) \end{bmatrix} \mathrm{d}\Gamma\,\mathrm{d}\tau \right.$$
$$\left. - \int_0^t \cancel{\int_\Gamma} \begin{bmatrix} T_{ij}^s(t-\tau,\mathbf{y},\mathbf{x}) & Q_j^s(t-\tau,\mathbf{y},\mathbf{x}) \\ T_i^f(t-\tau,\mathbf{y},\mathbf{x}) & Q^f(t-\tau,\mathbf{y},\mathbf{x}) \end{bmatrix} N_e^f(\mathbf{x}) \begin{bmatrix} u_i^{ef}(\tau) \\ p^{ef}(\tau) \end{bmatrix} \mathrm{d}\Gamma\,\mathrm{d}\tau \right\}. \tag{2.11}$$

Next, a time discretization has to be introduced. Since no time dependent fundamental solutions are known, the 'Convolution Quadrature Method' developed by Lubich [63, 64] is an effective choice compared to inverting the Laplace domain fundamental solutions at every collocation point in every time step using a series expansion [27]. A brief explanation of the convolution quadrature method can be found in appendix B.3.

Hence, after dividing the time period t in N intervals of equal duration Δt, i.e., $t = N\Delta t$, the convolution integrals between the fundamental solutions and the nodal values in (2.11) are approximated by the convolution quadrature method, i.e., the quadrature formula

$$y(t) = \int_0^t f(t-\tau)\, g(\tau)\,\mathrm{d}\tau \quad \rightarrow \quad y(n\Delta t) = \sum_{k=0}^{n} \omega_{n-k}(\Delta t)\, g(k\Delta t), \tag{2.12}$$

is applied to the integral equation (2.11). The weights ω_{n-k} are determined by the Laplace transformed function $\hat{f}$ and a linear multistep method. This results in the following boundary element time stepping formulation, $n = 0, 1, \ldots, N$

$$\begin{bmatrix} c_{ij}(\mathbf{y}) & 0 \\ 0 & c(\mathbf{y}) \end{bmatrix} \begin{bmatrix} u_i^s(\mathbf{y},n\Delta t) \\ p(\mathbf{y},n\Delta t) \end{bmatrix} = \sum_{e=1}^{E} \sum_{f=1}^{F} \sum_{k=0}^{n} \left\{ \begin{bmatrix} \omega_{n-k}^{ef}\left(\hat{U}_{ij}^s,\mathbf{y},\Delta t\right) & -\omega_{n-k}^{ef}\left(\hat{P}_j^s,\mathbf{y},\Delta t\right) \\ \omega_{n-k}^{ef}\left(\hat{U}_i^f,\mathbf{y},\Delta t\right) & -\omega_{n-k}^{ef}\left(\hat{P}^f,\mathbf{y},\Delta t\right) \end{bmatrix} \begin{bmatrix} t_i^{ef}(k\Delta t) \\ q^{ef}(k\Delta t) \end{bmatrix} \right.$$
$$\left. - \begin{bmatrix} \omega_{n-k}^{ef}\left(\hat{T}_{ij}^s,\mathbf{y},\Delta t\right) & \omega_{n-k}^{ef}\left(\hat{Q}_j^s,\mathbf{y},\Delta t\right) \\ \omega_{n-k}^{ef}\left(\hat{T}_i^f,\mathbf{y},\Delta t\right) & \omega_{n-k}^{ef}\left(\hat{Q}^f,\mathbf{y},\Delta t\right) \end{bmatrix} \begin{bmatrix} u_i^{ef}(k\Delta t) \\ p^{ef}(k\Delta t) \end{bmatrix} \right\} \tag{2.13}$$

with the weights corresponding to (B.16), e.g.,

$$\omega_{n-k}^{ef}\left(\hat{U}_{ij}^s,\mathbf{y},\Delta t\right) = \frac{\mathscr{R}^{-(n-k)}}{L} \sum_{\ell=0}^{L-1} \int_\Gamma \hat{U}_{ij}^s\left(\frac{\gamma\left(e^{i\ell\frac{2\pi}{L}}\mathscr{R}\right)}{\Delta t},\mathbf{y},\mathbf{x}\right) N_e^f(\mathbf{x})\,\mathrm{d}\Gamma\; e^{-i(n-k)\ell\frac{2\pi}{L}}. \tag{2.14}$$

Note, the calculation of the integration weights is only based on the Laplace transformed fundamental solutions which are available. Therefore, with the time stepping procedure (2.13) a boundary element formulation for poroelastodynamics is given without time dependent fundamental solutions.

To obtain a system of algebraic equations from equation (2.13), collocation is used at every node of the shape functions $N_e^f(\mathbf{x})$. The integration over the boundary Γ in the integration weights ω_{n-k}^{ef} is handled in the next section. According to $t-\tau=(n-k)\Delta t$, the integration weights ω_{n-k}^{ef} only depend on the difference $n-k$. This property is analogous to elastodynamic time domain BE formulations (see, e.g., [44]) and can be used to establish a recursion formula ($m=n-k$)

$$\omega_0(\mathbf{C})\,\mathbf{d}^n=\omega_0(\mathbf{D})\,\bar{\mathbf{d}}^n+\sum_{m=1}^{n}\left(\omega_m(\mathbf{U})\,\mathbf{t}^{n-m}-\omega_m(\mathbf{T})\,\mathbf{u}^{n-m}\right)\quad n=1,2,\ldots,N \tag{2.15}$$

with the time dependent integration weights ω_m containing the Laplace transformed fundamental solutions $\mathbf{U}$ and $\mathbf{T}$, respectively (see, equation (2.14)). Similarly, $\omega_0(\mathbf{C})$ and $\omega_0(\mathbf{D})$ are the corresponding integration weights of the first time step related to the unknown and known boundary data in time step n $\mathbf{d}^n$ and $\bar{\mathbf{d}}^n$, respectively. Finally, a direct equation solver is applied.

2.2 Dimensionless Variables

In [84], dimensionless variables suggested by Chen and Dargush [27] were introduced to achieve stable numerical solutions. The dimensionless spatial and temporal variables are

$$\tilde{x}_i=\frac{x_i}{A},\ \tilde{t}=\frac{t}{B}\,. \tag{2.16}$$

These non-dimensional variables are connected with dimensionless material parameters

$$\tilde{E}=\frac{E}{C},\ \tilde{\kappa}=\frac{BC}{A^2}\kappa,\ \tilde{\rho}=\frac{A^2}{B^2C}\rho\,, \tag{2.17}$$

where

$$A=\rho\kappa V,\ B=\rho\kappa,\ C=\rho V^2,\quad V=\sqrt{\frac{K+\frac{4}{3}G+\alpha^2\frac{R}{\phi^2}}{\rho}}\,, \tag{2.18}$$

where V is the compression wave speed of a poroelastic solid with an inviscid interstitial fluid. K,G and other moduli and linear combinations thereof are transformed as E.

This gives

$$x_i\to\frac{x_i}{\rho\kappa V}\quad t\to\frac{t}{\rho\kappa} \tag{2.19}$$

and

$$\begin{aligned} K&\to\frac{K}{K+\frac{4}{3}G+\alpha^2\frac{R}{\phi^2}} & G&\to\frac{G}{K+\frac{4}{3}G+\alpha^2\frac{R}{\phi^2}} & R&\to\frac{R}{K+\frac{4}{3}G+\alpha^2\frac{R}{\phi^2}}\\ \kappa&\to\kappa=1 & \rho&\to\frac{\rho}{\rho}=1 & \rho_f&\to\frac{\rho_f}{\rho}\end{aligned}\,. \tag{2.20}$$

For the incompressible model, the compressional wave speed is infinite and the scaling factor V was replaced with

$$V=\sqrt{\frac{K+\frac{4}{3}G}{\rho}}\,, \tag{2.21}$$

which works fine in 3-d but not in 2-d. The problem was identified as a loss of precision related to the fact that $\lim_{r\to\infty}\ln r\to\infty$ whereas all other terms in the fundamental solutions tend to zero with $r\to\infty$

(see also section 1.3). As the solutions of the Helmholtz and Laplace operators, assembled to form ψ in (1.48), are determined up to an additive constant, the following "trick" was used to solve this numerical problem: in the numerical evaluation of the fundamental solutions, the term $\ln r$ was replaced with

$$\ln r - \ln r_{max} = \ln \frac{r}{r_{max}} , \tag{2.22}$$

where $r_{max} = max\|\mathbf{x}\|$ is the maximum distance from the origin over all points of the discrete geometry.

This motivated a study done by Kielhorn [59], who proposed another set of dimensionless variables, marked "Fall 7 (Variante 4)" in the work, as the best options from all variants taken into account,

$$A = max\|\mathbf{x}\| = r_{max},\ B = t_e,\ C = E , \tag{2.23}$$

where t_e is the length of the time interval of interest. This set is used for both compressible and incompressible poroelasticity in the numerical examples.

No extensive testing has been done, but both sets of dimensionless variables seem to yield better results compared to a computation without any transformation. In most cases, the latter set (2.23) gives better numerical results, i.e., a larger stability region, but there are also examples where the opposite is true. No clear dependency has been recognized during the tests.

2.3 Element Types and Shape Functions

As mentioned before, four possibly different shape functions ${}^{u}N_e^f, {}^{t}N_e^f, {}^{p}N_e^f$, and ${}^{q}N_e^f$ need to be chosen in (2.10) to approximate the state variables on the discretized boundary using the nodal values. For clarity, the approximation formulas for the displacements u_i^s and the pore pressure p, based on the nodal values $u_i^{ef}(t)$, $p^{ef}(t)$ at the node f of element e and the corresponding shape functions, are recalled

$$u_i^s(\mathbf{x},t) = \sum_{e=1}^{E} \sum_{f=1}^{{}^{u}F} {}^{u}N_e^f(\mathbf{x})\, u_i^{ef}(t) , \quad p(\mathbf{x},t) = \sum_{e=1}^{E} \sum_{f=1}^{{}^{p}F} {}^{p}N_e^f(\mathbf{x})\, p^{ef}(t) . \tag{2.24}$$

The tractions t_i^s and flux q are handled in the same way. The simplest choice are isoparametric elements, i.e., taking identical shape functions for all quantities and the geometry. Another option, common in finite elements for poroelasticity [62], is to choose the shape function for p and q one degree lower than for u_i^s and t_i^s, e.g., ${}^{u}N_e^f(\mathbf{x})$, ${}^{t}N_e^f(\mathbf{x})$ linear and ${}^{p}N_e^f(\mathbf{x})$, ${}^{q}N_e^f(\mathbf{x})$ constant (see Figs. 2.1 and 2.2). Note that then also the number of nodes per element for the displacement, ${}^{u}F$, differs from that for pressure, ${}^{p}F$ [78]. These mixed elements have been added to the BEM implementation in both 2-d and 3-d.

To calculate the integration weights ω_{n-k}^{ef} in (2.13), spatial integration over the boundary Γ has to be performed. The essential constituents of the Laplace transformed fundamental solutions are exponential functions in 3-d and Bessel functions in 2-d, i.e., the integrands are smooth except for $r = 0$. Therefore, the regular integrals are evaluated by the standard Gaussian quadrature rule. In 3-d, the weakly singular parts of the integrals in (2.14) are regularized by polar coordinate transformation. The strongly singular integrals in (2.14) are equal to those of elastostatics or acoustics, respectively, and, hence, the regularization methods known from these theories can be applied, e.g., the method suggested by Guiggiani and Gigante [57]. Also in 2-d, the singularities have the same order as in the known cases of elastostatics or acoustics (see (A.16)). The singular integrals are evaluated analytically for linear and constant shape

functions [93, 98]. Some details concerning the analytical singular integration can be found in the next section 2.4.

In the subsequent numerical examples, three different triangular element types are used, the linear isoparametric triangular element `li-dr`, the constant element with linear geometry `ko-dr`, and the mixed triangular element `lk-dr` with linear and constant shape functions, shown in Fig. 2.1. All three elements have linear geometry and three nodes in the corners of the triangle. These are used with linear shape functions for all state variables by `li-dr`, but only for u_i^s and t_i^s by `lk-dr`, which has an additional mid-element node with constant shape function for the degrees of freedom corresponding to p and q (see Tab. 2.1). The `ko-dr` element uses the mid-element node with constant shape function for all state variables.

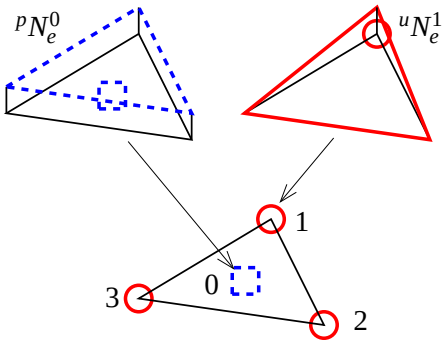

Figure 2.1: `lk-dr` element: Shape functions

Element	$^uN_e^f$, $^tN_e^f$	$^pN_e^f$, $^qN_e^f$
`li-2D`, `li-dr`	linear	linear
`lk-2D`, `lk-dr`	linear	constant

Table 2.1: Element types

The `lk-dr` element brings in an increase of the total degrees of freedom. The factor of increase depends on the particular geometry and discretization. In the example presented in section 3.2 it is about 1.2. Such a factor corresponds to an extension of the CPU time by 1.7 compared to the isoparametric linear element.

Similarly to 3-d, in 2-d, the mixed linear-constant element `lk-2D`, shown in Fig. 2.2(c), has an extra mid-element node connected with a constant shape function for the pore pressure p and flux q. Only the degrees of freedom corresponding to solid displacements u_i^s and tractions t_i^s are defined at the endpoints with linear shape functions.

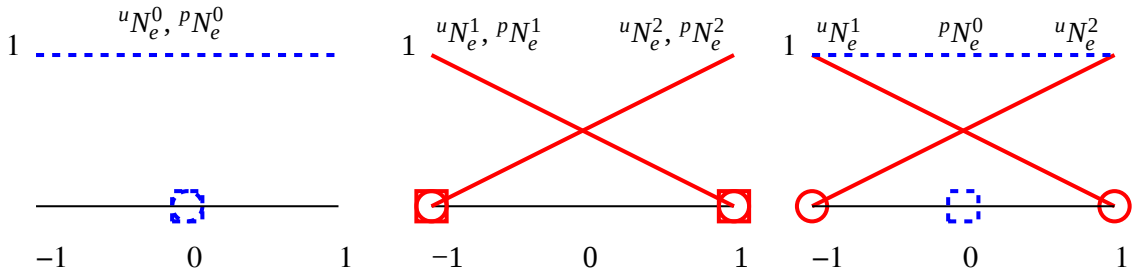

(a) `ko-2D` element (b) `li-2D` element (c) `lk-2D` element

Figure 2.2: Elements in 2-d: Shape functions

Contrary to 3-d, in a 2-d model the total degrees of freedom remains the same for the mixed `lk-2D` element as for the isoparametric linear element, but the CPU time extends about $1.3\times$. The essential source of the extra operations is the need to evaluate the fundamental solutions for more distinct distance arguments.

For illustration, a block of the system matrix (similar to the local element matrix in FEM) with rows and columns corresponding to elements $\mathscr{E}$ and e, respectively, is presented for both `li-2D` and `lk-2D` elements. Only the first term (i.e., with U,P and t,q) on the right hand side in (2.13) is included as example, as the other one (with T,Q and u,p) is analogical. Note that depending on the boundary condition corresponding to each degree of freedom (row in the block), u_i^s respectively p is given and t_i^s respectively q is unknown or vice versa. The given term contributes to the right hand side and the unknown one to the system matrix. The block is in the case of the `li-2D` element

$$\begin{bmatrix} \omega_{n-k}^{e1}\left(\hat{U}_{ij}^s(\mathbf{y}^{\mathscr{E}1}),{}^uN_e^1\right) & -\omega_{n-k}^{e1}\left(\hat{P}_j^s(\mathbf{y}^{\mathscr{E}1}),{}^pN_e^1\right) & \omega_{n-k}^{e1}\left(\hat{U}_{ij}^s(\mathbf{y}^{\mathscr{E}1}),{}^uN_e^2\right) & -\omega_{n-k}^{e1}\left(\hat{P}_j^s(\mathbf{y}^{\mathscr{E}1}),{}^pN_e^2\right) \\ \omega_{n-k}^{e1}\left(\hat{U}_i^f(\mathbf{y}^{\mathscr{E}1}),{}^uN_e^1\right) & -\omega_{n-k}^{e1}\left(\hat{P}^f(\mathbf{y}^{\mathscr{E}1}),{}^pN_e^1\right) & \omega_{n-k}^{e1}\left(\hat{U}_i^f(\mathbf{y}^{\mathscr{E}1}),{}^uN_e^2\right) & -\omega_{n-k}^{e1}\left(\hat{P}^f(\mathbf{y}^{\mathscr{E}1}),{}^pN_e^2\right) \\ \omega_{n-k}^{e2}\left(\hat{U}_{ij}^s(\mathbf{y}^{\mathscr{E}2}),{}^uN_e^1\right) & -\omega_{n-k}^{e2}\left(\hat{P}_j^s(\mathbf{y}^{\mathscr{E}2}),{}^pN_e^1\right) & \omega_{n-k}^{e2}\left(\hat{U}_{ij}^s(\mathbf{y}^{\mathscr{E}2}),{}^uN_e^2\right) & -\omega_{n-k}^{e2}\left(\hat{P}_j^s(\mathbf{y}^{\mathscr{E}2}),{}^pN_e^2\right) \\ \omega_{n-k}^{e2}\left(\hat{U}_i^f(\mathbf{y}^{\mathscr{E}2}),{}^uN_e^1\right) & -\omega_{n-k}^{e2}\left(\hat{P}^f(\mathbf{y}^{\mathscr{E}2}),{}^pN_e^1\right) & \omega_{n-k}^{e2}\left(\hat{U}_i^f(\mathbf{y}^{\mathscr{E}2}),{}^uN_e^2\right) & -\omega_{n-k}^{e2}\left(\hat{P}^f(\mathbf{y}^{\mathscr{E}2}),{}^pN_e^2\right) \end{bmatrix} \begin{bmatrix} t_i^{e1} \\ q^{e1} \\ t_i^{e2} \\ q^{e2} \end{bmatrix} \tag{2.25}$$

and for the `lk-2D` element

$$\begin{bmatrix} \omega_{n-k}^{e1}\left(\hat{U}_{ij}^s(\mathbf{y}^{\mathscr{E}1}),{}^uN_e^1\right) & \omega_{n-k}^{e1}\left(\hat{U}_{ij}^s(\mathbf{y}^{\mathscr{E}1}),{}^uN_e^2\right) & -\omega_{n-k}^{e1}\left(\hat{P}_j^s(\mathbf{y}^{\mathscr{E}1}),{}^pN_e^0\right) \\ \omega_{n-k}^{e2}\left(\hat{U}_{ij}^s(\mathbf{y}^{\mathscr{E}2}),{}^uN_e^1\right) & \omega_{n-k}^{e2}\left(\hat{U}_{ij}^s(\mathbf{y}^{\mathscr{E}2}),{}^uN_e^2\right) & -\omega_{n-k}^{e2}\left(\hat{P}_j^s(\mathbf{y}^{\mathscr{E}2}),{}^pN_e^0\right) \\ \omega_{n-k}^{e0}\left(\hat{U}_i^f(\mathbf{y}^{\mathscr{E}0}),{}^uN_e^1\right) & \omega_{n-k}^{e0}\left(\hat{U}_i^f(\mathbf{y}^{\mathscr{E}0}),{}^uN_e^2\right) & -\omega_{n-k}^{e0}\left(\hat{P}^f(\mathbf{y}^{\mathscr{E}0}),{}^pN_e^0\right) \end{bmatrix} \begin{bmatrix} t_i^{e1} \\ t_i^{e2} \\ q^{e0} \end{bmatrix} \tag{2.26}$$

where $\mathbf{y}^{\mathscr{E}f}$ is the position of the f-th node of element $\mathscr{E}$ and t_i^{ef}, q^{ef} are the nodal values at the f-th node of element e. The Δt and $k\Delta t$ arguments are omitted for space reasons as well as the $\mathbf{x}$ argument of the fundamental solutions, which runs through the element e when computing the integral for ω_{n-k}^{ef} in (2.14).

The dimension of the local matrix for the isoparametric element in (2.25) is $2\times(2+1)=6$ (two nodes, each with one unknown vector t_i (2 DoFs) and one unknown scalar q (1 DoF)) and for the mixed in (2.26) $2\times 2+1=5$ (two end-nodes, each with one unknown vector t_i (2 DoFs) and one mid-node with one unknown scalar q (1 DoF)). The difference in the local matrix size is not directly connectected to a difference in the global number of degrees of freedom, as the values at endpoints (or triangle corners in 3-d) are shared with the neighbouring element(s) and those at the mid-element nodes are not. That makes differences in the size of the global matrix depend on the actual mesh topology.

2.4 Analytic Integration of Singularities in 2-d

When evaluating the integral (2.14) over the discretized boundary, the integral over Γ_e (part of the boundary approximated by element e) is singular if $\mathbf{y}\in\Gamma_e$, i.e., when the collocation point $\mathbf{y}$ is one of the element nodes in the case of point collocation. Only the terms in the fundamental solutions that require singular integration will be considered in the following.

In 2-d, taking into account the discretization (2.10), the integral to be solved has the form

$$\int_{\Gamma_e} a\ln r\, N_e^f(\mathbf{x})\, d\Gamma \tag{2.27}$$

for the weak singularities in (A.16b) or

$$\int_{\Gamma_e} b \frac{1}{r} N_e^f(\mathbf{x})\, d\Gamma \tag{2.28}$$

for the strongly singular terms in (A.16c).

All weak (logarithmic) singularities differ from each other (and from the known singularities from elastostatics) only in the constant a, independent of $\mathbf{x}$ on element e. Similarly, also the strong ($\frac{1}{r}$) singularities only differ by a constant factor, b. For example for the fundamental solution $\hat{P}^f$, representing the pore pressure due to a source in the fluid, $a = -\frac{s\rho_f}{2\pi\beta}$ and for the flux fundamental solution $\hat{Q}^f$, $b = -\frac{r_{,n}}{2\pi}$.

The shape functions (see section 2.3) are in the case of the linear element

$$N_e^1 = \frac{1-\eta}{2} \tag{2.29a}$$

$$N_e^2 = \frac{1+\eta}{2} \tag{2.29b}$$

and for the constant element

$$N_e^0 = 1\,. \tag{2.30}$$

All elements considered here, i.e., the isoparametric linear `li-2D`, the constant `ko-2D`, and the mixed `lk-2D` elements, have linear geometry, which is transformed from global coordinates to the interval $\eta = -1 \ldots 1$ in the following way

$$x_1 = x_1^1 \frac{1-\eta}{2} + x_1^2 \frac{1+\eta}{2} \tag{2.31a}$$

$$x_2 = x_2^1 \frac{1-\eta}{2} + x_2^2 \frac{1+\eta}{2} \tag{2.31b}$$

where

$$\mathbf{x}^f = \begin{bmatrix} x_1^f \\ x_2^f \end{bmatrix} \tag{2.32}$$

are the global coordinates of point f of the element. The Jacobian of this transformation is constant throughout the element

$$|J| = \frac{\ell}{2} \tag{2.33}$$

where $\ell = \|\mathbf{x}^2 - \mathbf{x}^1\|$ is the element length. After the transformation, the integrals (2.27) and (2.28) become

$$\int_{-1}^{1} a \ln r\, N_e^f(\eta) \frac{\ell}{2} d\eta \tag{2.34}$$

and

$$\int_{-1}^{1} b \frac{1}{r} N_e^f(\eta) \frac{\ell}{2} d\eta\,. \tag{2.35}$$

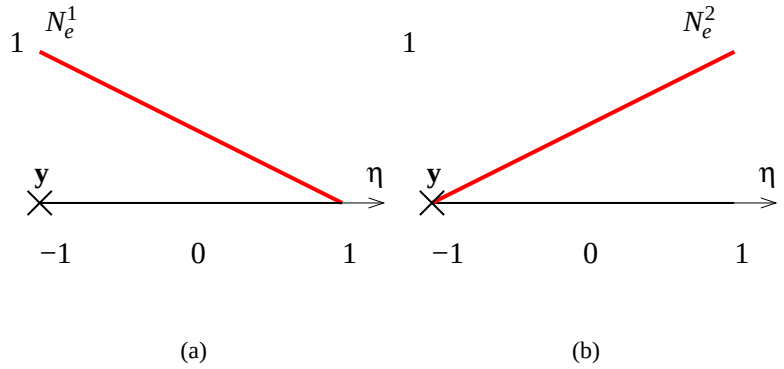

Figure 2.3: Linear shape functions, collocation at the endpoint $\eta = -1$

Weak singularity First consider the weak singular integral (2.34) for a linear element with the collocation point $\mathbf{y}$ at $\eta = -1$. In that case, the distance r from the collocation point to the integration point is $\frac{1+\eta}{2}\ell$. There are two possible relative positions of the collocation point to the point connected with the shape function in the integral. These two cases are shown in Fig. 2.3.

The integral with the shape function corresponding to the node at the other end of the element than the collocation point (see Fig. 2.3(b)) is regular because $\lim_{r\to 0} r\ln r = 0$ and can be integrated directly

$$\int_{-1}^{1} a \ln\left(\frac{1+\eta}{2}\ell\right) \frac{1+\eta}{2}\frac{\ell}{2}\,d\eta = \frac{a}{4}\ell(2\ln\ell - 1)\,. \tag{2.36}$$

This gives $-\frac{s\rho_f}{8\pi\beta}\ell(2\ln\ell-1)$ in the case of the pressure fundamental solution $\hat{P}^f$, which has earlier been selected as an example.

Only the integral with the shape function corresponding to the singular node (see Fig. 2.3(a)) exhibits the weakly singular behavior. It exists as an improper integral

$$\lim_{\varepsilon\to 0}\int_{-1+\varepsilon}^{1} a \ln\left(\frac{1+\eta}{2}\ell\right) \frac{1-\eta}{2}\frac{\ell}{2}\,d\eta = \frac{a}{4}\ell(2\ln\ell - 3)\,. \tag{2.37}$$

This gives $-\frac{s\rho_f}{8\pi\beta}\ell(2\ln\ell-3)$ for the $\hat{P}^f$ example.

In the case of the constant element, there is only one shape function and only one possible position of the singularity at the only collocation point (see Fig. 2.4). The distance r from the singularity to the integration point is $|\eta|\frac{\ell}{2}$. The integral (2.34) exists as an improper integral

$$\int_{-1}^{1} a \ln\left(\frac{\ell}{2}|\eta|\right) 1\,\frac{\ell}{2}\,d\eta = \lim_{\varepsilon\to 0} a\frac{\ell}{2}\left(\int_{-1}^{-\varepsilon}\ln\left(\frac{\ell}{2}(-\eta)\right)d\eta + \int_{\varepsilon}^{1}\ln\left(\frac{\ell}{2}\eta\right)d\eta\right) = a\ell(\ln\ell - 1)\,. \tag{2.38}$$

This gives $-\frac{s\rho_f}{2\pi\beta}\ell(\ln\ell-1)$ for the $\hat{P}^f$ example.

In the case of the mixed `lk-2D` element, the integrals with the solid displacement due to a force in the solid $\hat{U}_{ij}^s$ are identical to those for the `li-2D` element, whereas the one with the pore pressure fundamental solution $\hat{P}^f$ is the same as for the `ko-2D` element. Only the flux due to a force in the solid $\hat{Q}_j^s$ and the tractions due to a source in the fluid $\hat{T}_i^f$ need to be handled separately. For these terms coupling the fluid and the solid, new combinations of the collocation point position and shape function occur,

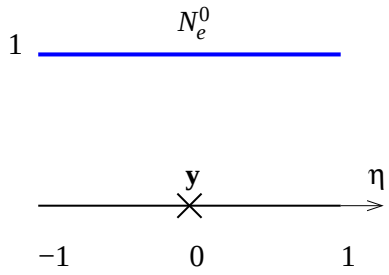

Figure 2.4: Constant shape function, collocation at the midpoint $\eta = 0$

i.e., collocation at endpoint and a constant shape function or collocation at midpoint and a linear shape function (see also (2.26)).

With $\hat{Q}_j^s$, a singularity at the endpoint is integrated with a constant shape function (see Fig. 2.5), with $\hat{T}_i^f$

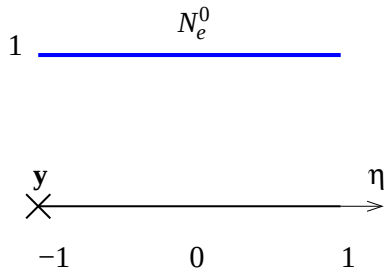

Figure 2.5: Constant shape function, collocation at the endpoint $\eta = -1$

vice versa, i.e., a singularity at the midpoint with a linear shape function (see Fig. 2.6).

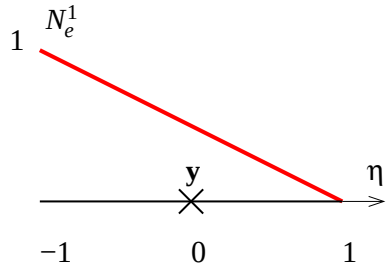

Figure 2.6: Linear shape function, collocation at the midpoint $\eta = 0$

For $\hat{Q}_j^s$, the integral (2.34) again exists as an improper integral

$$\int_{-1}^{1} a \ln\left(\frac{1+\eta}{2}\,\ell\right) 1\,\frac{\ell}{2}\,d\eta = \lim_{\varepsilon\to 0} a\,\frac{\ell}{2}\int_{-1+\varepsilon}^{1} \ln\left(\frac{1+\eta}{2}\,\ell\right) d\eta = a\,\ell(\ln\ell - 1)\,, \tag{2.39}$$

where $a = \frac{1}{4\pi}\left(\frac{\beta}{G} + \frac{\alpha}{K+\frac{4}{3}G}\right) n_j$.

Similarly, also for $\hat{T}_i^f$, the integral (2.34) exists as an improper integral

$$\begin{aligned}&\int_{-1}^{1} a \ln\left(\frac{\ell}{2}|\eta|\right) \frac{1-\eta}{2} \frac{\ell}{2} d\eta \\ &= \lim_{\varepsilon\to 0} a \frac{\ell}{2}\left(\int_{-1}^{-\varepsilon} \ln\left(\frac{\ell}{2}(-\eta)\right) \frac{1-\eta}{2} d\eta + \int_{\varepsilon}^{1} \ln\left(\frac{\ell}{2}\eta\right) \frac{1-\eta}{2} d\eta\right) = \frac{a}{2}\ell(\ln\frac{\ell}{2}-1)\end{aligned} \tag{2.40}$$

where $a = \frac{-s^2\rho_f}{2\pi} \frac{\alpha G+\beta(K+\frac{1}{3}G)}{\beta(K+\frac{4}{3}G)} n_i$.

Strong singularity To integrate the strongly singular terms from (A.16c), the boundary near the singularity is modified as shown in Fig. 2.7, where **n** denotes the outward surface normal. The integral (2.28) is split in two parts, over Γ_ε and over $\Gamma - \Gamma_\varepsilon$

$$\int_\Gamma b_{ij} \frac{1}{r} N_e^f(\mathbf{x})\, d\Gamma = \lim_{\varepsilon\to 0} \int_{\Gamma_\varepsilon} b_{ij} \frac{1}{r} N_e^f(\mathbf{x})\, d\Gamma_\varepsilon + \lim_{\varepsilon\to 0} \int_{\Gamma-\Gamma_\varepsilon} b_{ij} \frac{1}{r} N_e^f(\mathbf{x})\, d\Gamma\,. \tag{2.41}$$

Note that in the case of collocation at the end of an element (`li-2D` and `lk-2D` elements), this procedure involves two neighboring elements.

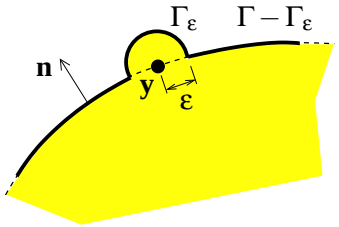

Figure 2.7: Integration of a strong singularity

The first integral is combined with the right hand side from equation (2.6) to form the integral free term (see also (2.8))

$$c_{ij} = \delta_{ij} + \lim_{\varepsilon\to 0} \int_{\Gamma_\varepsilon} b_{ij} \frac{1}{r} N_e^f(\mathbf{x})\, d\Gamma_\varepsilon\,. \tag{2.42}$$

It only depends on the geometry and, for T_{ij}^s, on the Poisson's ratio. For smooth boundary, this results in $c_{ij} = \frac{1}{2}\delta_{ij}$, for an arbitrary angle between the neighboring elements see [69].

The second integral on the right hand side of equation (2.41) exists as a Cauchy principal value integral. Similarly to the weak singular case, the element geometry is transformed to $\eta = -1\ldots 1$. The distance r from the collocation point to the integration point is then $\frac{1+\eta}{2}\ell$ for collocation at $\eta = -1$, respectively $\frac{1-\eta}{2}\ell$ for collocation at $\eta = 1$.

Note that when integrating over the element with the singularity, $r_{,n} = 0$ due to linear geometry ($\mathbf{r} \perp \mathbf{n}$), which makes all terms containing $r_{,n}$ from (A.16c) zero. Therefore, the last integral in (2.41) with $\hat{Q}^f$ is zero and from $\hat{T}_{ij}^s$ only

$$b_{ij} = -\frac{(1-2\nu)(n_j r_{,i} - n_i r_{,j})}{4\pi(1-\nu)r} \tag{2.43}$$

remains. The diagonal term for $i = j$ is clearly zero, and only the non-diagonal terms need to be integrated. The sign of b_{ij} changes at the collocation point, as the direction of **r** changes.

First look at the linear element. Similarly to the weakly singular case, the integral with the shape function corresponding to the node at the other end of the element than the collocation point (see Fig. 2.3(b)) is regular ($\frac{r}{r}=1$) and can be integrated directly

$$\int_{-1}^{1} b_{ij}\,\frac{2}{(1+\eta)\,\ell}\,\frac{1+\eta}{2}\,\frac{\ell}{2}\,d\eta = b_{ij}\,. \tag{2.44}$$

The integral with the shape function corresponding to the singular node (see Fig. 2.3(a)) exhibits strongly singular behavior. In this case two neighboring elements have to be considered (see Fig. 2.8) to evaluate the integral (2.35), taking into account that b_{ij} from (2.43) changes sign at the collocation point (in this case on the element boundary), i.e., $b_{ij}^{e_1} = -b_{ij}^{e_2} = -b_{ij}$

$$\begin{aligned}&\lim_{\varepsilon\to 0}\left(\int_{-1}^{1-\varepsilon} b_{ij}^{e_1}\,\frac{1}{r}\,N_{e_1}^{f}(\eta)\,\frac{\ell_1}{2}\,d\eta + \int_{-1+\varepsilon}^{1} b_{ij}^{e_2}\,\frac{1}{r}\,N_{e_2}^{f}(\eta)\,\frac{\ell_2}{2}\,d\eta\right)\\ &= b_{ij}\lim_{\varepsilon\to 0}\left(\int_{-1}^{1-\varepsilon}\frac{-2}{(1-\eta)\,\ell_1}\,\frac{1+\eta}{2}\,\frac{\ell_1}{2}\,d\eta + \int_{-1+\varepsilon}^{1}\frac{2}{(1+\eta)\,\ell_2}\,\frac{1-\eta}{2}\,\frac{\ell_2}{2}\,d\eta\right) = b_{ij}\,(\ln\ell_2 - \ln\ell_1)\,.\end{aligned} \tag{2.45}$$

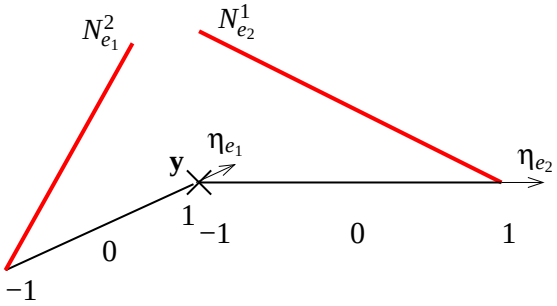

Figure 2.8: Linear shape functions, collocation at the endpoint

In the case of the constant element, there is only one shape function and only one possible position of the singularity at the only collocation point (see Fig. 2.4). The distance r from the singularity to the integration point is $|\eta|\,\frac{\ell}{2}$. The integral (2.34) exists as an improper integral

$$\int_{-1}^{1} b_{ij}\,\frac{1}{\frac{\ell}{2}\,|\eta|}\,1\,\frac{\ell}{2}\,d\eta = b_{ij}^{+}\lim_{\varepsilon\to 0}\left(\int_{-1}^{-\varepsilon}\frac{-1}{-\eta}\,d\eta + \int_{\varepsilon}^{1}\frac{1}{\eta}\,d\eta\right) = 0\,, \tag{2.46}$$

where b_{ij}^{+} denotes the value of b_{ij} to the right of the singularity, i.e., for $\eta = 0\ldots 1$.

In the case of the mixed `lk-2D` element, the integrals with the tractions fundamental solutions $\hat{T}_{ij}^{s}$ are identical to the `li-2D` element and the integral with the flux fundamental solution $\hat{Q}^{f}$ is the same as for the `ko-2D` element. None of the solid-fluid coupling terms are strongly singular. That means all the strongly singular integrals occuring for the `lk-2D` element have already been handled above for the linear and constant elements.

3 Validation by Comparison to a 1-d Analytical Solution

To validate the BEM program, a study comparing the BEM results to the 1-d analytical solution [1] from [84] has been done for the compressible and incompressible models of two different materials. The material constants for Berea sandstone, i.e., a porous rock, and water saturated coarse sand, i.e., a soil, are given in Tab. 3.1. For this comparison, the Poisson's ratio of the solid frame ν is set to 0 [2]. For the geometry simulating the 1-d column in 2-d and 3-d, see Figs. 3.1 and 3.14. The column is 3 m high, 1 m wide, and, in 3-d, 1 m deep. On the top, it is excited by a traction jump according to a unit step function $t_y(\mathbf{x},t) = 1\,\mathrm{N/m^2}\,H(t)$. The top surface with load is permeable and all the remaining surfaces, i.e., the sides and the vertically supported bottom, are impermeable. On the sides, only sliding along the surface is allowed, movements in the perpendicular direction are blocked.

	$K, G\ [\frac{N}{m^2}]$	$\rho, \rho_f\ [\frac{kg}{m^3}]$	ϕ	$R\ [\frac{N}{m^2}]$	α	$\kappa\ [\frac{m^4}{Ns}]$
Berea	$8 \cdot 10^9$	2458	0.19	$4.7 \cdot 10^8$	0.778	$1.9 \cdot 10^{-10}$
sandstone	$6 \cdot 10^9$	1000				
Soil	$2.1 \cdot 10^8$	1884	0.48	$1.2 \cdot 10^9$	0.981	$3.55 \cdot 10^{-9}$
	$9.8 \cdot 10^7$	1000				

Table 3.1: Material data

3.1 Validation in 2-d

In 2-d, the BEM model of the column described above consists of 32 nodes and 32 elements, as shown in Fig. 3.1. A finer discretization has 128 nodes and 128 elements. It will be shown that the problem can solved with the BEM implementation. The results obtained using three different element types will be compared.

Compressible rock For the Berea sandstone, the analytical solution can be well approximated by the numerical results. In Fig. 3.2, the vertical displacement at Point P (see Fig. 3.1) is shown. Only the results for the coarse discretization have been included in this plot, as they can already hardly be

[1] More correctly, it should be called "semi-analytical", as the time domain solution has been obtained numerically from the Laplace domain 1-d analytical solution, applying the Convolution Quadrature Method [63, 64]

[2] Note that this only disables the lateral contraction for the long-time (drained) material behavior. For the short-time response (undrained), $\nu_u \neq 0$ and lateral contraction still plays a role

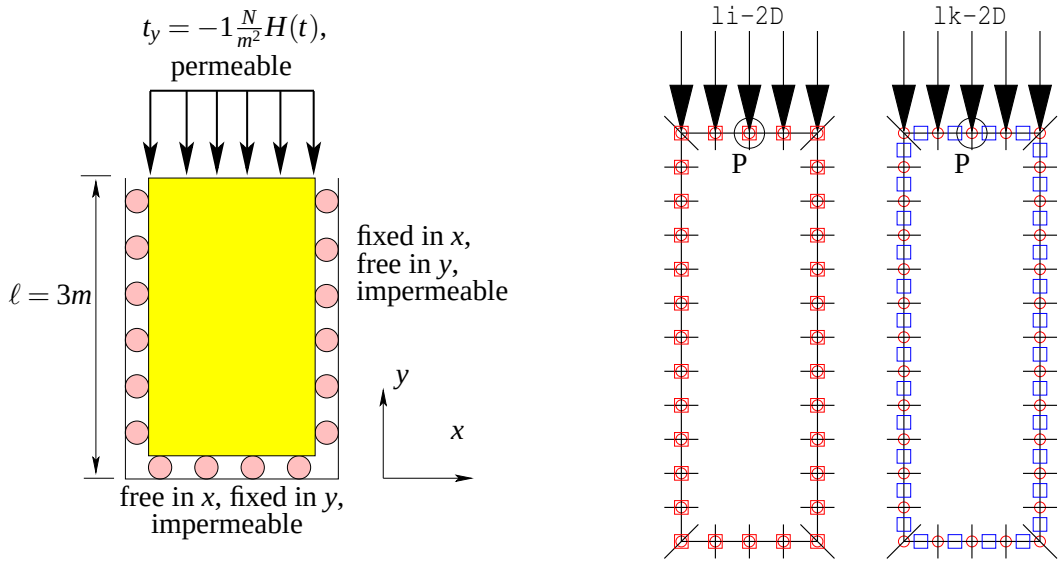

Figure 3.1: Comparison to 1-d analytical solution: 2-d geometry and discretization

distinguished from the analytical solution, and the finer one comes even closer. Also the pore pressure

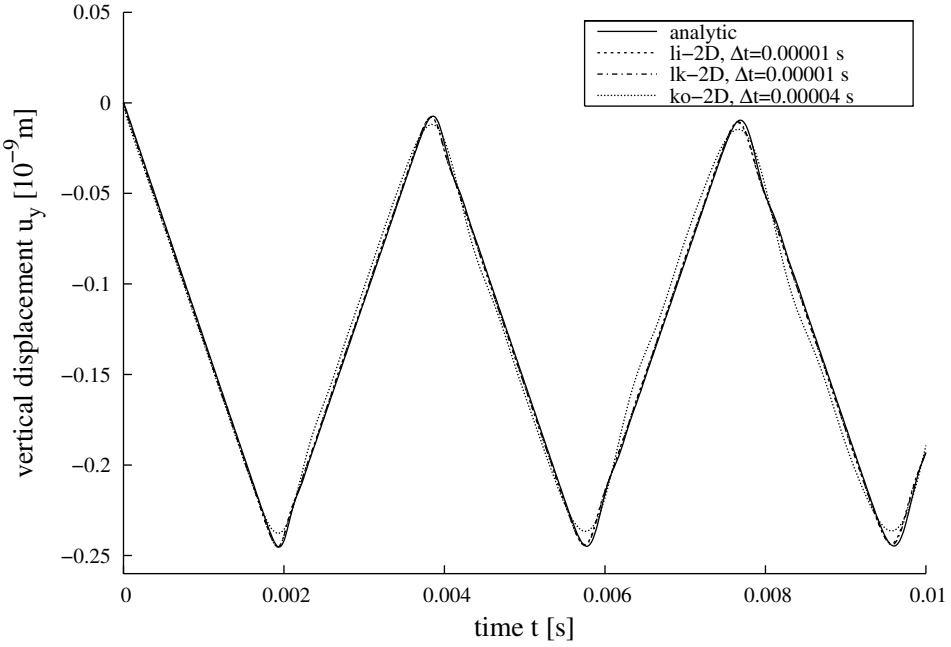

Figure 3.2: 2-d BEM and 1-d analytical solution for rock: Displacement at point *P*

at the support, presented in Fig. 3.3, clearly converges to the analytical solution with mesh refinement. On the coarser mesh with 32 elements in Fig. 3.3(a), the results for the mixed and linear elements can be hardly distinguished from each other. On the finer with mesh with 128 elements in Fig. 3.3(b), the `li-2D` and `lk-2D` results coincide completely. There is no difference in the lower stability limit on the

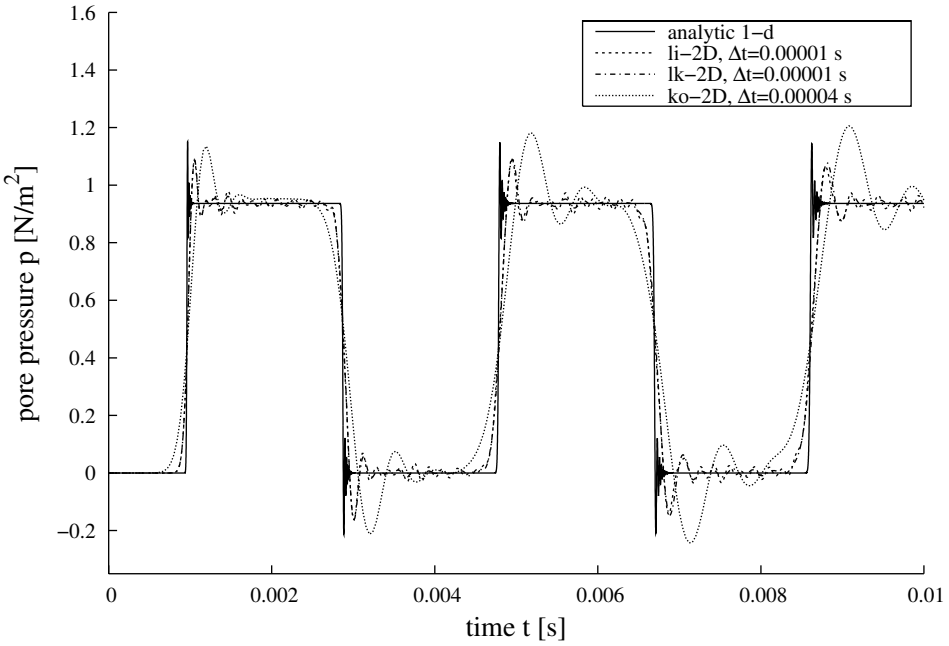

(a) coarse mesh (32 elements)

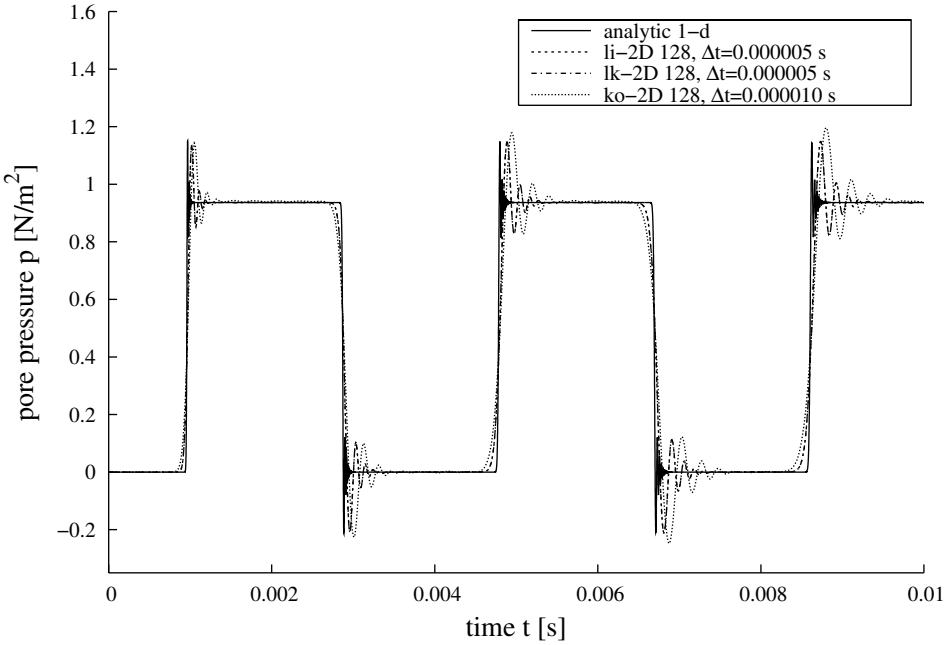

(b) finer mesh (128 elements)

Figure 3.3: 2-d BEM and 1-d analytical solution for rock: Pore pressure at support

timestep [3] between the linear isoparametric and mixed linear-constant elements. The optimal timestep on the coarser mesh is $\Delta t = 1 \cdot 10^{-5}$ s for both the linear and the mixed element, and $\Delta t = 4 \cdot 10^{-5}$ s for the constant element. On the finer mesh (denoted by "128"), $\Delta t = 0.5 \cdot 10^{-5}$ s has been used for the `li-2D` and `lk-2D` elements, and $\Delta t = 1 \cdot 10^{-5}$ s for `ko-2D`.

In this case of compressible rock, no differences have been found between the mixed element and linear elements.

Incompressible rock If the same problem is considered for a material with incompressible constituents, the solution changes (see also [87]). The vibration corresponding to the fast compressional wave disappears, which means the behavior is now governed predominantly by the relative fluid to solid movement, because the shear deformations should not play any significant role in this 1-d setup. The analytical solutions for the vertical displacement u_y at the top surface are compared for the two models in Fig. 3.4(a). The analytical solutions for the pore pressure p at the support are compared in Fig. 3.4(b). The difference in the deformations of an order of magnitude, which suggest that for this material, the model with incompressible constituents is not likely to work well even for different, more realistic, boundary conditions in chapter 4.

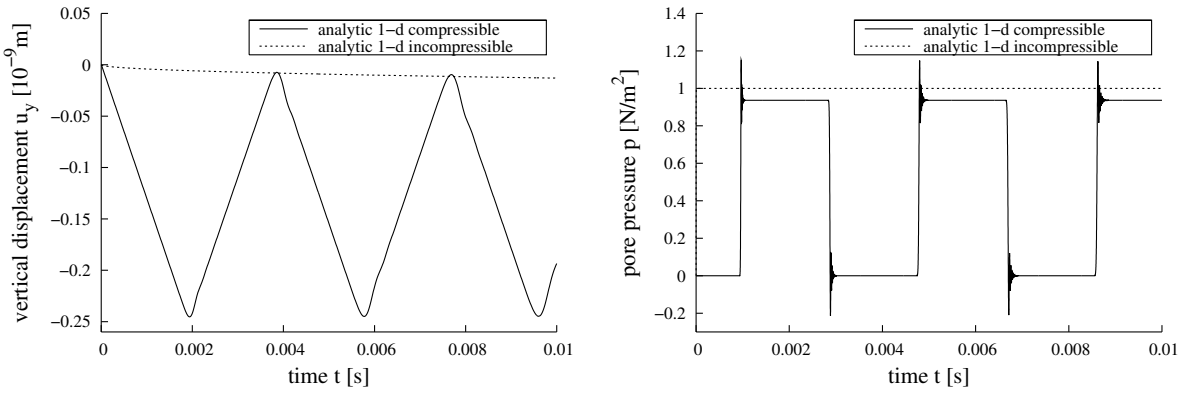

(a) Displacement at point P

(b) Pore pressure at support

Figure 3.4: 1-d analytical solution for compressible and incompressible rock

The numerical results for the vertical displacement u_y are presented in Fig. 3.5. Only the results for the coarser mesh are shown. On the finer mesh, they optically coincide with the analytical solution, which suggests that the results converge to the analytical solution with mesh refinement. No substantial differences can be observed between the element types.

The results for the pore pressure p are presented in Fig. 3.6. Similarly to the displacement results, there are not any noticeable differences between the element types, just the oscillations are somewhat smaller for the `lk-2D` element than for `li-2D`. For all element types, the oscillations originating from the jump at $t = 0$ s are less pronounced on the finer mesh.

[3] As in other BEM implementations, there is a **lower** stability limit, i.e., a minimum time step length condition for a stable numerical solution. Note that with conditionally stable Finite Differences schemes or Finite Elements, there is usually an **upper** limit on the time step length.

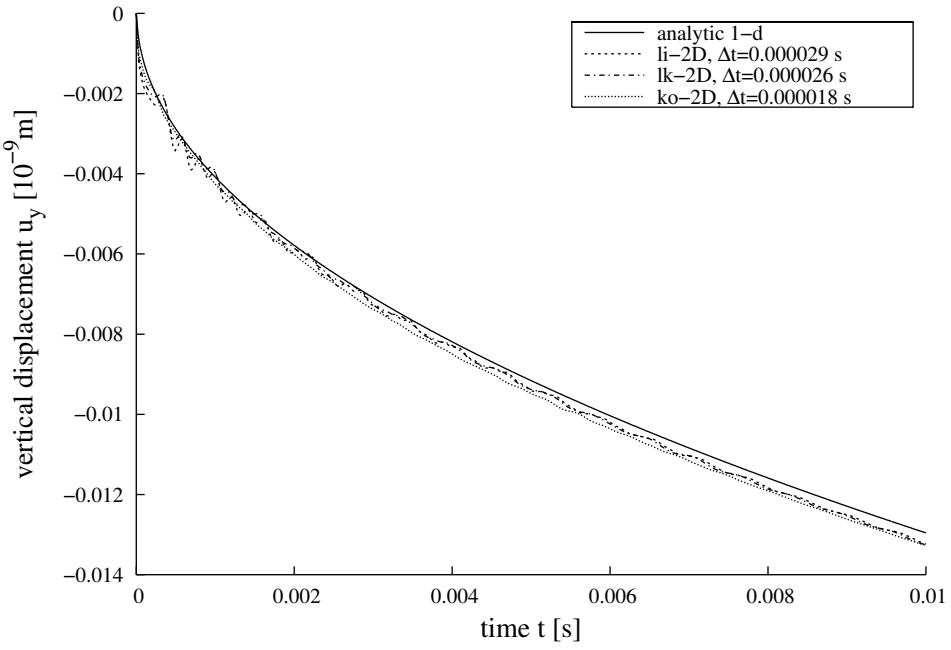

Figure 3.5: 2-d BEM and 1-d analytical solution for incompressible rock: Displacement at point *P*

On the coarser mesh, the optimal timesteps $\Delta t = 2.9 \cdot 10^{-5}$ s for the `li-2D` element, $\Delta t = 2.6 \cdot 10^{-5}$ s for `lk-2D`, and $\Delta t = 1.8 \cdot 10^{-5}$ s for `ko-2D` are used in the computation. The lower stability limit is slightly better for the mixed element compared to the isoparametric linear, but worse than the constant element. On the finer mesh, $\Delta t = 1 \cdot 10^{-5}$ s is used for all three element types.

In this case of incompressible rock, the mixed element offers better stability over the linear one. However, the incompressible model is not a good description of this material.

Compressible soil Fig. 3.7 displays the displacement results at point *P* for both meshes. On the coarser mesh, the mixed element shows slightly weaker numerical damping compared to the linear element. On the finer mesh, the results can not be distinguished from each other and hardly from the analytical solution. Therefore, only one of them (the `li-2D` element) has been included in the plot.

The pore pressure results in Fig. 3.8 are almost identical for the `li-2D` and `lk-2D` elements even on the coarser mesh. Only the constant element needs a substantially longer time step and therefore it differs more from the analytical solution. Considering the pressure results, the coarse mesh is obviously a too crude approximation for this material, not being able to resolve the jumps sharply. The results for the finer mesh look noticeably better, clearly converging to the analytical solution.

For the soil, the mixed element brings a small improvement in the lower stability limit on the timestep, $\Delta t = 0.00011$ s compared to the $\Delta t = 0.00012$ s for linear isoparametric. For the constant element, the optimal timestep is $\Delta t = 0.00033$ s. On the finer mesh, $\Delta t = 2.5 \cdot 10^{-5}$ s has been used for all elements.

Incompressible soil Similarly as for the incompressible rock, the analytical solution is different from the compressible model. However, the difference is not as extreme as for the rock. In chapter 4, the

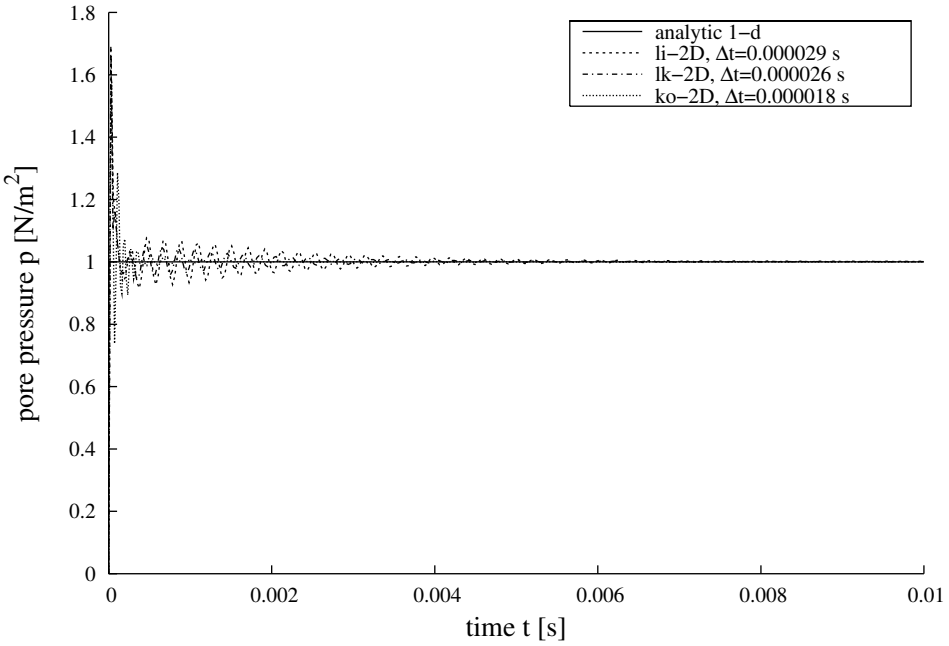

(a) coarse mesh (32 elements)

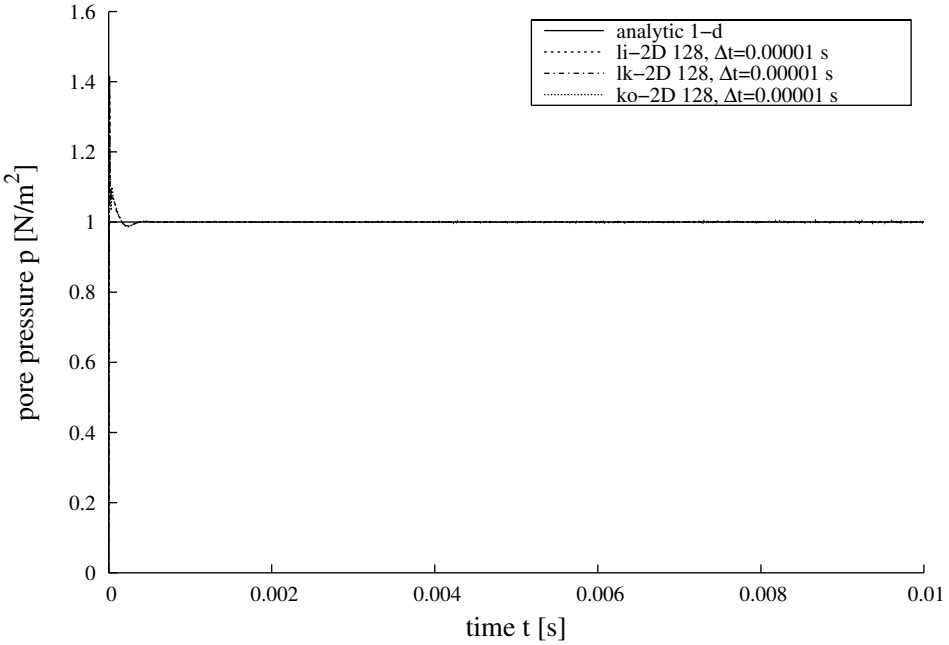

(b) finer mesh (128 elements)

Figure 3.6: 2-d BEM and 1-d analytical solution for incompressible rock: Pore pressure at support

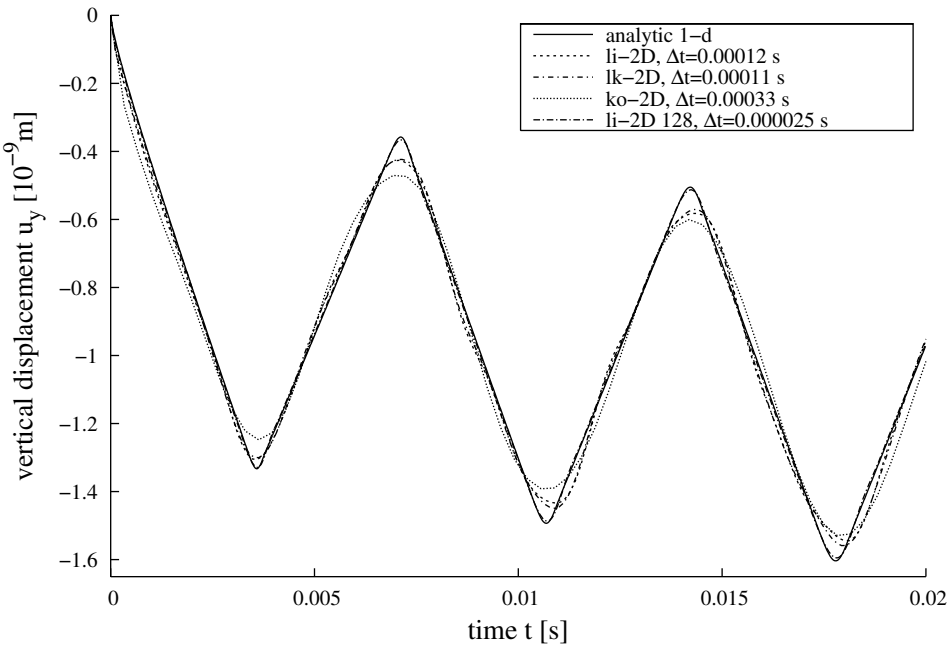

Figure 3.7: 2-d BEM and 1-d analytical solution for soil: Displacement at point *P*

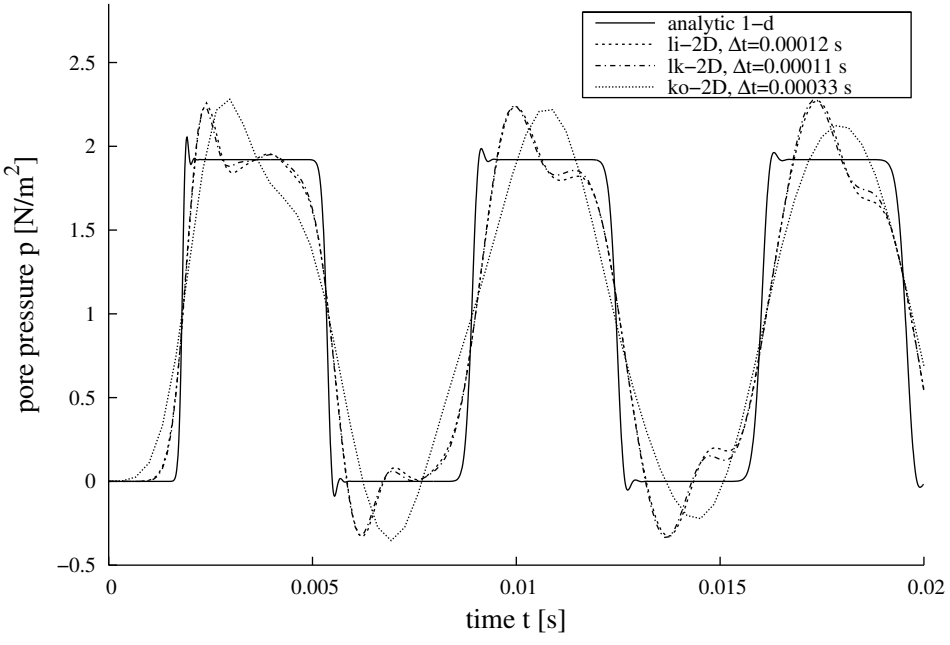

Figure 3.8: 2-d BEM and 1-d analytical solution for soil: Pore pressure at support

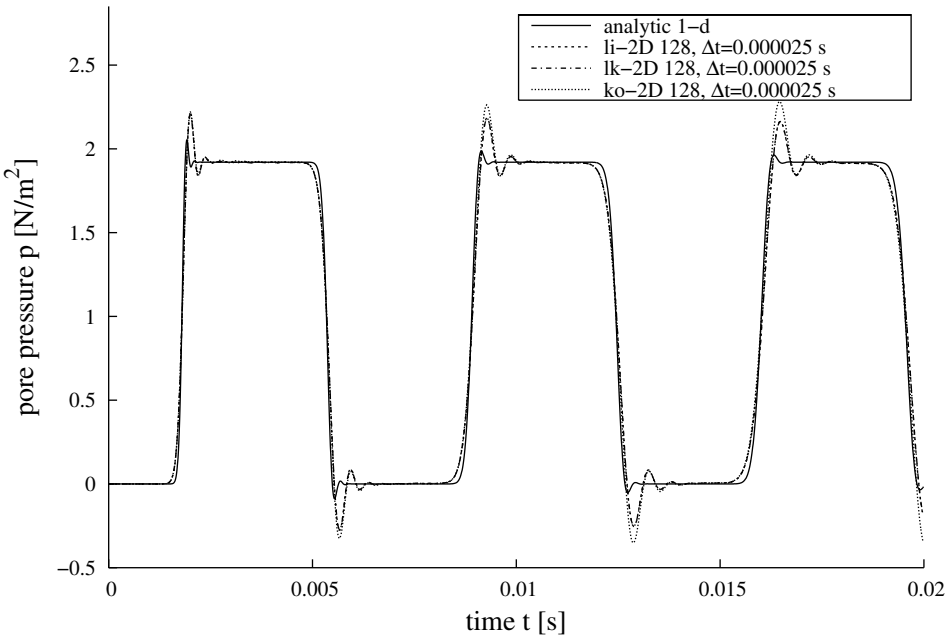

Figure 3.9: 2-d BEM and 1-d analytical solution for soil: Pore pressure at support, finer mesh

two models will be tested and compared on a more realistic example. The analytical solutions for the vertical displacement u_y at the top surface is compared for the two models in Fig. 3.10(a). The analytical solutions for the pore pressure p at the support are compared in Fig. 3.10(b)

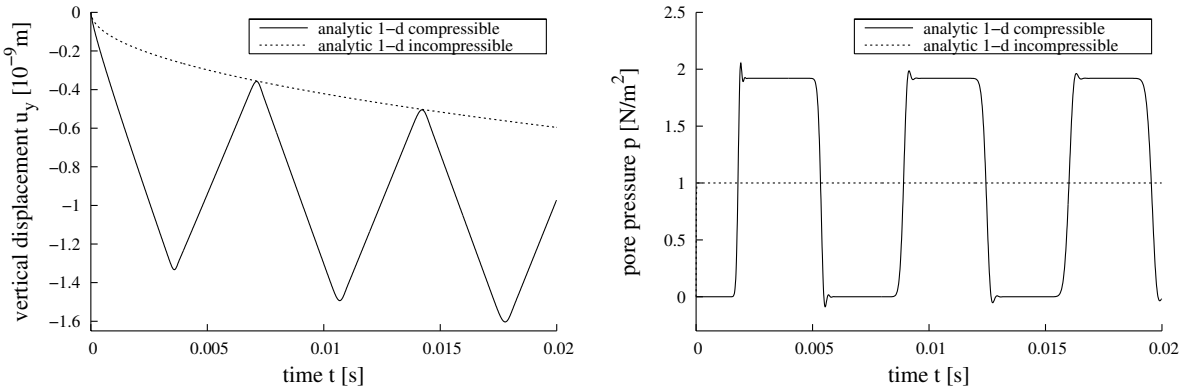

(a) Displacement at point P

(b) Pore pressure at support

Figure 3.10: 1-d analytical solution for compressible and incompressible soil

The displacement u_y at the top surface and the pore pressure p at the support are plotted against time in Figs. 3.11 and 3.12. The optimal timesteps used on the coarser mesh with 32 elements are $\Delta t = 0.0002\,\mathrm{s}$ for the linear and $\Delta t = 0.00015\,\mathrm{s}$ for the mixed and constant elements. When the timestep is made shorter

(but not under the stability limit), i.e., $\Delta t = 0.00013\,\mathrm{s}$ for `li-2D` or $\Delta t = 0.00012\,\mathrm{s}$ for `lk-2D`, the solutions exhibit oscillatory behavior (especially in the pressure results), but these do not grow (explode), even during much longer time intervals than displayed here. On the finer mesh, the timestep $\Delta t = 0.0001\,\mathrm{s}$ is used for all element types. Only the pressure results are included in the plot in Fig. 3.13, as the displacements on the finer mesh could hardly be distinguished from the analytical solution.

The pore pressure results are presented in Fig. 3.13. The displacements on the finer mesh in 2-d could hardly be distinguished from the analytical solution. The oscillations, especially in the pressure solution, originating from the jump at $t = 0\,\mathrm{s}$ are much less pronounced than on the coarse mesh for all three element types.

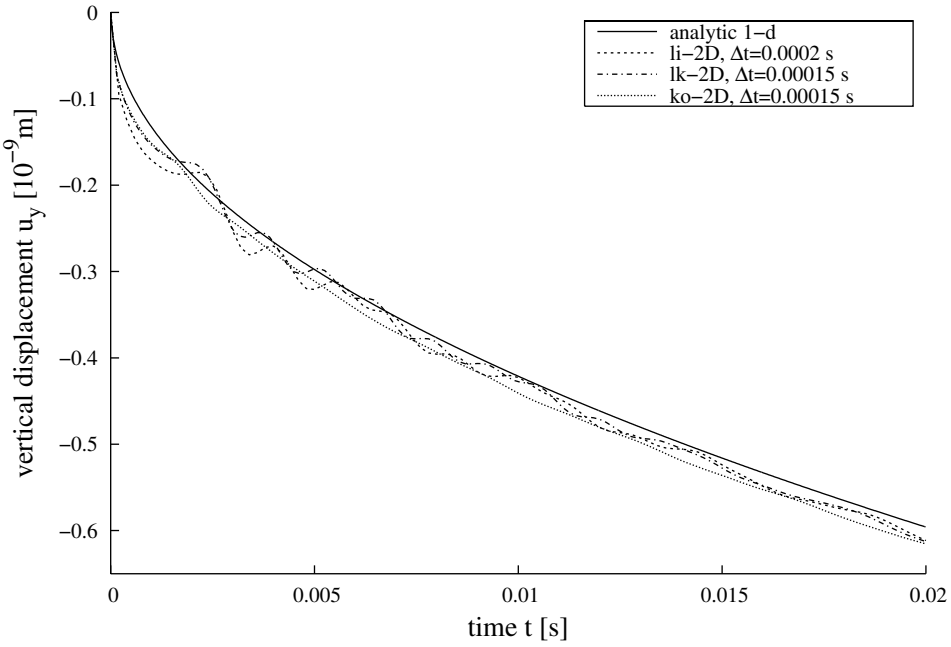

Figure 3.11: 2-d BEM and 1-d analytical solution for incompressible soil: Displacement at point *P*

For this problem, the mixed element offers a slightly better stability limit over the isoparametric linear element. It also shows less oscillatory behavior when getting close to the limit.

3.2 Validation in 3-d

In 3-d, the BEM model of the column described above on page 42 consists of 252 linear triangular elements on 128 nodes (see Fig. 3.14(b)). The finer mesh in Fig. 3.14(c) has 700 elements and 352 nodes. As in 2-d, the problem can be solved and the results appear to converge to the analytical solution with mesh refinement. However, it should be noted that the finer 3-d mesh divides the edge of 1 m length in 5 element lengths, whereas the coarse 2-d mesh has 4 elements on the same length. Therefore, when comparing with the 2-d results, it can be expected that the finer 3-d discretization with 700 elements produces results comparable to those from the coarse 2-d mesh with 32 elements.

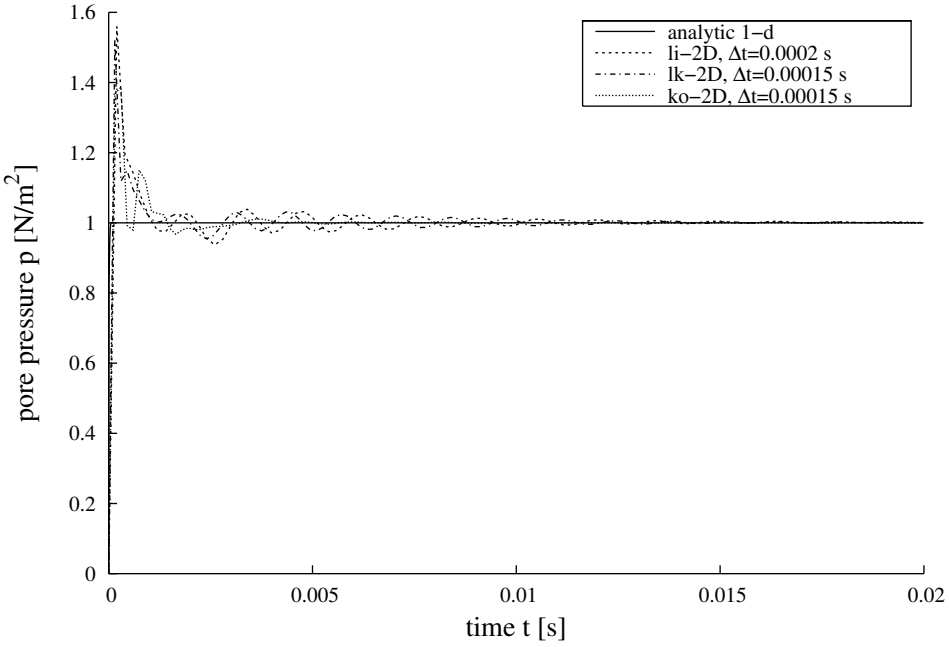

Figure 3.12: 2-d BEM and 1-d analytical solution for incompressible soil: Pore pressure at support

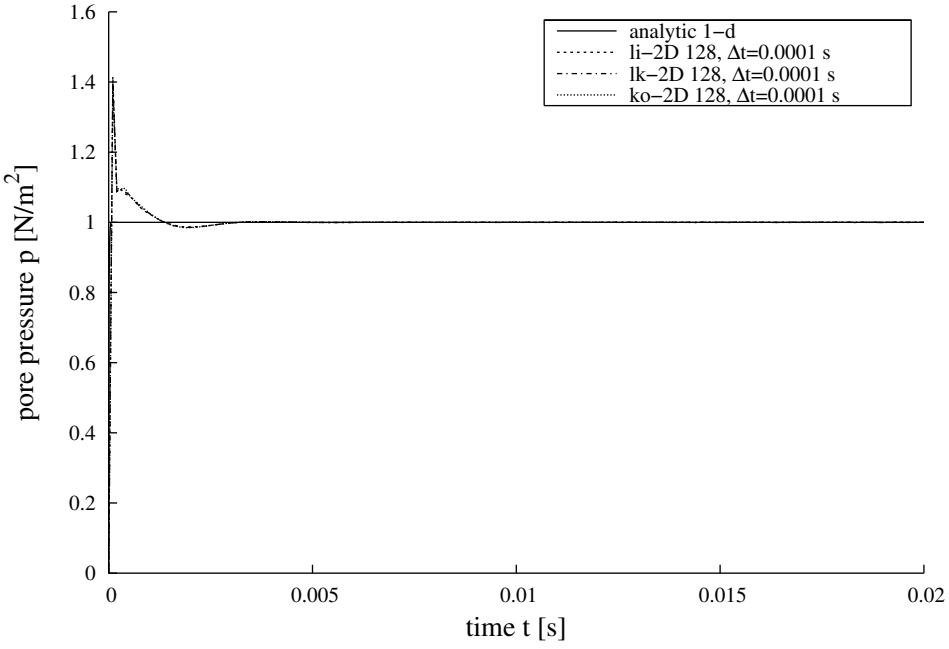

Figure 3.13: 2-d BEM and 1-d analytical solution for soil: Pore pressure at support, finer mesh

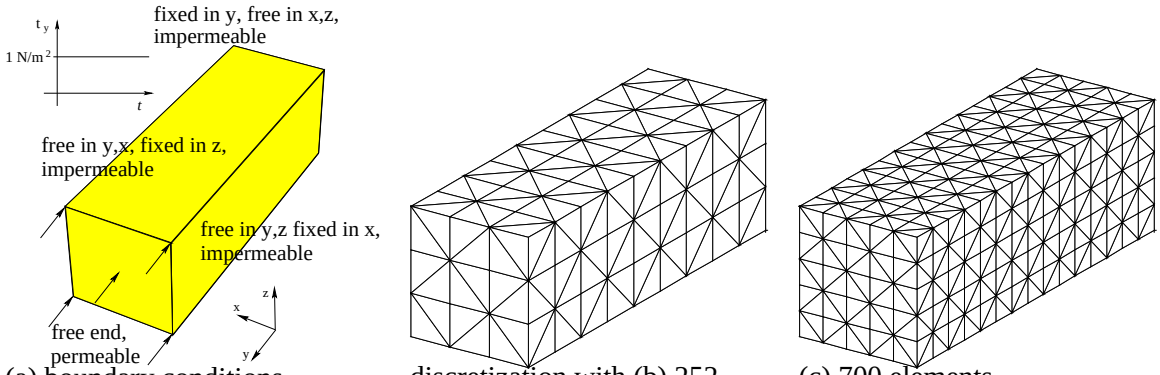

(a) boundary conditions discretization with (b) 252 (c) 700 elements

Figure 3.14: Comparison to 1-d analytical solution: 3-d geometry and discretization

Compressible rock The displacements of the porous rock at point *P* are presented in Fig. 3.15. Only the results for the coarser mesh are included, as those on the finer one lie very close to each other and the analytical solution. The differences between the element types are more visible in the pore pressure

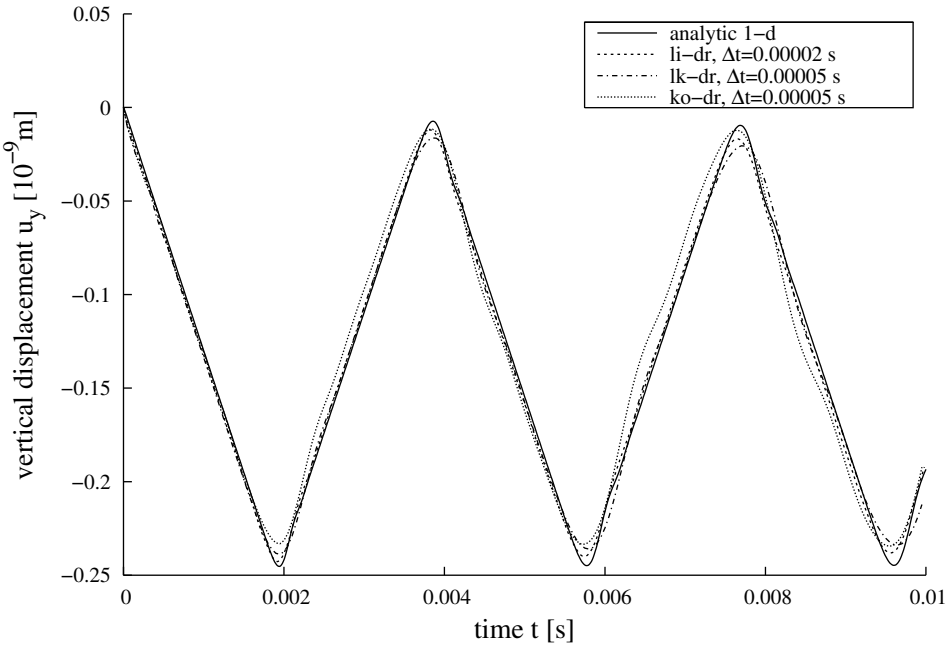

Figure 3.15: 3-d BEM and 1-d analytical solution for rock: Displacement at point *P*

plot in Fig. 3.16. The linear element comes closer to the analytical solution than the both other element types.

For the porous rock, the isoparametric linear element `li-dr` offers the shortest possible timestep $\Delta t = 0.00002\,\mathrm{s}$ on the mesh with 252 elements, whereas the mixed and constant elements `lk-dr` and `ko-dr` only allow $\Delta t = 0.00005\,\mathrm{s}$. On the finer mesh with 700 elements, the timestep $\Delta t = 0.000025\,\mathrm{s}$ is used for both the linear and mixed elements, and $\Delta t = 0.00005\,\mathrm{s}$ for the constant element.

In this case, the linear element clearly delivers the best stability and results from the three.

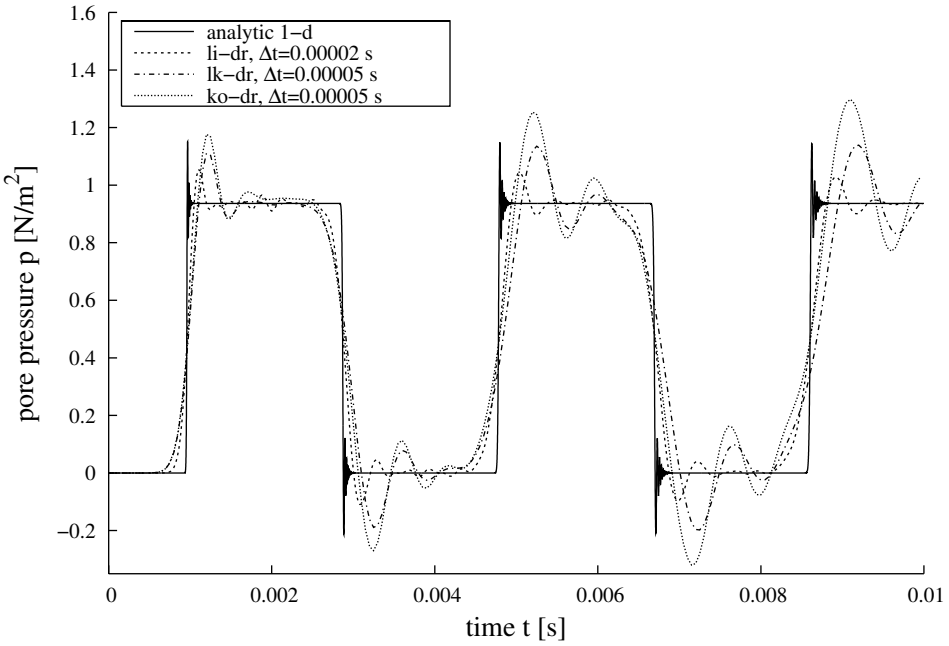

(a) 252 elements

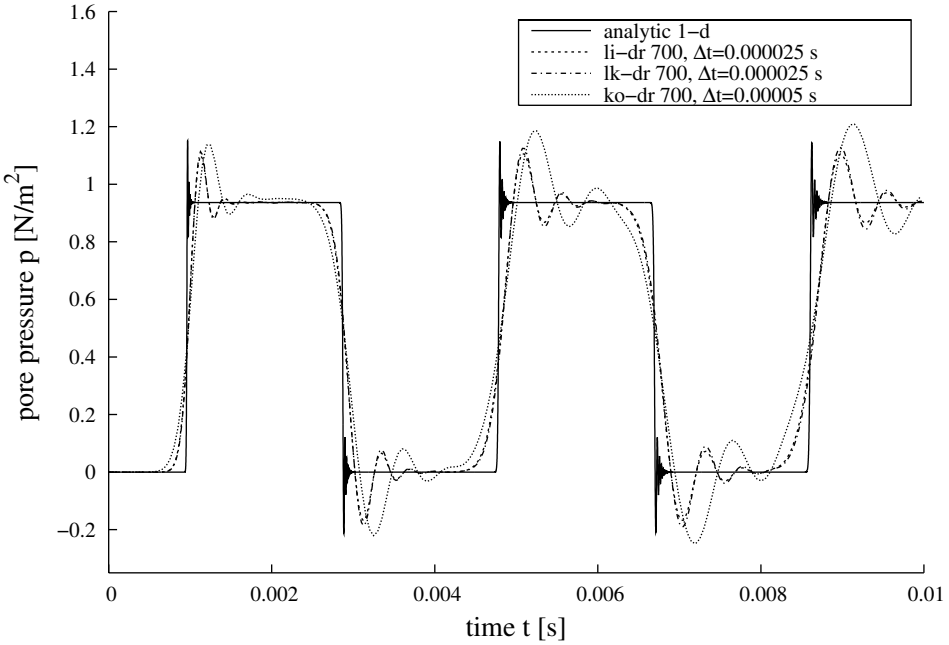

(b) 700 elements

Figure 3.16: 3-d BEM and 1-d analytical solution for rock: Pore pressure at support

Incompressible rock The displacement results for the incompressible model of Berea sandstone are shown in Fig. 3.17. The timestep length is $\Delta t = 0.0001\,\mathrm{s}$ for the linear element and $\Delta t = 0.0002\,\mathrm{s}$ for the mixed. Here, the selected timesteps are not the shortest stable ones. The initial oscillations extinct with time and get smaller when the mesh is refined. With a shorter timestep, i.e., $\Delta t = 0.0001\,\mathrm{s}$ for `lk-dr` or $\Delta t = 0.00005\,\mathrm{s}$ for `li-dr`, these initial oscillations stay visible for a much longer time interval. On the finer mesh, the timestep $\Delta t = 0.0002\,\mathrm{s}$ is used for both the `li-dr` and `lk-dr` elements. Again, the results on the finer mesh are closer to the analytical solution. Also in the pore pressure results in Fig. 3.18, the initial oscillations disappear faster on the finer mesh. Also in this case, the `li-dr` element offers better performance than the mixed `lk-dr` element.

Compressible soil For soil, the optimal time steps used on the coarse 252 element mesh are $\Delta t = 0.0003s$ for the `li-dr` element, $\Delta t = 0.0004s$ for the `lk-dr` element, and $\Delta t = 0.0005s$ for the `ko-dr` element. For the finer mesh, an identical timestep, $\Delta t = 0.0002\,\mathrm{s}$, has been chosen for both the linear and mixed elements, and $\Delta t = 0.0004\,\mathrm{s}$ for the constant element. The displacement results are shown in Fig. 3.19. The linear element allows the shortest timestep and comes closest to the analytical solution. The pore pressure behavior in Fig. 3.20 is essentially the same as for the displacements. Again, the mixed element has no advantages over the isoparametric linear.

Incompressible soil In Fig. 3.21, the displacements at the surface are displayed for all three element types on the two meshes. On the mesh with 252 elements, the timesteps selected are $\Delta t = 0.0004\,\mathrm{s}$ for the linear and constant elements and $\Delta t = 0.0005\,\mathrm{s}$ for the mixed. Near the lower stability limit, there is a region (for `li-dr` at $\Delta t = 0.0003\,\mathrm{s}$ and at $\Delta t = 0.0004\,\mathrm{s}$ for `lk-dr`) where there are large oscillations (especially in the pressure results), but these do not grow (explode), even during much longer time intervals than displayed here.

The results for the finer mesh in Fig. 3.21(b) are noticeably closer to the analytical solution than for the coarser. When comparing these results with the 2-d, note that the element edge length of the finer 3-d mesh is similar to the coarse mesh in 2-d. The pore pressure behavior in Fig. 3.22 is essentially the same as for the displacements. As in all previous 3-d cases, the mixed element is worse than the linear.

3.3 Conclusions and Comments to the Validation

For all element types in both 2-d and 3-d applied to both rock and soil, the results appear to converge to the analytical solution as the mesh is refined. The discretization used in the 3-d case is coarser compared to that in 2-d with an element edge length of $\frac{1}{4}\,\mathrm{m}$ versus $\frac{1}{3}\,\mathrm{m}$ on the coarser mesh and $\frac{1}{16}\,\mathrm{m}$ versus $\frac{1}{5}\,\mathrm{m}$ on the finer mesh, respectively. As expected, the 2-d results are closer to the analytical solution.

In 2-d, the mixed elements bring minor improvements over the isoparametric in terms of stability and result quality. In 3-d, the mixed elements do not bring any improvements. They produce worse results and have a narrower stability region than the isoparametric. The result of the comparison may depend on the choice of dimensionless variables. However, no clear dependency has been recognized during the tests.

One of the possible reasons for different behavior of the element types in 2-d versus 3-d are the different approaches to singular integration. In 2-d, the singular parts of the integrals are computed analytically, whereas in 3-d, they are evaluated numerically. Another difference is in the total degrees of freedom, in

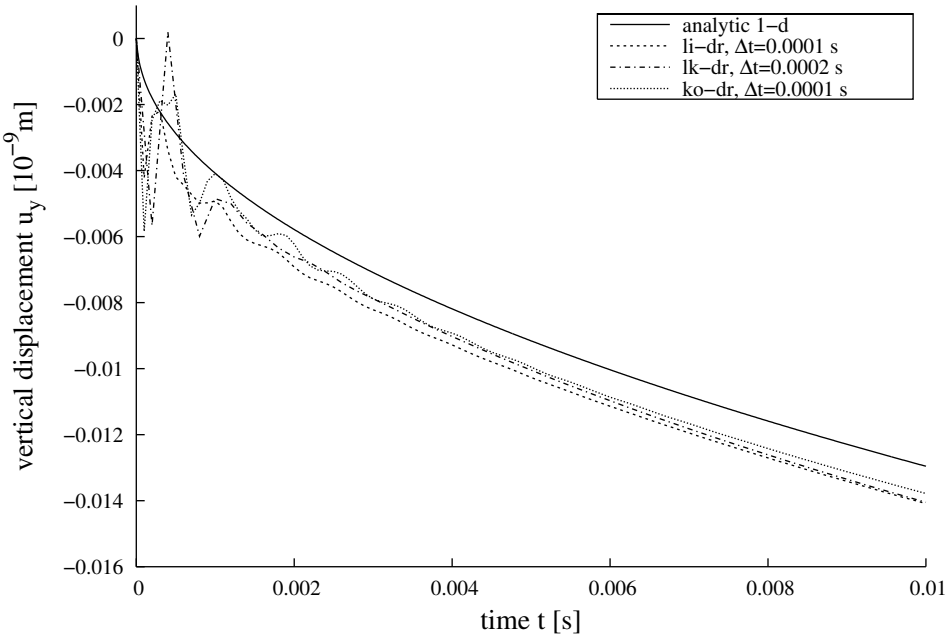

(a) 252 elements

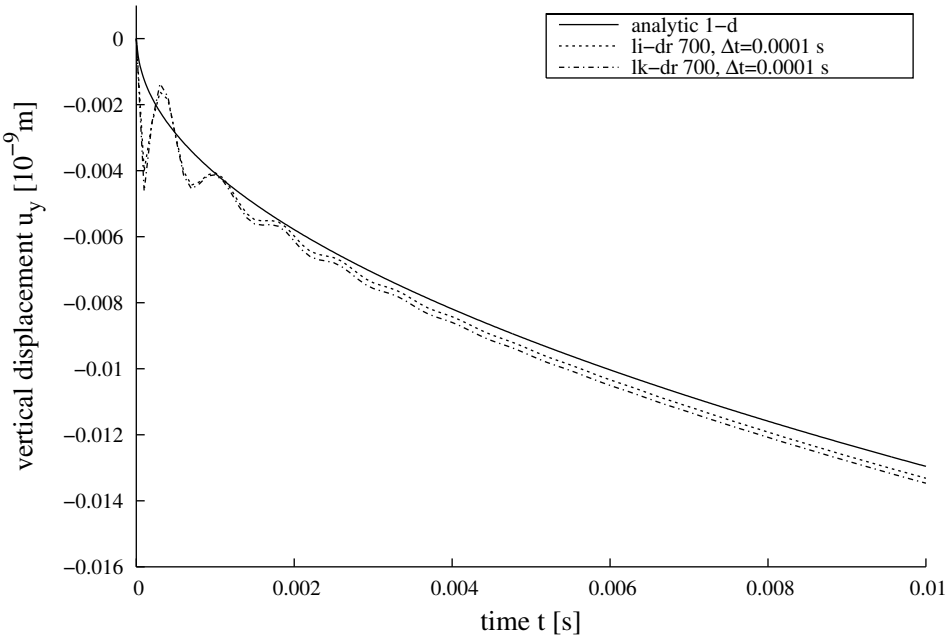

(b) 700 elements

Figure 3.17: 3-d BEM and 1-d analytical solution for incompressible rock: Displacement at point *P*

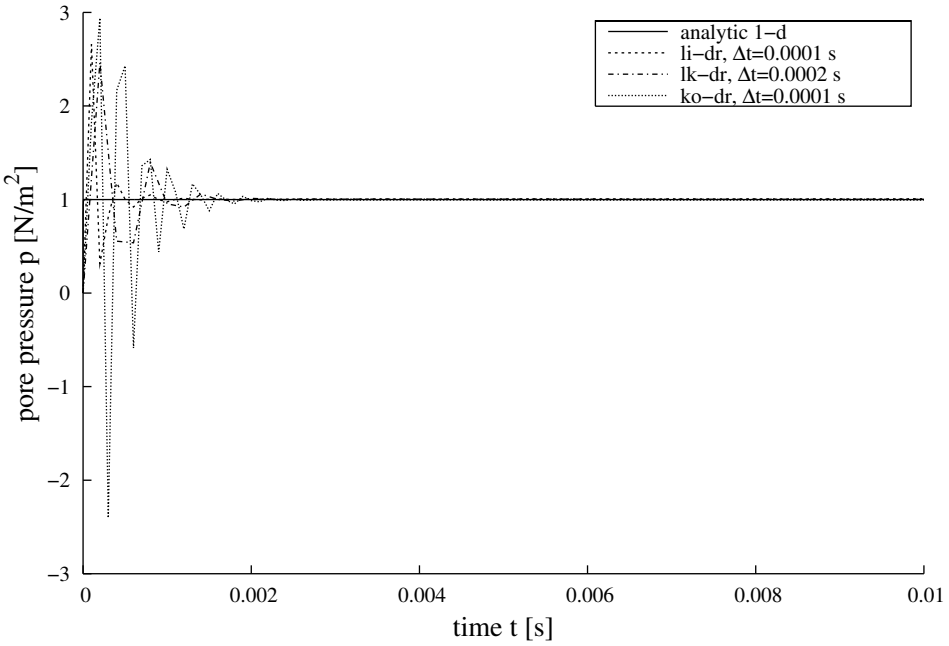

(a) 252 elements

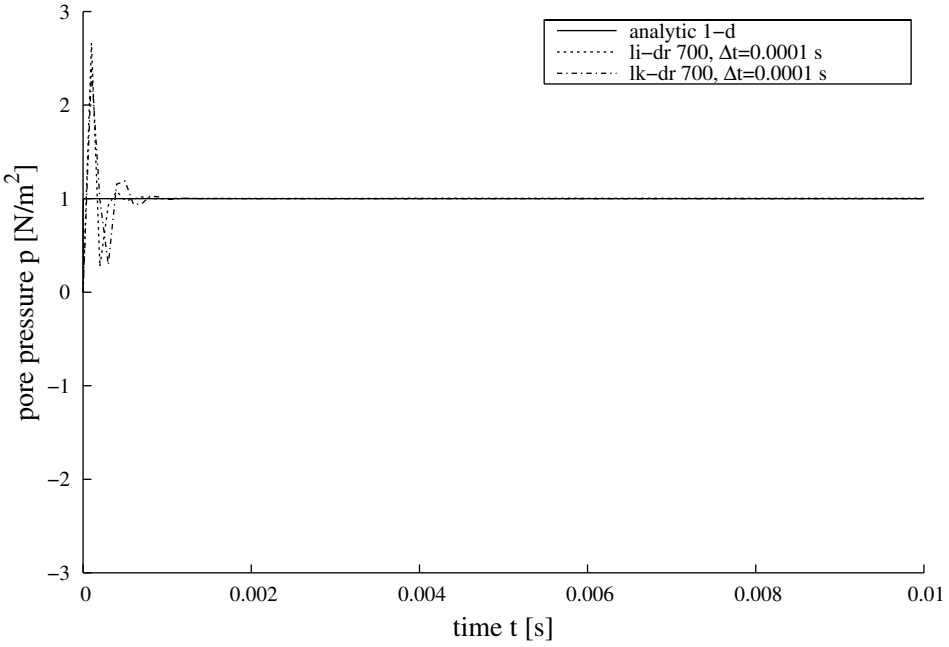

(b) 700 elements

Figure 3.18: 3-d BEM and 1-d analytical solution for incompressible rock: Pore pressure at support

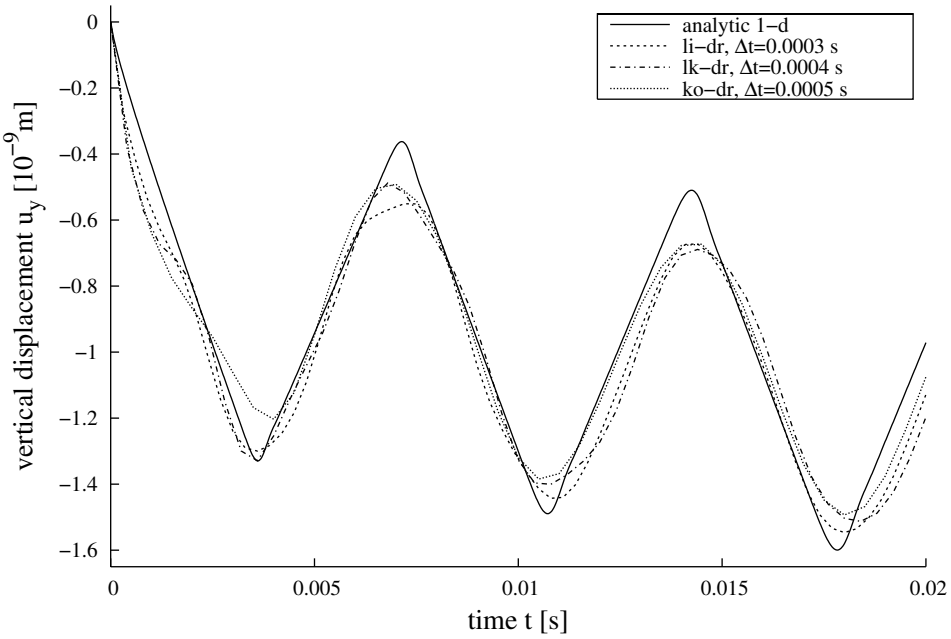

(a) 252 elements

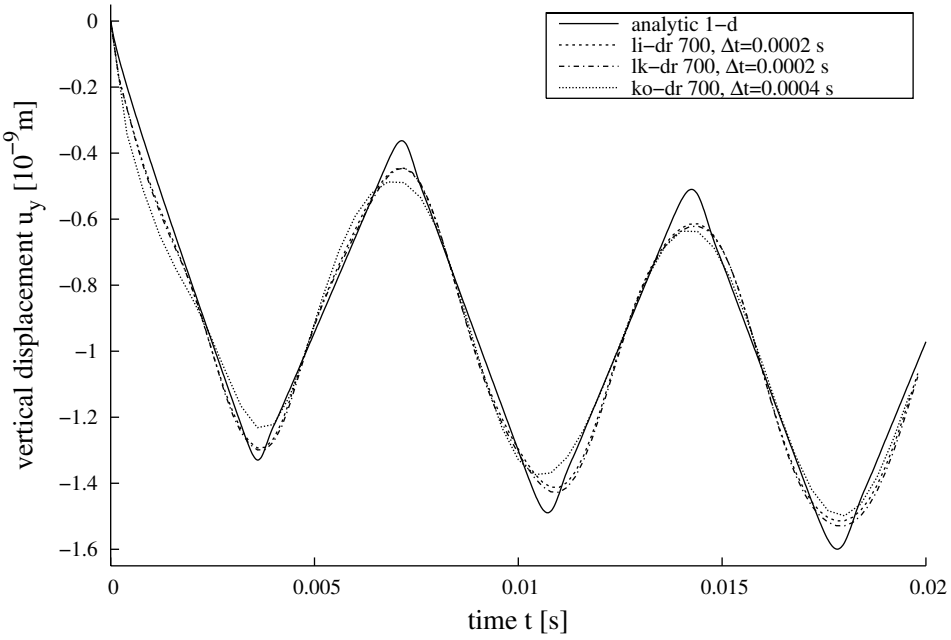

(b) 700 elements

Figure 3.19: 3-d BEM and 1-d analytical solution for soil: Displacement at point *P*

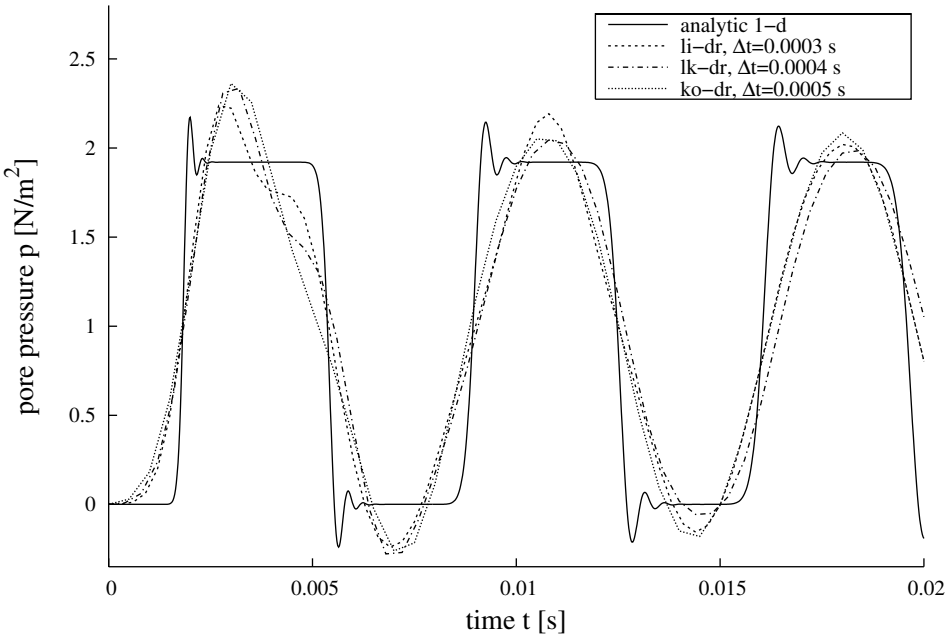

(a) 252 elements

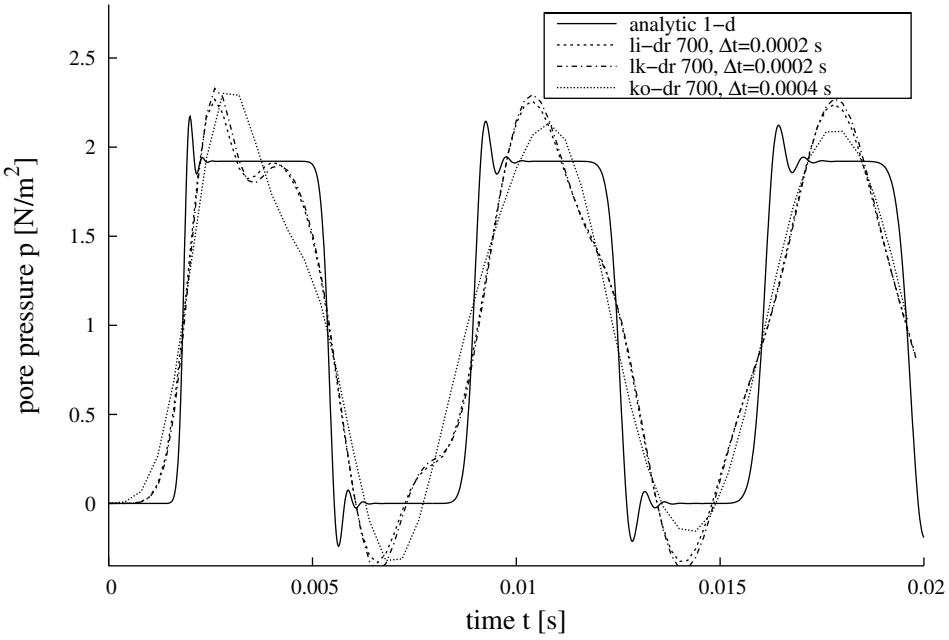

(b) 700 elements

Figure 3.20: 3-d BEM and 1-d analytical solution for soil: Pore pressure at support

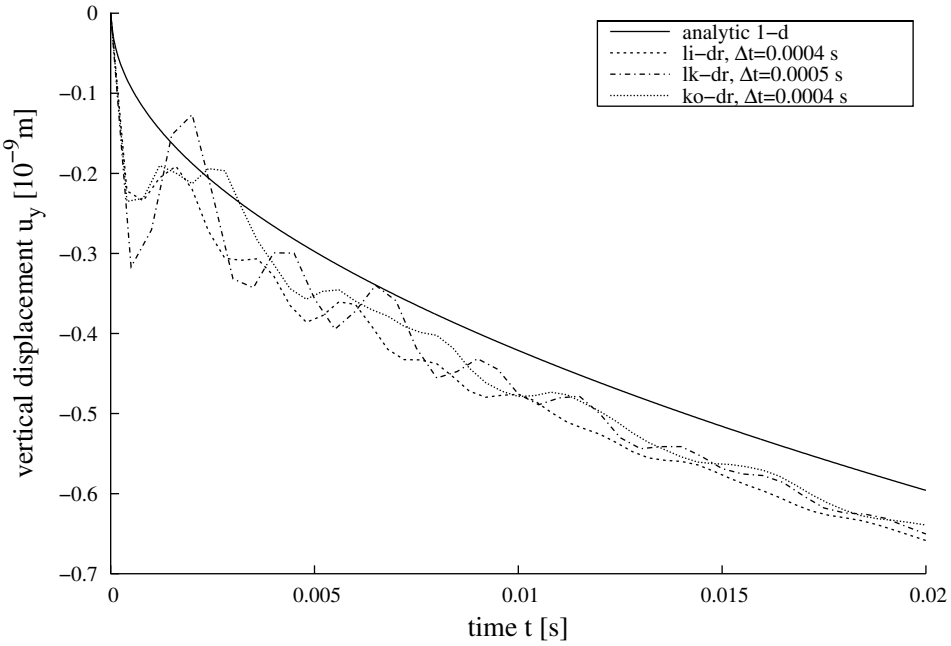

(a) 252 elements

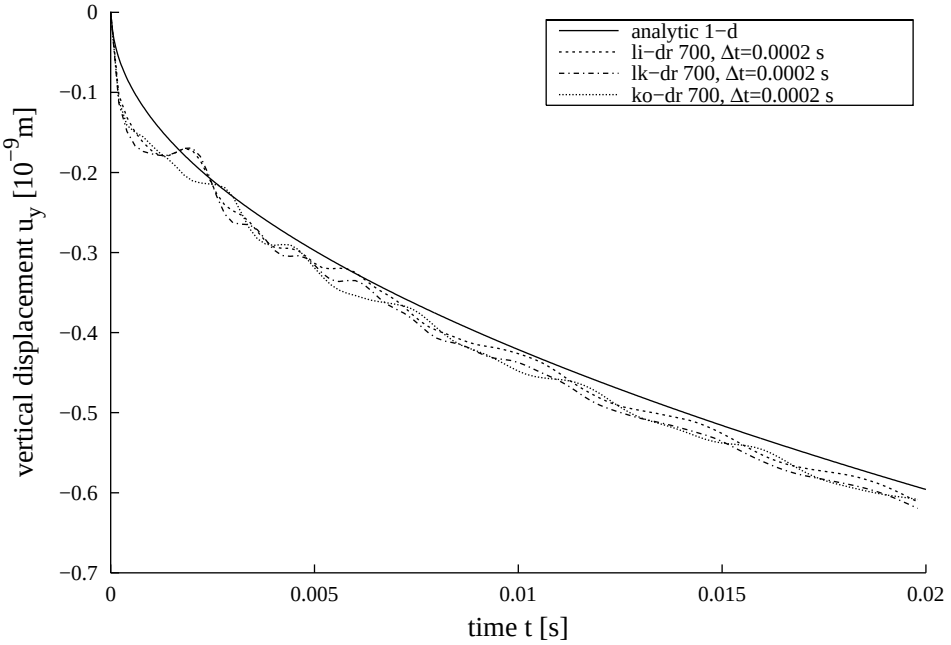

(b) 700 elements

Figure 3.21: 3-d BEM and 1-d analytical solution for incompressible soil: Displacement at point *P*

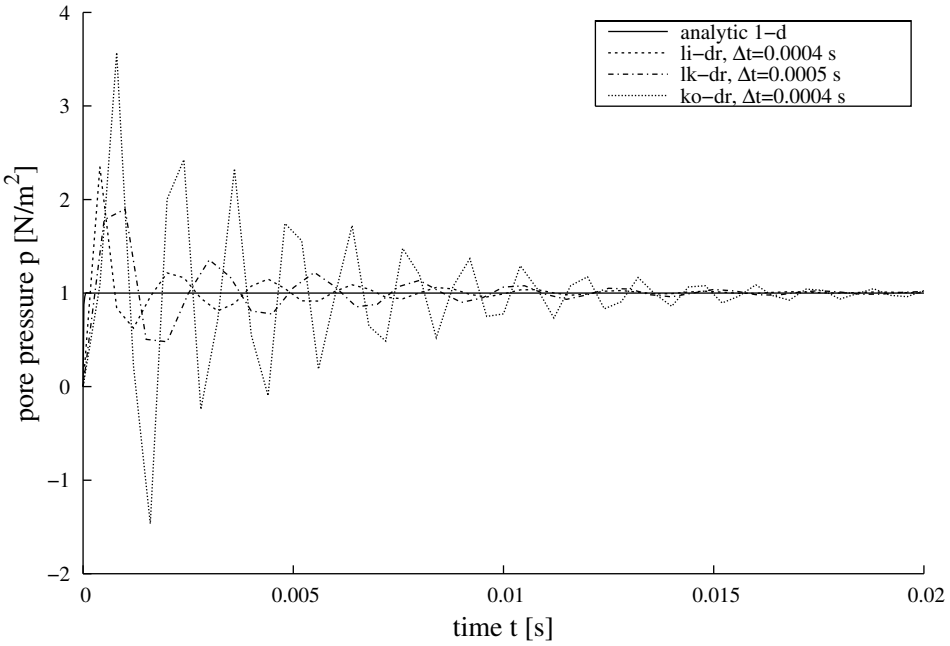

(a) 252 elements

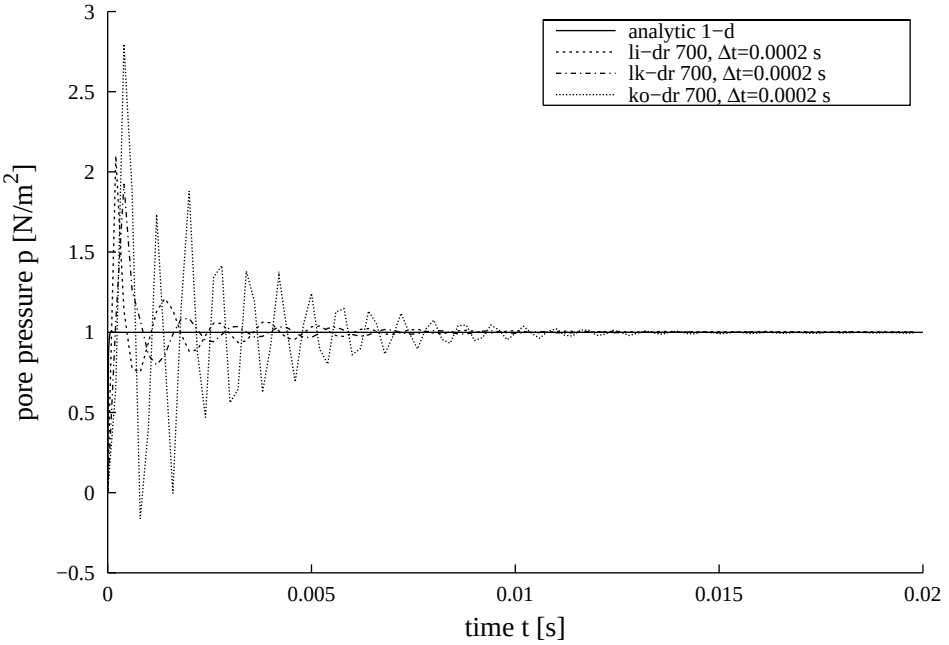

(b) 700 elements

Figure 3.22: 3-d BEM and 1-d analytical solution for incompressible soil: Pore pressure at support

the 2-d examples there is no element type dependent difference, in 3-d there are more nodes for constant approximation (mid-nodes) than for linear (element corners). This leads to additional degrees of freedom if some quantity is approximated with a lower degree shape function.

For the rock, the same discretization produces much better results than for the soil. This can be explained by the material dependent difference in the ratios of the fast compressional and shear wave speeds. Although the wave speeds are frequency dependent, the estimation for infinite permeability $\kappa \to +\infty$ can be used to generate an approximate idea about the ratio. For the Berea sandstone, the ratio of the fast compressional to the shear wave speed is $\frac{c_p}{c_s} \approx 2$, for the soil it is $\frac{c_p}{c_s} \approx 6$.

The bigger difference between the wave speeds in the case of the soil would require different meshes (or at least different timesteps for the same mesh) to resolve each of the waves optimally. As there only is a single mesh, it is clear the results are worse for the soil compared to the Berea sandstone, where the difference between the wave speeds is smaller.

The poroelastodynamic BEM implementation has been tested on examples representing a 1-d problem in both 2-d and 3-d. It has been shown that it approximates the 1-d analytical solution very well. In the next chapter, it will be used to model wave propagation.

4 Wave Propagation in Poroelastic Materials

There are two basic types of waves, *longitudinal* (also called P-, primary, pressure, compressional, dilatational, irrotational, or extension waves), where the particles move along the same line the wave propagates, and *transverse* (S-, secondary, shear, rotational, or distortion waves), with particle movement in a direction perpendicular to the propagation direction.

One longitudinal wave, called *compressional* in the following, and one transverse wave, referred to as *shear*, exist in a 2-d homogeneous isotropic linear elastic solid. In 3-d, shear waves can be polarized in any direction perpendicular to the propagation direction. Shear waves in a plane parallel respectively perpendicular to the surface are traditionally referred to as *horizontal* (*SH*) respectively *vertical* (*SV*) shear waves.

On surfaces and interfaces, *surface waves* can propagate due to conversion effects by reflection and refraction. The geometrical attenuation with distance is lower than for bulk waves, e.g., for a point source in 3-d, if r denotes the distance of the observer from the source, the amplitude decreases as $\frac{1}{\sqrt{r}}$ for surface waves compared to $\frac{1}{r}$ for bulk waves [1]. If energy is radiated away from the surface, the wave is called *leaky* (or its name is prefixed with pseudo-), and it attenuates exponentially along the distance traveled.

For example on a traction free surface, depending on Poisson's ratio and the incidence angle, a compressional wave can reflect as a compressional wave, as compressional plus vertical shear waves (see Fig. 4.1), or even vertical shear wave only (*mode conversion*). Similarly, again depending on Poisson's ratio and the incidence angle, a vertical shear wave reflects as vertical shear only, vertical shear and compressional, or compressional wave only.

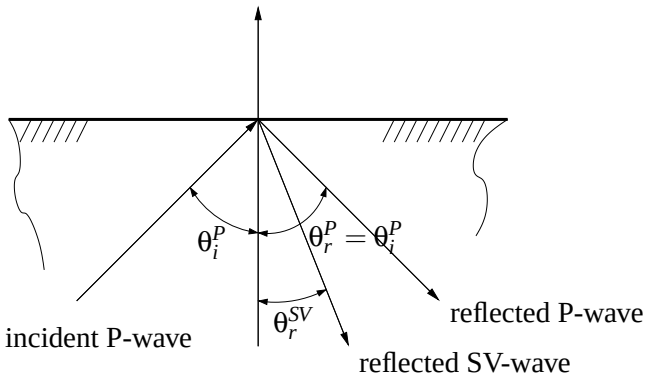

Figure 4.1: Reflection of a compressional wave

[1] Note that energy depends quadratically on the amplitude, hence the energy density attenuates with $\frac{1}{r}$ for surface waves and $\frac{1}{r^2}$ for bulk waves.

The interaction of the pressure and vertically polarized shear waves near a free surface lead to a wave traveling along the surface, called *P-SV* or *Rayleigh* wave. It propagates with a speed slower than both of the waves it is composed from. As the horizontal and vertical displacements are not in phase, the particles follow an elliptical trajectory in the vertical plane. Displacements due to this wave can be observed up to a depth of about two wavelengths, reaching a maximum near the surface and then decaying exponentially with increasing depth.

Similar to the Rayleigh waves on surfaces, *Stoneley* (Scholte) waves can propagate along interfaces between two solids or a solid and a fluid. Their existence is bound to a certain range of ratios of the densities and the shear moduli of the two materials [1]. Artificial seismograms for a pulse excitation propagating along a free surface, solid-solid, and solid-fluid interface are presented in [55] for several sets of material data.

In layered media, the horizontally polarized shear wave can lead to a surface wave known as *Love* or Q-wave. An example setup is a layer with slower shear wave speed on top of a halfspace with a faster shear wave speed. The Love wave propagates with a speed between the two shear wave speeds. In the halfspace, it decays exponentially with increasing depth [72].

An overview of elastic waves in homogeneous isotropic solids can be found in [75] or more detailed in [1].

In Poroelastic materials a second longitudinal wave, called *slow compressional* wave (also known as P2, secondary compressional, or Biot's wave), exists in addition to the waves known from elasticity, i.e., the *fast* (or primary) *compressional* and the shear waves. Contrary to the fast compressional wave where the solid and fluid particles move in phase (see Fig. 4.2(a)), in the slow compressional wave, the solid and fluid move in opposite directions (Fig. 4.2(c)), which leads to a higher attenuation. This wave predicted by Biot's theory has been experimentally observed by Plona [77]. As in elasticity, the shear wave (Fig. 4.2(b)) is not connected with any volume change. Unlike in elasticity, all wave propagation speeds become frequency dependent and therefore time dependent. This introduces dispersion (see also section 1.3, especially the footnote on page 16).

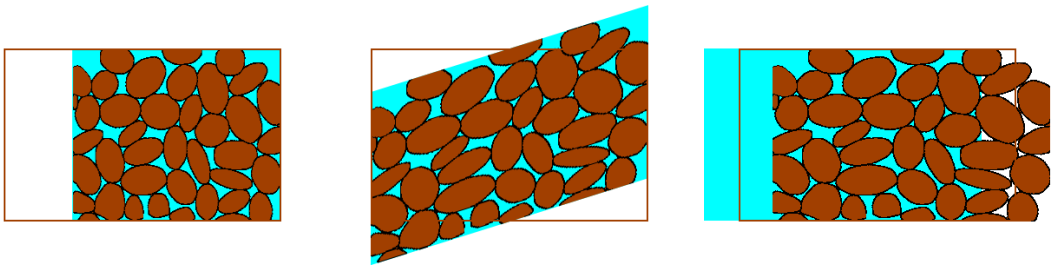

(a) fast compressional wave (b) shear wave (c) slow compressional wave

Figure 4.2: The three wave types in poroelastic materials

The additional wave over the elastic case makes more mode conversions possible on reflections. Only in special cases, like normal incidence or for an incident SV-wave at 45 degrees, solely the original wave is reflected without mode conversion at a free boundary of a porous solid [38]. The general case for an incident fast compressional case is illustrated in Fig. 4.3.

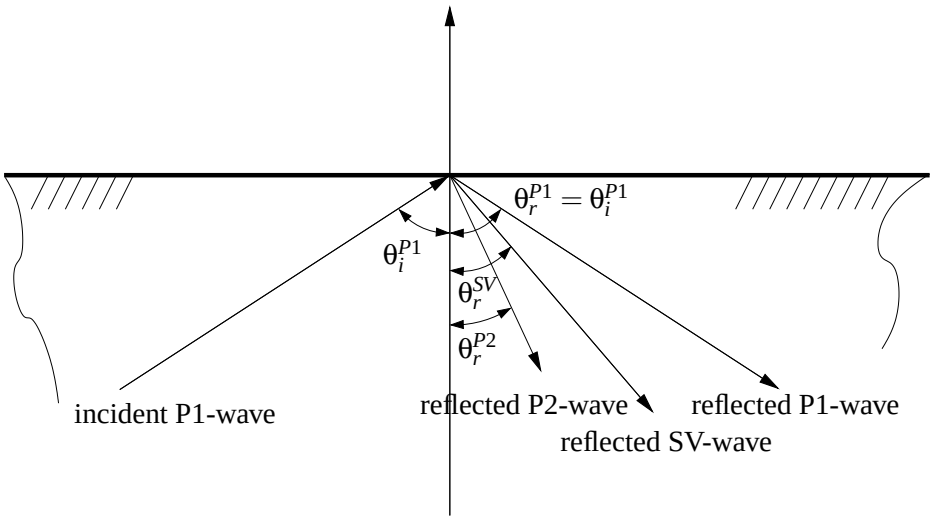

Figure 4.3: Reflection of a fast compressional wave

A Rayleigh wave similar to the elastic case, based on the fast compressional wave and the shear wave, propagates along traction free surfaces. Leaking into the slow compressional wave makes the Rayleigh wave dispersive [37].

Due to the additional slow compressional wave, one more surface wave exists. The *slow surface* wave (or true surface mode), has been predicted by Feng and Johnson [51] and experimentally observed by Nagy [70]. This additional wave propagates with speed slower than the slow compressional wave along impermeable surfaces (i.e., with closed pores) and only for a limited range of material parameters in the case of a permeable surface (i.e., with open pores). Unlike the fast compressional wave, the speed of the slow compressional wave is usually lower than that of the shear wave. This situation resembles a solid-fluid interface with the compressional wave in the fluid slower than the shear wave, where the Stoneley wave can propagate. Therefore, the discussed slow surface wave is sometimes called Stoneley wave [2].

In a porous layer over a halfspace, a Love wave similar to the elastic case can develop [36].

In the following, wave propagation and the influence of the incompressible modeling on various wave types in poroelastic materials will be studied numerically.

4.1 2-d Poroelastic Column

To compare the numerical behavior of the implemented element types, a 2-d poroelastic column is considered. The column of 3 m (height) $\times$ 1 m (width) is fixed and impermeable on one end, and excited by a traction jump according to a unit step function $t_y(\mathbf{x},t) = 1\,\mathrm{N/m^2}\,H(t)$ on the other end, which is modeled free and permeable (see Fig. 4.4). The remaining surfaces are traction free and permeable (i.e., with pore pressure assumed to be zero). Note that unlike the validation example in chapter 3, horizontal displacements are now possible on the sides. The BEM model consists of 32 nodes and 32 elements - linear isoparametric `li-2D`, constant `ko-2D`, and mixed linear/constant `lk-2D`. The finer discretization consists of 128 elements on 128 nodes.

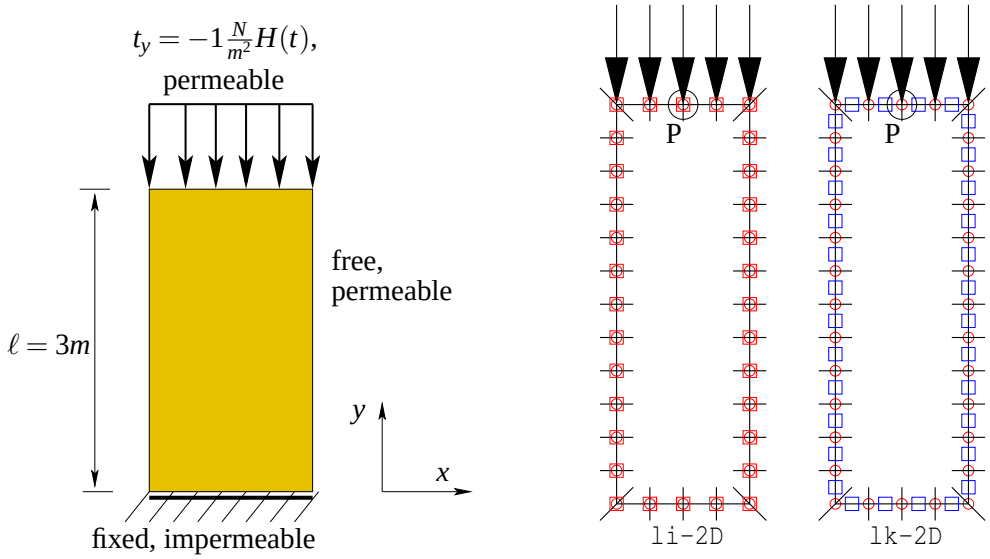

Figure 4.4: 2-d column: Geometry, boundary conditions, and discretization

The figures 4.5 respectively 4.6 show the displacement u_y at the column surface midpoint and the pore pressure p at the column base midpoint, respectively, plotted against time for the `li-2D`, `lk-2D`, and `ko-2D` elements. On the coarser mesh, the optimal timestep has been chosen for each element type. The stability region is slightly larger for the `lk-2D` element on the mesh with 32 elements: $\Delta t = 0.00017\,\mathrm{s}$ compared to $0.00018\,\mathrm{s}$ for `li-2D`. The results for the finer mesh (denoted '128') have been computed with the same timestep $\Delta t = 0.00005\,\mathrm{s}$ for all element types. As there are no visible differences, only the `li-2D` element results are presented for the finer mesh. In the pore pressure solution in Fig. 4.6, some oscillations arise with the arrival of the fast compressional wave (the first non-zero pressure value) induced by the load application at $t = 0\,\mathrm{s}$. They are damped and have completely dissipated at about $t = 0.02\,\mathrm{s}$.

As described in section 2.3, with the linear isoparametric element all the state variables are localized at the geometry nodes, i.e., the element end-nodes. For the mesh with 32 elements in Fig. 4.4, this gives $3 \times 32 = 96$ total degrees of freedom in the case of the `li-2D` element. The mixed linear-constant element defines the solid displacement u_i (respectively traction t_i) at the end-nodes and has an extra mid-node for the pore pressure p (respectively flux q), which yields in total $2 \times 32 + 1 \times 32 = 96$ degrees of freedom. Thus, the total number of degrees of freedom is the same for the linear and mixed elements (this will be different later in the 3-d example). Nevertheless, the CPU time needed extends about $1.3\times$. The essential source of the extra operations is the need to evaluate the fundamental solutions for more distinct distance arguments. Clearly, the mixed element does not offer advantages that would be worth the extra computational cost.

Incompressible Figs. 4.7 and 4.8 show the displacement u_y at point P on the top surface and the pore pressure p in the middle of the support for the compressible and incompressible models. Unlike the validation example in chapter 3, there are not large differences between the compressible and incompressible models of soil. That is due to the boundary conditions, which differ substantially from the validation example.

However, the lower stability limits are not the same as in the compressible case. In Figs. 4.9 and 4.10,

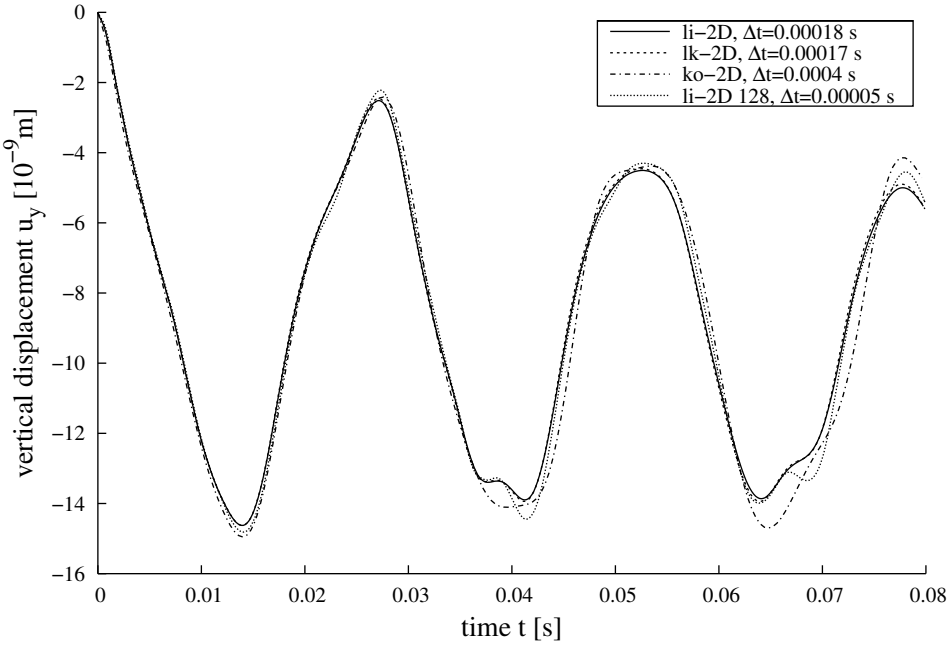

Figure 4.5: 2-d column: Displacement at point *P*

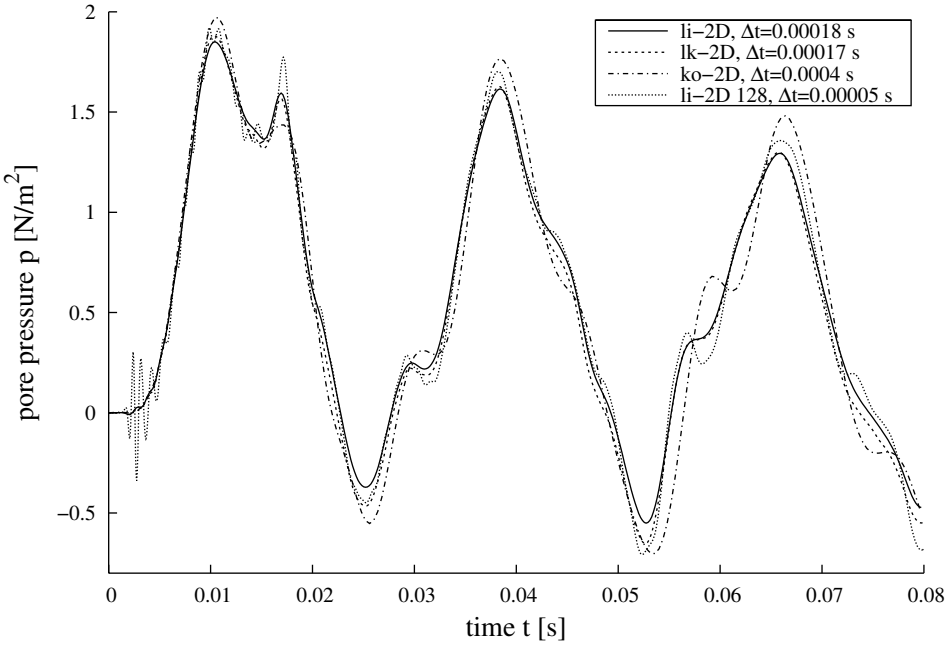

Figure 4.6: 2-d column: Pore pressure at support midpoint

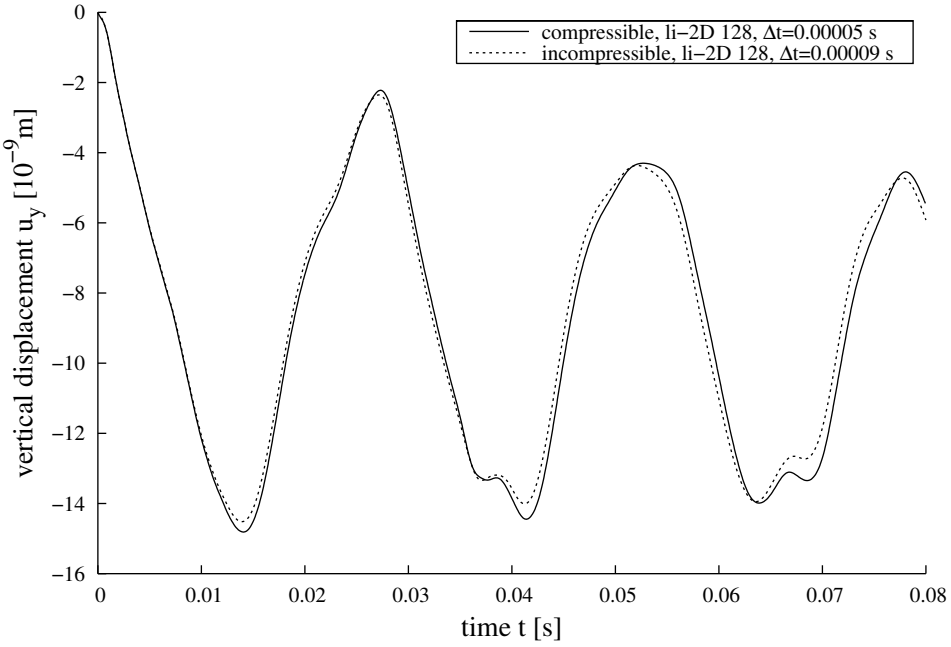

Figure 4.7: Compressible and incompressible 2-d column: Displacement at point *P*

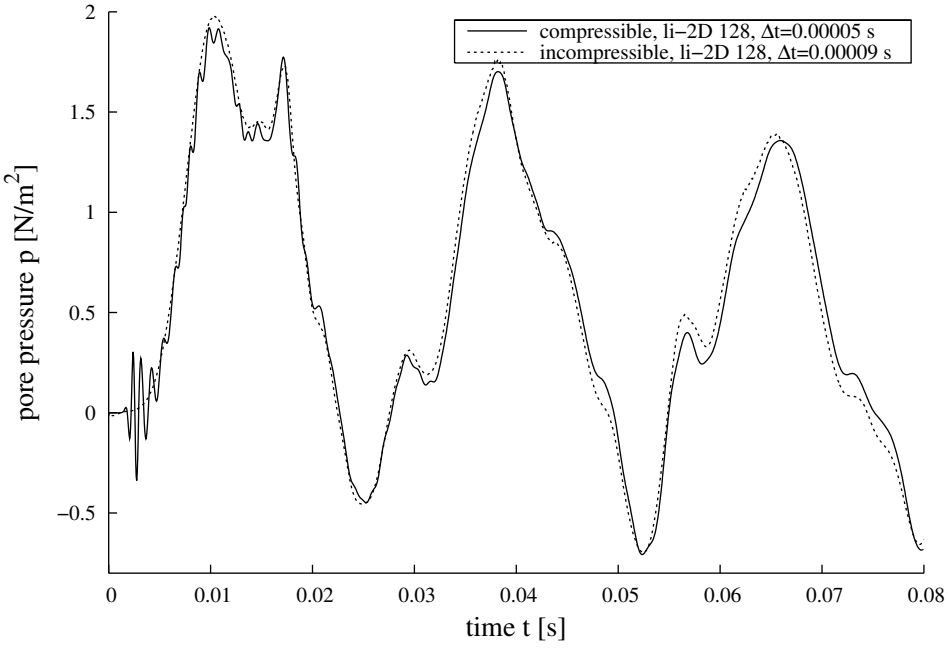

Figure 4.8: Compressible and incompressible 2-d column: Pore pressure at support midpoint

for each element the displacement respectively pressure results are displayed for the optimal timestep, $\Delta t = 0.00039\,\mathrm{s}$ for the `li-2D` element, $\Delta t = 0.00018\,\mathrm{s}$ for `lk-2D`, and $\Delta t = 0.0003\,\mathrm{s}$ for `ko-2D`. In this case, the mixed element allows to achieve better results than the linear isoparametric on the same mesh. On the finer mesh, the results for all element types get closer to each other and almost coincide. Therefore, only one solution on the finer mesh (128 `lk-2D` elements at $\Delta t = 0.00005\,\mathrm{s}$) is included in the plot as a reference.

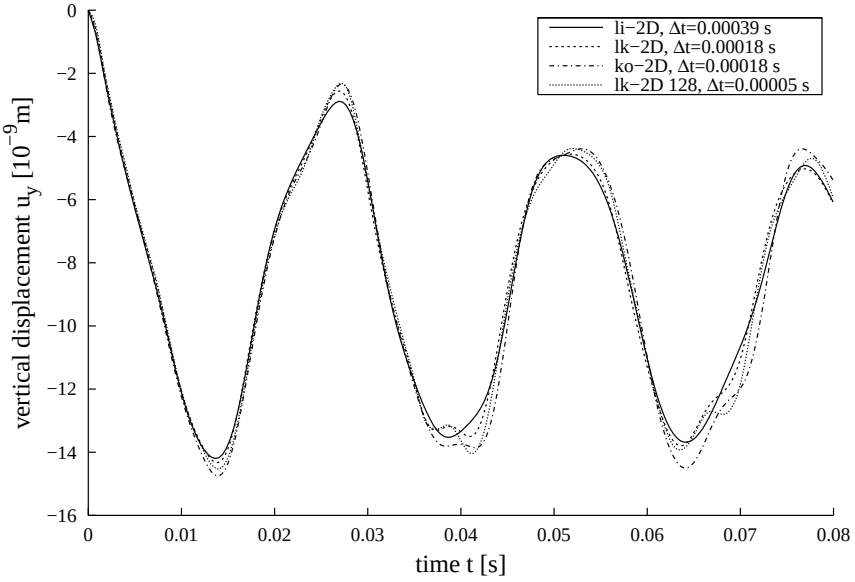

Figure 4.9: Incompressible 2-d column: Displacement at point *P*

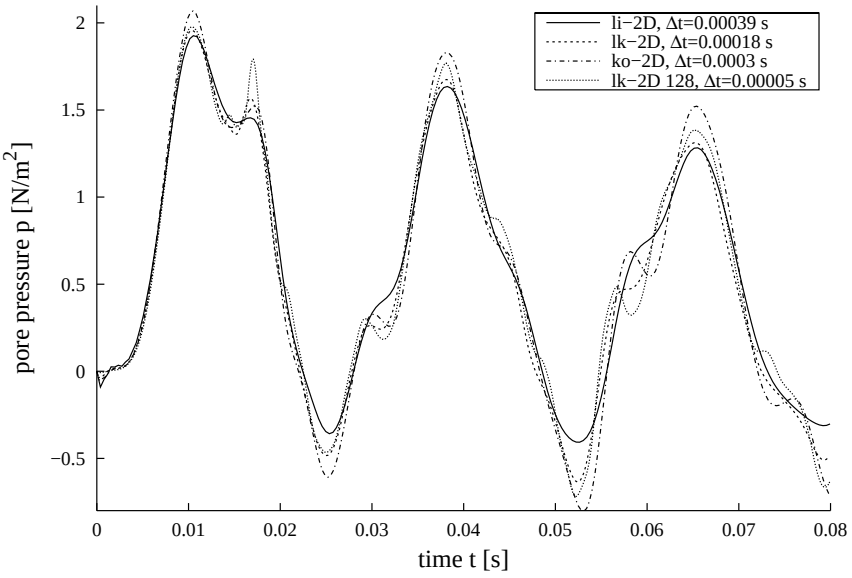

Figure 4.10: Incompressible 2-d column: Pore pressure at support midpoint

4.2 3-d Poroelastic Column

The column of 3 m (length) $\times$1 m (height) $\times$1 m (width) is fixed and impermeable on one end, and excited by a traction jump according to a unit step function $t_y(\mathbf{x},t) = 1\,\mathrm{N/m^2}\,H(t)$ on the other end, which is modeled free and permeable. The remaining surfaces are traction free and permeable (i.e., with pore pressure assumed to be zero). Note that unlike the validation example in chapter 3, horizontal displacements are now possible on the sides. The geometry is discretized with 328 linear triangular elements on 166 nodes, non-uniformly refined near edges and corners (see Fig. 4.11(b)). In contrast

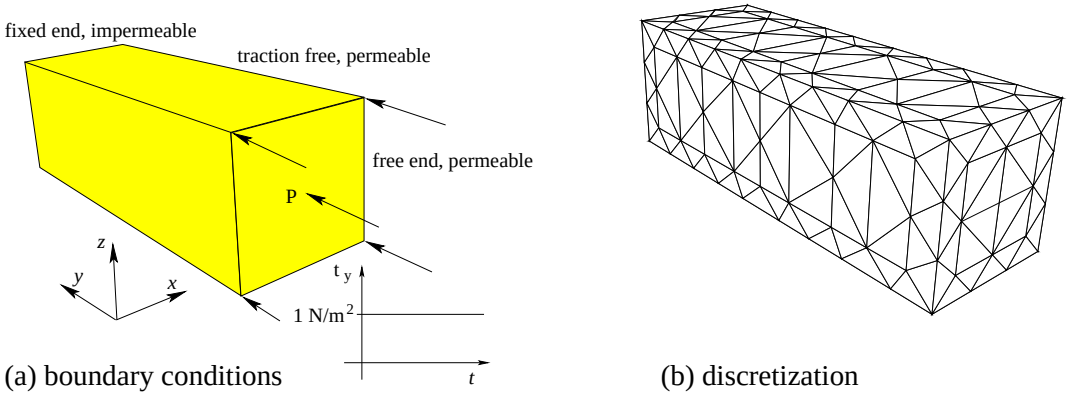

(a) boundary conditions (b) discretization

Figure 4.11: Geometry, boundary conditions, and discretization of a 3-d column

to the isoparametric `li-dr` elements, where the geometry nodes (triangle corners) are also used for all the state variables, the newly implemented mixed `lk-dr` elements employ them only for u_i and t_i and need 328 additional mid-element nodes for p and q. Thus, there are in total $4 \times 166 = 664$ or $3 \times 166 + 1 \times 328 = 826$ degrees of freedom for the isoparametric or mixed elements, respectively.

First the compressible model is considered. In Fig. 4.12, the displacement u_y at point P at the loaded end is plotted versus time t. Fig. 4.13 shows the pore pressure p in the middle of the supported end. The time step size of $\Delta t = 0.0005\,\mathrm{s}$ is chosen for all element types. The optimal timestep (lower stability limit) has been found at $\Delta t = 0.0005\,\mathrm{s}$ for the mixed `lk-dr` element and $\Delta t = 0.00048\,\mathrm{s}$ for the isoparametric linear `li-dr`, but as the dimensionless variables as defined in (2.23) include the length of the time interval (see section 2.2), the stability limit shifts slightly with changes in the total time.

The results for the constant elements exhibit the smallest amount of numerical damping, but the total number degrees of freedom is also about the double of that of the linear elements. Besides that, the plots do not exhibit much differences, especially in the displacement results. The results for the `li-dr` and `lk-dr` elements almost coincide. In the pressure plot, a small difference in favor of the mixed element which shows less numerical damping can be observed. On the other hand, also the disadvantage in the lower stability limit $\Delta t = 0.0005\,\mathrm{s}$ for `lk-dr` compared to $\Delta t = 0.00048\,\mathrm{s}$ for `li-dr` can not be considered substantial.

At the same time, the total number of the degrees of freedom increased by a factor of about 1.2, resulting in longer computation time by a factor of 1.7, which corresponds to the quadratic dependence between

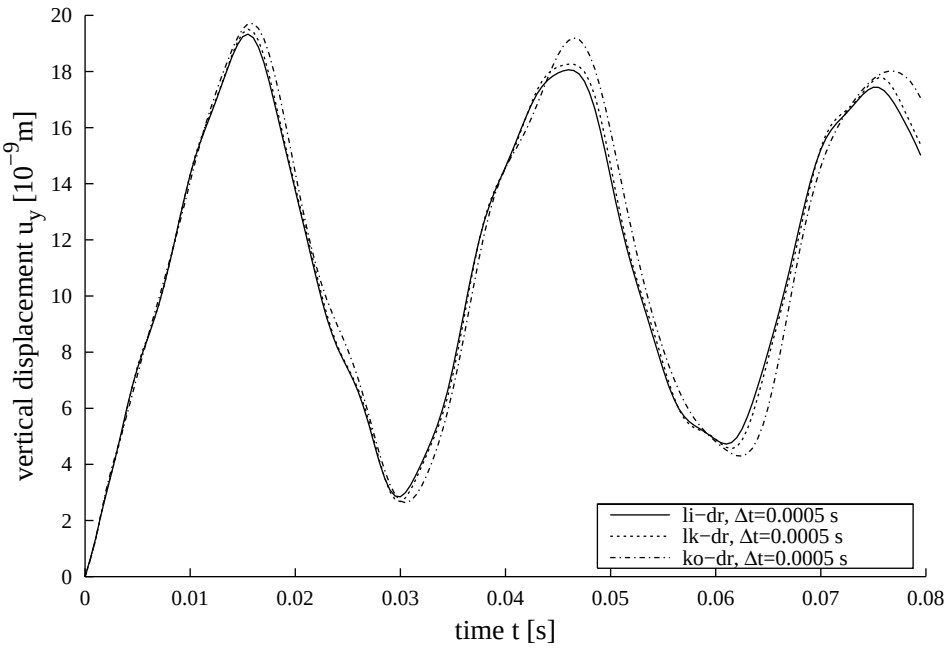

Figure 4.12: Compressible 3-d column: Displacement at point *P*

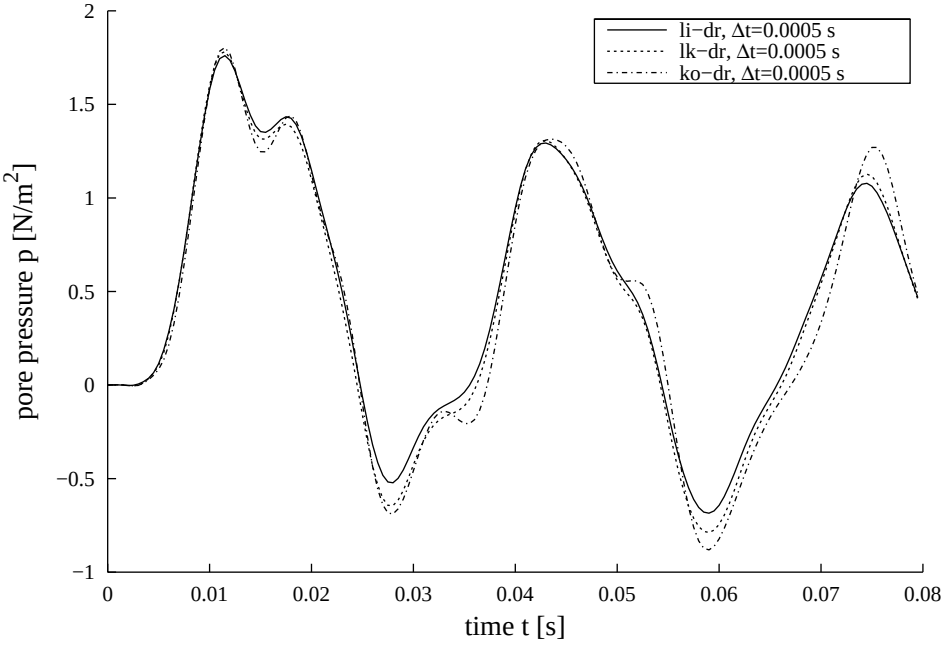

Figure 4.13: Compressible 3-d column: Pore pressure at support midpoint

the degrees of freedom and the number of operations. Clearly, there are no improvements that would offset this extra computational cost of the mixed element.

Now, the results of the incompressible model will be considered. In Figs. 4.14(a) and 4.14(b), the displacement and the pore pressure for the compressible and incompressible models are compared for the linear element and timestep length $\Delta t = 0.0005\,\mathrm{s}$. Unlike the test in chapter 3, there are no noticeable

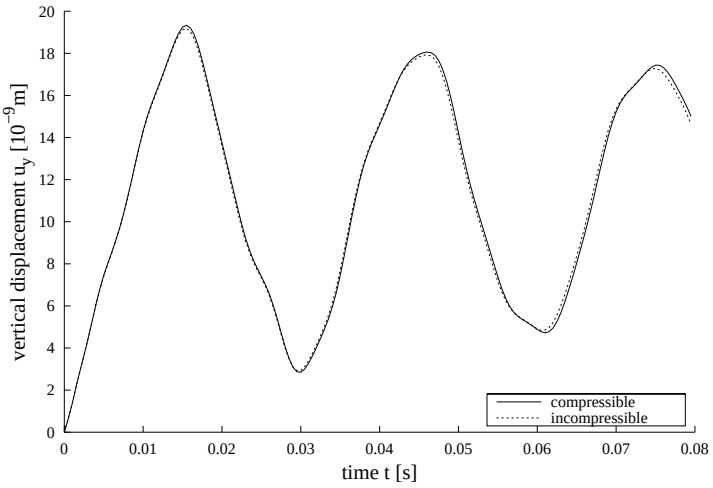

(a) 3-d column: Displacement at point *P*

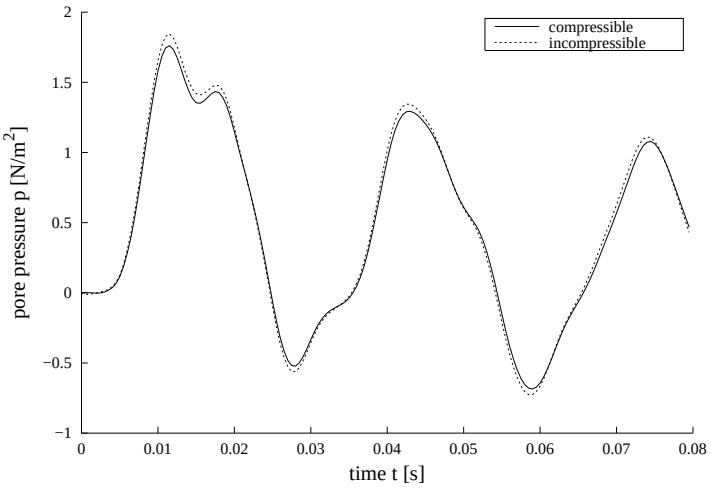

(b) 3-d column: Pore pressure at support midpoint

differences between the models with compressible and incompressible constituents. On the mesh used, the differences between the models are of the same order as those between the element types. There is also no difference in the stability region compared to the compressible model.

4.3 2-d Poroelastic Halfspace

In the following, the 2-d halfspace is discretized as usual when using the Boundary Element Method. For this mesh, wave propagation is studied and the compressible and incompressible models are compared for two different materials, a rock and a soil. Another example is introduced for comparison to a Finite Element model of the Theory of Porous Media with incompressible constituents.

4.3.1 Compressible and Incompressible Models for Two Materials

To model a poroelastic halfspace in 2-d, the surface line is discretized with 51 elements on 52 nodes, as displayed in Fig. 4.14. The finer mesh on which the presented results have been computed has 204 elements on 205 nodes. Linear isoparametric elements `li-2D` are used, except for the incompressible soil which is modeled using the mixed linear-constant `lk-2D` elements. The data for both materials used, a soil and a rock (Berea sandstone), may be found in Tab. 3.1. The time step used is $\Delta t = 2 \cdot 10^{-4}$ s for the soil and $\Delta t = 3 \cdot 10^{-5}$ s for the rock. In the middle of the discretized part, the load $t_y = -1000 \frac{N}{m^2}(H(t) - H(t-t_1))$ is applied at $t = 0s$ and vanishing at $t_1 = 0.004$ s for the soil, respectively $t_1 = 0.0003$ s for the rock. The loaded area is 1 m long and impermeable. The rest of the surface is traction free and permeable.

The wave arrivals will be observed at two surface points, A in 10 m distance from the loaded area, and B in 20 m distance, and at internal points at 0.5 m, 5 m, and 15 m meters depth below the point B.

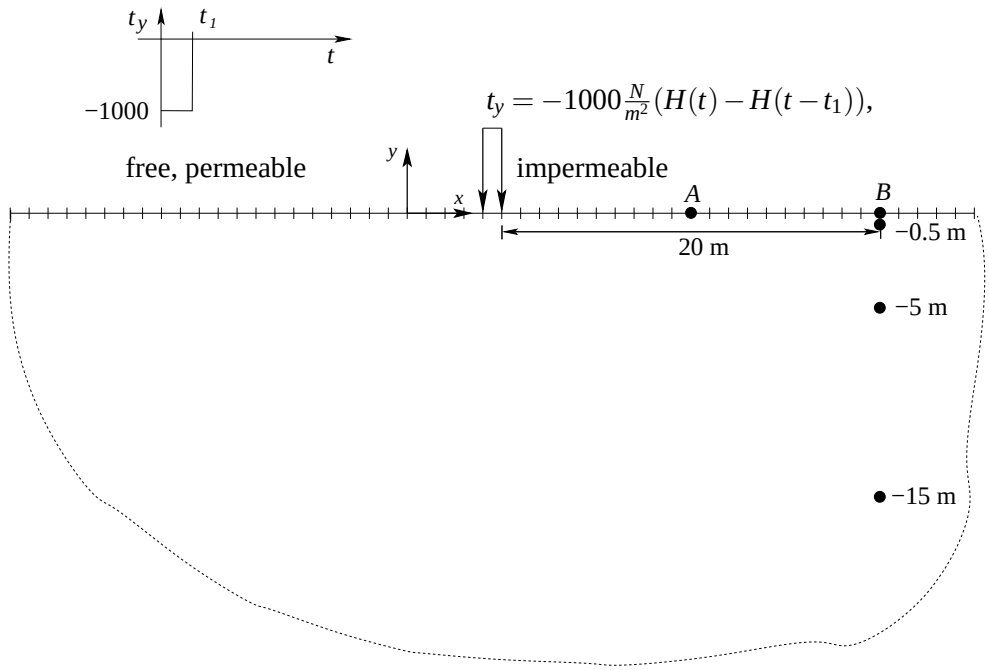

Figure 4.14: Poroelastic halfspace in 2-d: Geometry and boundary conditions

The vertical displacement and the pore pressure at the midpoint of the loaded area are displayed versus

time in Figs. 4.15 and 4.21, respectively 4.16 and 4.22. It can be observed how both the displacement and the pore pressure return to zero after the load disappears.

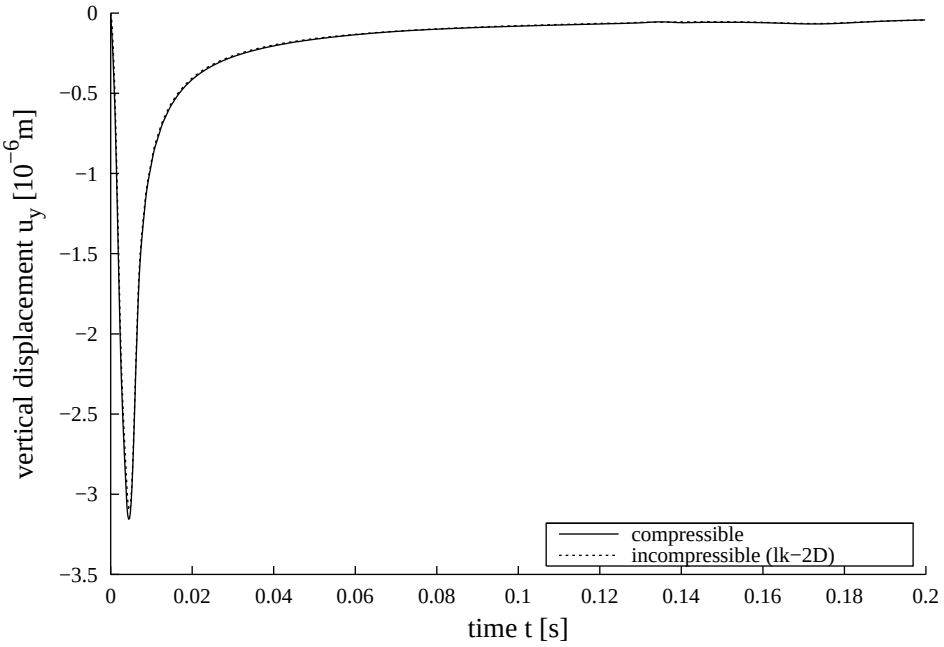

Figure 4.15: Poroelastic soil halfspace in 2-d: Vertical displacement under load

Before examining further results, it may be convenient to look at the ratios of the compression moduli. There is $K/K_s = 0.22, K/K_f = 2.42$ for the rock and $K/K_s = 0.019, K/K_f = 0.064$ for the soil. Hence, the incompressible modelling can be expected to fail for the rock and to give good results for the soil, which is confirmed by the following results for the two materials.

Soil In Fig. 4.17, the vertical displacement at point *B*, 20 m from the loaded area, is plotted against time. The fast compressional wave arrival (the first nonzero displacement) can be observed at about $t = 0.015$ s for the compressible model and at $t = 0$ s for the incompressible, which corresponds to the infinite propagation speed of this wave. Other than that, no differences between the two models are visible in the graph. The Rayleigh wave peak appears at about $t = 0.1$ s. The disturbance at about $t = 0.12s$ has been identified as fast compressional wave reflected when the Rayleigh wave reaches the end of the discretization.

In Fig. 4.18, the vertical displacement at point *B* and several interior points down to 15 m below it (see Fig. 4.14) is presented for the compressible model to study how the amplitudes and arrival times change with increasing depth. The peak corresponding to the Rayleigh wave has a larger amplitude in 0.5 m depth than on the surface, and then decreases with increasing depth, which corresponds to the known behavior of this surface wave. In 5 m depth it is remarkably smaller than on the surface, but does not noticeably decrease further when moving down to 15 m depth. Besides that, in 5 m depth the peak arrives earlier than on the surface, although the surface point is closer to the load. These observations suggest that 5 m from the surface the Rayleigh wave already disappears and the shear wave (which always propagates faster than the Rayleigh wave) becomes visible.

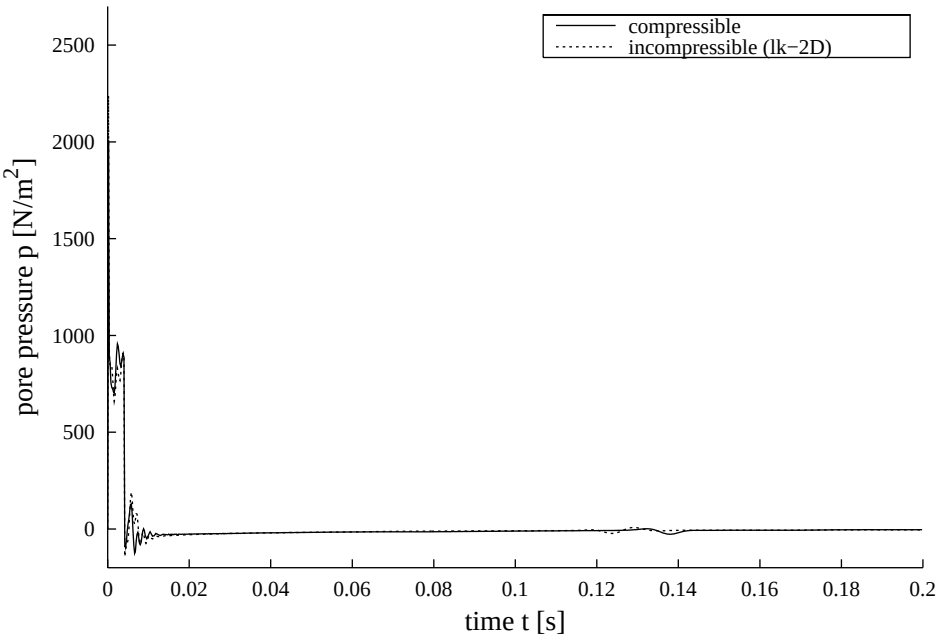

Figure 4.16: Poroelastic soil halfspace in 2-d: Pore pressure under load

Fig. 4.19 presents the pore pressure results at the internal points below the surface point *B*. Note that the big plot only displays the beginning of the time interval and has a different timescale. The complete time interval is shown in the small overview plot. The same waves as in the displacement plot can also been observed, except for the shear wave which brings no volume change and therefore has no effect on the pressure. The Rayleigh wave peak only occurs at $0.5\,\mathrm{m}$ depth.

The most visible feature in the graph are pressure changes due to the fast compressional wave. In the incompressible model, the pressure jumps up at the time when the load is applied ($t = 0\,\mathrm{s}$) and back down when it disappears ($t = 0.004\,\mathrm{s}$). In the compressible results, the peak appears at about $t = 0.015\,\mathrm{s}$. From the internal points considered, the maximum pore pressure reached due to the fast compressional wave is the largest at the deepest observation point. As the load is directional (i.e., not a pure pressure source), this observation can be explained with the changing angle between the vertical load direction and the distance vector from the load to the observation point. For such load, the amplitudes of both longitudinal (compressional) and transverse (shear) waves in a solid depend on propagation direction. Compressional waves propagate with maximum amplitude along the load direction line, and the amplitude decreases as the direction to the observation point declines from this direction. Similarly, shear waves reach the maximum amplitude when propagating in a direction perpendicular to the load.

In Figs. 4.20(a) and 4.20(b), the particle orbits of the points *A* and *B* are plotted. The loop at the beginning (in the upper right corner) corresponds to the fast compressional wave, followed by the elliptical movement typical for the Rayleigh wave. It can be observed that the ratio of the amplitudes of the fast compressional wave (bulk) and of the Rayleigh wave (surface) change with the distance from load. This is a consequence of the difference in geometrical attenuation, resulting in slower amplitude decrease for surface waves.

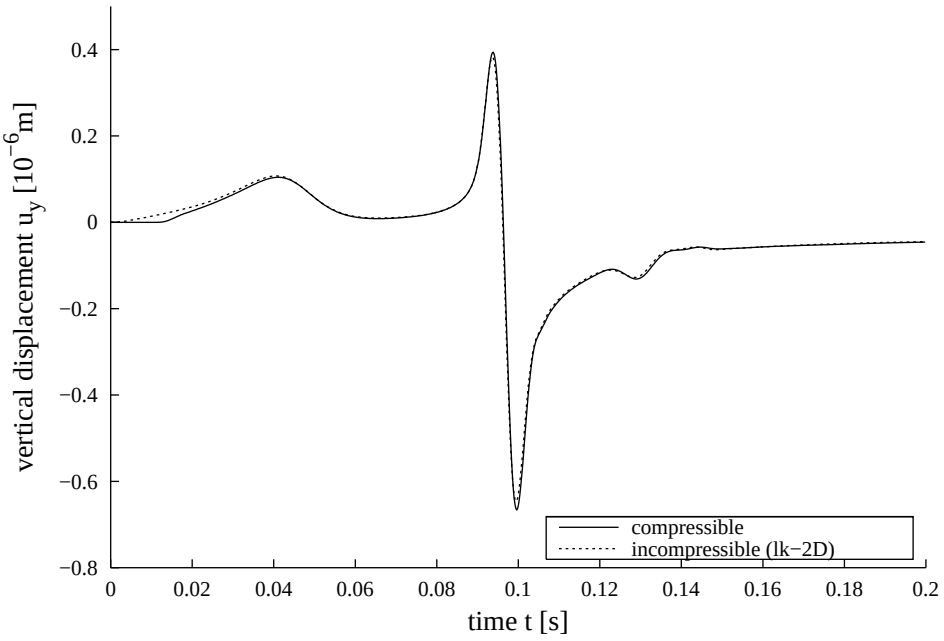

Figure 4.17: Poroelastic soil halfspace in 2-d: Vertical displacement at point *B*

Berea Sandstone Unlike for the soil, the differences between the models with compressible and incompressible constituents are clearly visible for the rock even in the displacement plots. The maximum displacement in Fig. 4.21 is about 30% smaller for the incompressible model. The difference is even larger at point *B* in 20 m distance in Fig. 4.23. These differences support the expectations that this material can not be well modelled assuming incompressible constituents.

The vertical displacement at the surface point *B* and at the internal points in $0.5\,\mathrm{m}, 5\,\mathrm{m}$, and 15 m depth below it is displayed in Fig. 4.24. The fast compressional wave arrival (the first nonzero displacement) can be observed at $t = 0.006\,\mathrm{s}$ for the compressible model (at the internal points, with delays due to the longer distances travelled).

At about $t = 0.012\,\mathrm{s}$, the Rayleigh wave peak appears. For the incompressible model, it causes smaller displacements (see also the particle orbit plot in Figs. 4.26(a) and 4.26(b)), and arrives somewhat earlier compared to the compressible model. That corresponds to a small increase in the propagation speed resulting from the infinite speed of the fast compressional wave. The behavior of the Rayleigh wave peak with increasing depth is very similar to the soil. The amplitude has a maximum near the surface, then decreases. In 5 m depth it effectively disappears and the shear wave becomes visible.

The disturbance arriving at about $t = 0.019\,\mathrm{s}$ ($t = 0.017\,\mathrm{s}$ for the incompressible model) has been identified as a fast compressional wave originating from a reflection of the Rayleigh wave at the end of discretization.

Fig. 4.25, presents the pore pressure results below the surface point *B*. The same waves as in the displacement plot can also been observed, except for the shear wave which brings no volume change and therefore has no effect on the pressure. As for the soil, the increase in the maximum pore pressure reached in the fast compressional wave with increasing depth can be explained with the changing angle

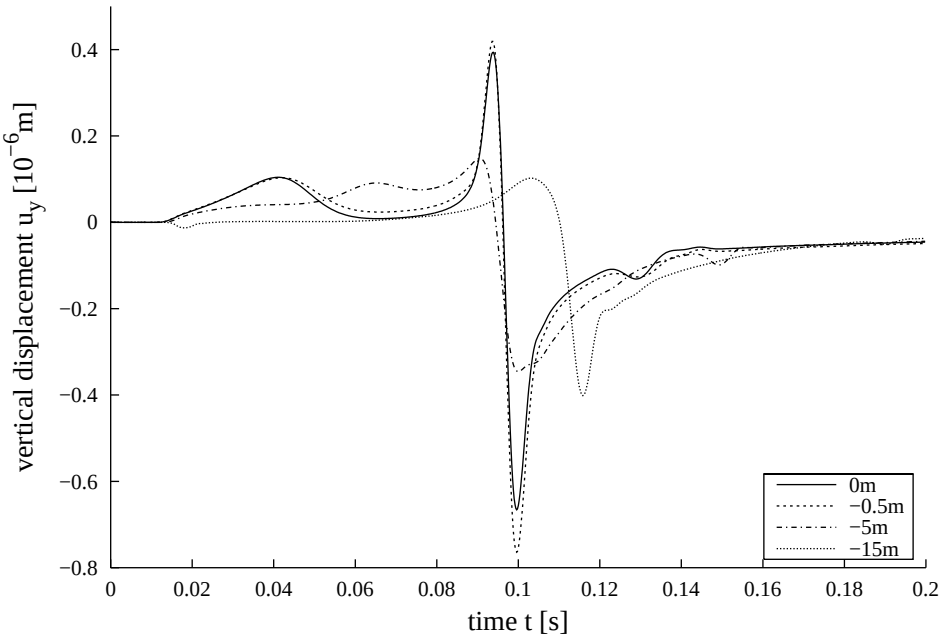

Figure 4.18: Compressible poroelastic soil halfspace in 2-d: Vertical displacement at and below point *B*

to the vertical load direction.

In Figs. 4.26(a) and 4.26(b), the particle orbits of the points *A* and *B* are plotted. The loop of the fast compressional wave is followed by the eliptical trajectory of the Rayleigh wave. As for the soil, the amplitude ratios of the waves change with distance, the bulk wave decreases much faster. Unlike for soil, the difference between the compressible and incompressible models is large. The displacements are much smaller for the incompressible material. The loop of the fast compressional wave is almost a line in the compressible case.

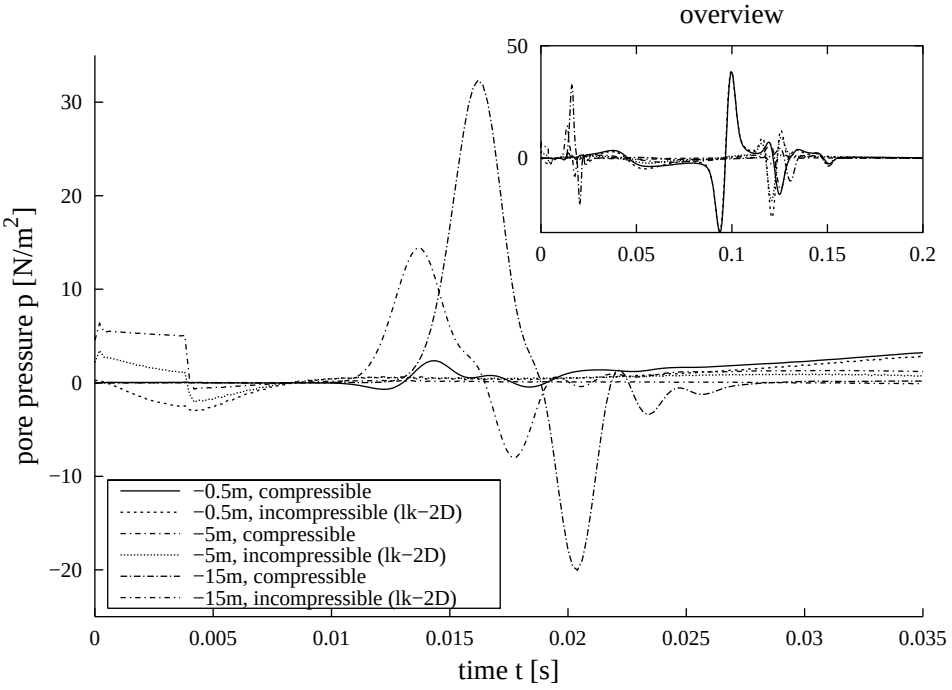

Figure 4.19: Poroelastic soil halfspace in 2-d: Pore pressure at and below point *B*

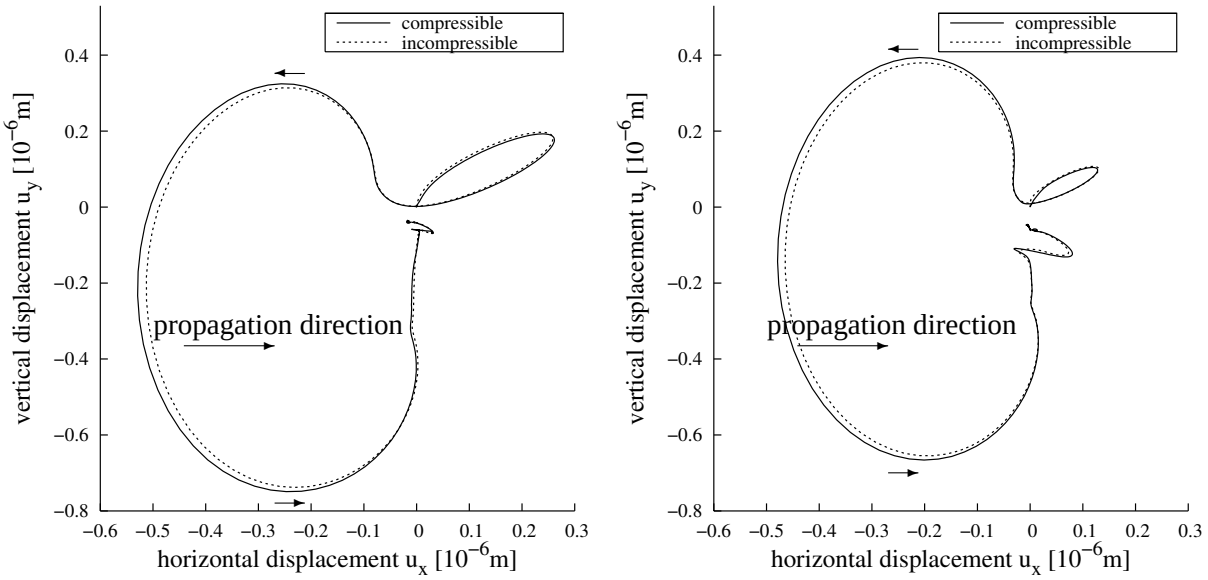

(a) point *A*

(b) point *B*

Figure 4.20: Poroelastic rock halfspace in 2-d: Particle orbits of points *A* and *B*

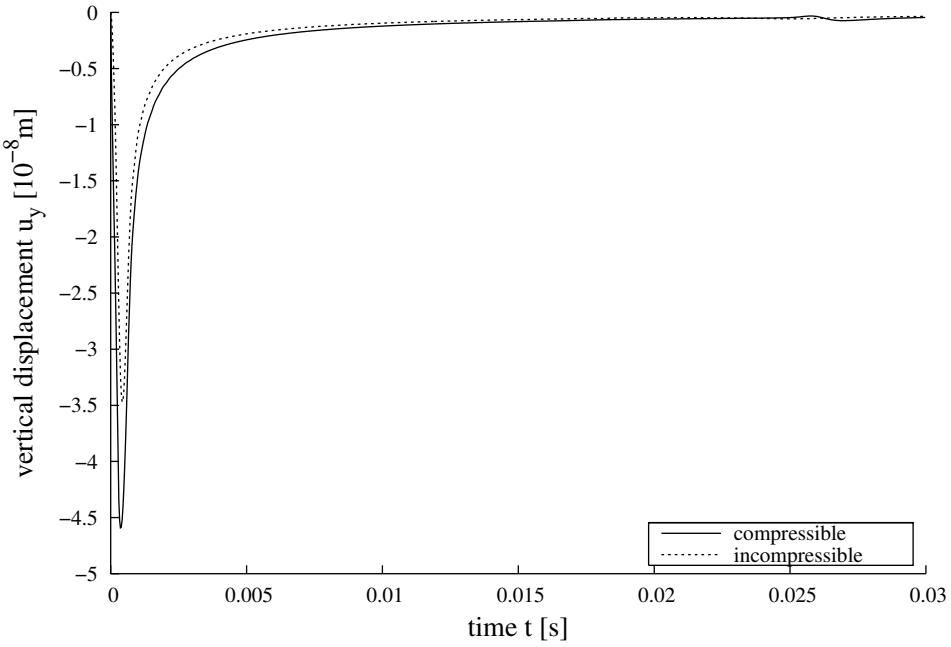

Figure 4.21: Poroelastic rock halfspace in 2-d: Vertical displacement under load

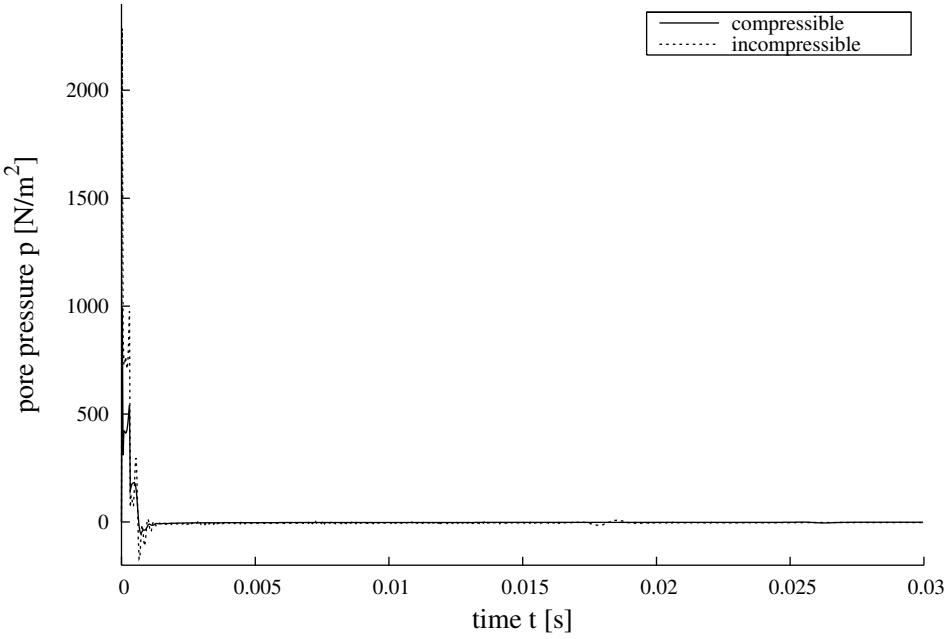

Figure 4.22: Poroelastic rock halfspace in 2-d: Pore pressure under load

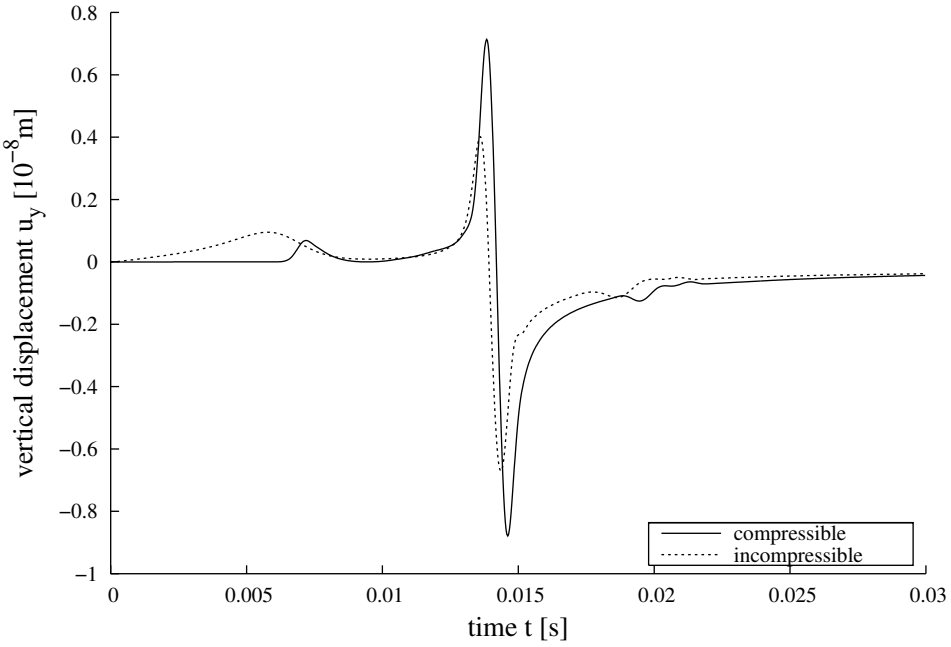

Figure 4.23: Poroelastic rock halfspace in 2-d: Vertical displacement at point *B*

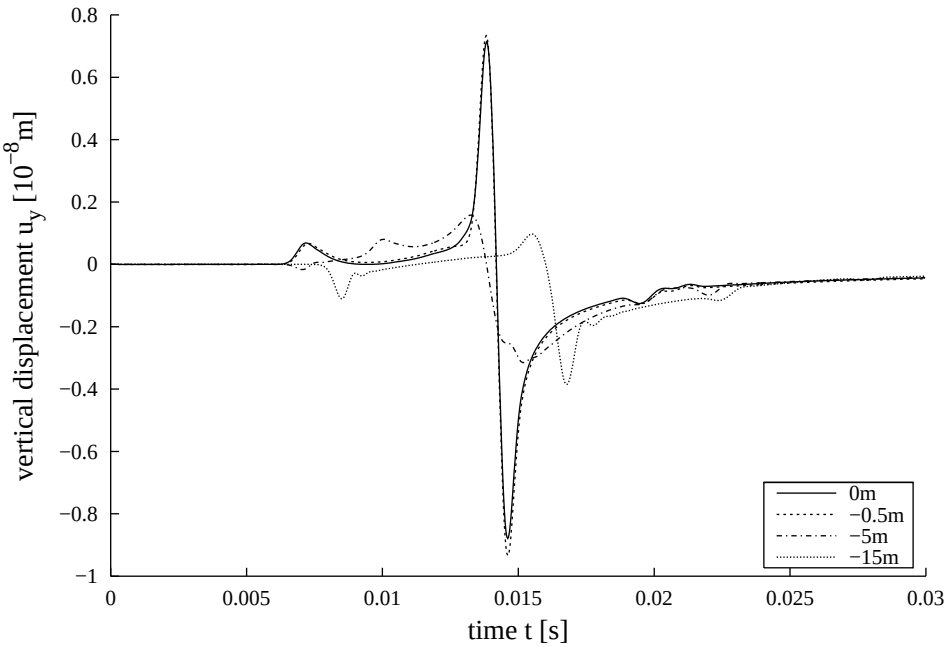

Figure 4.24: Poroelastic rock halfspace in 2-d: Vertical displacement at and below point *B*

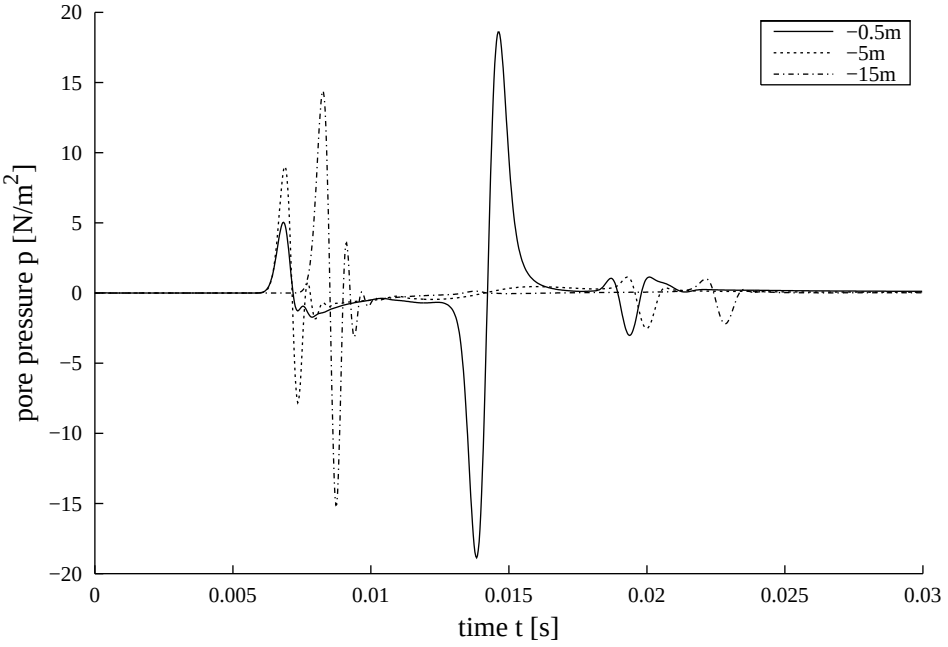

Figure 4.25: Poroelastic rock halfspace in 2-d: Pore pressure at point *B*

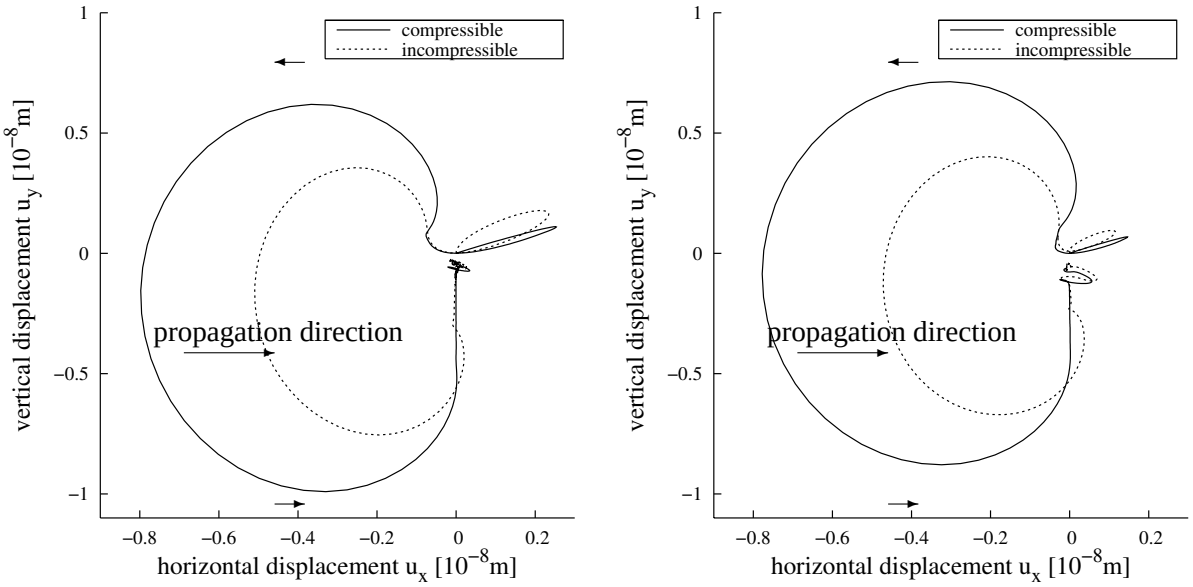

(a) point *A*

(b) point *B*

Figure 4.26: Poroelastic rock halfspace in 2-d: Particle orbits of points *A* and *B*

4.3.2 Comparison to Incompressible TPM FEM

For comparison to a 2-d FEM incompressible TPM formulation [22], the surface wave propagation example from the article has been computed with BEM. The model in Fig. 4.27 has an area of 20 m width and 10 m height. At the left and right boundaries, horizontal displacements are blocked. At the bottom, vertical displacements are blocked. The surface is permeable (pore pressure $p = 0$), the sides and the bottom are impermeable.

The BEM mesh consists of 120 elements on 120 nodes (element length $\frac{1}{2}$ m), the original FEM discretization has 1800 elements (element length $\frac{1}{3}$ m).

The load consists of a single vertical force at the surface midpoint. The force is time dependent

$$\begin{aligned} F(t) = 100\sin(78.54t)\,[\text{kN}] \text{ for } 0 < t < 0.04\,\text{s}, \\ F(t) = 0 \text{ for } t > 0.04\,\text{s}\,, \end{aligned} \tag{4.1}$$

i.e., a half period of the sinus function, starting at $t = 0$ and vanishing at $t = 0.04s$.

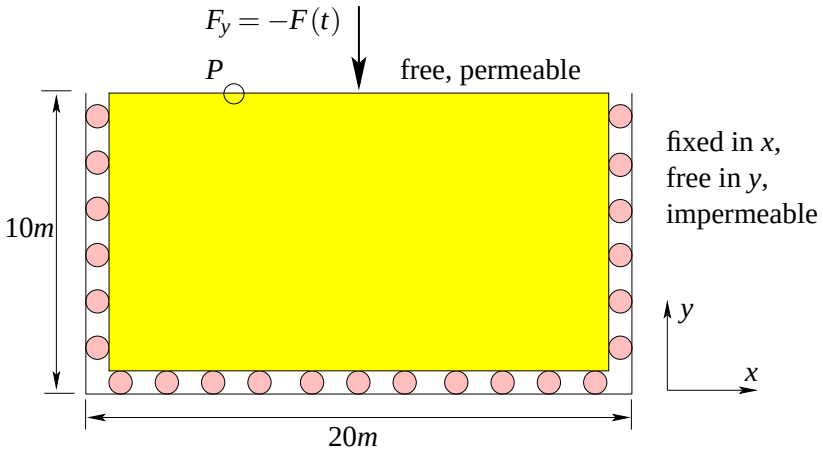

Figure 4.27: Comparison to TPM: Geometry and boundary conditions

According to [87], if the apparent mass density ρ_a is set to zero, the incompressible Biot's theory is equivalent to the incompressible TPM. The material parameters are converted following the equivalence formulas provided in the article and can be found in Tab. 4.1.

$K\,[\frac{N}{m^2}]$	$G\,[\frac{N}{m^2}]$	$\rho\,[\frac{kg}{m^3}]$	$\rho_f\,[\frac{kg}{m^3}]$	ϕ	$\kappa\,[\frac{m^4}{Ns}]$
$1.21 \cdot 10^7$	$5.58 \cdot 10^6$	1670	1000	0.33	$1 \cdot 10^{-6}$

Table 4.1: Comparison to TPM: Material data

The deformed geometry at $t = 0.07s, 0.11s$, and $0.15s$ is shown in Figs. 4.28, 4.29, and 4.30, magnified by a factor of 500. FEM results from [22] are included for comparison. With BEM, additionaly to the boundary, the displacements have been evaluated at 351 internal nodes (9 layers with 1 m vertical spacing, 39 nodes in each layer, distributed equidistantly with $\frac{1}{2}$ m spacing).

The most visible feature in the sequence of pictures is the Rayleigh wave, the two disturbances travelling along the surface in both directions from the load point. The BEM results do not significantly differ from those from FEM. The oscillations near the load point in FEM are probably of numerical (discretization related) origin.

In Fig. 4.31, the particle orbit of the point P at $x = 5\,\mathrm{m}$, $y = 10\,\mathrm{m}$ is plotted for both BEM and FEM [22]. The loop at the beginning (in the upper left corner) corresponds to the fast compressional wave, followed by the elliptical movement typical for the Rayleigh wave. When comparing the FEM and BEM results, note that the scales of the x axis are not identical, that only the Rayleigh wave part of the particle orbit is presented in Fig. 4.31(b), and the sampling in time is much rougher. Again, the FEM and BEM results are qualitatively the same. However, there is a visible difference in the particle orbit plot regarding the horizontal displacement at the end of the inspected time interval. The negative final horizontal displacement in the FEM results might be related to the oscillations visible in the deformations plots near the load.

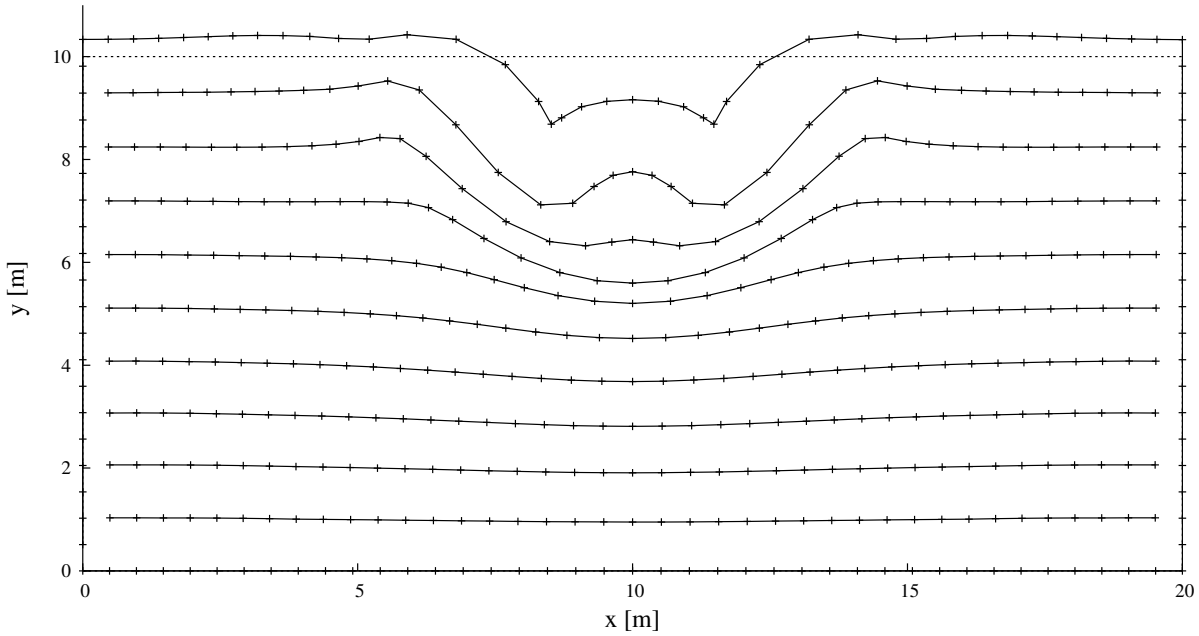

(a) BEM

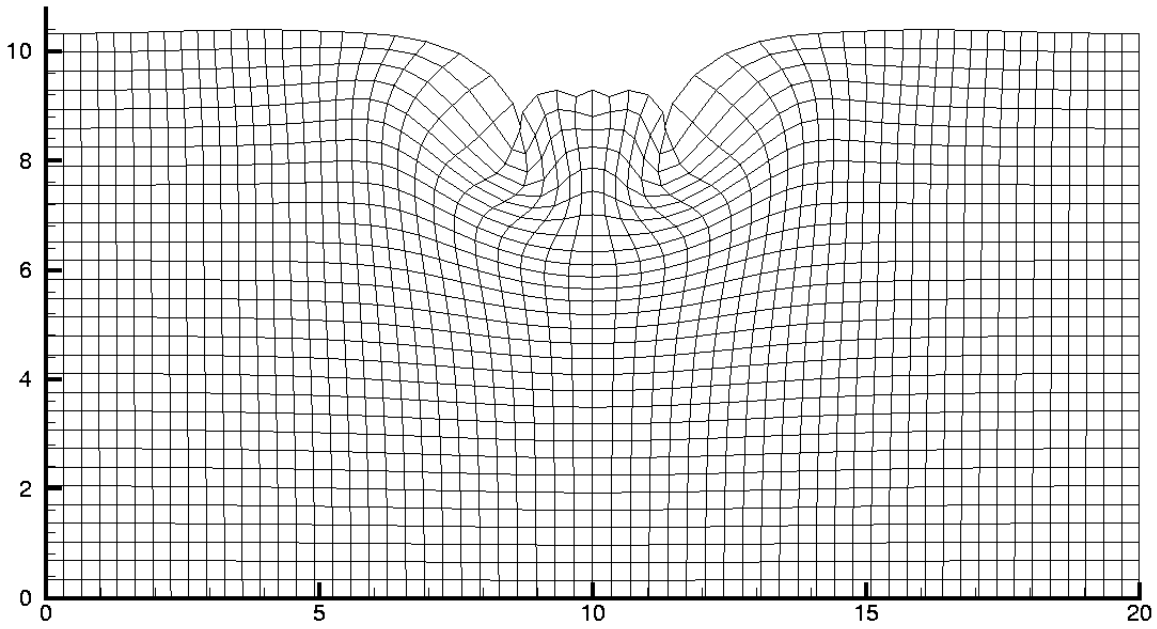

(b) FEM

Figure 4.28: Deformed geometry at $t = 0.07s$, magnification factor 500 (FEM from [22])

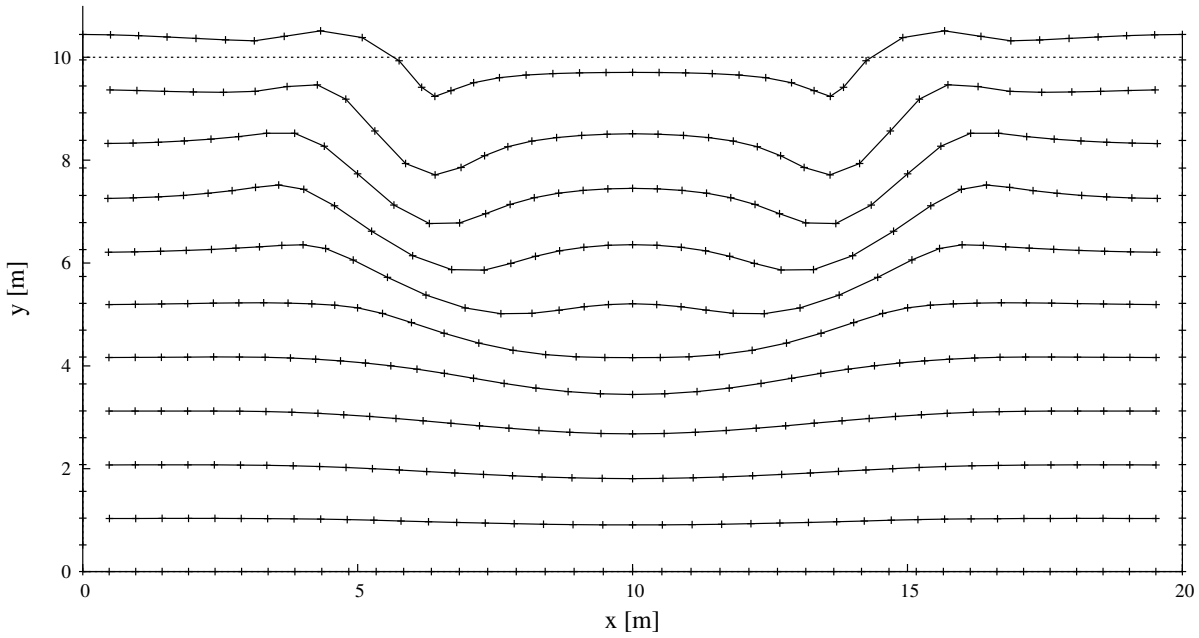

(a) BEM

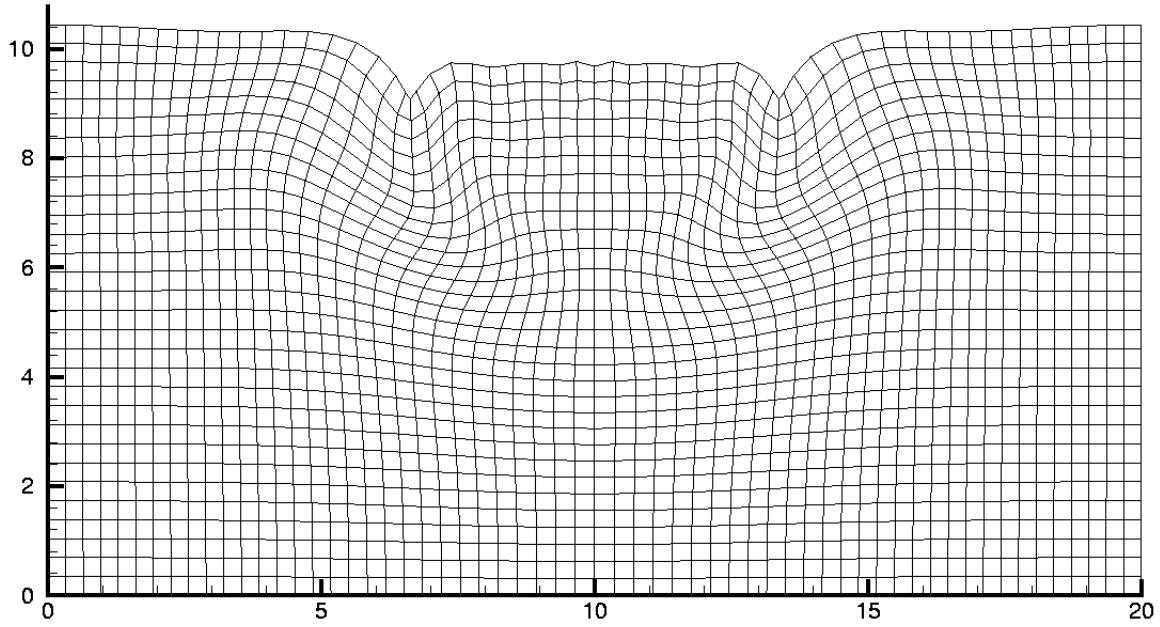

(b) FEM

Figure 4.29: Deformed geometry at $t = 0.11s$, magnification factor 500 (FEM from [22])

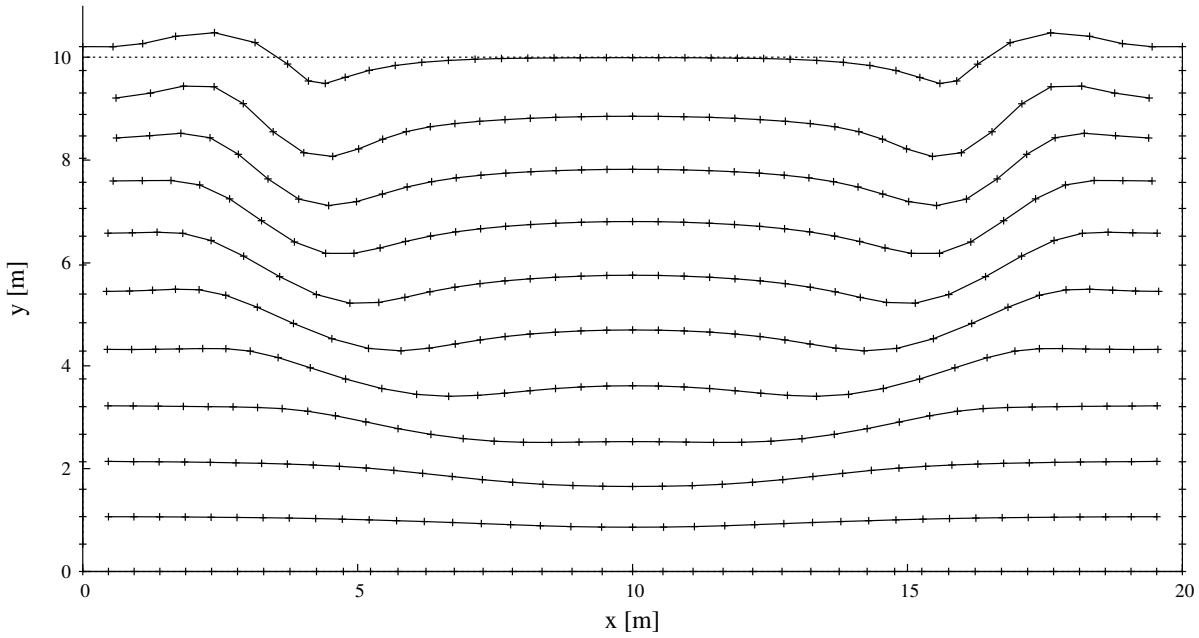

(a) BEM

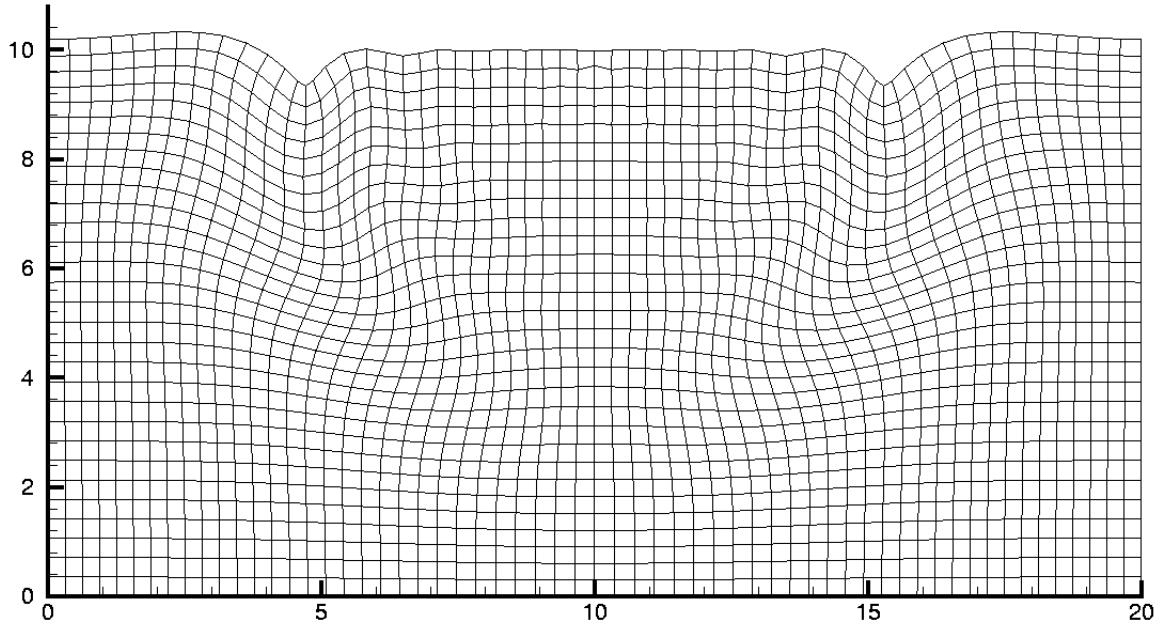

(b) FEM

Figure 4.30: Deformed geometry at $t = 0.15s$, magnification factor 500 (FEM from [22])

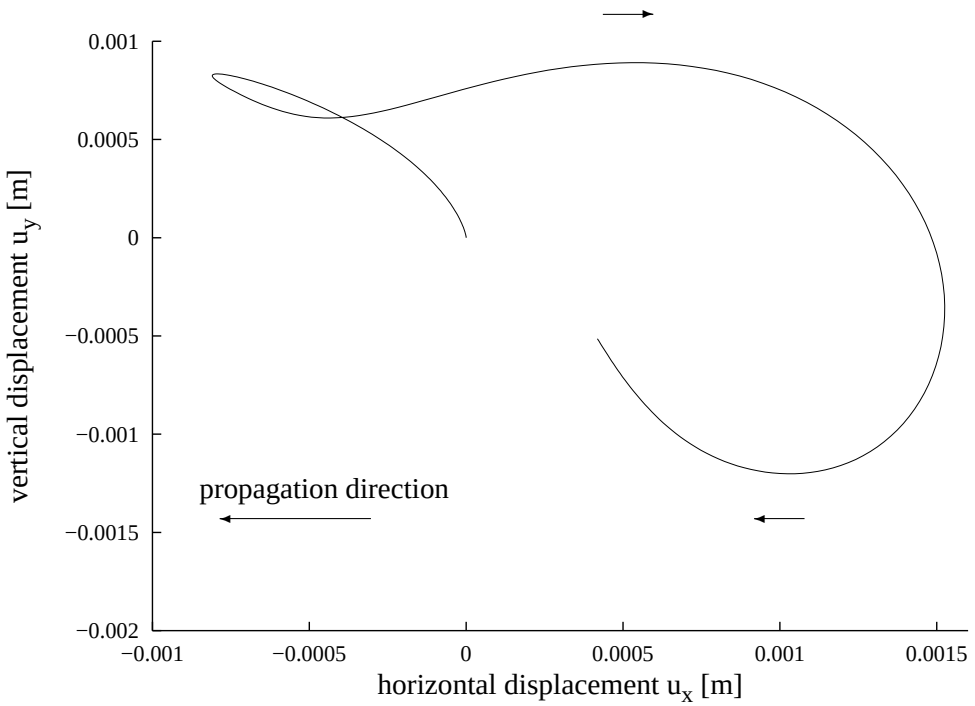

(a) BEM

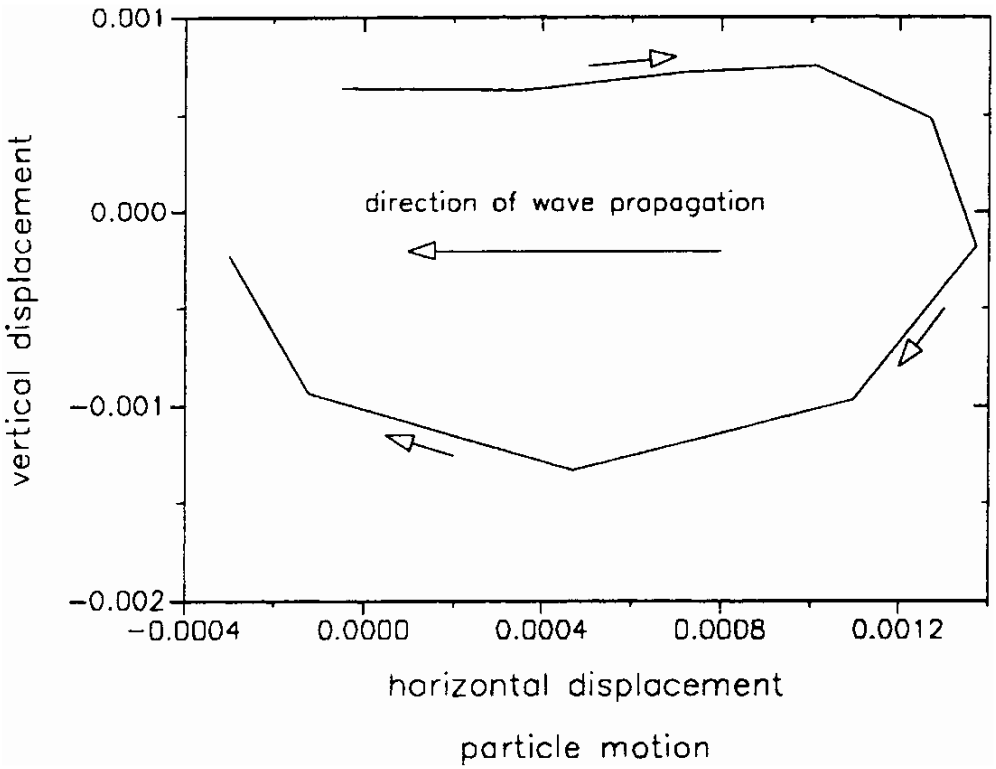

(b) FEM

Figure 4.31: Particle orbit of point P at $x = 5\,\mathrm{m}$, $y = 10\,\mathrm{m}$ (FEM from [22])

4.4 3-d Poroelastic Halfspace

To compare the compressible and incompressible models with respect to wave propagation in a poroelastic halfspace in 3-d, a rectangular surface patch 33 m long and 6 m wide has been discretized with 396 linear triangular elements on 242 nodes, as shown in Fig. 4.32. An area of $1\,\mathrm{m}^2$ is loaded with a vertical traction $t_z = -1000\,\frac{\mathrm{N}}{\mathrm{m}^2}\,H(t)$ applied at $t = 0s$. The rest of the surface is traction free and permeable (zero pore pressure). The material data for soil may be found in Tab. 3.1. As shown before, the rock can not be modeled incompressible and, therefore, it is not considered here any more. Note that the 2-d example in section 4.3 has a different time history of the load.

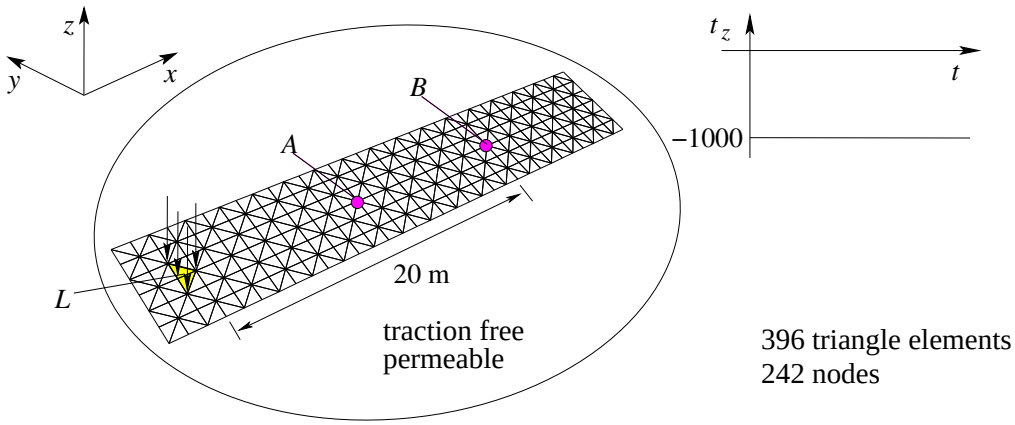

Figure 4.32: 3-d poroelastic halfspace: Geometry, boundary conditions, and discretization

The vertical displacement of point L in the loaded area is displayed against time in Fig. 4.33. It can be observed how the displacement approaches a stationary value (quasi-static solution). There is a small difference between the compressible and incompressible models, which appears at the beginning and then keeps almost unchanged. This may be related to the difference in bulk compressibility corresponding to the constituents compressibility neglected by the incompressible model (infinite fluid and solid compression moduli). The differences from the 2-d example in section 4.3.1 originate from the different load geometry[2] and time history.

The vertical displacements at the surface point B (20 m from the loaded area) and in 5 m, 10 m, and 15 m depth underneath it are plotted against time in Fig. 4.34. Two wave arrivals can be clearly distinguished, the fast compressional wave at about $t = 0.01s$ ($t = 0s$ in the incompressible model, due to the infinite propagation speed of the fast compressional wave) and the Rayleigh wave at about $t = 0.1s$.

Displacement changes with depth can be observed. At the surface, the fast compressional wave causes a movement with upward vertical component (see also the particle orbit plot in Fig. 4.36(a)). On the other hand, at the internal points, the vertical component is directed downwards, following the radiation direction from the loaded area. The amplitude of the Rayleigh wave peak at about $t = 0.1s$ decreases with increasing depth, as expected for a surface wave.

The pore pressure results under the surface point B, in depths from 5 m to 15 m, are presented in Fig. 4.35. Unlike in the displacement results, the difference between the compressible and incompressible models is clearly visible for the pore pressure. The fast compressional wave arrives at about $t = 0.01s$ in the case

[2] The 2-d load would correspond to an infinite width of the loaded area in 3-d (plain strain).

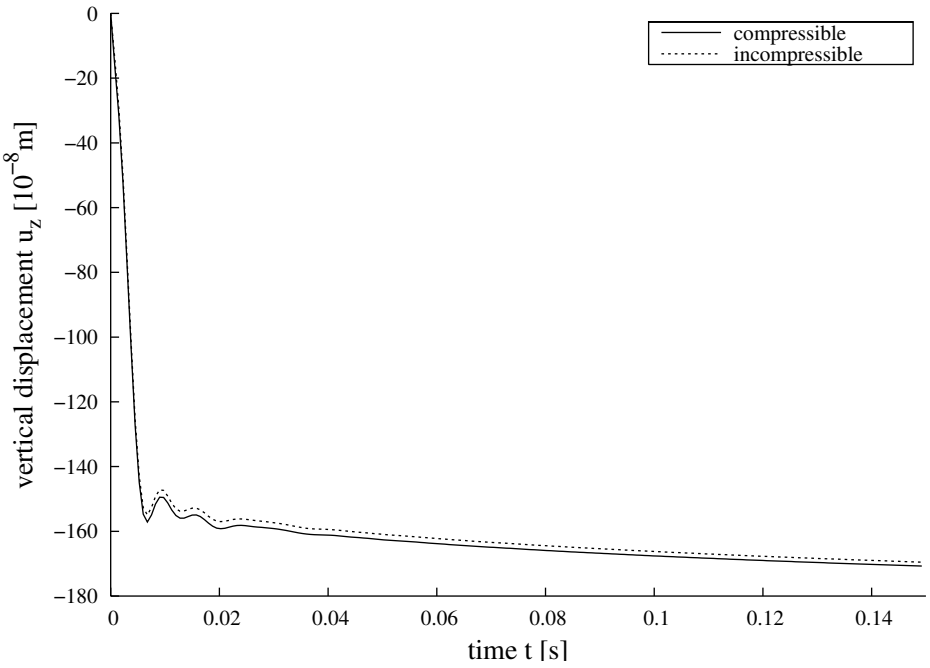

Figure 4.33: Poroelastic halfspace in 3-d: Vertical displacement at point L under load

of the compressible model, first to the point closest to the surface, later to the internal points due to the longer distance from the loaded area. In the incompressible case, the pulse arrives at $t = 0s$, regardless of distance, and reaches a higher maximum compared to the compressible model. At the point at 5 m depth, the effect of the Rayleigh wave is visible (at about $t = 0.1s$, see also Fig. 4.34). As expected, this effect disappears with increasing depth.

In Fig. 4.36, the trajectories of the particles in the vertical $(x-z)$ plane (particle orbits) are plotted for the points A and B. The straight line at the beginning (in the upper right part of the graph) corresponds to the fast compressional wave, followed by the elliptical movement typical for the Rayleigh wave. The curve ends near the long time (quasi-static) displacement. The absolute displacements are smaller for the more distant point B. It can be observed that the ratio of the amplitudes of the fast compressional wave (bulk) and of the Rayleigh wave (surface) change with the distance from load. This is a consequence of the difference in geometrical attenuation, resulting in slower amplitude decrease for surface waves.

The difference between the compressible and incompressible models is most apparent in the region corresponding to the fast compressional wave. Besides that, the deformations are marginally smaller in the case of the incompressible constituents. Both differences follow expectations.

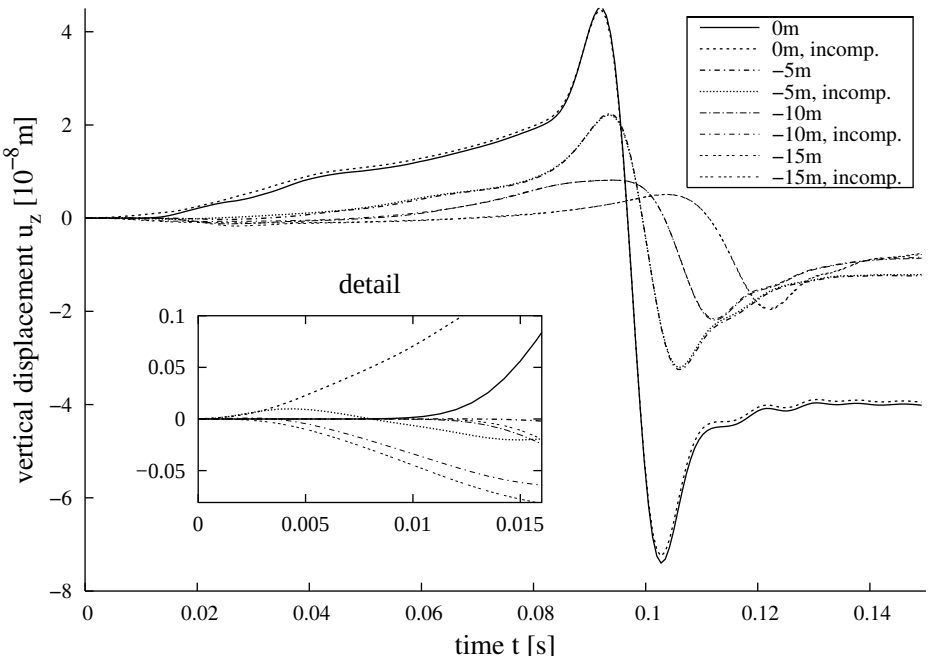

Figure 4.34: Poroelastic halfspace in 3-d: Vertical displacement at point *B*

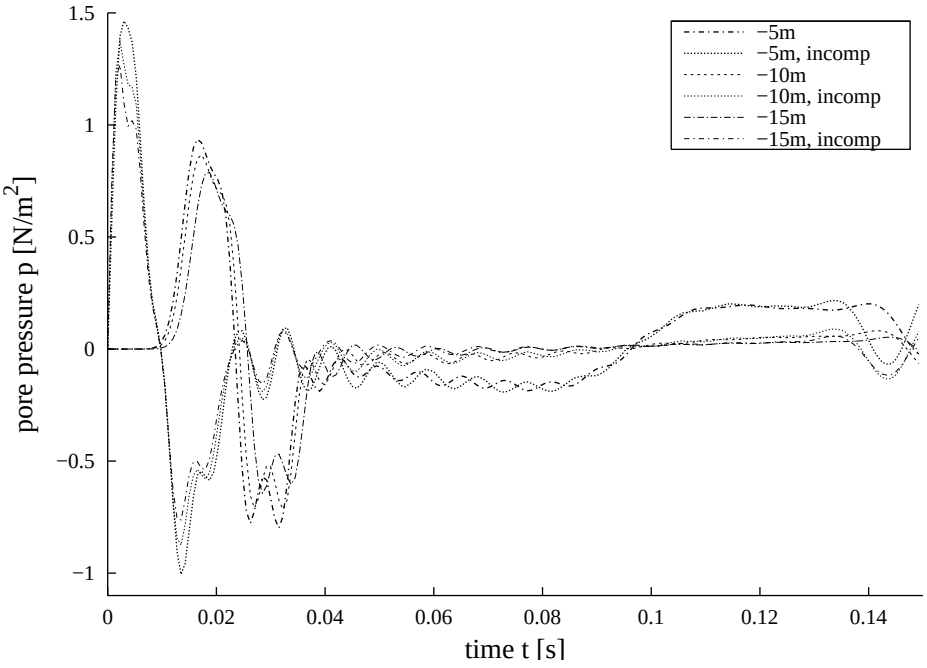

Figure 4.35: Poroelastic halfspace in 3-d: Pore pressure under point *B*

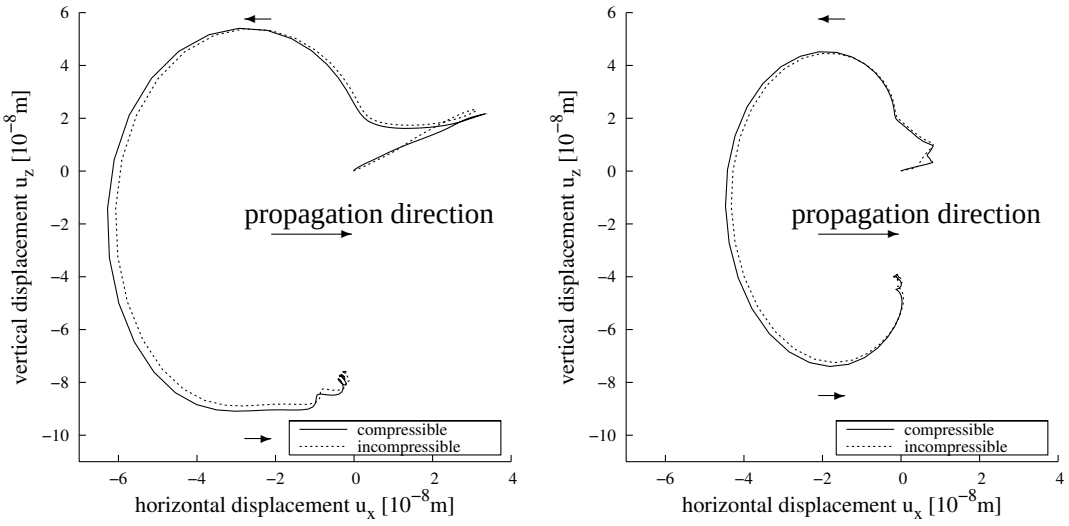

(a) Particle orbit of point *A*

(b) Particle orbit of point *B*

Figure 4.36: Poroelastic halfspace in 3-d: Particle orbits of points *A* and *B*

Conclusions

The existing time dependent 3-d BEM implementation for Biot's theory of poroelasticity based on the Convolution Quadrature Method has been further developed and extended. Support for 2-d problems has been added, utilizing available fundamental solutions. Fundamental solutions for incompressible poroelasticity have been developed in both 2-d and 3-d, and implemented in the program. Further, mixed elements combining linear and constant shape functions have been added and their numerical behavior has been compared to isoparametric elements. The program has been validated on examples for which analytical solutions are available. Finally, the numerical model has been used to study wave propagation in poroelastic materials, concentrating on the influence of material incompressibility on various wave types in semi-infinite domains.

Incompressible constituents Based on Biot's theory, in the present work, fundamental solutions for the special case of incompressible constituents are deduced and compared to the fundamental solutions of the compressible case. This has been done not only for the representation with the solid displacement and the pore pressure as unknowns, but also for the solid displacement and fluid displacement formulation. For both representations, different models for incompressible constituents are given. The fundamental solutions are determined using Hörmander's method.

The derivation of the fundamental solutions has reconfirmed the known fact that the solid displacements and the pore pressure are sufficient for describing the behavior of a poroelastic continuum. Further, it has been shown that the incompressible model based on the solid and fluid displacement formulation is not suited to describe the dynamic behavior of a poroelastic medium. In general, in an incompressible model an infinite wave speed of the fast compressional wave is assumed. Hence, the question arises whether such an approximation makes sense in a wave propagation calculation. The presented fundamental solutions show differences for higher frequencies, i.e., short times, in comparison to the compressible model. Therefore, it can be concluded that an incompressible model can only be used in wave propagation problems if not the short time behavior is considered and also if the ratios of the compression moduli of the solid and fluid are very small compared to the frame (drained) compression modulus.

The developed fundamental solutions have been implemented in the BEM program and tested on examples resembling a 1-d problem with a known analytical solution. Numerical experiments have been conducted to study the suitability and limits of the incompressible model for two different materials. The tests confirmed the expectations. Assuming both constituents are incompressible, the propagation speed of the fast compressional wave becomes infinite, the slow compressional wave speed changes, and the shear wave remains unchanged. The amplitude of the Rayleigh wave decreases and its propagation speed slightly increases. The incompressible model also changes the steady state (consolidation) displacement (to the extent that the initial short-time difference does not disappear).

For some materials (e.g., loose grain with fluid), where there are no noticeable differences between the compressible and incompressible models, the incompressible model can be recommended to achieve better performance. The speedup compared to the compressible computation is problem dependent. In the examples the computation time decreased about 20% in 3-d and about 15% in 2-d cases.

Mixed elements Mixed linear-constant elements have been implemented in both 2-d and 3-d BEM. The results are compared to those of isoparametric linear elements. In 2-d, the difference in CPU time extends by a factor of 1.3 compared to linear isoparametric elements. However the (negligeably) shorter possible time step (as in other time dependent BEM implementations, the timestep has to be longer than a limiting value to achieve a stable computation) does not bring any noticeable improvement to the results for the compressible model. The difference is more pronounced for the incompressible model, where the mixed element, in at least some cases, offers a considerable reduction of the lower stability limit and less oscillatory behavior near the limit.

In most of the 3-d tests, the mixed element is worse than the isoparametric in terms of both the quality of numerical results and the stability. At best minor improvements have been observed in the quality of numerical results, but the computation time extends by a factor of 1.7 due to the increase in the total degrees of freedom. In this case, the advantages clearly do not correspond to the increased computational costs, as one can achieve better results with the same effort using a finer discretization with linear isoparametric elements. This corresponds to the conclusions in the reference [92].

Wave propagation in poroelastic halfspace The BEM implementation has been used to study wave propagation in a poroelastic halfspace in both 2-d and 3-d. Not only the bulk waves, but also the Rayleigh wave traveling along the free surface have been captured. As predicted by the theory, the amplitude of the Rayleigh wave is maximum near the surface and then attenuates exponentially with increasing depth. To model interface waves or interaction with a structure, an efficient domain coupling method needs to be added to the implementation.

The extended Boundary Element program has been tested and can solve wave propagation problems in poroelastic materials with compressible or incompressible constituents in both two and three dimensions. For future development of the BEM program, it may be possible to accelerate the computation by implementing the Fast Multipole Method, Adaptive Cross Approximation (ACA), or some other far field approximation technique. A Galerkin formulation may also be considered to better handle the singularities and eventually bring a faster convergence rate and extend the stability region.

A Explicit Expressions for the Fundamental Solutions

The explicit expressions of the poroelastodynamic fundamental solutions for the unknowns solid displacements u_i^s and pore pressure p and for solid displacements and fluid displacements u_i^s and u_i^f are given in the following for a 2-d and a 3-d continuum, for compressible as well as incompressible constituents.

A.1 Unknown Solid Displacements u_i^s and Pore Pressure p (u_i^s-p-model)

A.1.1 Compressible Model

3-d The elements of the matrix $\mathbf{G4}^{comp}$ (1.42) are the displacements caused by a Dirac force in the solid

$$\hat{U}_{ij}^s = \frac{1}{4\pi r\left(\rho-\beta\rho_f\right)s^2}\left[R_1\frac{\lambda_4^2-\lambda_2^2}{\lambda_1^2-\lambda_2^2}e^{-\lambda_1 sr} - R_2\frac{\lambda_4^2-\lambda_1^2}{\lambda_1^2-\lambda_2^2}e^{-\lambda_2 sr} + \left(\delta_{ij}\lambda_3^2 s^2 - R_3\right)e^{-\lambda_3 sr}\right] \tag{A.1a}$$

with $R_k = \left(3r_{,i}r_{,j}-\delta_{ij}\right)/r^2 + \lambda_k s\left(3r_{,i}r_{,j}-\delta_{ij}\right)/r + \lambda_k^2 s^2 r_{,i}r_{,j}$ and
$\lambda_4^2 = \left(\rho-\beta\rho_f\right)/\left(K+4/3\,G\right)$. The pressure caused by the same load is

$$\hat{P}_j^s = \frac{\left(\alpha-\beta\right)\rho_f r_{,j}}{4\pi\beta s\left(K+\frac{4}{3}G\right)r\left(\lambda_1^2-\lambda_2^2\right)}\left[\left(\lambda_1 s+\frac{1}{r}\right)e^{-\lambda_1 sr} - \left(\lambda_2 s+\frac{1}{r}\right)e^{-\lambda_2 sr}\right]. \tag{A.1b}$$

For a Dirac source in the fluid the respective displacement solution is

$$\hat{U}_i^f = s\hat{P}_i^s \tag{A.1c}$$

and the pressure

$$\hat{P}^f = \frac{s\rho_f}{4\pi r\beta\left(\lambda_1^2-\lambda_2^2\right)}\left[\left(\lambda_1^2-\lambda_4^2\right)e^{-\lambda_1 sr} - \left(\lambda_2^2-\lambda_4^2\right)e^{-\lambda_2 sr}\right]. \tag{A.1d}$$

In the above given solutions, the roots $\lambda_i,\ i=1,2,3$ from (1.37) are used.

In the derivation of the poroelastodynamic boundary integral equation (2.9) several abbreviations (2.7) corresponding to an *adjoint* traction or flux are introduced. First, the *adjoint* traction solution is presented. However, due to the extensive expression only parts are given

$$\hat{T}_{ij}^s = \left[\left(\left(K-\frac{2}{3}G\right)\hat{U}_{kj,k}^s + \alpha s\hat{P}_j^s\right)\delta_{i\ell} + G\left(\hat{U}_{ij,\ell}^s + \hat{U}_{\ell j,i}^s\right)\right]n_\ell \tag{A.2}$$

$$\hat{U}^s_{kj,k}\delta_{i\ell}n_\ell = \frac{r_{,j}n_i}{4\pi r\left(\rho-\beta\rho_f\right)\left(\lambda_1^2-\lambda_2^2\right)}\left[e^{-\lambda_1 sr}\left(\frac{1}{r}+s\lambda_1\right)\lambda_1^2\left(\lambda_2^2-\lambda_4^2\right)\right.$$
$$\left.-e^{-\lambda_2 sr}\left(\frac{1}{r}+s\lambda_2\right)\lambda_2^2\left(\lambda_1^2-\lambda_4^2\right)\right]$$

$$\begin{aligned}&\left(\hat{U}^s_{ij,\ell}+\hat{U}^s_{\ell j,i}\right)n_\ell\\ &=\frac{1}{4\pi r\left(\rho-\beta\rho_f\right)}\left[\frac{6R_5}{s^2r^3}\left(\frac{\lambda_4^2-\lambda_2^2}{\lambda_1^2-\lambda_2^2}e^{-\lambda_1 sr}-\frac{\lambda_4^2-\lambda_1^2}{\lambda_1^2-\lambda_2^2}e^{-\lambda_2 sr}-e^{-\lambda_3 sr}\right)\right.\\ &\quad+\frac{6R_5}{sr^2}\left(\frac{\lambda_4^2-\lambda_2^2}{\lambda_1^2-\lambda_2^2}\lambda_1e^{-\lambda_1 sr}-\frac{\lambda_4^2-\lambda_1^2}{\lambda_1^2-\lambda_2^2}\lambda_2e^{-\lambda_2 sr}-\lambda_3e^{-\lambda_3 sr}\right)\\ &\quad+\frac{2R_6}{r}\left(\frac{\lambda_4^2-\lambda_2^2}{\lambda_1^2-\lambda_2^2}\lambda_1^2e^{-\lambda_1 sr}-\frac{\lambda_4^2-\lambda_1^2}{\lambda_1^2-\lambda_2^2}\lambda_2^2e^{-\lambda_2 sr}-\lambda_3^2e^{-\lambda_3 sr}\right)\\ &\quad-2sr_{,n}r_{,i}r_{,j}\left(\frac{\lambda_4^2-\lambda_2^2}{\lambda_1^2-\lambda_2^2}\lambda_1^3e^{-\lambda_1 sr}-\frac{\lambda_4^2-\lambda_1^2}{\lambda_1^2-\lambda_2^2}\lambda_2^3e^{-\lambda_2 sr}-\lambda_3^3e^{-\lambda_3 sr}\right)\\ &\quad\left.-\lambda_3^2\left(\delta_{ij}r_{,n}+r_{,i}n_j\right)\left(s\lambda_3+\frac{1}{r}\right)e^{-\lambda_3 sr}\right]\end{aligned}$$

with $R_5 = r_{,j}n_i + r_{,i}n_j + r_{,n}\left(\delta_{ij}-5r_{,i}r_{,j}\right)$ and $R_6 = r_{,j}n_i + r_{,i}n_j + r_{,n}\left(\delta_{ij}-6r_{,i}r_{,j}\right)$. The other explicit expressions are

$$\hat{Q}^s_j = \frac{n_i}{4\pi r\left(\rho-\beta\rho_f\right)s^2}\left[\frac{e^{-\lambda_1 sr}}{\lambda_1^2-\lambda_2^2}R_1\left(\beta\lambda_2^2-\alpha\lambda_4^2\right)-\frac{e^{-\lambda_2 sr}}{\lambda_1^2-\lambda_2^2}R_2\left(\beta\lambda_1^2-\alpha\lambda_4^2\right)\right.\tag{A.3}$$
$$\left.+\beta e^{-\lambda_3 sr}\left(R_3-\delta_{ij}s^2\lambda_3^2\right)\right]$$

$$\begin{aligned}\hat{T}_i^f = \frac{\rho_f}{4\pi r\beta\left(\lambda_1^2-\lambda_2^2\right)}&\left[\frac{n_j\left(\alpha-\beta\right)2G}{K+\frac{4}{3}G}\left(R_2e^{-\lambda_2 sr}-R_1e^{-\lambda_1 sr}\right)\right.\\ &+s^2n_i\left\{\frac{\left(\alpha-\beta\right)\left(K-\frac{2}{3}G\right)}{K+\frac{4}{3}G}\left(\lambda_2^2e^{-\lambda_2 sr}-\lambda_1^2e^{-\lambda_1 sr}\right)\right.\\ &\left.\left.+\alpha\left[\left(\lambda_1^2-\lambda_4^2\right)e^{-\lambda_1 sr}-\left(\lambda_2^2-\lambda_4^2\right)e^{-\lambda_2 sr}\right]\right\}\right]\end{aligned}\tag{A.4}$$

$$\begin{aligned}\hat{Q}^f = \frac{r_{,n}}{4\pi r\left(\lambda_1^2-\lambda_2^2\right)}&\left[\left(s\lambda_2+\frac{1}{r}\right)\left(\lambda_2^2-\lambda_4^2\frac{\rho-\alpha\rho_f}{\rho-\beta\rho_f}\right)e^{-\lambda_2 sr}\right.\\ &\left.-\left(s\lambda_1+\frac{1}{r}\right)\left(\lambda_1^2-\lambda_4^2\frac{\rho-\alpha\rho_f}{\rho-\beta\rho_f}\right)e^{-\lambda_1 sr}\right].\end{aligned}\tag{A.5}$$

Note that as R_k contain terms indexed with i and j, the Einstein summation convention is used where R_k is multiplied with another term containing some of these indices, e.g., with n_i.

2-d In 2-d, the expressions for displacements induced by a force in the solid are

$$\hat{U}_{ij}^s = \frac{1}{2\pi s^2(\rho-\beta\rho_f)}\left[\frac{\lambda_4^2-\lambda_2^2}{\lambda_1^2-\lambda_2^2}R_1^{2d} - \frac{\lambda_4^2-\lambda_1^2}{\lambda_1^2-\lambda_2^2}R_2^{2d} - R_3^{2d} + \delta_{ij}s^2\lambda_3^2 K_0(\lambda_3 sr)\right] \tag{A.6a}$$

and the pressure for the same load is

$$\hat{P}_j^s = \frac{\rho_f(\alpha-\beta)r_{,i}}{2\pi\beta}\,\frac{K_1(\lambda_1 sr)\lambda_1 - K_1(\lambda_2 sr)\lambda_2}{(\lambda_1^2-\lambda_2^2)(K+\frac{4}{3}G)}\,. \tag{A.6b}$$

The roots λ_i, $i=1,2,3$ are the same as in the 3-d case (1.37). The displacement fundamental solution for a source in the fluid is

$$\hat{U}_i^f = s\hat{P}_j^s \tag{A.6c}$$

and the pressure solution is

$$\hat{P}^f = \frac{s\rho_f}{2\pi\beta}\,\frac{(\lambda_1^2-\lambda_4^2)K_0(\lambda_1 sr) - (\lambda_2^2-\lambda_4^2)K_0(\lambda_2 sr)}{\lambda_1^2-\lambda_2^2}\,. \tag{A.6d}$$

The abbreviation $R_k^{2d} = \frac{2r_{,i}r_{,j}-\delta_{ij}}{r}\lambda_k sK_1(\lambda_k sr) + r_{,i}r_{,j}s^2\lambda_k^2 K_0(\lambda_k sr)$ is used in equations (A.6). Further, K_0 and K_1 denote the modified Bessel functions of second kind.

The explicit formulas for the adjoint tractions and flux are

$$\begin{aligned}
\hat{T}_{ij}^s = \frac{1}{\pi}\Bigg(&\frac{sr_{,j}n_i}{2(\lambda_1^2-\lambda_2^2)(\rho-\beta\rho_f)}(K-\frac{2}{3}G)\Big(\lambda_1^3K_1(\lambda_1 sr)(\lambda_2^2-\lambda_4^2) - \lambda_2^3K_1(\lambda_2 sr)(\lambda_1^2-\lambda_4^2)\Big)\\
&+\frac{r_{,j}n_i\alpha s\rho_f(\alpha-\beta)}{2(K+\frac{4}{3}G)\beta(\lambda_1^2-\lambda_2^2)}\Big(\lambda_1K_1(\lambda_1 sr) - \lambda_2K_1(\lambda_2 sr)\Big)\\
&+\frac{\lambda_4^2-\lambda_2^2}{\lambda_3^2(\lambda_1^2-\lambda_2^2)}\left(\frac{R_7}{r}\lambda_1\Big(\lambda_1K_0(\lambda_1 sr) + \frac{2K_1(\lambda_1 sr)}{sr}\Big) - r_{,i}r_{,j}r_{,n}s\lambda_1^3K_1(\lambda_1 sr)\right)\\
&-\frac{\lambda_4^2-\lambda_1^2}{\lambda_3^2(\lambda_1^2-\lambda_2^2)}\left(\frac{R_7}{r}\lambda_2\Big(\lambda_2K_0(\lambda_2 sr) + \frac{2K_1(\lambda_2 sr)}{sr}\Big) - r_{,i}r_{,j}r_{,n}s\lambda_2^3K_1(\lambda_2 sr)\right)\\
&-\frac{R_7}{r\lambda_3}\Big(\lambda_3K_0(\lambda_3 sr) + \frac{2K_1(\lambda_3 sr)}{sr}\Big) - \frac{r_{,n}(\delta_{ij}-2r_{,i}r_{,j}) + r_{,i}n_j}{2}s\lambda_3K_1(\lambda_3 sr)\Bigg)
\end{aligned} \tag{A.7a}$$

$$\begin{aligned}
\hat{Q}_j^s = \frac{1}{2\pi(\rho-\beta\rho_f)}\Bigg(&\frac{r_{,j}r_{,n}}{\lambda_1^2-\lambda_2^2}\Big(\lambda_1^2(\beta\lambda_2^2-\alpha\lambda_4^2)K_0(\lambda_1 sr) - \lambda_2^2(\beta\lambda_1^2-\alpha\lambda_4^2)K_0(\lambda_2 sr)\Big)\\
&+\frac{2r_{,n}r_{,j}-n_j}{(\lambda_1^2-\lambda_2^2)sr}\Big(\lambda_1(\beta\lambda_2^2-\alpha\lambda_4^2)K_1(\lambda_1 sr) - \lambda_2(\beta\lambda_1^2-\alpha\lambda_4^2)K_1(\lambda_2 sr)\Big)\\
&+\beta\Big(\frac{2r_{,n}r_{,j}-n_j}{sr}\lambda_3K_1(\lambda_3 sr) + (r_{,n}r_{,j}-n_j)\lambda_3^2K_0(\lambda_3 sr)\Big)\Bigg)
\end{aligned} \tag{A.7b}$$

$$\begin{aligned}\hat{T}_i^f = & \frac{\rho_f}{2\pi(K+\frac{4}{3}G)\beta(\lambda_1^2-\lambda_2^2)} \\ & \Bigg(2r_{,i}r_{,n}(\alpha-\beta)G\Big(\big(s^2\lambda_2^2K_0(\lambda_2 sr)+\frac{s\lambda_2}{r}K_1(\lambda_2 sr)\big)-\big(s^2\lambda_1^2K_0(\lambda_1 sr)+\frac{s\lambda_1}{r}K_1(\lambda_1 sr)\big)\Big) \\ & -2(n_i-r_{,i}r_{,n})(\alpha-\beta)Gs\Big(\frac{\lambda_2}{r}K_1(\lambda_2 sr)-\frac{\lambda_1}{r}K_1(\lambda_1 sr)\Big) \\ & +n_is^2\Big((\alpha-\beta)(K-\frac{2}{3}G)\lambda_2^2-\alpha(K+\frac{4}{3}G)(\lambda_2^2-\lambda_4^2)\Big)K_0(\lambda_2 sr) \\ & -n_is^2\Big((\alpha-\beta)(K-\frac{2}{3}G)\lambda_1^2-\alpha(K+\frac{4}{3}G)(\lambda_1^2-\lambda_4^2)\Big)K_0(\lambda_1 sr)\Bigg)\end{aligned} \tag{A.7c}$$

$$\hat{Q}^f = \frac{s\,r_{,n}}{2\pi(\lambda_1^2-\lambda_2^2)}\left(\Big(\frac{\rho-\alpha\rho_f}{\rho-\beta\rho_f}\lambda_4^2-\lambda_1^2\Big)\lambda_1K_1(\lambda_1 sr)-\Big(\frac{\rho-\alpha\rho_f}{\rho-\beta\rho_f}\lambda_4^2-\lambda_2^2\Big)\lambda_2K_1(\lambda_2 sr)\right), \tag{A.7d}$$

where $R_7 = r_{,n}(\delta_{ij}-4r_{,i}r_{,j})+r_{,j}n_i+r_{,i}n_j$ and the derivative of the distance vector in direction of the boundary normal $r_{,n}=\frac{\partial r}{\partial n}$.

A.1.2 Incompressible Model

3-d For the case of incompressible constituents, the displacements caused by a Dirac force in the solid are

$$\hat{U}_{ij}^s = \frac{1}{4\pi r\,(\rho-\beta\rho_f)\,s^2}\left[R_1\frac{\lambda_4^2}{\lambda_1^2}e^{-\lambda_1 sr}-R_2\frac{\lambda_4^2-\lambda_1^2}{\lambda_1^2}+\left(\delta_{ij}\lambda_3^2s^2-R_3\right)e^{-\lambda_3 sr}\right] \tag{A.8a}$$

with the same abbreviations R_1, R_3, λ_4 as in the compressible case, $R_2 = (3r_{,i}r_{,j}-\delta_{ij})/r^2$, and $\lambda_{1,3}$ from (1.46). The pressure caused by the same load is

$$\hat{P}_j^s = \frac{(1-\beta)\,\rho_f r_{,j}}{4\pi\beta\left(K+\frac{4}{3}G\right)rs\lambda_1^2}\left[\left(\lambda_1 s+\frac{1}{r}\right)e^{-\lambda_1 sr}-\frac{1}{r}\right]. \tag{A.8b}$$

For a Dirac source in the fluid the respective displacement solution is

$$\hat{U}_i^f = s\hat{P}_i^s \tag{A.8c}$$

and the pressure solution

$$\hat{P}^f = \frac{s\rho_f}{4\pi r\beta\lambda_1^2}\left[\left(\lambda_1^2-\lambda_4^2\right)e^{-\lambda_1 sr}+\lambda_4^2\right]. \tag{A.8d}$$

In the derivation of the poroelastodynamic boundary integral equation (2.9) several abbreviations (2.7) corresponding to an *adjoint* traction or flux are introduced. First, the *adjoint* traction solution is presented. However, due to the extensive expression only parts are given

$$\hat{T}_{ij}^s = \left[\left(\left(K-\frac{2}{3}G\right)\hat{U}_{kj,k}^s+s\hat{P}_j^s\right)\delta_{i\ell}+G\left(\hat{U}_{ij,\ell}^s+\hat{U}_{\ell j,i}^s\right)\right]n_\ell \tag{A.9}$$

$$\hat{U}^s_{kj,k}\delta_{i\ell}n_\ell = \hat{U}^s_{kj,k}n_i = -\frac{r_{,j}n_i}{4\pi r\,(\rho-\beta\rho_f)\,\lambda_1^2}\left[e^{-\lambda_1 sr}\left(\frac{1}{r}+s\lambda_1\right)\lambda_1^2\lambda_4^2\right]$$

$$\begin{aligned}
&\left(\hat{U}^s_{ij,\ell}+\hat{U}^s_{\ell j,i}\right)n_\ell \\
&\quad=\frac{1}{4\pi r\,(\rho-\beta\rho_f)}\left[\frac{6R_5}{s^2r^3}\left(\frac{\lambda_4^2}{\lambda_1^2}e^{-\lambda_1 sr}-\frac{\lambda_4^2-\lambda_1^2}{\lambda_1^2}-e^{-\lambda_3 sr}\right)\right. \\
&\qquad+\frac{6R_5}{sr^2}\left(\frac{\lambda_4^2}{\lambda_1^2}\lambda_1 e^{-\lambda_1 r}-\lambda_3 e^{-\lambda_3 r}\right)+\frac{2R_6}{r}\left(\frac{\lambda_4^2}{\lambda_1^2}\lambda_1^2 e^{-\lambda_1 sr}-\lambda_3^2 e^{-\lambda_3 sr}\right) \\
&\qquad\left.-2s\,r_{,n}r_{,i}r_{,j}\left(\frac{\lambda_4^2}{\lambda_1^2}\lambda_1^3 e^{-\lambda_1 sr}-\lambda_3^3 e^{-\lambda_3 sr}\right)-\lambda_3^2\left(\delta_{ij}r_{,n}+r_{,i}n_j\right)\left(s\lambda_3+\frac{1}{r}\right)e^{-\lambda_3 sr}\right]
\end{aligned}$$

with $R_5 = r_{,j}n_i + r_{,i}n_j + r_{,n}\left(\delta_{ij}-5r_{,i}r_{,j}\right)$ and $R_6 = r_{,j}n_i + r_{,i}n_j + r_{,n}\left(\delta_{ij}-6r_{,i}r_{,j}\right)$. The other explicit expressions are

$$\begin{aligned}
\hat{Q}^s_j = \frac{n_i}{4\pi r\,(\rho-\beta\rho_f)\,s^2}\left[\frac{e^{-\lambda_1 sr}}{\lambda_1^2}R_1\left(-\lambda_4^2\right)-\frac{1}{\lambda_1^2}R_2\left(\beta\lambda_1^2-\lambda_4^2\right)\right. \\
\left.+\beta e^{-\lambda_3 sr}\left(R_3-\delta_{ij}s^2\lambda_3^2\right)\right]
\end{aligned} \tag{A.10}$$

$$\begin{aligned}
\hat{T}^f_i = \frac{\rho_f}{4\pi r\beta\lambda_1^2}\left[\frac{n_j\,(1-\beta)\,2G}{K+\frac{4}{3}G}\left(R_2-R_1e^{-\lambda_1 sr}\right)\right. \\
+n_i s^2\left\{\frac{(1-\beta)\left(K-\frac{2}{3}G\right)}{K+\frac{4}{3}G}\left(-e^{-\lambda_1 sr}\lambda_1^2\right)\right. \\
\left.\left.+\left[\left(\lambda_1^2-\lambda_4^2\right)e^{-\lambda_1 sr}+\lambda_4^2\right]\right\}\right]
\end{aligned} \tag{A.11}$$

$$\hat{Q}^f = \frac{r_{,n}}{4\pi r\lambda_1^2}\left[\left(s\lambda_1+\frac{1}{r}\right)\left(\frac{\rho-\rho_f}{\rho-\beta\rho_f}\lambda_4^2-\lambda_1^2\right)e^{-\lambda_1 sr}-\frac{1}{r}\lambda_4^2\frac{\rho-\rho_f}{\rho-\beta\rho_f}\right]. \tag{A.12}$$

2-d The above presented 3-d solution for the incompressible model can be simply achieved by the limit $\lambda_2 \to 0$, contrary to the 2-d solutions as shown on page 19. Computing them following the formulas in section 1.3 yields for the displacement fundamental solutions

$$\hat{U}^s_{ij} = \frac{1}{2\pi s^2(\rho-\beta\rho_f)}\left[\frac{\lambda_4^2}{\lambda_1^2}R_1^{2d}-\frac{\lambda_4^2-\lambda_1^2}{\lambda_1^2}\frac{2r_{,i}r_{,j}-\delta_{ij}}{r^2}-R_3^{2d}+\delta_{ij}s^2\lambda_3^2K_0(\lambda_3 sr)\right] \tag{A.13a}$$

with the roots λ_1 and λ_3 from equation (1.46) and the other abbreviations from the compressible solution. Equation (A.13a) is the result due to a single force in the solid. The respective pressure solution for such a load is

$$\hat{P}^s_j = \frac{r_{,i}\rho_f}{2\pi s\beta}\,\frac{(1-\beta)\left(\lambda_1 srK_1(\lambda_1 sr)-1\right)}{\lambda_1^2 r(K+\frac{4}{3}G)}\,. \tag{A.13b}$$

The result due to a source in the fluid is given by

$$\hat{U}_i^f = s\hat{P}_j^s \tag{A.13c}$$

and the pressure by

$$\hat{P}^f = \frac{s\rho_f}{2\pi\beta}\,\frac{(\lambda_1^2-\lambda_4^2)K_0(\lambda_1 sr)-\lambda_4^2\ln(r)}{\lambda_1^2}\,. \tag{A.13d}$$

The explicit formulas for the adjoint tractions and fluxes are

$$\begin{aligned}
\hat{T}_{ij}^s = \frac{1}{2\pi(K+\frac{4}{3}G)}\Bigg[& -\left(\left(K-\frac{2}{3}G\right)s\lambda_1 r_{,j}n_i - \frac{s\rho_f(1-\beta)}{\beta\lambda_1}r_{,j}n_i + s\lambda_1 G(r_{,i}n_j + r_{,n}\delta_{ij})\right)K_1(\lambda_1 sr) \\
& + \frac{\beta\lambda_1^2(K+\frac{1}{3}G)-\rho_f(1-\beta)^2}{(\lambda_3^2-\lambda_1^2)\beta}\left(2R_7\left(\frac{K_0(\lambda_1 sr)}{r}+\frac{2K_1(\lambda_1 sr)}{r^2 s\lambda_1}\right)\right. \\
& \qquad \left. + s\lambda_1(r_{,i}n_j - 2r_{,n}r_{,j}r_{,i} + r_{,n}\delta_{ij})K_1(\lambda_1 sr)\right) \\
& - \frac{\beta\lambda_3^2(K+\frac{1}{3}G)-\rho_f(1-\beta)^2}{(\lambda_3^2-\lambda_1^2)\beta}\left(2R_7\left(\frac{K_0(\lambda_3 sr)}{r}+\frac{2K_1(\lambda_3 sr)}{r^2 s\lambda_3}\right)\right. \\
& \qquad \left. + s\lambda_3(r_{,i}n_j - 2r_{,n}r_{,j}r_{,i} + r_{,n}\delta_{ij})K_1(\lambda_3 sr)\right) \\
& + \frac{\rho_f(1-\beta)}{\beta\lambda_1^2}\left(4(1-\beta)\frac{R_7}{r^3 s^2\lambda_3^2} - \frac{r_{,j}n_i}{r}\right)\Bigg]
\end{aligned} \tag{A.14a}$$

$$\begin{aligned}
\hat{Q}_j^s = \frac{1}{2\pi(K+\frac{4}{3}G)}\Bigg(& -(2r_{,n}r_{,j}-n_j)(1-\beta)\frac{K_1(\lambda_1 sr)}{rs\lambda_1} \\
& - \frac{\beta\lambda_1^2(K+\frac{1}{3}G)-\rho_f(1-\beta)^2}{(\lambda_3^2-\lambda_1^2)G}\left((r_{,n}r_{,j}-n_j)K_0(\lambda_1 sr) + (2r_{,n}r_{,j}-n_j)\frac{K_1(\lambda_1 sr)}{rs\lambda_1}\right) \\
& + \frac{\beta\lambda_3^2(K+\frac{1}{3}G)-\rho_f(1-\beta)^2}{(\lambda_3^2-\lambda_1^2)G}\left((r_{,n}r_{,j}-n_j)K_0(\lambda_3 sr) + (2r_{,n}r_{,j}-n_j)\frac{K_1(\lambda_3 sr)}{rs\lambda_3}\right) \\
& - (n_j\beta + (1-\beta)r_{,n}r_j)K_0(\lambda_1 sr) + (2r_{,n}r_{,j}-n_j)(1-\beta)\frac{1}{r^2 s^2\lambda_1^2}\,\frac{\rho-\rho_f}{\rho-\beta\rho_f}\Bigg)
\end{aligned} \tag{A.14b}$$

$$\begin{aligned}
\hat{T}_i^f = \frac{s^2\rho_f}{2\pi(K+\frac{4}{3}G)\beta}\Bigg(& \left(\left(-(K-\frac{2}{3}G)(1-\beta) - \frac{\lambda_3^2}{\lambda_1^2}G + (K+\frac{4}{3}G)\right)n_i - 2Gr_{,i}r_{,n}(1-\beta)\right)K_0(\lambda_1 sr) \\
& + 2G(2r_{,i}r_{,n}-n_i)(1-\beta)\left(\frac{1}{r^2 s^2\lambda_1^2} - \frac{K_1(\lambda_1 sr)}{rs\lambda_1}\right) - \frac{\lambda_3^2}{\lambda_1^2}G\ln(r)n_i\Bigg)
\end{aligned} \tag{A.14c}$$

$$\hat{Q}^f = \frac{r_{,n}}{2\pi}\left(\frac{(\rho-\rho_f)}{\lambda_1^2(K+\frac{4}{3}G)}\left(s\lambda_1 K_1(\lambda_1 sr)-\frac{1}{r}\right)-s\lambda_1 K_1(\lambda_1 sr)\right), \tag{A.14d}$$

where $R_7 = r_{,n}(\delta_{ij}-4r_{,i}r_{,j})+r_{,j}n_i+r_{,i}n_j$ and the derivative of the distance vector in direction of the boundary normal $r_{,n}=\frac{\partial r}{\partial n}$.

A.1.3 Singular Behavior

The singularities computed in section 1.3.1 have the same form for both the compressible and incompressible models, only $\alpha=1$ has to be substituted in the expressions for $\hat{Q}_j^s$ and $\hat{T}_i^f$. The singularities of the displacement and pressure fundamental solutions from (1.62) and (1.63) are repeated here and the singularities of the adjoint tractions and fluxes are added.

3-d For $r\to 0$, the 3-d fundamental solutions can be rewritten as

$$\begin{aligned} &\textit{Regular}\\ &\hat{P}_i^s,\ \hat{U}_i^f = \mathscr{O}\left(r^0\right) \end{aligned} \tag{A.15a}$$

$$\begin{aligned} &\textit{Weakly singular}\\ \hat{U}_{ij}^s &= \underbrace{\frac{1}{16\pi G(1-\nu)}\left\{r_{,i}r_{,j}+(3-4\nu)\delta_{ij}\right\}\frac{1}{r}}_{\text{Elastostatics}}+\mathscr{O}\left(r^0\right)\\ \hat{P}^f &= \frac{s\rho_f}{4\pi\beta}\frac{1}{r}+\mathscr{O}\left(r^0\right)\\ \hat{Q}_j^s &= \frac{1}{16\pi G(1-\nu)}\left\{\alpha(1-2\nu)(r_{,n}r_{,j}-n_j)-2\beta(1-\nu)(r_{,n}r_{,j}+n_j)\right\}\frac{1}{r}+\mathscr{O}\left(r^0\right)\\ \hat{T}_i^f &= \frac{\rho_f s^2}{8\pi\beta}\frac{1-2\nu}{1-\nu}\left\{(\alpha-\beta)r_{,i}r_{,n}+n_i\left(\alpha+\beta\frac{1}{1-2\nu}\right)\right\}\frac{1}{r}+\mathscr{O}\left(r^0\right) \end{aligned} \tag{A.15b}$$

$$\begin{aligned} &\textit{Strongly singular}\\ \hat{T}_{ij}^s &= \underbrace{\frac{-\left[(1-2\nu)\delta_{ij}+3r_{,i}r_{,j}\right]r_{,n}+(1-2\nu)(r_{,j}n_i-r_{,i}n_j)}{8\pi(1-\nu)\ r^2}}_{\text{Elastostatics}}+\mathscr{O}\left(r^0\right)\\ \hat{Q}^f &= \underbrace{-\frac{r_{,n}}{4\pi r^2}}_{\text{Acoustics}}+\mathscr{O}\left(r^0\right). \end{aligned} \tag{A.15c}$$

2-d The 2-d fundamental solutions exhibit the following behavior for distances close to zero

$$\begin{aligned} &\textit{Regular}\\ &\hat{P}_i^s,\ \hat{U}_i^f = \mathscr{O}\left(r^0\right) \end{aligned} \tag{A.16a}$$

Weakly singular

$$\begin{aligned}
\hat{U}^s_{ij} &= \underbrace{\frac{1}{8\pi G(1-\nu)}\left\{r_{,i}r_{,j} - (3-4\nu)\,\delta_{ij}\ln r\right\}}_{\text{Elastostatics}} + \mathscr{O}\left(r^0\right) \\
\hat{P}^f &= -\frac{s\rho_f}{2\pi\beta}\ln r + \mathscr{O}(r^0) \\
\hat{Q}^s_j &= \frac{n_j}{8\pi G}\left(2\beta + \frac{\alpha(1-2\nu)}{(1-\nu)}\right)\ln r + \mathscr{O}(r^0) \\
\hat{T}^f_i &= -\frac{n_i s^2\rho_f}{4\pi\beta(1-\nu)}\Big(\alpha(1-2\nu)+\beta\Big)\ln r + \mathscr{O}(r^0)
\end{aligned} \tag{A.16b}$$

Strongly singular

$$\begin{aligned}
\hat{T}^s_{ij} &= \underbrace{-\frac{2r_{,n}r_{,i}r_{,j} + (1-2\nu)(r_{,n}\delta_{ij} + n_j r_{,i} - n_i r_{,j})}{4\pi(1-\nu)r}}_{\text{Elastostatics}} + \mathscr{O}(r^0) \\
\hat{Q}^f &= \underbrace{-\frac{r_{,n}}{2\pi r}}_{\text{Acoustics}} + \mathscr{O}(r^0)\,.
\end{aligned} \tag{A.16c}$$

A.2 Unknown Solid Displacements u_i^s and Fluid Displacements u_i^f (u_i^s-u_i^f-model)

For the u_i^s-u_i^f-model, only the displacement fundamental solutions have been computed. As they provide enough information about the character of this model, which is not used in the BEM implementation, the derivatives (or traction fundamental solutions) are not needed and therefore not presented.

A.2.1 Compressible Model

3-d The explicit expressions of the poroelastodynamic fundamental solutions are given in the following. The upper left of the four submatrices of the matrix $\mathbf{G6}^{comp}$ (1.43) corresponds to the displacements caused by a Dirac force in the solid

$$\hat{U}^{ss}_{ij} = \frac{1}{4\pi r\,(\rho - \beta\rho_f)\,s^2}\left[R_1\frac{\lambda_4^2-\lambda_2^2}{\lambda_1^2-\lambda_2^2}e^{-\lambda_1 sr} - R_2\frac{\lambda_4^2-\lambda_1^2}{\lambda_1^2-\lambda_2^2}e^{-\lambda_2 sr} + \left(\delta_{ij}\lambda_3^2 s^2 - R_3\right)e^{-\lambda_3 sr}\right] \tag{A.17a}$$

with the roots λ_i, $i=1,2,3$ from (1.37), $\lambda_4^2 = (\rho - \beta\rho_f)/(K + 4/3\,G)$, and the R_k from the u_i^s-p-formulation. Comparing the above fundamental solution (A.17a) with the corresponding solution in the u_i^s-p-formulation (A.1a) it is seen that they are identical. The relative fluid displacements caused by the same load and the solid displacements caused by a force in the fluid are

$$\hat{U}^{sf}_{ij} = \hat{U}^{fs}_{ij} = \frac{\phi-\beta}{\phi}\hat{U}^{ss}_{ij} - \frac{1}{4\pi r s^2\left(K+\frac{4}{3}G\right)}\frac{\alpha-\beta}{\phi\left(\lambda_1^2-\lambda_2^2\right)}\left\{R_1 e^{-\lambda_1 sr} - R_2 e^{-\lambda_2 sr}\right\}\,. \tag{A.17b}$$

For a Dirac force in the fluid the respective fluid displacement solution is

$$\hat{U}_{ij}^{ff} = \frac{(\phi-\beta)^2}{\phi^2}\hat{U}_{ij}^{ss} + \frac{1}{4\pi r s^2\left(K+\frac{4}{3}G\right)}\frac{\beta}{\phi^2\rho_f\left(\lambda_1^2-\lambda_2^2\right)}\Bigg\{ \\ R_1 e^{-\lambda_1 sr}\left(\lambda_1^2\left(K+\frac{4}{3}G\right)-(\rho-\beta\rho_f)-2\rho_f(\phi-\beta)\frac{\alpha-\beta}{\beta}\right) \\ -R_2 e^{-\lambda_2 sr}\left(\lambda_2^2\left(K+\frac{4}{3}G\right)-(\rho-\beta\rho_f)-2\rho_f(\phi-\beta)\frac{\alpha-\beta}{\beta}\right)\Bigg\}. \tag{A.17c}$$

Traction and flux fundamental solutions might be defined and derived in a way similar to equation (2.7) for the u_i^s-p-formulation. As only the u_i^s-p-formulation is used in the BEM program, they are not needed and therefore not derived.

2-d The 2-d fundamental solutions for the u_i^s-u_i^f-formulation have a similar structure as the above given 3-d solutions. The first of the four submatrices of the matrix $\mathbf{G6}^{comp}$ (1.43) corresponds the displacements caused by a Dirac force in the solid

$$\hat{U}_{ij}^{ss} = \frac{1}{2\pi s^2(\rho-\beta\rho_f)}\left[\frac{\lambda_4^2-\lambda_2^2}{\lambda_1^2-\lambda_2^2}R_1^{2d} - \frac{\lambda_4^2-\lambda_1^2}{\lambda_1^2-\lambda_2^2}R_2^{2d} - R_3^{2d} + \delta_{ij}s^2\lambda_3^2 K_0(\lambda_3 sr)\right], \tag{A.18a}$$

with the roots $\lambda_i,\ i=1,2,3$ from (1.37), $\lambda_4^2=(\rho-\beta\rho_f)/(K+4/3G)$, and the R_k^{2d} from the u_i^s-p-formulation. As before in the 3-d case, the fundamental solution (A.18a) is identical to the corresponding one (A.6a) of the u_i^s-p-formulation. The relative fluid displacements caused by the same load are identical to the solid displacements caused by a force in the fluid

$$\hat{U}_{ij}^{sf} = \hat{U}_{ij}^{fs} = \frac{\phi-\beta}{\phi}\hat{U}_{ij}^{ss} - \frac{1}{2\pi s^2\left(K+\frac{4}{3}G\right)}\frac{\alpha-\beta}{\phi\left(\lambda_1^2-\lambda_2^2\right)}\left\{R_1^{2d}-R_2^{2d}\right\}. \tag{A.18b}$$

For a Dirac force in the fluid the respective relative fluid displacement solution is

$$\hat{U}_{ij}^{ff} = \frac{(\phi-\beta)^2}{\phi^2}\hat{U}_{ij}^{ss} + \frac{\beta}{2\pi s^2\left(K+\frac{4}{3}G\right)\phi^2\rho_f}\frac{1}{\left(\lambda_1^2-\lambda_2^2\right)}\Bigg\{ \\ R_1^{2d}\left(\lambda_1^2\left(K+\frac{4}{3}G\right)-(\rho-\beta\rho_f)-2\rho_f(\phi-\beta)\frac{\alpha-\beta}{\beta}\right) \\ -R_2^{2d}\left(\lambda_2^2\left(K+\frac{4}{3}G\right)-(\rho-\beta\rho_f)-2\rho_f(\phi-\beta)\frac{\alpha-\beta}{\beta}\right)\Bigg\}. \tag{A.18c}$$

A.2.2 Incompressible Model

In this case the matrix of fundamental solutions $\mathbf{G6}^{incomp}$ is given in (1.59), but the explicit expression of the displacement fundamental solution due to a single force in the solid must be given. It is in 3-d

$$\hat{U}_{ij}^{ss} = \frac{1}{4\pi r(\rho-\beta\rho_f)s^2}\left[R_1 e^{-\lambda_1 sr} + \left(\delta_{ij}\lambda_3^2 s^2 - R_3\right)e^{-\lambda_3 sr}\right] \tag{A.19}$$

and in 2-d

$$\hat{U}_{ij}^{ss} = \frac{1}{2\pi s^2(\rho-\beta\rho_f)}\left[R_1^{2d} - R_3^{2d} + \delta_{ij}s^2\lambda_3^2 K_0(\lambda_3 sr)\right] \tag{A.20}$$

with the roots $\lambda_i,\ i=1,3$ from (1.52) and the R_k and R_k^{2d} from the u_i^s-p-formulation.

A.2.3 Singular Behavior

As explained before (see page 101), no tractions fundamental solutions were defined nor derived for the u_i^s-u_i^f-formulation, and therefore only the singular behavior of the displacement fundamental solutions has been analyzed. The singularities of all computed fundamental solutions for both the compressible and the incompressible u_i^s-u_i^f-models are presented in section 1.3.1.

B Mathematical Preliminaries

In the following, a few necessary mathematical definitions are recalled. For a rigorous presentation of these definitions the reader is referred to the mathematical literature.

B.1 Matrix of Cofactors

The *matrix of cofactors* of an $n \times n$ square matrix $\mathbf{A}$ is defined as

$$\mathbf{A}^{co} = \begin{bmatrix} a_{11}^{co} & \dots & a_{1n}^{co} \\ \vdots & \ddots & \vdots \\ a_{n1}^{co} & \dots & a_{nn}^{co} \end{bmatrix}^T , \tag{B.1}$$

where a_{ij}^{co} is the *cofactor* of element a_{ij} of the matrix $\mathbf{A}$. The cofactor is the determinant of the matrix with row i and column j deleted, prefixed with a sign depending on the element position, i.e.,

$$a_{ij}^{co} = (-1)^{i+j} \begin{vmatrix} a_{11} & \dots & a_{1\,j-1} & a_{1\,j+1} & \dots & a_{1n} \\ \vdots & \ddots & \vdots & \vdots & \ddots & \vdots \\ a_{i-1\,1} & \dots & a_{i-1\,j-1} & a_{i-1\,j+1} & \dots & a_{i-1\,n} \\ a_{i+1\,1} & \dots & a_{i+1\,j-1} & a_{i+1\,j+1} & \dots & a_{i+1\,n} \\ \vdots & \ddots & \vdots & \vdots & \ddots & \vdots \\ a_{n1} & \dots & a_{n\,j-1} & a_{n\,j+1} & \dots & a_{nn} \end{vmatrix} . \tag{B.2}$$

Details may be found, e.g., in [76]. One of the most important properties of the cofactor matrix is its relation to the inverse matrix

$$\mathbf{A}^{-1} = \frac{1}{\det(\mathbf{A})} \mathbf{A}^{co} . \tag{B.3}$$

B.2 Distributions or Generalized Functions

In many engineering fields, physical phenomena can not be described by functions, e.g., a point force at $x = a$ is everywhere zero except at the point $x = a$. Such a phenomenon is mostly treated with the Dirac "function". However, this is not a function but a distribution or generalized function. Also, sometimes it is necessary to differentiate a piecewise defined function, which is only possible in the theory of distributions. This theory was introduced by Schwartz [89]. Here, very briefly the definitions in a non

mathematical way are given. Details or more mathematical rigorous treatment can be found, e.g., in [54] or [80]. The following definitions are taken from [80].

First, a more general definition of functions the *linear functional*

$$\langle f, \varphi \rangle = \int_{-\infty}^{\infty} f(x)\, \varphi(x)\, \mathrm{d}x \tag{B.4}$$

has to be introduced with the *test function* $\varphi(x)$. Contrary to the classical function which associates a number $y = f(x)$ with every point x (the value of f at x), in the definition (B.4) the value of the functional $\langle f, \varphi \rangle$ is also a number, but represents a "weighted average" of the function f weighted by the test function φ. Such an indirect description of a function is common in engineering. A measuring instrument, such as a voltmeter, does not measure the instantaneous value $f(t_0)$ of the voltage at time t_0, but rather a weighted average over a short time period of time $2T : 1/2T \int_{t_0-T}^{t_0+T} f(t)\, \varphi(t)\, \mathrm{d}t$, where φ is a characteristics of the measuring instrument.

For our purpose here, the treatment of integral- and differential equations, it will be convenient to restrict the term test function to those functions φ that are continuous, have continuous derivatives of all orders, and vanish outside of a certain finite interval, i.e.,

DEFINITION B.2.1 A *test function* φ belongs to the space of C^∞ functions and has a compact support. The *support* of a function $f(x)$ is the closure of the set of points on which $f(x) \neq 0$.

To find a function in C^∞, i.e., vanishing outside of a certain finite interval and with continuous derivatives of all orders, is easy, but for a test function the derivatives of all orders must also be continuous at the boundaries, i.e., they must also vanish. The following function fulfills all conditions and, therefore, can be test a function

$$\varphi(x) = \begin{cases} e^{\frac{1}{x^2-1}} & |x| < 1 \\ 0 & |x| \geq 1\,. \end{cases} \tag{B.5}$$

The compact support in equation (B.5) is $[-1, 1]$ and all derivatives vanish at $|x| = 1$ [91].

For the following a definition of convergence of a test function is necessary:

DEFINITION B.2.2 A sequence $\varphi_n(x)$ of test functions *converges to zero* ($\varphi_n \to 0$) if:

(a) for each k, the sequence of kth derivatives $\varphi_1^{(k)}, \varphi_2^{(k)}, \ldots$ converges uniformly to zero;

(b) the φ_n have uniformly bounded supports, i.e., there is an interval $[a, b]$, independent of n, such that every $\varphi_n(x)$ vanishes outside of $[a, b]$.

Similarly, it is valid that $\varphi_n \to \varphi$ if the sequence $(\varphi - \varphi_n) \to 0$.

With the definition of the linear functional, now, the derivative of function f can be defined even if f is not continuous at every point. The derivative of a linear functional and later also of a distribution is given

$$\langle f', \varphi \rangle = \int_{-\infty}^{\infty} f'(x)\, \varphi(x)\, \mathrm{d}x = -\int_{-\infty}^{\infty} f(x)\, \varphi'(x)\, \mathrm{d}x = -\langle f, \varphi' \rangle\,. \tag{B.6}$$

For a continuously differentiable function f equation (B.6) results from integration by parts. The boundary terms in the partial integration vanish due to the compact support of the test function φ. A very important and often used not continuous function is the *Heaviside* or *Unit step* function

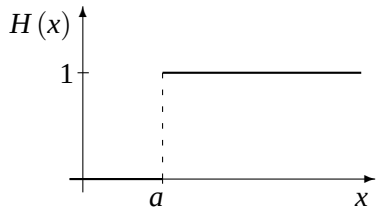

$$H(x-a) = \begin{cases} 0 & x < a \\ 1 & x > a \,. \end{cases} \tag{B.7}$$

With definition (B.6) a derivative for all x is possible

$$\begin{aligned} \langle H'(x-a), \varphi \rangle &= -\langle H(x-a), \varphi' \rangle = -\int_{-\infty}^{\infty} H(x-a)\,\varphi'(x)\,\mathrm{d}x = -\int_{a}^{\infty} \varphi'(x)\,\mathrm{d}x \\ &= \varphi(a) \ , \end{aligned} \tag{B.8}$$

using the property $H(x<a) = 0$ and in the last step that a test function vanishes as $x \to \infty$ (compact support). However, the result is not a function in the usual sense, it is a *distribution* or *generalized function*. The distribution in (B.8) is known as the *Dirac* distribution $\delta(x)$ with the known *filter* property

$$\int_{-\infty}^{\infty} \delta(x-a)\,\varphi(x)\,\mathrm{d}x = \varphi(a) \ . \tag{B.9}$$

As a consequence of equation (B.8), it is found

$$H'(x-a) = \delta(x-a) \quad \text{and} \quad H(x-a) = \int_{-\infty}^{x-a} \delta(t)\,\mathrm{d}t = \begin{cases} 0 & x < a \\ 1 & x > a \,. \end{cases} \tag{B.10}$$

With (B.9) a distribution was introduced without a definition which will follow now:

DEFINITION B.2.3 A *distribution* T is a mapping from the set of all test functions into the real or complex numbers, such that the following conditions hold:

(a) (Linearity) $\langle T, a\varphi(x) + b\psi(x) \rangle = a \cdot \langle T, \varphi(x) \rangle + b \cdot \langle T, \psi(x) \rangle$ for all test functions φ, ψ and all constants a, b.

(b) (Continuity) If $\varphi_n(x) \to 0$ in the sense defined in definition B.2.2, then $\langle T, \varphi_n(x) \rangle \to 0$

DEFINITION B.2.4 Let $f(x)$ be a piecewise continuous function on the real axis. Then we define the distribution T_f corresponding to f by

$$\langle T_f, \varphi(x) \rangle = \int_{-\infty}^{\infty} f(x)\,\varphi(x)\,\mathrm{d}x \,. \tag{B.11}$$

With the last definition the connection between the "normal" functions and the distributions are given. Distributions which are definable in terms of locally integrable functions according to equation (B.11) are called *regular* distributions. All other distributions are called *singular* distributions.

Finally, the properties of the distributions must be presented.

DEFINITION B.2.5 Let S and T be arbitrary distributions. Then we define new distributions $S+T, aT\,(a=\text{constant}), T', T\,(ax)\,(a\neq 0 \text{ is constant}), T\,(x-a), g\,(x)\,T\,(x)$ (where $g\,(x)$ is a C^{∞} function) by:

$$\langle S+T,\varphi\rangle = \langle S,\varphi\rangle + \langle T,\varphi\rangle \tag{B.12a}$$

$$\langle aT,\varphi\rangle = a\langle T,\varphi\rangle \tag{B.12b}$$

$$\langle T',\varphi\rangle = -\langle T,\varphi'\rangle \tag{B.12c}$$

$$\langle T\,(ax),\varphi\rangle = |a|^{-1}\langle T,\varphi\left(\frac{x}{a}\right)\rangle \tag{B.12d}$$

$$\langle T\,(x-a),\varphi\rangle = \langle T,\varphi\,(x+a)\rangle \tag{B.12e}$$

$$\langle g\,(x)\,T\,(x),\varphi\rangle = \langle T,g\,(x)\,\varphi\,(x)\rangle \tag{B.12f}$$

These, together with convolution (see, e.g., [80]), are the primary operations on distributions. This may seem a rather restrictive list, e.g., there is no definition for the product $S\cdot T$ of two distributions. Unfortunately, the price to be paid for introducing generalized functions (distributions) is that many operations on ordinary functions make no sense in this wider context.

The derivative of a functional was introduced with (B.6) which can be directly applied to distribution as equation (B.12c) shows. For a repeated derivation the rule (B.12c) can be generalized

$$\langle D^k T,\varphi\,(x)\rangle = (-1)^k\,\langle T,\varphi^{(k)}\,(x)\rangle \tag{B.13}$$

with the differential operator D^k denoting the k-th derivative. Thus, equation (B.13) yields the remarkable conclusion that every distribution can be differentiated as often as desired. A distribution can of course be generated by functions which are not differentiable in the ordinary sense, but the theory of distribution provides a way to differentiate such functions in the distributional sense resulting in a distribution, e.g., the Heaviside function.

A final remark must be added. All of the above mentioned can be applied also to n-dimensional distributions.

B.3 Convolution Quadrature Method

The 'Convolution Quadrature Method' developed by Lubich numerically approximates a convolution integral for $n=0,1,\ldots,N$

$$y\,(t)=\int_0^t f\,(t-\tau)\,g\,(\tau)\,\mathrm{d}\tau \quad\rightarrow\quad y\,(n\Delta t)=\sum_{k=0}^{n}\omega_{n-k}\,(\Delta t)\,g\,(k\Delta t)\,, \tag{B.14}$$

by a quadrature rule whose weights are determined by the Laplace transformed function $\hat{f}$ and a linear multistep method. This method was originally published in [63] and [64]. Application to the boundary element method may be found in [86]. Here, a brief overview of the method is given.

In formula (B.14), the time t is divided in N equal steps Δt. The weights $\omega_n(\Delta t)$ are the coefficients of the power series

$$\hat{f}\left(\frac{\gamma(z)}{\Delta t}\right) = \sum_{n=0}^{\infty} \omega_n(\Delta t)\, z^n \tag{B.15}$$

with the complex variable z. The coefficients of a power series are usually calculated with Cauchy's integral formula. After a polar coordinate transformation, this integral is approximated by a trapezoidal rule with L equal steps $\frac{2\pi}{L}$. This leads to

$$\omega_n(\Delta t) = \frac{1}{2\pi i} \int\limits_{|z|=\mathscr{R}} \hat{f}\left(\frac{\gamma(z)}{\Delta t}\right) z^{-n-1}\,\mathrm{d}z \approx \frac{\mathscr{R}^{-n}}{L} \sum_{\ell=0}^{L-1} \hat{f}\left(\frac{\gamma\left(\mathscr{R}e^{i\ell\frac{2\pi}{L}}\right)}{\Delta t}\right) e^{-in\ell\frac{2\pi}{L}}, \tag{B.16}$$

where $\mathscr{R}$ is the radius of a circle in the domain of analyticity of $\hat{f}(z)$.

The function $\gamma(z)$ is the quotient of the characteristic polynomials of the underlying multistep method, e.g., for a BDF 2, $\gamma(z) = \frac{3}{2} - 2z + \frac{1}{2}z^2$. The used linear multistep method must be $A(\alpha)$-stable and stable at infinity [64]. Experience shows that the BDF 2 is the best choice [82]. Therefore, it is used in all calculations in this thesis.

If one assumes that the values of $\hat{f}(z)$ in (B.16) are computed with an error bounded by ε, then the choice $L = N$ and $\mathscr{R}^N = \sqrt{\varepsilon}$ yields an error in ω_n of size $\mathscr{O}\left(\sqrt{\varepsilon}\right)$ [63]. Several tests conducted in [85] lead to the conclusion that the parameter $\varepsilon = 10^{-10}$ is the best choice for the kind of functions dealt with here. The assumption $L = N$ leads to a order of complexity $\mathscr{O}\left(N^2\right)$ for calculating the N coefficients $\omega_n(\Delta t)$. Due to the exponential function at the end of formula (B.16) this can be reduced to $\mathscr{O}(N \log N)$ using the technique of the Fast Fourier Transformation (FFT).

Notation Index

$\mathbf{A}$	matrix or matrix differential operator
$\mathbf{A}^*$	adjoint operator matrix
$\mathbf{A}^{co}$	matrix of cofactors
$\mathbf{a}$	vector
$a(t)$	source in the pore fluid
α	Biot's effective stress coefficient
β	abbreviation defined in equation (1.19)
c_{ij}	integral free term
$\gamma = 0.577216$	Euler constant
$\gamma(z) = \frac{\rho(z)}{\sigma(z)}$	characteristic function of the multistep method
δ_{ij}	Kronecker symbol
$\delta(t)$	Dirac distribution
E	Young's modulus
ε_{ij}	component of the solid strain tensor
F_i	component of bulk body force
$\mathbf{G}$	fundamental solutions matrix
G	shear modulus
$H(t)$	Heaviside- or unit step function
$\mathbf{I}$	identity matrix
K	compression modulus
K^s	compression modulus of the solid grains
K^f	compression modulus of the fluid
$K_i(z)$	i-th order modified Bessel function of second kind
κ	permeability
L	amount of integration steps for determining ω_n
λ_k	root of the operator matrix determinant (1.37)
N	total amount of time steps
$N_e^f(\mathbf{x})$	spatial shape function
$\mathbf{n}$, n_i	normal vector, it's component
ν	Poisson's ratio
P_j^s, P^f	pore pressure fundamental solutions
p	pore pressure

ϕ	porosity
Q_j^s, Q^f	flux fundamental solutions
q	specific flux
ρ	bulk density
ρ_f	fluid density
ρ_s	solid density
ρ_a	apparent mass density
$r = \lvert\mathbf{x}-\mathbf{y}\rvert$	distance of the points $\mathbf{x}$ and $\mathbf{y}$
$\mathbf{r} = \mathbf{x}-\mathbf{y}$	distance vector
R	poroelastic material parameter (1.2)
$\mathscr{R}$	radius of a circle in the domain of analyticity of $\hat{f}\left(\frac{\gamma(z)}{\Delta t}\right)$
$s \in \mathbb{C}$	complex Laplace variable
σ_{ij}	component of the total stress tensor
σ_{ij}^s, σ^f	solid respectively fluid partial stress
T_{ij}^s, T_i^f	fundamental solutions of the traction
t_i	traction vector component
t, τ	time
Δt	time step size
U_{ij}^s, U_i^f	fundamental solutions of the displacement
u_i^s, u_i^f	displacement vector component
V	volume
ω_n	integration weight
Ω, Γ	domain with boundary
ζ	variation of fluid volume per unit reference volume
$()^s, ()^f$	solid, fluid
$\lVert\cdot\rVert$	norm of $\cdot$
$\frac{\partial}{\partial()}$	partial derivative
∂_i or $()_{,i}$	partial derivative with respect to x_i
$\nabla = [\partial_i]^T$, $\nabla^2 = \partial_i\partial_i$	Nabla operator
$\dot{()}$	time derivative
$f(t) * g(t)$	convolution of the functions $f(t)$ and $g(t)$
$f(x) = \mathscr{O}(g(x))$	Landau symbol: $\lim_{x\to x_0}\left\lvert\frac{f(x)}{g(x)}\right\rvert < C$
$\mathscr{L}\{f(t)\}, \hat{f}(s)$	Laplace transform of f
$\mathscr{L}^{-1}\{\hat{f}(s)\}$	inverse Laplace transform of f
$\Re(s), \Im(s)$	real and imaginary part of complex number s

Bibliography

[1] Achenbach, J.D.: *Wave Propagation in Elastic Solids*. North Holland, 1980.

[2] Albers, B.: Surface Waves in Two-Component Poroelastic Media on Impermeable Boundaries – Numerical Analysis in the Whole Frequency Domain. *Preprint Weierstraß-Institut für Angewandte Analysis und Stochastik*, (862), 2003.

[3] Astley, R.J.: Infinite Elements for Wave Problems: A Review of Current Formulations and an Assessment of Accuracy. *International Journal for Numerical Methods in Engineering*, **49**(7), 951–976, 2000.

[4] Auriault, J.-L.; Borne, L.; Chambon, R.: Dynamics of Porous Saturated Media, Checking of the Generalized Law of Darcy. *Journal of the Acoustical Society of America*, **77**(5), 1641–1650, 1985.

[5] Banerjee, P.K.; Butterfield, R.: Boundary Element Methods in Geomechanics. In *Finite Elements in Geomechanics*. (Gudehus, G., Ed.), J. Wiley and Sons, London, 529–570, 1977.

[6] Beskos, D.E.: Boundary Element Methods in Dynamic Analysis. *Applied Mechanics Review*, **40**(1), 1–23, 1987.

[7] Beskos, D.E.: Introduction to Boundary Element Methods. In *Boundary Element Methods in Mechanics*. (Beskos, D.E., Ed.), Mechanics and Mathematical Methods, North-Holland, Amsterdam, New York, 1–21, 1987.

[8] Beskos, D.E.: Boundary Element Methods in Dynamic Analysis: Part II (1986-1996). *Applied Mechanics Review*, **50**(3), 149–197, 1997.

[9] Biot, M.A.: General Theory of Three-Dimensional Consolidation. *Journal of Applied Physics*, **12**, 155–164, 1941.

[10] Biot, M.A.: Theory of Elasticity and Consolidation for a Porous Anisotropic Solid. *Journal of Applied Physics*, **26**, 182–185, 1955.

[11] Biot, M.A.: Theory of Deformation of a Porous Viscoelastic Anisotropic Solid. *Journal of Applied Physics*, **27**(5), 459–467, 1956.

[12] Biot, M.A.: Theory of Propagation of Elastic Waves in a Fluid-Saturated Porous Solid.I. Low-Frequency Range. *Journal of the Acoustical Society of America*, **28**(2), 168–178, 1956.

[13] Biot, M.A.: Theory of Propagation of Elastic Waves in a Fluid-Saturated Porous Solid.II. Higher Frequency Range. *Journal of the Acoustical Society of America*, **28**(2), 179–191, 1956.

[14] Bonnet, G.: Basic Singular Solutions for a Poroelastic Medium in the Dynamic Range. *Journal of the Acoustical Society of America*, **82**(5), 1758–1762, 1987.

[15] Bonnet, G.; Auriault, J.-L.: Dynamics of Saturated and Deformable Porous Media: Homogenization Theory and Determination of the Solid-Liquid Coupling Coefficients. In *Physics of Finely Divided Matter*. (Boccara, N.; Daoud, M., Eds.), Springer Verlag, Berlin, 306–316, 1985.

[16] Boutin, C.; Bonnet, G.; Bard, P.Y.: Green Functions and Associated Sources in Infinite and Stratified Poroelastic Media. *The geophysical Journal of the Royal Astonomiacl Society*, **90**, 521–550, 1987.

[17] Bowen, R.M.: Theory of Mixtures. In *Continuum Physics*. (Eringen, A.C., Ed.), Vol. III, Acadenic Press, New York, 1–127, 1976.

[18] Bowen, R.M.: Incompressible Porous Media Models by use of the Theory of Mixtures. *International Journal of Engineering Science*, **18**, 1129–1148, 1980.

[19] Bowen, R.M.: Compressible Porous Media Models by use of the Theory of Mixtures. *International Journal of Engineering Science*, **20**(6), 697–735, 1982.

[20] Brebbia, C.A.; Domínguez, J.: Boundary Element Methods for Potential Problems. *Applied Mathematical Modeling*, **1**, 372–378, 1977.

[21] Brebbia, C.A.; Telles, J.C.F.; Wrobel, L.C.: *Boundary Element Techniques*. Springer-Verlag, Berlin, New York, 1984.

[22] Breuer, Stefan: Quasi-Static and Dynamic Behavior of Saturated Porous Media with Incompressible Constituents. *Transport in Porous Media*, **34**, 285–303, 1999.

[23] Bulant, P.: Two-point ray tracing in 3-D. *Pure and Appl. Geophys.*, **148**, 421–447, 1996.

[24] Burridge, R.; Vargas, C.A.: The Fundamental Solution in Dynamic Poroelasticity. *The geophysical Journal of the Royal Astonomiacl Society*, **58**, 61–90, 1979.

[25] Chen, J.: Time Domain Fundamental Solution to Biot's Complete Equations of Dynamic Poroelasticity. Part I: Two-Dimensional Solution. *International Journal of Solids and Structures*, **31**(10), 1447–1490, 1994.

[26] Chen, J.: Time Domain Fundamental Solution to Biot's Complete Equations of Dynamic Poroelasticity. Part II: Three-Dimensional Solution. *International Journal of Solids and Structures*, **31**(2), 169–202, 1994.

[27] Chen, J.; Dargush, G.F.: Boundary Element Method for Dynamic Poroelastic and Thermoelastic Analysis. *International Journal of Solids and Structures*, **32**(15), 2257–2278, 1995.

[28] Cheng, A. H.-D.; Badmus, T.; Beskos, D.E.: Integral Equations for Dynamic Poroelasticity in Frequency Domain with BEM Solution. *Journal of Engineering Mechanics ASCE*, **117**(5), 1136–1157, 1991.

[29] Cheng, A. H.-D.; Detournay, E.: On Singular Integral Equations and Fundamental Solutions of Poroelasticity. *International Journal of Solids and Structures*, **35**(34-35), 4521–4555, 1998.

[30] Cruse, T.A.: A Direct Formulation and Numerical Solution of the General Transient Elastodynamic Problem, II. *Journal of Mathematical Analysis and Applications*, **22**, 341–355, 1968.

[31] Cruse, T.A.; Rizzo, F.J.: A Direct Formulation and Numerical Solution of the General Transient Elastodynamic Problem, I. *Journal of Mathematical Analysis and Applications*, **22**, 244–259, 1968.

[32] de Boer, R.: *Theory of Porous Media*. Springer-Verlag, Berlin, 2000.

[33] de Boer, R.; Ehlers, W.: Theorie der Mehrkomponentenkontinua mit Anwendungen auf bodenmechanische Probleme, Teil I. Forschungsbericht aus dem Fachbereich Bauwesen 40, Universität - GH Essen, 1986.

[34] de Boer, R.; Ehlers, W.: A Historical Review of the Formulation of Porous Media Theories. *Acta Mechanica*, **74**, 1–8, 1988.

[35] de Boer, R.; Ehlers, W.: The Development of the Concept of Effective Stresses. *Acta Mechanica*, **83**, 77–92, 1990.

[36] Deresiewicz, H.: The Effect of Boundaries on Wave Propagation in a Liquid-Filled Porous Solid: II. Love Wave in a Porous Layer. *Bulletin of the Seismological Society of America*, **51**, 51–59, 1961.

[37] Deresiewicz, H.: The Effect of Boundaries on Wave Propagation in a Liquid-Filled Porous Solid: IV. Surface Waves in a Half-Space. *Bulletin of the Seismological Society of America*, **52**, 627–638, 1962.

[38] Deresiewicz, H.; Rice, J.T.: The Effect of Boundaries on Wave Propagation in a Liquid-Filled Porous Solid: III. Reflection of Plane Waves at a Free Plane Boundary (General Case). *Bulletin of the Seismological Society of America*, **52**, 595–625, 1962.

[39] Detournay, E.; Cheng, A. H.-D.: *Fundamentals of Poroelasticity*, Vol. II, *Comprehensive Rock Engineering: Principles, Practice & Projects*, Chapter 5, 113–171. Pergamon Press, 1993.

[40] Diebels, S.: Mikropolare Zweiphasenmodelle: Formulierung auf der Basis der Theorie Poröser Medien. Bericht Nr. II-4, Universität Stuttgart, Institut für Mechanik, Lehrstuhl II, 2000.

[41] Diebels, S.; Ehlers, W.: Dynamic Analysis of a Fully Saturated Porous Medium Accounting for Geometrical and Material Non-Linearities. *International Journal for Numerical Methods in Engineering*, **39**, 81–97, 1996.

[42] Domínguez, J.: An Integral Formulation for Dynamic Poroelasticity. *Journal of Applied Mechanics, ASME*, **58**, 588–591, 1991.

[43] Domínguez, J.: Boundary Element Approach for Dynamic Poroelastic Problems. *International Journal for Numerical Methods in Engineering*, **35**(2), 307–324, 1992.

[44] Domínguez, J.: *Boundary Elements in Dynamics*. Computational Mechanics Publication, Southampton, 1993.

[45] Ehlers, W.: Poröse Medien – ein kontinuumsmechanisches Modell auf der Basis der Mischungstheorie. Forschungsbericht aus dem Fachbereich Bauwesen 47, Universität - GH Essen, 1989.

[46] Ehlers, W.: Compressible, Incompressible and Hybrid Two-phase Models in Porous Media Theories. *ASME: AMD-Vol.*, **158**, 25–38, 1993.

[47] Ehlers, W.: Constitutive Equations for Granular Materials in Geomechanical Context. In *Continuum Mechanics in Environmental Sciences and Geophysics*. (Hutter, K., Ed.), CISM Courses and Lecture Notes, No. 337, Springer-Verlag, Wien, 313–402, 1993.

[48] Ehlers, W.; Graf, T.; Ammann, M.: Theoretical and Numerical Formulation of Unsaturated Soil with Application to Embankment Problems. *Tagungsband 4. Workshop Porous Media*, Zentrum für Angewandte Geowissenschaften, Tübingen, on CD, 2003.

[49] Ehlers, W.; Kubik, J.: On Finite Dynamic Equations for Fluid-Saturated Porous Media. *Acta Mechanica*, **105**, 101–117, 1994.

[50] Fedelinski, P.; Alliabadi, M. H.: The time-domain DBEM for rapidly growing cracks. *International Journal for Numerical Methods in Engineering*, **40**(9), 1555–1572, 1997.

[51] Feng, S.; Johnson, D.L.: High-frequency Acoustic Properties of a Fluid/Porous Solid Interface.I. New surface mode. *Journal of the Acoustical Society of America*, **74**(3), 906–914, 1983.

[52] Fillunger, P.: Der Auftrieb von Talsperren, Teil I-III. *Österr. Wochenschrift für den öffentlichen Baudienst*, 532–570, 1913.

[53] Fredholm, I.: Sur une Classe d'Equations Fonctionelles. *Acta Mathematica, Sweden*, **27**, 365–390, 1903.

[54] Gel'fand, I. M.; Shilov, G. E.: *Generalized Functions*, Vol. I. Academic Press, New York and London, 1964.

[55] Gilbert, F.; Laster, S.J.: Excitation and Propagation of Pulses on an Interface. *Bulletin of the Seismological Society of America*, **52**, 299–319, 1962.

[56] Graff, K. F.: *Wave Motion in Elastic Solids*. Oxford University Press, 1975.

[57] Guiggiani, M.; Gigante, A.: A General Algorithm for Multidimensional Cauchy Principal Value Integrals in the Boundary Element Method. *Journal of Applied Mechanics, ASME*, **57**, 906–915, 1990.

[58] Hörmander, L.: *Linear Partial Differential Operators*. Springer-Verlag, 1963.

[59] Kielhorn, L.: *Modellierung von Wellenausbreitung in porösen Böden: Dimensionslose Variablen für eine Randelementformulierung*. Diplomarbeit, Technische Universität Braunschweig, Institut für Angewandte Mechanik, Fachbereich Bauingenieurwesen, 2004.

[60] Kim, Y.K.; Kingsbury, H.B.: Dynamic Characterization of Poroelastic Materials. *Experimental Mechanics*, **19**, 252–258, 1979.

[61] Kupradze, V.D.: *Potential Methods in the Theory of Elasticity*. Israel Program for Scientific Translations, Jerusalem, 1965.

[62] Lewis, R.W.; Schrefler, B.A.: *The Finite Element Method in the Static and Dynamic Deformation and Consolidation of Porous Media*. John Wiley and Sons, Chichester, 1998.

[63] Lubich, C.: Convolution Quadrature and Discretized Operational Calculus. I. *Numerische Mathematik*, **52**, 129–145, 1988.

[64] Lubich, C.: Convolution Quadrature and Discretized Operational Calculus. II. *Numerische Mathematik*, **52**, 413–425, 1988.

[65] Manolis, G.D.; Beskos, D.E.: Integral Formulation and Fundamental Solutions of Dynamic Poroelasticity and Thermoelasticity. *Acta Mechanica*, **76**, 89–104, 1989. Errata [66].

[66] Manolis, G.D.; Beskos, D.E.: Corrections and Additions to the Paper "Integral Formulation and Fundamental Solutions of Dynamic Poroelasticity and Thermoelasticity". *Acta Mechanica*, **83**, 223–226, 1990.

[67] Mansur, W. J.: *A Time-Stepping Technique to Solve Wave Propagation Problems Using the Boundary Element Method*. Phd thesis, University of Southampton, 1983.

[68] Mansur, W.J.; Brebbia, C.A.: Transient Elastodynamics Using a Time-Stepping Technique. In *Boundary Elements*. (Brebbia, C.A.; Futagami, T.; Tanaka, M.; Tanaka, M., Eds.), Springer-Verlag, Berlin, 677–698, 1983.

[69] Mantič, V.: A new Formula for the C-matrix in the Somigliana Identity. *Journal of Elasticity*, **33**, 191–201, 1993.

[70] Nagy, P.B.: Observation of a new surface mode on a fluid-saturated permeable solid. *Applied Physics Letters*, **60**(22), 2735–2737, 1992.

[71] Norris, A.N.: Radiation from a Point Source and Scattering Theory in a Fluid-Saturated Porous Solid. *Journal of the Acoustical Society of America*, **77**(6), 2012–2023, 1985.

[72] Nowack, R.L.: EAS 557 Introduction to Seismology. Lecture notes, Purdue University, http://web.ics.purdue.edu/ nowack/eas557.html, 2004.

[73] Okuda, H.; Nakajima, K.; Iizuka, M.; Chen, L.; Nakamura, H.: Parallel Finite Element Analysis Platform for the Earth Simulator : GeoFEM. *International Conference on Computational Science 2003*, http://geofem.tokyo.rist.or.jp/report_common/GeoFEM03_001.pdf, Submitted to the Workshop of Computational Earthquake Physics and Solid Earth System Simulation, 2003.

[74] Ortner, N.: Regularisierte Faltung von Distributionen. Teil 2: Tabelle von Fundamentallösungen. *Zeitschrift für angewandte Mathematik und Physik*, **31**, 155–173, 1980.

[75] Pao, Y.-H.: Elastic Waves in Solids. *Journal of Applied Mechanics, ASME*, **50**, 1152–1164, 1983.

[76] Pease, M.C.: *Methods of Matrix Algebra*, Vol. 16, *Mathematics in Science and Engineering*. Academic Press, 1965.

[77] Plona, T.J.: Observation of a Second Bulk Compressional Wave in Porous Medium at Ultrasonic Frequencies. *Applied Physics Letters*, **36**(4), 259–261, 1980.

[78] Pryl, D.; Schanz, M.: Comparison of mixed and isoparametric boundary elements in time domain poroelasticity. *Engineering Analysis with Boundary Elements*, (accepted), 2005.

[79] Rashed, Y.F.: Boundary Element Primer 5: Fundamental Solutions – II Matrix Operators. *Boundary Element Communications: An International Journal*, **13**(2), 35–45, 2002.

[80] Richards, J.I.; Youn, H.K.: *Theory of Distributions: A Non-technical Introduction*. Cambridge University Press, 1990.

[81] Royer, D.; Dieulesaint, E.: *Elastic Waves in Solids: I Free and Guided Propagation*. Springer-Verlag, Berlin Heidelberg, 2000.

[82] Schanz, M.: A Boundary Element Formulation in Time Domain for Viscoelastic Solids. *Communications in Numerical Methods in Engineering*, **15**, 799–809, 1999.

[83] Schanz, M.: Application of 3-d Boundary Element Formulation to Wave Propagation in Poroelastic Solids. *Engineering Analysis with Boundary Elements*, **25**(4-5), 363–376, 2001.

[84] Schanz, M.: *Wave Propagation in Viscoelastic and Poroelastic Continua: A Boundary Element Approach*. Lecture Notes in Applied Mechanics. Springer-Verlag, Berlin, Heidelberg, New York, 2001.

[85] Schanz, M.; Antes, H.: Application of 'Operational Quadrature Methods' in Time Domain Boundary Element Methods. *Meccanica*, **32**(3), 179–186, 1997.

[86] Schanz, M.; Antes, H.: A New Visco- and Elastodynamic Time Domain Boundary Element Formulation. *Computational Mechanics*, **20**(5), 452–459, 1997.

[87] Schanz, M.; Diebels, S.: A Comparative Study of Biot's Theory and the Linear Theory of Porous Media for Wave Propagation Problems. *Acta Mechanica*, **161**(3-4), 213–235, 2003.

[88] Schanz, M.; Pryl, D.: Dynamic Fundamental Solutions for Compressible and Incompressible Modeled Poroelastic Continua. *International Journal of Solids and Structures*, **41**(15), 4047–4073, 2004.

[89] Schwartz, L.: *Théorie des distributions*. Herman, Paris, 1966.

[90] Sommerfeld, A.: *Partielle Differentialgleichungen in der Physik*. Verlag Harri Deutsch, Frankfurt/Main, 1978.

[91] Stakgold, I.: *Green's Functions and Boundary Value Problems*. Pure and Applied Mathematics. John Wiley & Sons, 2nd edition, 1998.

[92] Steinbach, O.: Mixed approximations for boundary elements. *SIAM J. Numer. Anal.*, **38**, 401–413, 2000.

[93] Telles, J.C.F.: Elastostatic Problems. In *Topics in Boundary Element Research*. (Brebbia, C.A., Ed.), Vol. 3 Computational Aspects, Springer-Verlag, Berlin, Heidelberg, New York, 265–294, 1987.

[94] Truesdell, C.; Toupin, R.A.: The Classical Field Theories. In *Handbuch der Physik*. (Flügge, S., Ed.), Vol. III/1, Springer-Verlag, Berlin, 226–793, 1960.

[95] Vardoulakis, I.; Beskos, D.E.: Dynamic Behavior of Nearly Saturated Porous Media. *Mechanics of Composite Materials*, **5**, 87–108, 1986.

[96] von Terzaghi, K.: Die Berechnung der Durchlässigkeit des Tones aus dem Verlauf der hydromechanischen Spannungserscheinungen. *Sitzungsbericht der Akademie der Wissenschaften (Wien): Mathematisch–Naturwissenschaftlichen Klasse*, **132**, 125–138, 1923.

[97] Wiebe, Th.; Antes, H.: A Time Domain Integral Formulation of Dynamic Poroelasticity. *Acta Mechanica*, **90**, 125–137, 1991.

[98] Woelke, S.: *Erstellung eines C++ Programmes für 2-dimensionale elastostatische Problemstellungen*. Entwurf im vertiefungsfach technische mechanik, Technische Universität Braunschweig, Institut für Angewandte Mechanik, Fachbereich Bauingenieurwesen, 1997.

[99] Zienkiewicz, O.C.; Chang, C.T.; Bettess, P.: Drained, Undrained, Consolidating and Dynamic Behaviour Assumptions in soils. *Geophysics*, **30**(4), 385–395, 1980.

[100] Zienkiewicz, O.C.; Shiomi, T.: Dynamic Behaviour of Saturated Porous Media; The Generalized Biot Formulation and its Numerical Solution. *International Journal for Numerical and Analytical Methods in Geomechanics*, **8**, 71–96, 1984.

Braunschweiger Schriften zur Mechanik – BSM

Bisher erschienene Berichte in dieser Reihe

1–1990 Plonski, Thomas:
Dynamische Analyse von schnelldrehenden Kreiszylinderschalen

2–1991 Wegener, Konrad:
Zur Berechnung grosser plastischer Deformationen mit einem Stoffgesetz vom Überspannungstyp

3–1992 Gröhlich, Hubert:
Finite-Element-Formulierung für vereinheitlichte inelastische Werkstoffmodelle ohne explizite Fliessflächenformulierung

4–1992 Hesselbarth, Hanfried:
Simulation von Versetzungsstrukturbildung, Rekristallisation und Kriechschädigung mit dem Prinzip der zellulären Automaten

5–1992 Schlums, Hartmut:
Ein stochastisches Werkstoffmodell zur Beschreibung von Kriechen und zyklischem Verhalten metallischer Werkstoffe

6–1992 Kublik, Frithjof:
Vergleich zweier Werkstoffmodelle bei ein- und mehrachsigen Versuchsführungen im Hochtemperaturbereich

7–1992 Bechtloff, Jürgen:
Interpolationsverfahren höheren Grades für Robotersteuerungen

8–1993 Müller, Michael:
Dreidimensionale elastodynamische Analyse von Tanks mit fluidbenetzten Einbauten

9–1993 Senker, Peter:
Stabilitätsanalyse elastischer Rotorsysteme

10–1993 Cheng, Weimin:
Schallabstrahlung einer schwingenden Reisner/Mindlin Platte

11–1993 Wiebe, Thomas:
Wellenausbreitung in poroelastischen Medien: Untersuchung mit Randintegralgleichungen

12–1993 Hahne, Matthias:
Beschreibung der plastischen Längsdehnung bei Torsion mit einem makroskopischen Stoffgesetz

13–1993 Heisig, Gerald:
Zum statischen und dynamischen Verhalten von Tiefbohrsträngen in räumlich gekrümmten Bohrlöchern

14–1994 de Araújo, Francisco Célio:
Zeitbereichslösung linearer dreidimensionaler Probleme der Elastodynamik mit einer gekoppelten BE/FE-Methode

15–1994 Kristen, Martin:
Untersuchungen zur elektrischen Ansteuerung von Formgedächtnis-Antrieben in der Handhabungstechnik

16–1994 Latz, Kersten:
Dynamische Interaktion von Flüssigkeitsbehältern und Baugrund

17–1994 Jäger, Monika:
Entwicklung eines effizienten Randelementverfahrens für bewegte Schallquellen

18–1994 August, Martin:
Schwingungen und Stabilität eines elastischen Rades, das auf einer nachgiebigen Schiene rollt

19–1995 Erbe, Matthias:
Zur Simulation von Risswachstum in dreidimensionalen, elastisch-plastischen Strukturen mit der Methode der Finiten Elemente

20–1995 Gerdes, Ralf:
Ein stochastisches Werkstoffmodell für das inelastische Materialverhalten metallischer Werkstoffe im Hoch- und Tieftemperaturbereich

21–1995 Tröndle, Georg:
Effiziente Schallberechnung mit einem adaptiven Mehrgitterverfahren für die 3-D Randelementmethode

22–1996 Degenhardt, Richard:
Nichtlineare dynamische Bauwerksprobleme und Interaktion mit dem Baugrund

23–1996 Feise, Hermann Josef:
Modellierung des mechanischen Verhaltens von Schüttgütern

24–1996 Haubrok, Dietmar:
Reibungsfreie Kontaktprobleme der 2-D Elastostatik und -dynamik als Optimierungsaufgabe mit REM-Matrizen

25–1996 Lehmann, Lutz:
Numerische Simulation der Spannungs- und Geschwindigkeitsfelder in Silos mit Einbauten

26–1996 Klein, Ralf:
Dynamische Interaktion von dünnwandigen Tragwerken und Boden mit Abschirmschlitzen

27–1996 Kopp, Thilo:
Simulation grosser inelastischer Deformationen bei Torsionsversuchen

28–1997 Harder, Jörn:
Simulation lokaler Fliessvorgänge in Polykristallen

29–1997 Lewerenz, Malte Christian:
Zur numerischen Behandlung von Werkstoffmodellen für zeitabhängig plastisches Materialverhalten

30–1997 Meywerk, Martin:
Stabilität und Verschleiss bei auf Schienen laufenden Eisenbahnradsätzen

31–1997 Plagge, Frank:
Nichtlineares, inelastisches Verhalten von Spiralseilen

32–1997 Neubert, Michael:
Richtungsregelung beim Tiefbohren

33–1998 Sangi, Daryoush:
Die Versetzungsstrukturbildung in Metallen

34–1998 Thielecke, Frank:
Parameteridentifizierung von Simulationsmodellen für das viskoplastische Verhalten von Metallen - Theorie, Numerik, Anwendung -

35–1998 Vietgen, Jürgen:
Numerische Simulation duktilen Risswachstums unter Berücksichtigung von Schädigung

36–1998 Läer, Bernard:
Einfluss transienter Anregungen auf die Zylinderkopf-Akustik

37–1998 Scheld, Christian:
Auswirkungen dynamischer Interaktionen auf das Schwingungsverhalten von Tanks

38–1999 Baaran, Jens:
Schallfeldanalyse bei sich bewegenden schallerzeugenden Körpern

39–1999 Daros, Carlos:
Wellenausbreitung in unendlich ausgedehnten piezoelektrischen Medien mit transversal isotroper Symmetrie

40–2000 Nils, Wagner:
Untersuchung der Boden-Fahrzeug-Interaktion mit gekoppelten Rand- und Finite-Element-Methoden

41–2001 Langer, Sabine:
Schalltransmission durch Isolierverglasung

42–2001 Schacht, T.:
Orientierungsabhängige Rissbildung in duktilen Metallen

43–2002 Ackerman, Lutz:
Simulation der Schalltransmission durch Wände

44–2002 Barthold, Franz-Joseph:
Zur Kontinuummechanik inverser Geometrieprobleme

45–2002 Böhrnsen, Jens-Uwe:
Dynamisches Verhalten von Schüttgütern beim Entleeren aus Silos

46–2002 Zorn, C.:
Plastisch instabile Verformung aufgrund dynamischer Reckalterung und korrelierten Versetzungsgleitens

47–2002 Küsel, M.:
Wellige Verschleissmuster auf Laufflächen von Eisenbahnrädern

48–2002 Bross, S.:
Versetzungsdynamik und Reckalterung als Ursache instabilen Materialverhaltens beim Portevin-Le Chatelier-Effekt

49–2002 Vesper, Matthias:
Modellierung von Korn und Korngrenze in polykristallinen Gefügen

50–2003 Steindorf, Jan:
Partitionierte Verfahren für Probleme der Fluid-Struktur Wechselwirkung

51–2003 Meyer, Marcus:
Reduktionsmethoden zur Simulation des aeroelastischen Verhaltens von Windkraftanlagen

52–2003 Wittich, Hauke:
Inhomogene Gleitung bei nahgeordneten CuAl-Legierungen

53–2003 Hupfer, Knut:
Einfluss der Mikrostruktur auf die Festigkeitseigenschaften von Metallschäumen

54–2004 Schmelzer, Martin:
Identifikation der Parameter von Zeitbereichsmodellen linear-viskoelastischer Werkstoffe

55–2004 Ostendorf, Michael:
Geschwindigkeitsmessungen in Silos mit der Particle Image Velocimetry

56–2004 Engelhardt, Marek:
Numerische Verfahren zur Identifizierung von Fehlstellen aus Randdaten

57–2004 Keese, Andreas:
Numerical Solution of Systems with Stochastic Uncertainties - A General Purpose Framework for Stochastic Finite Elements

58–2005 Pryl, Dobromil:
Influences of Poroelasticity on Wave Propagation: A Time Stepping Boundary Element Formulation